

THE IMPACT OF THE MANUFACTURING PROCESS ON
THE SURFACE QUALITY OF POLYETHYLENE
TEREPHTHALATE OPTICAL FILM

Amy Margaret Christine Seaman

A thesis submitted to the University of Birmingham for the degree of

DOCTORATE OF ENGINEERING

School of Chemical Engineering

College of Engineering and Physical Sciences

University of Birmingham

April 2023

UNIVERSITY OF
BIRMINGHAM

University of Birmingham Research Archive

e-theses repository

This unpublished thesis/dissertation is copyright of the author and/or third parties. The intellectual property rights of the author or third parties in respect of this work are as defined by The Copyright Designs and Patents Act 1988 or as modified by any successor legislation.

Any use made of information contained in this thesis/dissertation must be in accordance with that legislation and must be properly acknowledged. Further distribution or reproduction in any format is prohibited without the permission of the copyright holder.

ABSTRACT

This study aims to understand the ways in which the conditions of the manufacturing process of polyethylene terephthalate film can affect the surface quality of clear optical films. The purpose of gaining this understanding was to improve on existing cleaning methods and processing conditions that are currently insufficient and lead to a decrease in surface quality over time.

Flexible electronics is a growing industry within the technology sector. This growth drives demand for screens which are both flexible and scratch resistant. DuPont Teijin Films (DTF) focuses on rapid innovative product development and aspires to produce high quality, optically clear film for flexible electronic applications. An obstacle to development is the requirement for impeccable surface quality. Through this work it has been confirmed that the presence of contamination on the surfaces contacting the film within the manufacturing line is the key culprit for exacerbating surface defect formation. The project is split into three distinct parts that all aimed to deliver a deeper understanding of this problem.

The first stage of this work was to characterise the debris found on the manufacturing line to confirm the hypothesised formation pathways. Debris was analysed using a variety of analytical techniques and found it to be primarily composed of the products of PET hydrolytic and oxidative degradation.

Next, this work measured the adhesive forces present between the interacting surfaces on the line and aimed to recommend an appropriate cleaning strategy based on an understanding of these interactions. The adhesive force was measured by colloidal probe atomic force microscopy, but no consistent results were found. This is hypothesised to be due

to the contributions of surface roughness and humidity making repeatable results a challenge to acquire.

Finally, this work aimed to understand how the presence of contamination impacts surface defect formation. New lab-based models for scratch modelling at the micro-scale and for creating pseudo-dirtied surfaces were developed. Topographical and friction measurements revealed that contamination was affecting the frictional properties of the rollers by modifications to both topography and surface energy of the surfaces.

Overall, this work was able to solidify and unify much of the historical and anecdotal hypotheses within DuPont Teijin Films of how contamination plays a role in surface defect formation. Armed with this understanding now allows the business to move towards solutions that target the root of the problem.

ACKNOWLEDGEMENTS

This thesis would not have been possible without the contributions of many people. First, to DuPont Teijin Films, the University of Birmingham, and the ESPRC, an enormous thanks for facilitating and supporting this project.

To Prof. Zhenyu Zhang, thank you for your guidance and teaching, most especially in learning atomic force microscopy and helping with endless troubleshooting. To Karl Rakos, thank you for being my guide in all things WYKO, and for always having a huge smile to brighten my day, no matter how many times the microscope had gone wrong. To James Coles, thank you for providing the invaluable link to production and helping with many late-night line visits. To Dr. Richard Greenwood, thank you for your direction throughout and making sure the logistics of the project always stayed on the track. To Dr. Kieran Looney, thank you for endless encouragement when I needed to hear it most, for your unequalled technical insight, and your unwavering support. And finally, to Pierre Moussalli, the supervisor without whom I would have given up many times over, thank you. For helping in long hours of calculations, for listening when things went wrong (which they did a lot), for supporting me when covid derailed things almost entirely, and for always helping me look on the bright side – I could not have done it without you – thank you.

To the other researchers who helped contribute to this work – Jessica Nix, Stephen Booth, David Burgess, Chris Jones, Barbara Santiago Gomez, and Katlego Balemoge – thank you, this report would not exist without you.

To my friends, who made me take breaks and let me vent when I needed to, thank you for your support. To my mum, to Brian, and to Graeme, Paul, and Beth, who love me no matter

what and push me to be my best, I love you. And finally, to my father, who inspired me to become a scientist, who gave me the tools to pursue my dream, and who is the first person I call when things get tough. This is dedicated to you.

The truth resists simplicity

– John Green.

TABLE OF CONTENTS

ABSTRACT	2
ACKNOWLEDGEMENTS.....	4
TABLE OF CONTENTS	6
TABLE OF FIGURES.....	15
LIST OF ABBREVIATIONS	27
1. INTRODUCTION	29
1.1 Aim	29
1.2 Motivation for the project	29
1.2.1 Flexible electronics	29
1.2.2 Market demands	30
1.2.3 Contamination and surface damage	30
1.3 Key Objectives.....	31
1.3.1 Chemical analysis of debris	31
1.3.2 Adhesion properties	32
1.3.3 Understanding scratch formation	32
1.4 DuPont Teijin Films	33
1.4.1 History of DuPont Teijin Films	33
1.4.2 DTF product portfolio	33
1.5 Polyethylene terephthalate Synthesis.....	33

1.5.1	Chemical synthesis	33
1.5.2	Direct esterification reaction.....	34
1.5.3	Polycondensation reaction.....	35
1.6	PET film processing	36
1.6.1	The film making process.....	36
1.6.2	Extrusion & Drying.....	37
1.6.3	Forward draw	38
1.6.4	Coating Unit.....	39
1.6.5	Sideways draw and crystallisation.....	39
1.6.6	Winding and slitting.....	40
1.6.7	Cleaning regimes on D52.....	40
1.6.8	Impact of cleaning	42
1.7	Summary of historic work at DTF	43
1.8	Project scope.....	46
2.	LITERATURE REVIEW AND THEORETICAL BACKGROUND.....	47
2.1	Degradation of PET	47
2.1.1	Relevance to project objectives	48
2.1.2	Thermal degradation	48
2.1.3	Thermo-oxidative degradation.....	52
2.1.4	Hydrolytic degradation.....	56

2.1.5	Degradation during PET processing.....	59
2.2	Contact mechanics.....	62
2.2.1	Relevance to project objectives	62
2.2.2	Forces contributing to surface interactions	62
2.2.3	Using AFM to measure surface forces.....	63
2.2.4	Adhesion	66
2.2.5	Contact mechanics models.....	69
2.2.6	Adhesion and surface roughness	74
2.2.7	Capillary forces	77
2.2.8	Capillary force modelling with AFM	79
2.2.9	Humidity dependent capillary force.....	81
2.2.10	Humidity dependent capillary force and vdW forces	83
2.2.11	Capillary force and surface roughness	85
2.2.12	Capillary forces, surface roughness and deformation	89
2.2.13	Summary.....	90
3.	METHODS AND MATERIALS.....	92
3.1	Chemical composition.....	92
3.1.1	Fourier Transform Infrared Spectroscopy	92
3.1.2	Raman Spectroscopy	93
3.1.3	Energy Dispersive X-ray Spectroscopy	93

3.1.4	Gas Chromatography Mass Spectrometry	94
3.1.5	Ultraviolet High Pressure/Performance Liquid Chromatography.....	95
3.2	Topography measurement	96
3.2.1	Coherence Scanning Interferometry.....	96
3.2.2	Atomic Force Microscopy.....	98
3.3	Surface energy/adhesion measurement	100
3.3.1	Contact angle goniometry	100
3.3.2	Force modulation mode	102
3.4	Friction Measurements.....	110
3.4.1	Lateral force microscopy	110
3.5	Scratch modelling using AFM.....	111
3.6	Materials utilised for measurements	113
3.6.1	PET Film	113
3.6.2	Roller surfaces	114
3.6.3	Cleaning pads.....	114
4.	ANALYSIS OF THE COMPOSITION OF CONTAMINATION FOUND ON PET PRODUCTION LINES.....	115
4.1	Hypotheses of debris generation.....	115
4.1.1	Sublimation-condensation mechanism.....	116
4.1.2	Abrasion mechanism	120
4.2	Deposition of contamination during PET film production.....	121

4.3	Analysis of contamination	122
4.3.1	Analysis of casting drum sample	122
4.3.2	Analysis of forward draw sample	134
4.3.3	Analysis of forward-draw-adjacent sample.....	137
4.3.4	Analysis of cleaning pad samples	142
4.4	Conclusions from analysis of contamination.....	148
5.	USING ATOMIC FORCE MICROSCOPY TO UNDERSTAND ADHESION OF CONTAMINATION TO SURFACES ON PET PRODUCTION LINE.....	151
5.1	Motivation.....	151
5.2	Technique selection	152
5.3	Experimental design	153
5.4	Results of adhesion measurements.....	157
5.4.1	Summary of all adhesion experiments.....	157
5.4.2	Comparing different tip geometry	164
5.4.3	Comparing different machines.....	166
5.4.4	Comparing different applied forces	168
5.4.5	Comparing different colloidal materials.....	169
5.5	Discussion of adhesion results.....	171
5.6	Conclusions from adhesion measurements	177
6.	UNDERSTANDING THE CONTRIBUTION OF CONTAMINATION TO SURFACE DEFECT FORMATION.....	179

6.1	Scratch formation during PET film production	179
6.2	Classification of scratch types.....	180
6.2.1	Replication marks	182
6.2.2	Needles	183
6.2.3	Scuff marks	186
6.3	Scratch modelling using atomic force microscopy	187
6.3.1	Impact of changing normal force	188
6.3.2	Impact of changing film processing stage	190
6.3.3	Impact of changing temperature.....	192
6.3.4	Conclusions from scratch modelling experiments	193
6.4	The forward draw unit	195
6.5	Film to roller relative movement during PET film production	196
6.5.1	Judder	197
6.5.2	Pre and post draw	197
6.5.3	Thermal expansion	198
6.5.4	Stress relaxation	200
6.6	Scratch orientation	204
6.7	Suitability of roller design.....	206
6.8	Challenges of in-line measurements	208
6.9	In-line measurements of surface roughness	209

6.9.1	Validity of replication tapes.....	209
6.9.2	Replica tapes on the production line	211
6.10	Laboratory model for surface roughness.....	214
6.10.1	Experimental set-up	214
6.4.1	Raman analysis of laboratory model.....	216
6.4.2	Coherence scanning interferometry analysis of laboratory model	218
6.11	Friction measurements of roller surfaces	221
6.11.1	Force board friction measurements.....	221
6.11.2	Lateral force microscopy friction measurements	226
6.11.3	Conclusions of frictional studies.....	228
6.12	Conclusions of analysis of scratch formation and friction	230
7.	CONCLUSIONS AND FUTURE WORK	232
7.1	Conclusions	232
7.2	Future work.....	235
8.	BIBLOGRAPHY	237
9.	APPENDICES.....	258
9.1	Historic DTF Reporting on the “Problem of White Powder”	258
9.1.1	1966	258
9.1.2	1982	259
9.1.3	1980s-1990s.....	259

9.1.4	1995	259
9.1.5	1998-1999.....	260
9.1.6	2002	260
9.1.7	2005	261
9.1.8	2006	261
9.1.9	2007	262
9.1.10	2008	265
9.1.11	2009 - 2010.....	266
9.1.12	2011	267
9.1.13	2012	268
9.2	Mechanisms of Scratching	270
9.2.1	Deformation regimes.....	272
9.2.2	Elastic to plastic indentation	273
9.2.3	Hardness	274
9.2.4	Tensile vs. ductile fracture.....	276
9.2.5	Brittle vs. ductile materials.....	277
9.2.6	Understanding scratching mechanics	278
9.2.7	Nanotribology and atomic force microscopy	278
9.2.8	Frictional properties of PET	279
9.2.9	Bulk properties of PET	280

9.3	Stick-slip behaviour	282
9.4	All adhesion experiments	283
9.5	Modelling adhesion	288
9.5.1	Model basis.....	288
9.5.2	Model inputs.....	291
9.5.3	Assumptions of the model	292
9.5.4	Results of the model.....	295

TABLE OF FIGURES

Figure 1: PET repeat unit	34
Figure 2: Diagram of the transesterification of ethylene glycol and terephthalic acid to form the PET monomer.....	35
Figure 3: Diagram of the polycondensation reaction of BHET to form PET polymeric chain. .	36
Figure 4: Schematic of a typical DTF BoPET film manufacturing line.....	37
Figure 5: Diagram of the PET film web.....	38
Figure 6: Schematic of a typical forward draw unit.	39
Figure 7: Schematic of line operation over a 72-hour period. W1, W2 and W3 refer to the finished film winders. Making implies product is being wound at that time interval.	41
Figure 8: Primary thermal degradation by scission at ester linkage in PET.	50
Figure 9: General oxidation scheme for polymer degradation.....	53
Figure 10: Chain scission reactions of hydroperoxides.	54
Figure 11: Formation of hydroperoxides in PET.....	55
Figure 12: Top: Homolytic O-O bond scission of PET hydroperoxide to form alkoxy macroradical and $\cdot\text{OH}$, Bottom: Homolytic O-O bond scission of PET hydroperoxide to form alkoxy macroradical and $\cdot\text{OOH}$	55
Figure 13: Chain scission mechanism for hydrolytic degradation of PET.	58
Figure 14: Schematic of AFM tip approaching a sample surface, showing how the end of the tip can be modelled as a sphere on plane geometry.	64
Figure 15: Schematic example of a force modulation mode force curve.	65
Figure 16: Diagram showing how indenter and surface roughness are approximated when modelled as a perfect sphere and a perfectly flat plane.....	74

Figure 17: Schematic of sphere on plane contact for a perfectly smooth plane in the presence of a bridging meniscus..... 78

Figure 18: Schematic of sphere-plane contact in the presence of a capillary layer that bridges across surface asperities..... 85

Figure 19: Schematic of sphere-plane contact for a rough surface in a low humidity case where capillary is bridging between an asperity and the contacting sphere. 87

Figure 20: Solid lines are theoretical values of adhesion; solid points are measured adhesion for surfaces with differently sized asperities. 88

Figure 21: Schematic of sphere-plane contact for a rough surface as modelled by Farshchi-Tabriziam Kappl and Butt, 2008). 88

Figure 22: Capillary force between sphere of radius $R = 2 \mu\text{m}$ and a planar surface versus relative humidity for different distances 'a' of closest approach. The vdW forces are given by the dashed line and were calculated using equation 4 and an a_0 of 0.17nm. The contact angle of both surfaces was set to 10° 89

Figure 23: Schematic showing how a filler particle can be located in a PET film. a) particle far below the surface - no surface effect seen. b) particle below the surface, some surface topography effects seen. c) particle at the surface, partially exposed d) part..... 98

Figure 24: Diagram of typical AFM with atomically sharp tip 99

Figure 25: Schematic of the measurement of contact angle (θ_c) for a droplet on a surface. 100

Figure 26: Example of a force curve. 103

Figure 27: Left: typical AFM set-up with tip mounted on tip. Right: adapted AFM tip with microparticle glued to cantilever (not to scale). 104

Figure 28: View down optical microscope of AFM probe held by micromanipulator in plane of focus. 106

Figure 29: View down optical microscope of AFM probe held by micromanipulator above plane of focus and surface with epoxy glue in plane of focus. 106

Figure 30: View down optical microscope. Left: AFM probe held by micromanipulator making contact with epoxy glue. Right: AFM probe being moved using micromanipulator to remove excess epoxy. 107

Figure 31: View down optical microscope of the beads on a glass slide in the plane of focus. Shadow of AFM probe held above the plane of focus can be seen in the bottom left 107

Figure 32: Side-on view of AFM probe after successful colloidal probe attachment viewed through optical microscope..... 108

Figure 33: Example graph of the relationship between force on cantilever and cantilever deflection for probes of different forces with the range of the photodiode highlighted. 109

Figure 34: Schematic of a portion of the scan area of AFM image. The grid represents a part of the total pixels in a typical 512 x 512 pixel image and the red line represents the path of the AFM tip across those pixels. 112

Figure 35: Schematic of AFM tip path across entire scan area in reduced line indentation method. 113

Figure 36: Photos of the casting drum from D52 production line with white powder build up at the edges and the centre portion obscured by condensation. Samples of powder have been removed leaving clean areas of the mirror-finish exposed..... 119

Figure 37: Example schematic of the forward draw showing alternate rolls (shown pale) where powder builds up where the drum side of the film lands. 119

Figure 38: EDX analysis of casting drum sample. Sample metallised in Al to improve sampling quality. Al peak appears in red.	123
Figure 39: XPS analysis of casting drum sample, Carbon environments. Inset: Major elements present by percentage concentration.	124
Figure 40: FTIR analysis of casting drum sample; measurement repeated 4 times (1, 2, 3, 4) to check homogeneity.	125
Figure 41: Terephthalic acid-bis(2-hydroxyethyl ester).	126
Figure 42: FTIR of casting drum powder (blue - Dumfries powder debris) and compared to literature samples of b) terephthalic acid, c) terephthalic acid, bis(2-hydroxyethyl)ester, d) PET cyclic trimer.	127
Figure 43: Raman analysis of casting drum sample (red) compared to literature traces for terephthalic acid (blue) and amorphous PET (pink).	128
Figure 44: GC-MS trace of casting drum powder (red). Black line is blank spectrum.	131
Figure 45: UV-HPLC analysis of casting drum powder. Top: Pure TA sample. Bottom: Casting drum sample.	132
Figure 46: EDX analysis of forward draw sample. Sample was metallised in Al which appears as a background peak in red.	135
Figure 47: Raman analysis of FED sample (blue) compared to sample from casting drum (red)	136
Figure 48: Photos of D52 forward draw. Area where FWD adjacent sample collected from metal work shown in red.	137
Figure 49: EDX analysis of FWD adjacent sample. Sample was metallised in Al which appears as a background peak in red.	138

Figure 50: EDX analysis of Silvo cleaner. Sample was metallised in Al which appears as a background peak in red.....	139
Figure 51: Raman analysis of FWD adjacent sample (red) compared to pure Silvo cleaner sample (blue).....	140
Figure 52: Raman analysis of FWD adjacent sample (red) and casting drum sample (blue).	141
Figure 53: Top: Topographical analysis by CSI of a visually clean area of D52 FWD automatic cleaning pads. Bottom: Topographical analysis by CSI of a visually contaminated area of D52 FWD automatic cleaning pads.....	143
Figure 54: EDX elemental analysis of left: clean automatic cleaning pad, right: contaminated automatic cleaning pad. Samples were metallised in Aluminium thus its presence in the starting sample cannot be detected.....	144
Figure 55: XPS elemental analysis of clean and contaminated automatic cleaning pads. Each measurement was repeated twice (labelled 1 and 2). Left: Majority elements, Right: Trace elements.....	145
Figure 56: Carbon 1s scan from XPS analysis of left: clean automatic cleaning pad, right: dirty automatic cleaning pad.....	146
Figure 57: FTIR analysis of top: clean automatic cleaning pad, bottom: contaminated cleaning pad from D52.....	148
Figure 58: Graph of adhesion vs. relative humidity for experimental measurements of mica and PET using a colloidal tip and compared to the modelled data for the same systems. Each point represents an average of 1200 independent measurements (see section 3.3.2.3 for explanation of collection method) and standard deviations of those repeats is given by the error bars.....	158

Figure 59: Pie chart showing the split of experiments where both adhesion to mica and adhesion to PET were measured via colloidal probe force modulation AFM indicating the number of experiments where PET adhesion exceeded mica adhesion vs. the number where mica adhesion exceeded PET adhesion.....159

Figure 60: Graph of adhesion vs. relative humidity for experimental measurements of mica and PET using a sharp AFM tip and compared to the modelled data for the same systems. Each point represents an average of 1200 independent measurements (see section 3.3.2.3 for explanation of collection method) and the standard deviation of those repeats is given by the error bars.....160

Figure 61: A selection of force-distance curves collected across the experiments shown in Figure __.162

Figure 62: Typical example of a force-distance curve of very low adhesion where the noise in the baseline of the non-contact region can be seen.....163

Figure 63: Typical examples of force-distance curves where the baseline was curved, even in the non-contact region, causing the curves to be eliminated from the analysis163

Figure 64: Average adhesion of mica and pet measured using a sharp tip across five experiments using the same set-up and environmental conditions. Each bar represents average of 1200 independent measurements (see section 3.3.2.3 for explanation of collection method) and standard deviation of those repeats is given by the error bars.....165

Figure 65: Average adhesion of mica and pet measured using a colloidal tip across five experiments using the same set-up and environmental conditions. Each bar represents average of 1200 independent measurements (see section 3.3.2.3 for explanation of collection method) and standard deviation of those repeats is given by the error bars.....165

Figure 66: Average adhesion of mica and PET measured using a colloidal probe across experiments conducted in Wilton using the same procedure. Each bar represents average of 1000 independent measurements (see section 3.3.2.3 for explanation of collection method) and standard deviation of those repeats is given by the error bars.....167

Figure 67: Average adhesion of mica and PET measured using a colloidal probe across experiments conducted in Birmingham using the same procedure. Each bar represents average of 1000 independent measurements (see section 3.3.2.3 for explanation of collection method) and standard deviation of those repeats is given by the error bars.....167

Figure 68: Average adhesion to PET using the same sharp AFM tip and varying the applied normal force. Each point represents the average of 1200 independent measurements (see section 3.3.2.3 for explanation of collection method) and standard deviation of those repeats is given by the error bars.....169

Figure 69: Adhesion of a PS probe to Mica and PET across 4 days of experiments and multiple repeats of each surface with the same experimental procedure. Each bar represents an average of 1200 independent measurements (see section 3.3.2.3 for explanation of collection method) and standard deviation of those repeats is given by the error bars.....170

Figure 70: Force-distance curve collected on mica surface using a polystyrene colloidal probe171

Figure 71: Modelled adhesion of a 5 μm radius colloidal sphere to a PET surface vs relative humidity on surfaces with different RMS values.173

Figure 72: AFM tapping mode images of a DTF BoPET finished film uncoated surface. Images have been scaled such that their z-axes are identical to show difference in topography.....174

Figure 73:(a) Two deformable planes in contact containing a fixed and rolling asperity. (b) The scratch produced for both the fixed and rolling asperity after a lateral movement of 2l (Smyth et al., 1998)..... 181

Figure 74: Replication scratches found on D52 film. Scratches appear identical in shape and form and were found at a specific separation distance..... 182

Figure 75: Image of a needle captured by Zeiss light microscope. 183

Figure 76: Image of scratch caused by CR2 on D52 captured by Zeiss light microscope. Length measurement reads 2.3 mm. Double headed arrow indicates machine direction axis. 184

Figure 77: Zeiss microscope and CSI images showing height of protrusions of two scratches. A): "Light" scratch with range of width 1.5 - 5.7 μm . B) "Heavy" scratch of width 3.8 – 6.6 μm . C) CSI image of scratch track with typical "ribbing" formations. 185

Figure 78: Optical Microscopy image of Scuffing defect taken with Zeiss light microscope. Length labels read 0.1 mm, 0.1 mm and 0.2 mm respectively left to right. Marker pen at top right is to help the surface focus. 187

Figure 79: Cross-section profiles of scratches in PET surface formed at ambient and elevated temperatures utilising 1V deflection..... 193

Figure 80: Schematic of a typical forward draw unit 196

Figure 81: Diagram showing how tension changes against distance for an idling cooling roll. 202

Figure 82: Diagram showing how tension changes against distance for a driven cooling roll 203

Figure 83: Diagram of film web as it travels through the stenter 205

Figure 84: a) Film as it enters the stenter with scratches across the web aligned in the MD. b): The same film after exit from the stenter after undergoing sideways draw and the resulting angle of the original scratches.....205

Figure 85: Graph of average surface roughness in microinches of cooling roll 1 measured via line profile vs tonnes of PET processed from installation onwards.....207

Figure 86: Comparison of true and replicated surfaces of roller surface. Top Left: Replicated surface at large field of view. Bottom Left: Replicated surface at small field of view. Top right: Real surface at large field of view. Bottom right: Real surface at small field of view.....210

Figure 87: Comparison of real and replicated surfaces of Melinex 383. Top left: Replicated surface at large field of view. Bottom left: Replicated surface at small field of view. Top right: Real surface at large field of view. Bottom right: Real surface at small field of view.....211

Figure 88: Graph of the S_{sk} values as measured by CSI of CR1 replica tapes taken when line was dirty and clean. Z-axis scale has been removed for proprietary reasons.212

Figure 89: Graph of S_v values measured by CSI of CR1 replica tapes taken when the line was dirty and clean. Z-axis scale has been removed for proprietary reasons213

Figure 90: Schematic of an idealised surface versus a surface where half the valleys are halved in depth and how the average plane and average valley depth changes.....213

Figure 91: Graph of S_a values measured by CSI of CR1 replica tapes taken when the line was dirty and clean. Z-axis scale has been removed for proprietary reasons214

Figure 92: Schematic illustration of laboratory rig for generating contamination on roller sample.215

Figure 93: Raman spectra of pseudo dirty roller compared to casting drum sample.217

Figure 94: Raman spectra of pseudo dirty roller sample compared to a clean roller.218

Figure 95: Images of roller surface in 3 different states imaged using CSI. a) Roller sample dirtied by exposure to molten PET vapours for 6 hours. b) Sample after subsequent rubbing with PET film (Pseudo dirty). c) Sample after cleaning with Silvo and ammonia hydroxide. Numerical z-scale has been omitted for proprietary reasons.....219

Figure 96: CAD design for component for force board friction measurements to allow intimate contact between PET film and roller surface.221

Figure 97: Force board stage. Left: with no attachment on arm and roller sample fixed beneath. Right: with 3D printed head attached (head not from this work and is provided to show an example for clarity).222

Figure 98: Graph showing average coefficient of dynamic friction from 1000 measurements for a clean and dirty roller as measured by force board during tangential motion. Error bars represent the standard deviation of the data set.....223

Figure 99: Histogram of coefficient of friction for pseudo dirty roller surface measured at 2 N applied force. Inset: Histogram of coefficient of friction for clean roller surface measured at 2 N applied force224

Figure 100: Graph showing average coefficient of dynamic friction for a clean and dirty roller as measured by force board during tangential motion, with dirty results split according to the bimodal distribution of the data. Error bars represent the standard deviation of the data set.225

Figure 101: Graph showing average coefficient of static friction for a clean and dirty roller as measured by force board during tangential motion. Error bars represent the standard deviation of the data set.225

Figure 102: Graph showing average coefficient of dynamic friction for a clean and dirty roller as measured by lateral force microscopy with a 5 μm scan area and 1 Hz scan rate. Error bars represent the standard deviation of the data set.227

Figure 103: Graph showing average coefficient of dynamic friction for a clean, dirty, and Silvo treated roller as measured by lateral force microscopy with a 5 μm scan area and 1 Hz scan rate. Error bars represent the standard deviation of the data set.228

Figure 104: Sampling locations for Bret Cooper’s work 2007.....263

Figure 105: Percentage of scratches found on the air and drumside of film samples analysed.263

Figure 106: Average direction of scratches found on drumside of film samples analysed. ...264

Figure 107: D52 drumside scratch length.264

Figure 108: Graph showing the number of needle scratches vs. time in mins since last CR2 clean during clear film production.266

Figure 109: Summary of the material science and mechanical considerations while studying the scratching behaviour of polymers (Lim, 2005).....271

Figure 110: Schematic of sphere on plane contact for predicting adhesion from theory.....288

Figure 111: Graph of normalised dry adhesion against λ values for sphere's of different radii.294

Figure 112: Schematic to show how varying models the surface compared to a sphere of a given radius (blue). Going from small λ on the left to large λ on the right.....294

Figure 113: Graph of adhesion vs relative humidity at 21°C for a 5000 nm radius sphere contacting perfectly smooth surfaces of PET and mica.295

Figure 114: Graph of adhesion vs relative humidity at 21°C for a 5 nm radius sphere contacting perfectly smooth surfaces of PET and mica.296

Figure 115: Graph of adhesion vs relative humidity at 21°C for a 5000 nm radius sphere contacting surfaces of PET and mica with RMS values of 2 and 0.5 nm respectively.....297

Figure 116: Graph of adhesion vs relative humidity at 21°C for a 5 nm radius sphere contacting surfaces of PET and mica with RMS values of 2 and 0.5 nm respectively.....298

LIST OF ABBREVIATIONS

AFM	Atomic force microscopy
BE	Blank edge
BHET	Bis(2-Hydroxyethyl) terephthalate
BoPET	Biaxially orientated polyethylene terephthalate
CR	Cooling roll
CSI	Coherence Scanning Interferometry
D52	Dumfries 52 production line
DMT	Derjaguin-Muller-Toporov
DTF	DuPont Teijin Films
EDX	Energy dispersive x-ray spectroscopy
EG	Ethylene glycol
FE	Feed edge
FMM	Force modulation mode
FTIR	Fourier transform infrared spectroscopy
FWD	Forward draw
GC-MS	Gas chromatography mass spectrometry
ICI	Imperial Chemical Industries
IR	Infrared
JKR	Johnson, Kendall and Roberts
LFM	Lateral force mode
MD	Machine direction

MDO	Machine direction orientator
PET	Polyethylene terephthalate
PH	Preheat roll
PS	Polystyrene
R&D	Research and development
RH	Relative humidity
RMS	Root mean squared
TA	Terephthalic acid
TD	Transverse direction
T_g	Glass transition temperature
UV-HPLC	Ultra-violet high pressure liquid chromatography
XPS	X-ray photoelectron spectroscopy

1. INTRODUCTION

1.1 AIM

This study aims to understand the ways in which the manufacturing process of polyethylene terephthalate (PET) film can affect the surface quality of clear optical films. This work focuses on understanding the composition, behaviour, and impact of contamination present during PET film production on surface quality. This work is especially relevant PET films for flexible electronic applications where the specifications for defect free products are exceedingly high.

1.2 MOTIVATION FOR THE PROJECT

1.2.1 FLEXIBLE ELECTRONICS

Flexible Electronics is a large and growing volume opportunity for super clear, “defect free” polyester films for consumer electronics and other applications (Mordor Intelligence, 2021). Flexible Electronics is a key focus area for DuPont Teijin Films (DTF) in their market development efforts, where they are presently viewed as an industry leader.

PET film is considered a great choice for components including touch screens, light collimated films, holographic reflector films, polarising films, diffusing films, electromagnetic interference shielding films, and can have desirable properties including being anti-scratch, anti-fingerprint. PET films are, by nature, flexible and the DTF biaxial process gives Biaxially orientated PET (BoPET) films high tensile strength. PET is also chemically inert and resistant to abrasion, heat, and moisture – and its surface properties can be easily further adapted with coatings as it has a smooth, regular surface. It is frequently used in display applications where there is a requirement for high dimensional control, thermal stability, and flatness.

1.2.2 MARKET DEMANDS

Products for the flexible electronic applications market demand very high surface quality. Films must be free of scratches and scuffs and any other visual defects, both for screen and printing applications. The films produced are transparent and range in thickness from 125 μm to 250 μm . Within DTF the clear films for the European flexible electronics market are currently manufactured on one of the units in the Dumfries Plant owned by DTF, unit D52.

The requirements for pristine surface quality have been increasing over time, and the business response has been focused on optimising existing equipment and processing conditions to meet that need. However, in recent years the level of improvement has plateaued, while customer expectations have not.

Customer targets for surface performance are striving:

- To continually reduce the maximum permitted single defect size (mms in length and microns in width)
- To continually reduce the number of smaller defects permitted per unit area
- To continually increase the distance between neighbouring permitted defects

1.2.3 CONTAMINATION AND SURFACE DAMAGE

At present, to meet this need, D52 requires many hours of downtime for cleaning regimes which help keep defect formation within an acceptable level. These cleaning routines consistently improve surface quality, leading to the assumption that the surface damage is caused or exacerbated by the presence of contamination or “debris”. However, this down time increases running costs and decreases efficiency on the production line. To achieve the targets set by customers at profitable efficiencies, improvements are required in the reduction

of contamination build-up, with the intention that better and more targeted cleaning strategies will reduce the need for full line stops.

The evidence that this debris or contamination is the main barrier to improved surface quality is derived from the fact that from the start of a production cycle, when the line is considered in a “pristine” condition, the product produced is well within specifications. Over the course of production this surface quality standard decreases, with the number of scratches increasing, particularly at the extreme edges of the web, until the film surface quality falls below customer specification. Then, after subsequent cleanings to remove contamination from the line, the original film surface quality is restored.

This work aims to expand and clarify understanding of this challenge across three objectives.

1.3 KEY OBJECTIVES

1.3.1 CHEMICAL ANALYSIS OF DEBRIS

The first objective of this project was to demonstrably confirm the composition of the debris found in the forward draw of the PET film line that is believed to be the exacerbator of surface damage during production of clear film grades.

In order to do this a vast array of chemo-analysis and spectroscopic techniques were employed. This work can be found in Chapter 4. Samples of contamination from various points on the production line were analysed using Raman, FTIR, EDX, XPS, MS-GS and UVPLC and compared to literature spectra. These data were also compared to the expected products of PET degradation which are known from the literature.

1.3.2 ADHESION PROPERTIES

The next objective of the project was to use colloidal probe microscopy to understand the adhesive properties of the PET and roller surfaces. The purpose of this was to understand how and where debris might accumulate on the line taking into account factors of temperature, contact time, normal contact force, surface roughness and relative humidity (RH), all of which can be replicated in an AFM measurement. This was to establish if debris is carried down the line, or if it lingers where it is generated. The results of this work can be found in Chapter 5. It was also hoped to be used to inform how cleaning methods should be employed in order to remove contamination.

1.3.3 UNDERSTANDING SCRATCH FORMATION

The final objective of this project was to understand the factors affecting the initiation and creation of scratches on PET film during production. This work can be found in Chapter 6. This begins first with collating and describing the types of scratches typically seen on films during production. A novel method for modelling scratching using atomic force microscopy as a micro-indenter is then shown and described.

Next, the factors influencing scratch formation and length are discussed. In particular, the sources of relative movement possible on the production line. The impact of friction was more closely examined in particular. Roller surfaces from the production line were analysed via coherence scanning interferometry and the clean and contaminated surfaces' frictional characteristics measured using lateral force microscopy and friction rig.

Understanding how scratches form in the context of this processing environment using micro- or even nano-scale experimental models and techniques has not been attempted before by

DTF. It presents an opportunity for DTF to understand the role of debris in defect formation at a fundamental level.

1.4 DUPONT TEIJIN FILMS

1.4.1 HISTORY OF DUPONT TEIJIN FILMS

DuPont Teijin Films (DTF) is a multinational company which began as a 50:50 joint venture between DuPont and Teijin in 2000. It was a merging of DuPont Polyester Films and Teijin Film assets, with the DuPont part having absorbed ICI Films in 1998. DuPont Teijin Films is a leading global producer of PET polyester films, focusing on specialty film products and related services for the Healthcare, Photovoltaics, Durable Labels, Imaging Media, Flexible Electronics and Packaging industries. Of these industries, the flexible electronics sector is one of the fastest growing.

1.4.2 DTF PRODUCT PORTFOLIO

DTF focuses on rapid new product and application development, which is possible due to the versatility of PET, despite its relatively simple chemistry. DTF has a vast range of products that are obtained by modification to the bulk and/or surface of the film using combinations of organic additives, inorganic colloidal particles, and organic and inorganic coatings. Multi-layer structures, produced by co-extrusion, allow yet further differentiation of the basic substrates.

1.5 POLYETHYLENE TEREPHTHALATE SYNTHESIS

1.5.1 CHEMICAL SYNTHESIS

Polyethylene terephthalate is a linear aromatic polyester. It has a rigid and planar structure which is imparted by the presence of aromatic rings with carboxylate groups in the backbone. The repeat unit of the polymer is shown in Figure 1. PET is a saturated polyester produced via

an esterification reaction to produce bis-hydroxyethyl terephthalate (BHET) and subsequent step-growth polymerisation. The formation of the BHET monomer can be achieved either by the transesterification of dimethyl terephthalate (DMT) and ethylene glycol (EG) or by the direct esterification reaction of terephthalic acid (TA) and ethylene glycol.

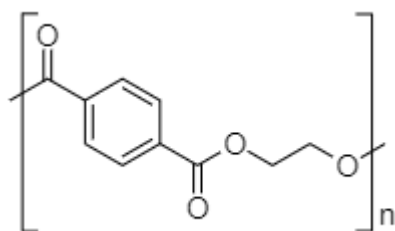


Figure 1: PET repeat unit

1.5.2 DIRECT ESTERIFICATION REACTION

Prior to the 1960's, the former DMT route was favoured as TA was not readily available as a starting material. However, in the late 1960's, the first industrial scale synthesis of TA was achieved and so the latter route has been used subsequently. This is a more favourable route as there is no need for a metal esterification catalyst, and an excess of EG is not required, unlike in the DMT route. The TA route is also more economical as the TA can be imported readily as a powder whereas dimethyl terephthalate comes as a hot liquid and hence cannot be transported easily across the world. In addition, TA esterification does not involve handling a methanol by-product.

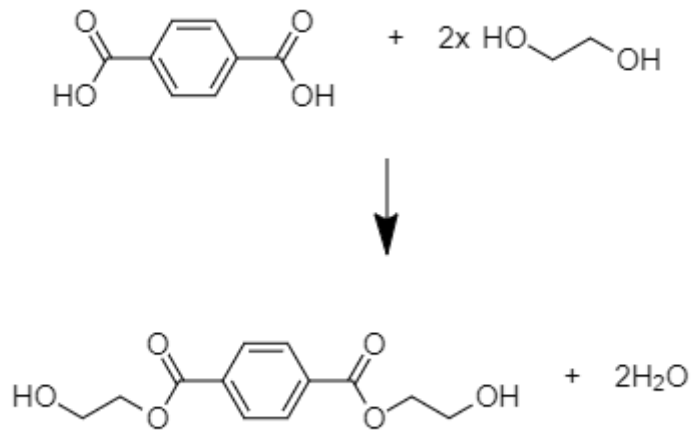


Figure 2: Diagram of the transesterification of ethylene glycol and terephthalic acid to form the PET monomer.

The reaction to form the ester bond is shown in Figure 2. Formation of the monomer releases two molecules of water as a biproduct. For every molecule of the acid, it requires two molecules of glycol. It is carried out under high pressure (~3 bar) and high temperature (230-260°C). The BHET acts as the monomer for the subsequent polycondensation polymerisation reaction.

1.5.3 POLYCONDENSATION REACTION

Following monomer production, the subsequent polymerisation proceeds in the presence of a catalyst (usually Sb₂O₃). This reaction requires high vacuum and high temperatures (in excess of 290°C) and results in long polymer chains, as shown in Figure 3. The reaction occurs in the melt phase leading to monomer coupling and the evolution of EG.

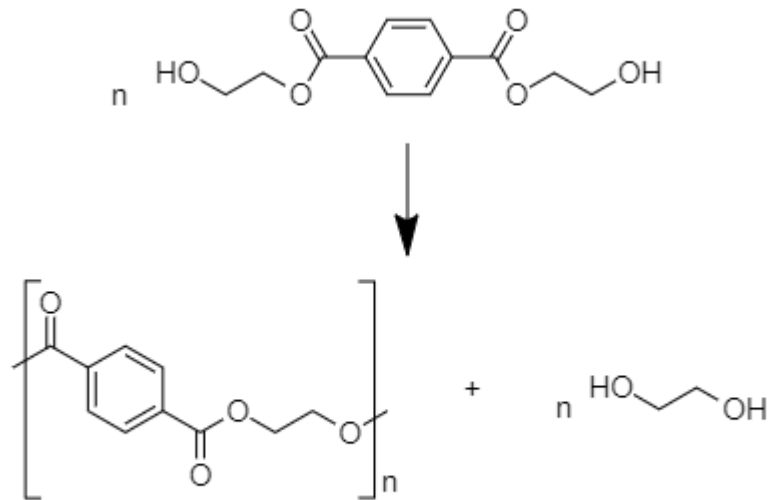


Figure 3: Diagram of the polycondensation reaction of BHET to form PET polymeric chain.

As the reaction proceeds and EG is produced (and removed via vacuum) the viscosity and molar mass of PET increases. Ideal average molar mass for PET for filming in the DTF process is a degree of polymerisation around 100.

1.6 PET FILM PROCESSING

1.6.1 THE FILM MAKING PROCESS

This section briefly describes the DTF production process to make PET films. While this description applies more generally to all of the processing lines within the DTF umbrella, specific focus is given to the Dumfries 52 unit as this is the line where the clear flexible electronic application products are manufactured. The filming process described was developed by Adams et al. in the late 1950s. (Adams and Gerber, 1957). A schematic of the process is shown in Figure 4.

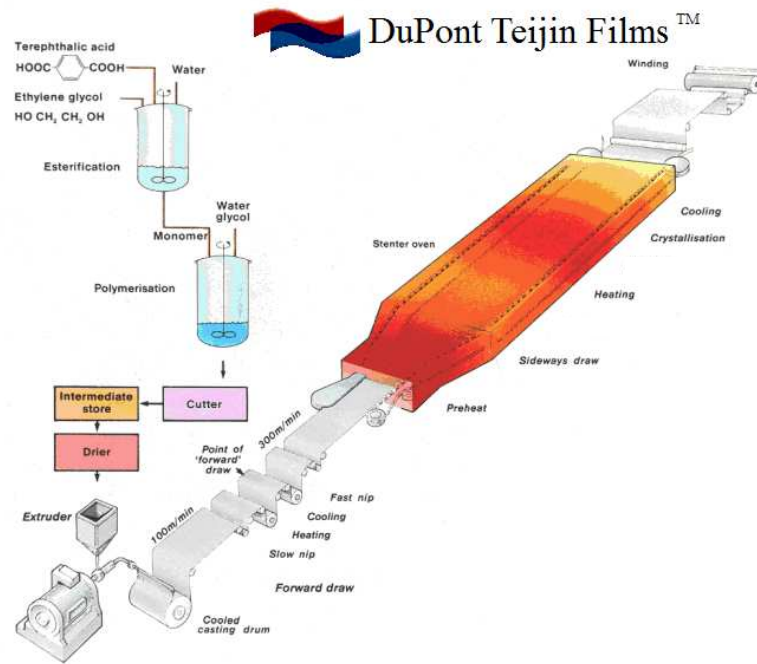


Figure 4: Schematic of a typical DTF BoPET film manufacturing line.

1.6.2 EXTRUSION & DRYING

After synthesis the resulting molten PET is extruded as a lace, cooled, and cut into chips. For the D52 unit this is done in a nearby batch polymer plant. After formation the chip is transported to the filming line where the chips are dried prior to the filming process. To do this, chips are heated to temperatures of $\sim 150^{\circ}\text{C}$ for 3 or more hours to remove any excess water which helps to prevent hydrolytic degradation of the PET chains. Higher temperatures are avoided as they can lead to thermo-oxidative degradation.

At the start of the filming process the PET chips are heated in an extruder through a combination of thermal and physical processes, filtered and then extruded through a die. The die has a slit shaped nozzle, so the molten PET emerges as a uniformly thick melt curtain onto a cooled casting drum which rapidly quenches the film. This sheet of PET is known as “cast” film. This film is amorphous, and the polymer chains are randomly orientated in every

direction throughout the film web. The side of the film web which contacts the casting drum first is known as the drumside, and the other is known as the airside. Often there can be differences in crystallinity of the two sides due to the different quenching rates at this stage of production. At this stage the film crystallinity is typically less than 25%.

Since the majority of dies used by DTF are so-called “end-fed”, the web can be characterised as the full spread of film from the feed edge (FE) which refers to the edge closer to the side of the die which the melt flows into, to blank edge (BE). This is shown schematically in Figure 5. Many parameters which are measured during product development are taken at a specified point on the web. A film making line can vary in width from one-to-many metres and produce film reels many kilometres in length.

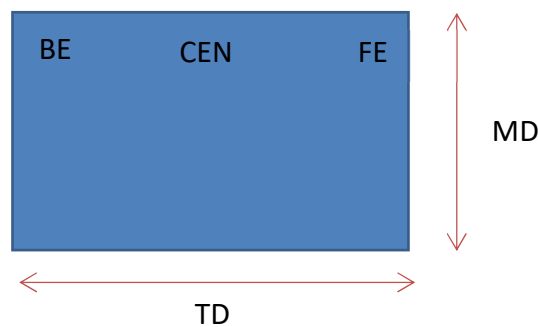


Figure 5: Diagram of the PET film web.

1.6.3 FORWARD DRAW

The cast film is then heated to approximately 90°C and stretched along its direction of travel to typically 3 to 3.5 times its original length in a unit of the production line known as the forward draw (FWD) or machine direction orientator (MDO). This produces a film which has molecules orientated in the direction of travel (machine direction, MD), with a typically crystallinity exceeding 30%. A schematic of a typical unit is shown in Figure 6.

The forward draw unit is particularly pertinent to the work of this project, so a more detailed description of this unit is detailed in Section 6.4.

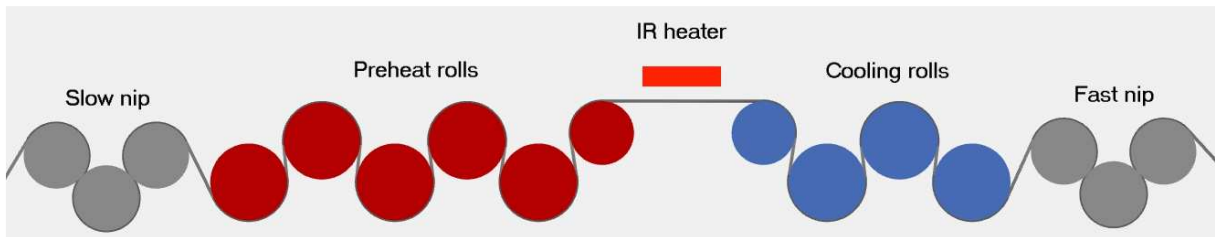


Figure 6: Schematic of a typical forward draw unit.

1.6.4 COATING UNIT

After the forward draw unit, the film then passes through the coating unit where a large range of aqueous coatings can be applied at the 1 - 10 micron thickness level to either the top or bottom of the film. At DTF this is most commonly achieved with gravure coating rolls. Example coatings include anti-fog, anti-suff, anti-static, adhesion pre-treats for ink, photopolymers and more, as well as coatings to promote or reduce slip.

1.6.5 SIDEWAYS DRAW AND CRYSTALLISATION

Following coating, the film then passes through a long compartmentalised forced convection air stenter, which has a sequence of heating and cooling zones. The film is gripped by clips connected by a chain which runs along a rail, and is again heated, the water evaporated from the coating (if present), and then stretched. This time the stretch is perpendicular to its direction of travel of the film. This is known as the transverse direction (TD) and is contactless. This results in a polymer film with molecules orientated biaxially, making it stronger in the plane of the sheet than it would otherwise be. This is known as BoPET (Biaxially orientated polyethylene terephthalate).

Finally, the film is exposed to high temperatures (220-240°C) and then cooled in stages. This step allows the desired level of polymer crystallinity to be achieved, typically between 45-50%. This is important as crystallinity is critical in many of the desirable properties of PET – for example thermal and dimensional stability, and tensile strength.

1.6.6 WINDING AND SLITTING

Following the sideways draw and crystallisation steps, the film moved through a transport zone before being wound onto reels which can be slit into different widths and lengths according to customer requirements.

1.6.7 CLEANING REGIMES ON D52

During a normal production cycle, the cleanliness of the line, and in particular the FWD unit is maintained with several cleaning regimes. In the context of this project is important to establish what cleaning methods are currently in use on D52.

1.6.7.1 *AUTOMATIC IN-LINE CLEANING*

Some of the cooling rolls are fitted with automatic cleaners that run along the underside of the roller once every few minutes. Anecdotal evidence (Coles, 2009a) states that film quality gets worse if they are not used. The automatic cleaners consist of a sandpaper-like material – Al₂O₃ particles encased in a resin- that can dislodge dirt/debris from the roller. They are changed approximately once a shift (every 12 hours) or more frequently if film quality is poor.

The automatic cleaners are found to improve surface quality of product if used and manual and full line cleans are required more often when they are not in use. However, they also come with some downsides. As will be discussed in Chapter 4 of this report, the pads are known to be accumulating chrome over time – indicated they are abrading away the roller surface. A second problem is that they also shed pad material into the production line over

time. This was discovered during an assessment of various pad types during a 2009 study where the weight change was measured per number of traverses of the cleaning pads on the roll (Coles, 2009a). Alumina particles from the sandpaper-like surface of the pads are gradually lost into the process where it can move further down the line, carried by the film, and cause issues elsewhere, such as in the coating heads, or causing scratches in the transport zones further down the production line. This gradual shedding also presumably comes with a decrease in pad performance over time, as the effective smoothing of the pad as it sheds its abrasive particles means it becomes less able to entrap debris and remove it from the roll.

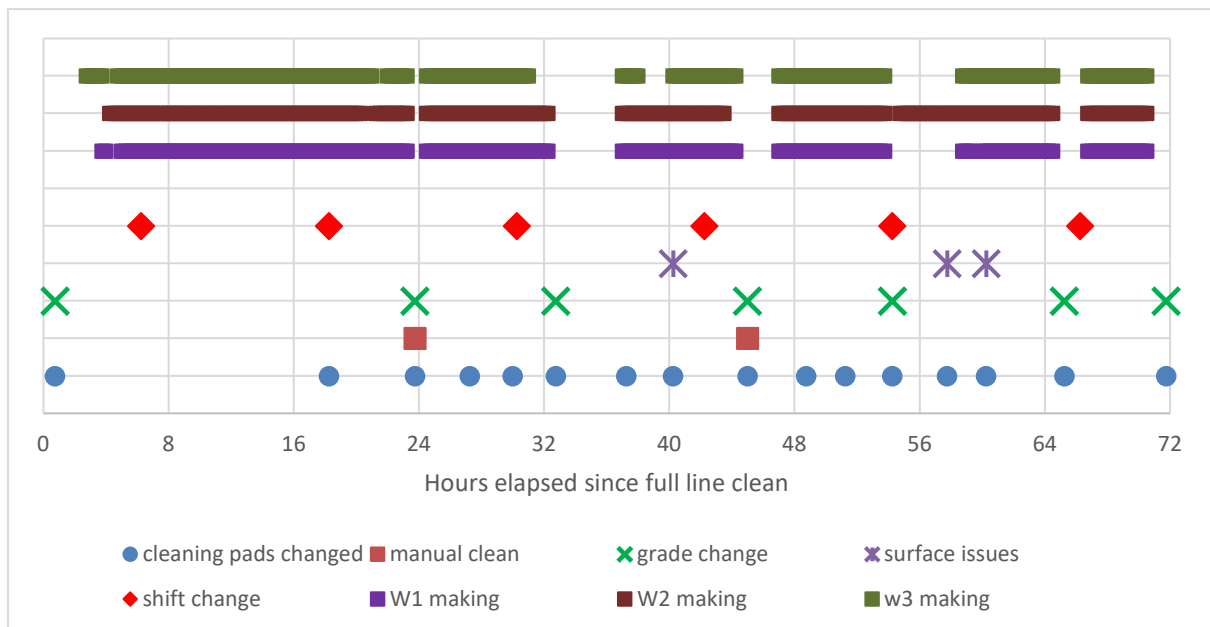


Figure 7: Schematic of line operation over a 72-hour period. W1, W2 and W3 refer to the finished film winders. Making implies product is being wound at that time interval.

At present the pads are changed multiple times per shift, as can be seen in Figure 7.

In summary, the pads, while better than nothing in terms of in-line cleaning, are potentially damaging to the rolls, cause problems in other systems, and have to be changed regularly, which is costly overall.

1.6.7.2 *MANUAL IN-LINE CLEANING*

During a grade change, pads on extendable rods are run manually by an operator along the underside of all rolls in the forward draw while they are rotating. These cleaning pads are similar to the automatic cleaning pads but have a larger grit size so are more abrasive. A manual clean can also be triggered if there are pervasive surface issues (especially repeat marks which can be identified by matching their frequency with individual roll diameters) during production. During manual cleans the in-line coating heads (baths containing recirculated coating liquid which is applied to the coating roll) must be removed as the pads shed grit which can clog the inline coating head. Therefore, during a manual clean the line will not be making coated products for flexible electronic applications.

1.6.7.3 *FULL LINE CLEAN*

The last resort for improving line cleanliness is to do a 'full-line clean'. This requires the line to shut down completely. All rolls – including casting drum and transport rolls are cleaned with ammonia solution and paper towels. Cooling rolls and sometimes the casting drum and preheats are also cleaned and polished with Silvo and a cleaning pad. Silvo is a polishing agent which contains isopropyl alcohol, silicon dioxide, ammonia solution and oleic acid.

1.6.8 IMPACT OF CLEANING

It is observable on the production line that there is a visual difference on the rolls from before compared to after cleaning, they go from matt-like to shiny. This matt-ness appears after 9 – 12 hours of running depending on the product and the process temperatures. Film surface quality from one line clean to the next tends to experience a slow and steady decline over the following 48 hours – this time is extended by in-line manual cleans.

1.7 SUMMARY OF HISTORIC WORK AT DTF

A full literature review of all the historic work at DTF relevant to this project can be found in appendix 9.1. A summary is presented below providing project context and supporting the project scope and aims. The historic work of DuPont Teijin Films into surface damage and contamination over the last 50 years is extensive, though the focus has continually shifted.

Initially, from the 1950's onwards, much of the focus was on identifying so-called "white powder" and removing it, especially around the stenter. A summary of this work was produced by Pemberton and Stening (Pemberton and Stening, 1966). This white powder was analysed and found to be made up of oligomers of PET as well as other short chain organic molecules bearing similarities to the building blocks of PET, for example terephthalic acid and terephthalic esters. This was believed to originate from PET degradation that occurred in the melt system and was released from the PET matrix in the subsequent heating zones of the production line.

More was learnt about such degradation processes and their products in the early 60s via laboratory tests and it was established that degradation rate was increased by heat, oxygen, and water. Improving air flow in the stenter, introducing more stable polymers, eliminating water and oxygen from the melt systems and other gradual improvements were made through the 70s and 80s (Donnellan, 1989c, 1989b; Donnellan and Cook, 1990). These improvements in the stenter, extruder and transportation rolls meant that by the 90s, the problems of white powder in the stenter were reduced and so the focus shifted to the forward draw where white powder was also seen at times.

It was also during the 90s that surface damage and scratching became more of a pressing concern to researchers, as higher quality control standards on surface were being imposed by

customers. Early in the work into the forward draw there was a general perception that contamination, in part caused by and in combination with relative movement between film web and rollers, was the source of surface damage, however the exact role the contamination played was unclear.

The forward draw – the region of the production line where the film is stretched along the machine direction - was of particular focus. This is because while contamination can theoretically occur anywhere on the line, the forward draw is the point on the line where film-roller contact is occurring with the highest likelihood of relative movement between the film and the roller. This relative movement can be the cause of scratch formation and is due to the temperature and speed changes of the film web around the draw. Therefore, work focused on minimising relative movement by ensuring good quenching of the film post-draw as well as optimising roller drives and tensions. This put direct investigation of contamination and its role on the back burner for several years.

Modelling and finite element analyses were used to correlate processing conditions with scratch length using models of stress relaxation and thermal contraction, and as a result gradual iterative improvements of processing conditions in the draw were made, for example, optimising the position of the IR heaters.

In the early 2000s focus shifted back to trying to fully understand the role contamination played, with the work of Bret Cooper (Beattie and Cooper, 2006; Cooper, 2007) being instrumental in driving understanding forward. He believed that debris clogging roller roughness was the key culprit, explaining why cleaning was effective in improving surface quality since it “restored” roller roughness. He used line profiles of rollers to measure surface roughness to prove this, although not quantitatively.

Additionally, work at this time found a considerable skew in the number of scratches on the drum side of the film, with 85% of observed scratches in a 2006 study being on the drumside. This was theorised to be due to degradation products inside the PET melt becoming trapped in the matrix upon the rapid quenching on the cast drum, as compared to the airside where they can escape and sublime out of the film at the casting drum. Only upon the film being heated in the forward draw can these trapped products escape, where they condense on the cool rollers. Hence on the rollers where the drumside lands there is often more contamination, and therefore more opportunity for possible surface damage.

Based on this observation, and other anecdotal evidence, the assumption was that the contamination in the forward draw was the same as had been seen in the stenter. This was only really reassessed in the early 2000's when it was found that in addition to a large proportion of organic components, the contamination in the forward draw also contained a number of inorganic components (Si/Al/Ti/Ba/S).

This led to two conflicting schools of thought, one where it was believed that contamination itself was the indenter for scratching, and the other where it was believed it affected surface roughness of the rollers, leading to more scratching.

Arguments in favour of the latter came in a 2007 study into the issues with a cooling roller where it was found that it was being smoothed by a faulty auto cleaner and no amount of cleaning could improve surface quality (Jones, 2007). This implied that it was the presence of a smoothed roll, rather than the presence of contamination, that worsened surface quality. Additionally, assessment of scratch appearance in 2011 (von Morgen, 2011) found no scratches where the indenting particle was retained in the scratch track. This indicated that contamination was not acting as an indenter.

Extensive work into optimising the automatic cleaners has been ongoing until present day, with minimal improvement since 2011 onwards. The majority of scratches, as was found in 2007, are under 0.5mm in length and occur most substantially at the film edges. This defect is referred to as “scuffing” (see Section 6.2.3).

1.8 PROJECT SCOPE

As covered in the summary above, there are a number of areas of this problem which are debated internally at DTF.

- i. The true composition of the contamination found in the forward draw of D52
- ii. The ways contamination impacts the severity of surface damage
 - a. As an indenter/gouger of the film
 - b. As an effective smoother of the rollers thereby promoting relative movement
 - c. A combination of a. and b.
- iii. Why automatic cleaners do not remove all the contamination

The scope of this work is to try to unify the existing knowledge and answer some of these questions. It will take a new approach of trying to understand the dynamic and complex situation of contaminated rolls contacting film by taking a bottom-up perspective.

2. LITERATURE REVIEW AND THEORETICAL BACKGROUND

The purpose of this literature review is to discuss and outline the key areas of theory and existing research which surround the specific topics in this report. By the nature of the fact that the project deals with several length scales, and a number of different techniques, this review covers two distinct theoretical areas.

In each case, the sections may be read independently or in conjunction with the relevant chapter:

- Section 2.1: This section includes the internal and external literature studies regarding the degradation processes of PET. This background pertains most particularly to the compositional analysis described in the first results chapter (Chapter 4) where it is shown that the majority of the contamination found is organic and derives from degradation processes.
- Section 2.2: This section explores the use of AFM as a tool for understanding surfaces beyond their topographical appearance. In particular, the focus will be on the literature studies using AFM for adhesion measurements and the validity of the AFM based models for this measurement as compared to contact mechanics such as Hertz, JKR and DMT theories.

In appendix 9.2 there is also a brief discussion theoretical background on the mechanics of scratch formation.

2.1 DEGRADATION OF PET

The degradation of PET is a well-studied process as it pertains directly to the material properties of the polymer. It plays an important role in every life phase of the polymer and

occurs under the influence of one or more of the following factors: heat, light, and oxygen. Weathering studies, where all three of these factors are present, have been of particular interest. In such studies the optical and physical properties of PET over its lifetime of use are investigated.

2.1.1 RELEVANCE TO PROJECT OBJECTIVES

During the DTF biaxial film forming process there are many points at which the PET is heated and subsequently cooled. It is known that these processing events can cause the breakdown of the polymer chains leading to small volatile components contained within the PET matrix. It has long been believed that these small volatile molecules are at least partly responsible for the contamination which appears on the line over time. Thus, it is important to understand the mechanisms by which PET breaks down and the resulting products.

2.1.2 THERMAL DEGRADATION

Thermal degradation is the result of heating and occurs during synthesis and processing of PET (Kelen, 1983). This degradation will occur as a function of how long the polymer is held at a particular temperature, with the rate increasing typically exponentially with temperature. Thermal degradation can occur with and without oxygen present. Degradation without oxygen tends to be studied under vacuum in order to see the degradation products more accurately. Degradation in these conditions occurs in one or both of two key routes: depolymerisation and substituent reactions.

Depolymerisation reactions are the reverse of the polymerisation step described in Section 1.4. During this reaction the polymer chain length decreases by the elimination of monomer units from the ends of the molecules. It can occur via a radical or non-radical based mechanism (Turnbull, 2013).

- Radical depolymerisations in polymers were well described by Grassie and Scott (Grassie and Scott, 1985), and it is notable that in addition to the monomer (re)production there is a competing reaction which involves intramolecular transfer which can produce oligomers of the molecule.
- Non-radical depolymerisation is also a chain scission reaction which occurs at the ester linkages, but without a radical to catalyse the reaction.

Substituent reactions can also occur. These are processes that take place without breaking the main polymer chain. They require the side substituents attached to the backbone of the polymer to be involved in the reaction. These can be elimination or cyclisation reactions.

Elimination reactions can take place at lower temperatures than depolymerisation reactions and will occur if one of the bonds within a chain substituent is weaker than the carbon-to-carbon bonds within the polymer backbone. These also result in chain shortening but the products formed, instead of being monomers or oligomers as in depolymerisation reactions, do not closely resemble the parent material. Cyclisation reactions occur between adjacent substituents on the polymer backbone and proceed at reasonably high temperatures, forming rings within the polymer chain, usually with the loss of a small molecule as part of the reaction (Turnbull, 2013).

The thermal oxidation of PET has been well studied and can be grouped into primary and secondary mechanisms.

2.1.2.1 PRIMARY THERMAL DEGRADATION PROCESSES IN PET

Thermal cleavage of the ester bond is considered the key mechanism of primary thermal degradation of PET. An overall mechanism for this can be seen in Figure 8.

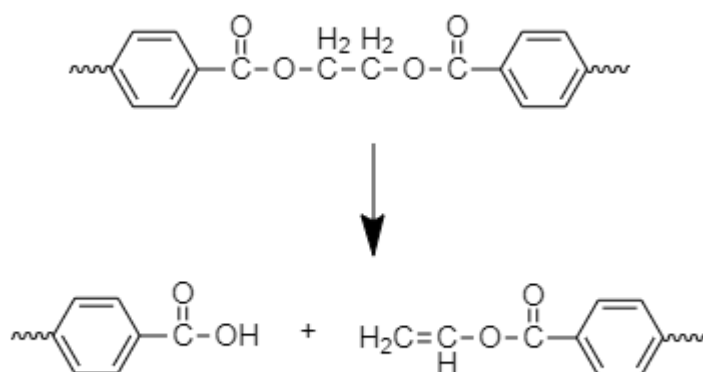


Figure 8: Primary thermal degradation by scission at ester linkage in PET.

This may proceed via ionic or radical mechanisms, the subject of which has been hotly debated in the literature (Buxbaum, 1968; McNeill and Bounekhel, 1991; Montaudo, Puglisi and Samperi, 1993; Bikiaris and Karayannidis, 1999; Pohl, 2002; Samperi *et al.*, 2004).

Assessing the validity of these different approaches is not within the scope of this report because in all cases the primary mechanism results in the chain scission of the ester linkage and yields a carboxylic acid and vinyl ester group as seen in Figure 8.

2.1.2.2 SECONDARY THERMAL DEGRADATION PROCESSES IN PET

After this initial chain scission, the subsequent degradation pathways can proceed in a plethora of ways. Secondary reactions tend to require higher temperatures than the primary reaction and produce a mixture of volatile and non-volatile products which can be seen in Table 1.

Highly volatile (Gaseous at -196°C)	Volatile (Gaseous at ambient)	Non-volatile (Solid state at ambient)
Carbon monoxide Methane	Acetophenone Acetaldehyde Aliphatic C1-4 hydrocarbons Ethylbenzene Styrene Toluene Ethylene Carbon dioxide Formaldehyde Methyl acetate Ketene Benzene Methanol 1,4 – dioxane	Terephthalic acid Benzaldehyde Benzoic acid Hydroxyethyl methyl terephthalate Vinyl benzoate Dimer fragments Divinyl terephthalate Terephthalaldehydic acid

Table 1: Major products reported from the thermal degradation of PET (Turnbull, 2013).

The literature findings indicate that the proportion of different degradation products depends on the temperatures used in the study (Buxbaum, 1968; McNeill and Bounekhel, 1991). The most common volatile products are highlighted in Table 1.

Acetaldehyde can reportedly form at temperatures as low as 200 - 300°C, temperatures which are frequently reached in the melt system of the polymer filming lines at DTF. There are several proposed mechanisms for this including:

- Internal scission of hydroxyl end group followed by the resulting vinyl alcohol undergoing rearrangement (Khemani, 2000)
- Transesterification of terminal vinyl groups (Grassie, 1984)
- Via addition of a carboxyl and vinyl groups (Grassie, 1984)

Terephthalic acid, however, forms at much higher temperatures, as reported by Sakata (Sakata *et al.*, 1996) and Chui (Chiu and Cheng, 1999) at temperatures of 430°C and 550°C

respectively. In both cases they reported that a mixture of terephthalic acid and benzoic acid was produced when PET was heated in the absence of oxygen.

The most thorough study of thermal degradation of PET was conducted by McNeill and Bounekhel (McNeill and Bounekhel, 1991). In this study, they proposed an extensive radical mechanism for all the products listed in Table 1. The basic reaction processes proposed in their work are found to be consistent no matter the operating temperature, however the proportion of different products does vary. For example, they found that the proportions of CO, CO₂ and acetaldehyde were the greatest at lower isothermal degradation temperatures. The authors propose that the mechanism is homolytic, which would explain why CO and CO₂ can form even as low as 200°C and how such a large range of products are possible.

The work of Chui and Cheng (Chiu and Cheng, 1999) also looked at the effect of time on PET thermal degradation and found that at 400°C the mass loss increased over time before levelling off after ~9 hours after a loss of ~45%. At 500°C the mass loss was closer to 80% after a shorter period of time.

2.1.3 THERMO-OXIDATIVE DEGRADATION

Thermal degradation in polymers, while it does proceed in the absence of oxygen, is much faster in the presence of it. This is known as thermo-oxidative degradation. It is possible at lower temperatures compared to its oxygen-free counterpart but mostly leads to very similar degradation products in addition to a few oxidising species.

Oxidative degradation proceeds by a free chain radical reaction where the key reactive species are hydroperoxides (Grassie and Scott, 1985). These act as both initiators and intermediates. There are separate initiation, propagation and termination steps which are summarised in Figure 9.

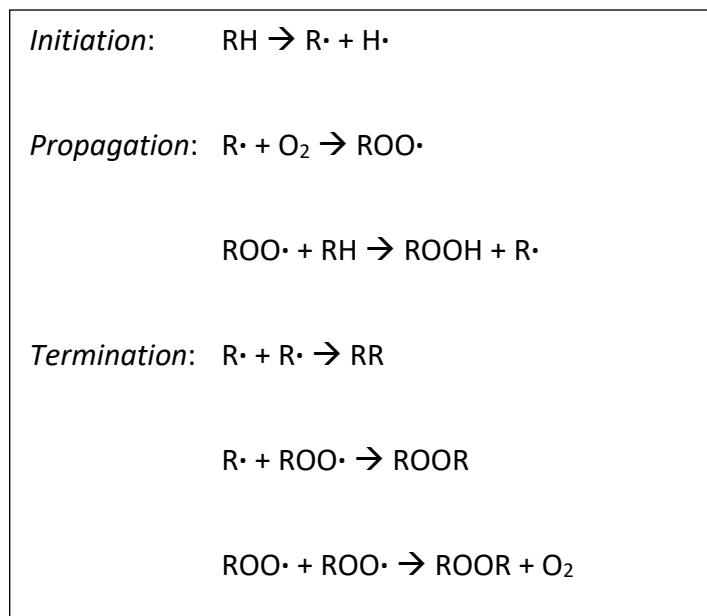


Figure 9: General oxidation scheme for polymer degradation.

It is not fully understood how the initiation reactions commence, but it is generally assumed that they form in the presence of radiation, heat, or mechanical stress and may even be affected by the presence of catalysts (Bamford and Tipper, 1975).

Following the propagation reaction which forms the hydroperoxides species (ROOH) and the polymer radical $R\cdot$, the radical can then go on to react with more oxygen and the cycle repeats. Assuming O_2 is in excess, the rate of reaction is a function of the strength of the R-H bond and the stability of the polymer radical.

In addition, since the hydroperoxides are unstable, they can undergo subsequent chain scission reactions which degrade the polymer chains further. This can be uni- or bi- molecular in nature, both of these mechanisms can be seen in Figure 10. Which of the two mechanisms occurs depends upon the concentration of the ROOH species, with a higher hydroperoxide concentration favouring the bimolecular process.

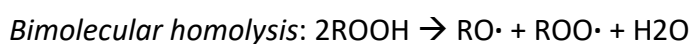
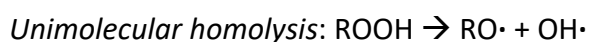


Figure 10: Chain scission reactions of hydroperoxides.

Intrinsic factors such as a polymer's crystallinity, molar mass and chemical structure can have a varying impact on its resistance to thermo-oxidative degradation (Kelen, 1983). Extrinsic factors such as oxygen and water concentration and the presence of chemical catalysts or inhibitors will also have an impact.

Thermo-oxidative degradation of PET has also been studied extensively, though the most prolific work is that of (Bolland and Gee, 1946). The mechanism for thermo-oxidative degradation of PET proceeds by the general scheme in Figure 11. This reaction is autocatalytic.

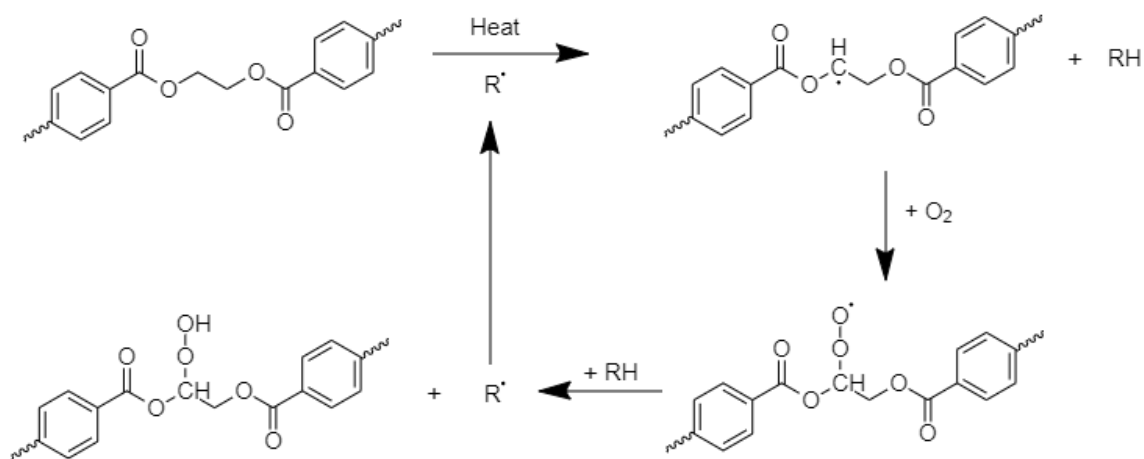


Figure 11: Formation of hydroperoxides in PET.

The second stage reaction is a homolytic bond scission of the hydroperoxide which proceeds by one of the two mechanisms shown in Figure 12.

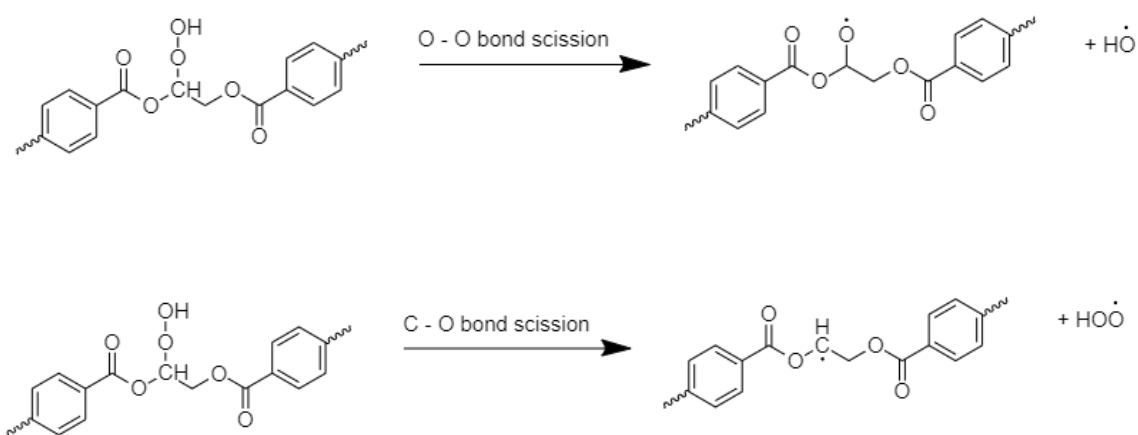


Figure 12: Top: Homolytic O-O bond scission of PET hydroperoxide to form alkoxy macroradical and $\cdot\text{OH}$, Bottom: Homolytic C-O bond scission of PET hydroperoxide to form alkoxy macroradical and $\cdot\text{OOH}$.

Once the radicals are formed, the reaction can then rapidly cascade into a number of further chain scission degradation reactions. This leads to the formation of chain fragments with vinyl esters, carboxylic acids, and oxygen and carbon radicals. As mentioned earlier, the exact route (uni or bi molecular) will vary depending on the concentration of hydroperoxides present

which depends on the chain length of the PET polymer. This is further complicated by the fact that thermo-oxidative processes are never happening in isolation from thermal degradation effects. This was shown by Botelho in 2001 (Botelho *et al.*, 2001), where they found that thermal degradation without oxygen is shown to contribute to overall degradation especially in the early reaction stages. This can be further complicated by the presence of catalysts (Zimmerman and Kim, 1980). As in thermal degradation, the proportion of different end products depends on the temperatures used and the mechanisms are enormously complex. A summary of the most common products of thermal oxidative degradation of PET can be seen in Table 2 (Dzięcioł and Trzeczcyński, 1998; Dzięcioł and Trzeczcyński, 2000).

Highly volatile (Gaseous at -196°C)	Volatile (Gaseous at ambient)	Non-volatile (Solid state at ambient)
Carbon monoxide	Styrene Benzene Acetaldehyde Aliphatic C1-4 hydrocarbons Formaldehyde	Terephthalic acid Benzoic acid 4 – acetyl benzoic acid 4-phenylbenzoic acid Monovinylterephthalate

Table 2: Summary of thermo-oxidative degradation products of PET.

2.1.4 HYDROLYTIC DEGRADATION

Hydrolytic degradation is arguably the most destructive form of degradation that can affect polymers, having the highest rate of reaction compared to thermal and oxidative degradation pathways (Seo and Cloyd, 1991). It generally requires the polymer to be in a glassy state above its glass transition temperature (T_g) and requires the presence of water. The rate of reaction is dependent on chemical structure, isomerism, and can be catalysed by a variety of substances including salt, acids, and bases.

Hydrolytic degradation of PET is perhaps the most studied of the three processes in the literature (Zimmerman and Kim, 1980; Ellison *et al.*, 1982; Allen *et al.*, 1994; Kint and Muñoz-Guerra, 1999; Launay, ThomINETTE and Verdu, 1999; Sammon, Yarwood and Everall, 2000). This is because, not only does it have the fastest rate of reaction by several orders of magnitude, but it is also of concern in weathering and ageing of products in their end use as it causes significant loss of mechanical properties (Seo and Cloyd, 1991; Hosseini *et al.*, 2007; Pirzadeh, Zadhoush and Haghghat, 2007). PET is also very hygroscopic (Jabarin and Lofgren, 1986) and will absorb water from the atmosphere making it very vulnerable to this process.

Hydrolytic degradation of PET proceeds by chain scission at the ester linkages leading to one carboxylic end group and one hydroxyl; the general mechanism is shown in Figure 13. One molecule of water is consumed in this process. Often the concentration of carboxyl end groups is used as a metric by which to monitor hydrolytic degradation.

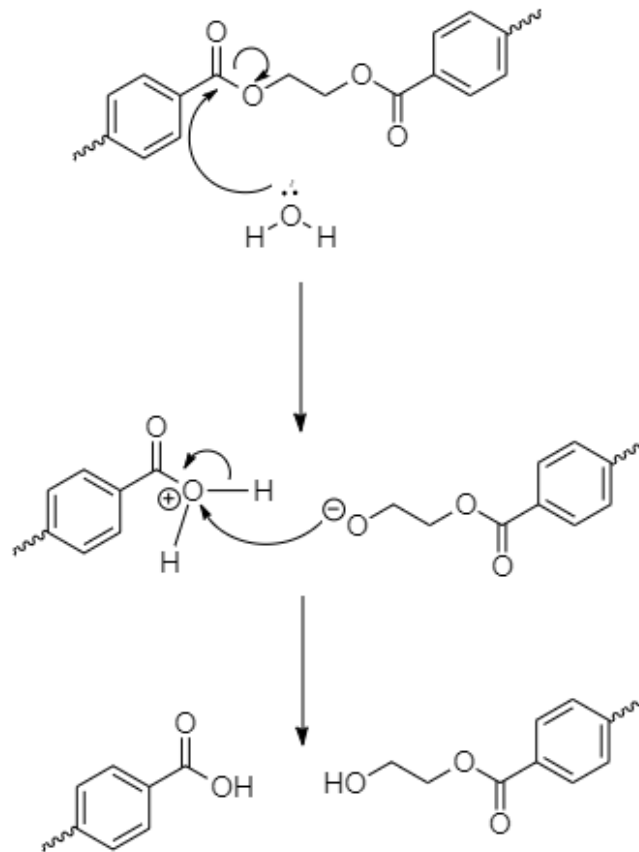


Figure 13: Chain scission mechanism for hydrolytic degradation of PET.

The reaction rate can be increased by acid or basic conditions. In the former case the acid protonates the in-chain oxygen atom of the ester which subsequently reacts with the water. In the latter case, the hydroxide anion attacks the oxygen in the carbonyl. In either case this decreases the activation energy of the process.

The concentration of carboxyl end groups is used to monitor hydrolytic degradation, but many argue they play a more complex role in the reaction. It has been proposed (Zimmerman and Kim, 1980; Sammon, Yarwood and Everall, 2000) that the mechanism can be considered autocatalytic, with the carboxyl end groups controlling the rate of reaction. They do this by increasing the degree of hydrophilicity of the PET, meaning more water will be favoured to penetrate the PET matrix, and thus react further. Since carboxyl end groups are also produced

by the reaction, this means that in an excess of water the rate of reaction would accelerate at an increasing rate. However, water penetration is also affected by the crystal packing of the polymer chains. Highly crystalline regions of PET are known to resist water ingress far more than amorphous regions (Allen *et al.*, 1994; Kint and Muñoz-Guerra, 1999).

PET is considered most vulnerable to hydrolytic degradation above its melt temperature and to a lesser extent above its glass transition temperature, indicating that the process is accelerated by the mobility of the polymer chains (Zimmerman and Kim, 1980; Sammon, Yarwood and Everall, 2000). In combination, this means the rate of reaction is controlled by temperature, chain length, humidity/water content and the crystallinity of the sample (Ballara and Verdu, 1989; Allen *et al.*, 1993). Since high temperatures are inherent to the PET film manufacturing process, great care is taken to ensure high molecular starting weight and minimal water content of PET during BoPET film processing.

One instance of chain scission in a single polymer chain does not yield any volatile products, however as the reaction proceeds, the molar mass of the resulting products decreases which eventually leads to oligomers small enough to be volatile. Additionally, the reaction produces R-OOH groups which are also vulnerable to other forms of degradation such as the thermal chain scission reactions shown in Figure 8.

2.1.5 DEGRADATION DURING PET PROCESSING

Degradation occurs in the melt system of the PET film processing plant via thermal degradation and hydrolytic degradation in the manner described above. Typical processing temperatures in the polymer melt flow system are between 275 – 305 °C.

Thermal degradation occurs simply because the melting temperatures are high enough to satisfy the activation temperatures for the mechanisms to proceed. Since the temperatures are at the lower end of the temperature range of thermal degradation, the resulting components will skew more towards acetaldehyde, CO, and CO₂, as described in Section 2.1.2.2.

Thermal oxidative degradation will occur, but to a lesser extent, as the melt system is either under vacuum or has expelled any conveying air in a full system and thus the rate of these reactions will be rate limited by the concentration of available oxygen while the PET is in the melt system. The only point at which the PET melt will be exposed to significant amounts of oxygen will be at the exit of the die, during the short path to the cooled casting drum, and for a part of the wrap on this drum, a time period of the order of a few seconds or less.

Hydrolytic degradation will also occur but will also be rate limited, in this case by the availability of water. In order to prevent hydrolytic degradation, PET chips are dried before processing – typically to below 40 ppm, or ideally less than 25 ppm to remove as much water as possible from the hygroscopic chip prior to melting. This step is especially critical in single screw extruders. Many factories in the DTF network utilise twin screw extruders which are able to extract any remaining water during the extrusion process. Despite these steps, some hydrolytic degradation will still occur potentially yielding some small chain oligomers.

In addition to the degradation that occurs in the melt system of the BoPET film processing line, it is also worth noting that the chip entering the system may also already contain some products other than the polymeric PET. This is because all the above processes may have occurred when the chip was formed. After the polymerisation step (for details of which can be found in Section 1.5), the resulting polymer is extruded before being chipped and at this

time may undergo some degradation. The non-volatile products of this will get cooled into the chip and can sometimes still be present when the chip is later extruded at the start of the melt system. The scope of this project is concerned with the products of PET degradation which may become part of the contamination found on the DTF BoPET production line. The products of degradation from these processes, which are non-gaseous at room temperature but gaseous at melting conditions, are those of primary concern.

After forming during chipping, extrusion, and in the melt system, during the subsequent steps of the filming process (extrusion, forward draw, and sideways draw), these small molecules will be able to sublime out of the PET matrix and condense on the surfaces of the PET film manufacturing line. This is covered in more detail in Chapter 4, and the historical work is discussed in Appendix 9.1 and summarised in Section 1.7.

2.2 CONTACT MECHANICS

2.2.1 RELEVANCE TO PROJECT OBJECTIVES

In this work it is of particular interest to understand the adhesion properties of the various interacting surfaces. This is important mechanically in the moment-by-moment contact events that happen during film production but also, and more critically in the context of this work, has a significant bearing on the ease with which surfaces can be cleaned. A surface with a strong adhesion force to dust, debris or other microscopic particulates will collect more contamination over time and it will be more difficult to clean. It is therefore important to understand the theoretical background of surface forces and contact mechanics. This will be covered in detail in the following sections and revisited during the adhesion work in Chapter 5.

2.2.2 FORCES CONTRIBUTING TO SURFACE INTERACTIONS

The forces between interacting surfaces depend on many factors; the geometry of the system, the mechanics of interaction, whether the system is in vacuum, in air, or in liquid, and the chemistry of the surfaces – especially any chemistry affecting hydrophobicity.

The forces that govern the behaviour of bulk materials are intramolecular; these are short range, strong, atom-to-atom forces such as ionic or covalent bonds. The forces which govern interface-interface surface interactions are weaker, long range, non-stoichiometric, intermolecular forces such as van der Waals forces (Hamaker, 1937a). Van der Waals forces, arise from induced dipole-dipole interactions between all molecules.

There are a great number of models that exist for these interface-interface attractive interactions which began with the original work of Hertz in the late 1800s on the elastic deformation of solids. (Hertz, 1878; Timoshenko and Goodier, 1951)

More recent developments in the last 50 years have allowed the field to expand. This includes the development of Surface Force Apparatus which allowed Van der Waals forces to be measured directly (Israelachvili and Adams, 1977), and then, more recently still, atomic force microscopy (AFM) which expanded the diversity of samples on which these forces could be measured, in addition to providing a more well defined geometry.

The purpose of this review to introduce the various pull-on and pull-off attractive and adhesive forces. The discussion will be framed in the context of an AFM force modulation measurement which allowed the steps of surface-surface interaction to be taken one at a time.

2.2.3 USING AFM TO MEASURE SURFACE FORCES

2.2.3.1 *VALIDITY OF AFM MODEL*

For the purposes of this review, the focus will be on models that use sphere-on-plane geometry, since this is what pertains most directly to atomic force microscopy. The majority of these models can be extended to plane-on-plane geometry by rearranging for the case of a sphere of infinite radius.

In the case of atomic force microscopy measurements – the experimental set-up of which is described in detail in Section 3.2.2.2 – adhesion forces can be directly measured by taking force curve measurements. The geometry of the system is such that it can be approximated

by a sphere-on-plane model with the radius of the sphere given as the radius of the end of the tip, as can be seen in Figure 14.

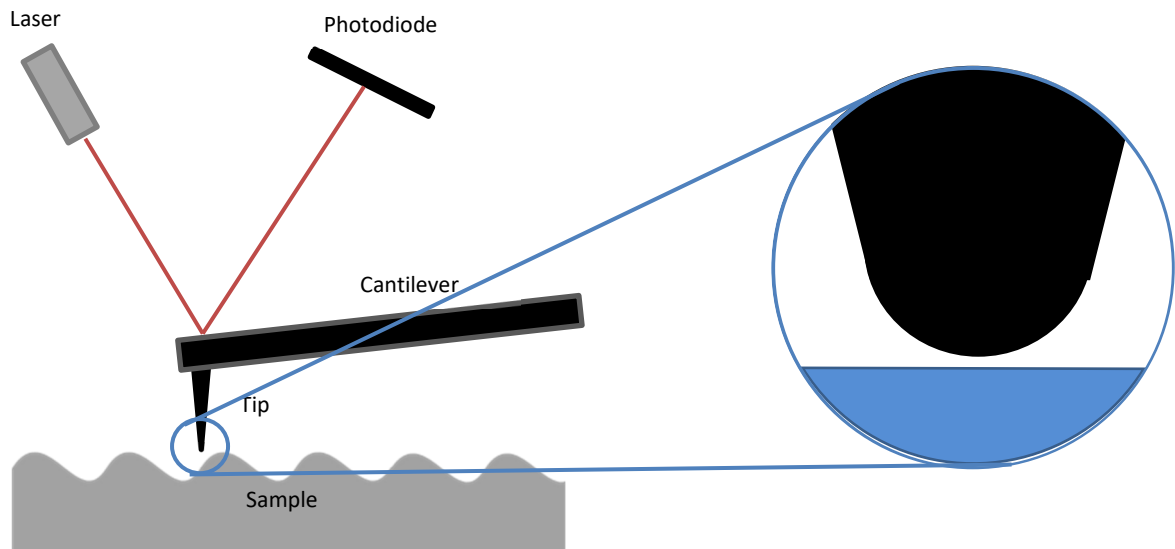


Figure 14: Schematic of AFM tip approaching a sample surface, showing how the end of the tip can be modelled as a sphere on plane geometry.

2.2.3.2 FORCE CURVES

To collect a force curve, the AFM tip is ramped along the vertical axis until contact is made with the surface of interest and then withdrawn at a set rate. A so-called force-distance curve is produced; this is simply a plot of tip-sample interaction force against the tip-sample distance.

The cantilever of the AFM can be modelled as a spring, where deflection during contact is proportional to force according to Hooke's Law:

$$F = -k_{cantilever}\delta_{cantilever}$$

Equation 1

Where k is the spring constant of the cantilever and δ is the deflection of the cantilever.

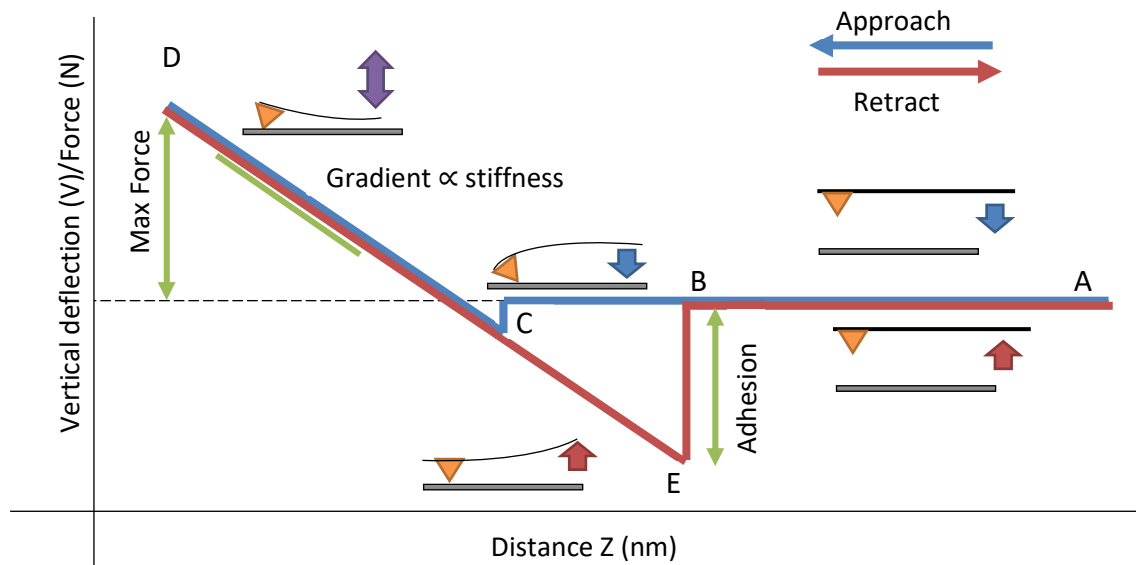


Figure 15: Schematic example of a force modulation mode force curve.

Figure 15 shows a typical force curve from an AFM force modulation experiment. The blue line represents the approach of the cantilever towards the surface and the red line its subsequent retraction. In this example the y axis is displayed as vertical deflection in volts which is analogous to the deflection of the end of the cantilever.

This example idealised force curve will be taken step by step to discuss the forces at play during this measurement. Since this report is especially concerned with adhesion forces, these will be covered in most detail.

2.2.3.3 ATTRACTIVE FORCES (PULL-ON)

Between point A and C is the non-contact region where the cantilever is descending towards the substrate surface but has not been affected by any long-range forces. At point C the tip will snap into contact with the surface as it begins to feel the effect of the attractive long-range forces between it and the surface. In a vacuum, the attractive forces which pull surfaces together can be divided into electrostatic and non-electrostatic forces.

The electrostatic forces come from the effect of electric fields on electric charges and are affected by surface roughness and mechanical deformation during contact (Cappella and Dietler, 1999). Electrostatic forces can be modelled as plane-plane, sphere-plane, a uniformly charged line, asymptotic, cylindrical or hyperboloid (Leite *et al.*, 2012).

Non electrostatic forces in a vacuum are comprised of the Van der Waals forces which result from the potential between the interacting surfaces and is derived from the Lennard Jones potential.

2.2.3.4 CONTACT REGION

Between points C and D, the probe is in the so-called “contact region” where the probe is in intimate contact with the surface and continues to descend in the z-direction. The force continues to increase as the surfaces are pushed together and, in some cases, the surfaces will deform.

2.2.3.5 ADHESIVE FORCES (PULL-OFF)

At point D the probe reverses direction and begins to move away from the surface again. Assuming there is no hysteresis in the deformation of the system, the lines between D and C should be identical for the approach and retract. During this region, the probe is feeling the adhesive forces associated with the interaction. Between points C and E, the probe continues to move away from the surface but remains in contact at the tip due to adhesive forces, until finally snapping away again at point E and returning to a non-contact region. The magnitude of these adhesive forces is found from the retract region between point C and E.

2.2.4 ADHESION

The adhesive force, that is, the force holding surfaces together in contact, is comprised of van der Waals, capillary, and electrostatic components (assuming there is no chemical bonding

taking place). Van der Waals forces are always present but the other two components are present only under certain circumstances.

Overall, therefore, it can be defined:

$$F_{adhesion} = F_{capillary} + F_{vdW} + F_{electrostatic}$$

Equation 2.

where $F_{adhesion}$ is the force of adhesion, $F_{capillary}$ is the capillary force, F_{vdW} is the van der Waal force and $F_{electrostatic}$ is the electrostatic force.

Assuming uncharged starting materials, the electrostatic element will be caused by charge transfer between the contacting materials. It is far more likely to come into play if there are inhomogeneities in the surfaces. By modelling the indenter-sample system as a sphere on a flat surface, the electrostatic force has been shown to be (Hao, 1991):

$$F_{electrostatic} = \pi \epsilon_0 V^2 \frac{R}{D}$$

Equation 3.

where R is the radius of the sphere, D is the separation distance, ϵ_0 is the permittivity constant and V is the voltage of cantilever deflection.

In a vacuum, the capillary force will not be present, (discussed more in Section 2.2.7). Therefore, the adhesion, and the focus of much of the literature prior to the turn of the century, is mostly due to van der Waals (vdW) forces.

vdW forces result from dipole and quadrupolar interactions between molecules that make up all materials no matter their phase state. vdW forces are the general name given to a set of

forces characterized by the same power dependence on the distance (r) between two bodies, all proportional to $1/r^6$. There are three contributions to the force, the Keesom Force (Keesom, 1915), the Debye Force (Debye, 1920), and London forces (London, 1930).

The general form for the vdW interaction energy between two bodies is given by the Derjaguin approximation:

$$F_{vdW} = \frac{AR}{6a_0^2}$$

Equation 4.

where A is the Hamaker constant, R is the radius of the contacting body, and a_0 is the distance of closest approach between the plane and the sphere. The Hamaker constant is dependent on the chemistry of the two materials and is generally determined either by the so-called Hamaker-type integration of all the intermolecular interactions (Hamaker, 1937b), or by the Lifshitz theory (Lifshitz, 1956). For much modern work Hamaker constants are found from reference tables rather than being calculated from first principles. The general form given in Equation 4 above can also be modified extensively to include a variety of geometries (Leite *et al.*, 2012) where they covered the mathematics of vdW force were covered in extensive detail.

Low humidity/in-vacuum AFM studies have been used to examine the magnitude of van der Waals forces, but often experimental values are lower than predicted by the simplistic theory; this is due to retardation effects. In a system which is at equilibrium and in the absence of air, the van der Waals forces are the most important contribution to the adhesion force. These forces are strongly dependent on contact area and so the contact mechanics must be well understood; this will be covered in the next section.

2.2.5 CONTACT MECHANICS MODELS

2.2.5.1 *HERTZIAN MODEL*

The simplest model for understanding the mechanics of contacting surfaces, i.e. the way in which they deform during contact, is the Hertzian model (Hertz, 1878). This theory, which considers no surface or adhesion forces at all, assumes that a completely smooth elastic sphere contacts a completely flat, infinitely rigid surface. The deformation of the sphere is modelled as a Hookean spring, referred to as perfectly elastic.

For bodies which deform in this way, the vdW adhesion forces acting between two perfectly elastic spheres can be modelled fairly easily, although in practice this model rarely applies. The Sneddon analysis (Sneddon, 1965) subsequently expanded this model to include the case of a rigid tip on an elastic surface.

2.2.5.2 *JKR AND DMT MODELS*

The more realistic approach is to include the work of surface forces in the calculation of deformation – so the behaviour is not purely Hertzian – for this the works of Johnson, Kendall, and Roberts (JKR) theory (Johnson, Kendall and Roberts, 1971) and Derjaguin, Muller and Toporov (DMT) theory (Derjaguin, Muller and Toporov, 1975) were pivotal.

Both models again assume perfectly flat surfaces with a rigid smooth sphere which is elastically deformable in contact. Both models have an advantage over calculating vdW forces from Equation 4 and its relations, since the separation distance a , which is often difficult, if not impossible to determine, does not need to be known. Instead, they use a surface energy or work of adhesion which captures all the surface forces in one value.

Work of adhesion is the work per unit area to create two new interfaces when previously connected surfaces are pulled apart. For example, if a system contains a solid in contact with

a liquid and then the two are pulled completely apart, there are two new interfaces formed, one solid/air and one liquid/air, while a solid/liquid interface is lost.

Defining the work of adhesion for these three phase interactions requires a dispersion and a hydrogen bonding component for each phase. These components are derived from surface tensions which can be determined theoretically via a variety of methods, but more commonly are referenced from published tables.

The JKR model (Johnson, Kendall and Robert, 1971) is valid for the adhesion of larger spheres with high surface energy and low Young's modulus. It models the sphere as elastic, as in Hertzian models, but additionally considers forces inside the contact radius.

$$F_{adhesion}^{JKR} = \frac{3}{2}\pi R\bar{\omega}_{ijk}$$

Equation 5.

where R is the radius of the contacting sphere and $\bar{\omega}_{ijk}$ is the work of adhesion between surfaces i and j in a medium k .

DMT model (Derjaguin, Muller and Toporov, 1975) is valid for small spheres of low surface energy and higher Young's modulus. It models the deformation of the sphere as elastic, as in Hertzian mechanics, but also considers the effect of forces between the two bodies outside the contact radius.

$$F_{adhesion}^{DMT} = 2\pi R\bar{\omega}_{ijk}$$

Equation 6.

Both models have had experimental papers, both in support of, and in conflict with them, before the conclusion was made that they applied to very different nano-mechanical systems (Attard and Parker, 1992).

2.2.5.3 *OTHER MODELS*

Much of the work in the subsequent decades in this field was focused on the DMT to JKR transition. Tabor (Tabor, 1977) introduced the concept of a dimensionless ratio of adhesion displacement (extension at contact detachment). This was later modified and discussed by Muller, Derjaguin and Toporov (Muller, Derjaguin and Toporov, 1983). One of the more complete theories is that of Maugis (Maugis, 1992) which introduces a dimensionless parameter λ which is large for big adhesive bodies and small for small rigid ones, which allows DMT and JKR to be resolved in one equation.

Further work of (Maugis and Pollock, 1984) developed a model based on JKR theory to also take into account plastic deformations. When plastic deformations occur, the adhesion depends on the applied load. Work by Carpick, Ogletree and Salmeron improved on this further in the late 90s (Carpick, Ogletree and Salmeron, 1999). Within contact mechanics whether a systems adhesion is more “DMT-like” or more “JKR-like” is judged using the General Transition Equation they describe in their work.

2.2.5.4 *AFM AGREEMENT WITH THESE MODELS*

Experimentally validating these models really became possible with the advent of AFM force modulation mode (FMM) – described in more detail in Section 3.3.2. Before this, a centrifuge could be used, but this was limited in the types and sizes of particles which could be measured.

DMT and JKR models both have a dependence on contact radius – this has been confirmed experimentally by Heim where they measured the adhesion of individual silica microspheres

with radii between 0.5 and 2.5 μm and found a linear dependence of the measured adhesion on the particle radius (Heim *et al.*, 1999).

For applied load, JKR and DMT expect no dependence on applied load because the models assume perfectly elastic interaction. This has been seen experimentally for low normal loads by several groups (Vakarelski, Ishimura and Higashitani, 2000; Vakarelski and Higashitani, 2001; Heim *et al.*, 2002).

However, numerous studies have experimentally found a dependence on applied load. They found agreement with the more complex models such as that of Maugis, which take some amount of non-elastic deformation into account (Schaefer *et al.*, 1994; Butt, Jaschke and Ducker, 1995; Gady *et al.*, 1998; Butt *et al.*, 1999; Reitsma, V. Craig and Biggs, 2000; Reitsma, V. S. J. Craig and Biggs, 2000).

None of the models described so far include a dependence on time or rate, which has been commented on through the literature to not always hold true, with many groups finding dependence on contact speed and dwell time of contact (Biggs and Spinks, 1998; Reitsma, V. Craig and Biggs, 2000; Reitsma, V. S. J. Craig and Biggs, 2000; Vakarelski *et al.*, 2001). This is due to viscoelastic or viscoplastic behaviour. AFM work on the dynamic aspect of contact is known as Dynamic Force Spectroscopy.

More complicated models have been developed to model viscoelastic and viscoplastic contact. (Rumpf, 1953; Vakarelski *et al.*, 2001; Beake and Leggett, 2002; Shulha *et al.*, 2004). However, even in this well-defined sphere-on-plane geometry, calculating the indentation for non-elastic contact becomes very mathematically complex and computationally expensive (Tomas, 2003) and few of the models have been rigorously experimentally confirmed.

Two notable works include:

- (Notbohm, Poon and Ravichandran, 2012) where elastic, viscoelastic, viscoplastic and plastic deformation during a contact in the context of AFM force modulation mode was thoroughly mathematically described.
- (Sun, Akhremitchev and Walker, 2004) where highly compliant materials were measured using AFM and it was found that JKR models failed because the contact point became impossible to determine accurately.

However, many of these works already mentioned (Ecke *et al.*, 2001; Toikka, Spinks and Brown, 2001; Heim *et al.*, 2002), while they found some agreement especially in the trends of JKR, DMT or Maugis model, consistently measured adhesions lower than is predicted. This is because these theories model the surfaces as atomically flat, ignoring surface roughness effects. Once interactions are happening outside of an ideal system, it is necessary to consider surface topography effects. These have been neglected so far in this discussion and will be covered in the next section.

2.2.6 ADHESION AND SURFACE ROUGHNESS

In all of the above cases the assumption of a perfect sphere and flat plane has been made. This will only be an approximation of the reality for contacting bodies, as shown in Figure 16. In experiments, the surfaces will almost never be perfectly flat and so significant work has been done in order to understand the relationship between measured adhesion force and surface roughness.

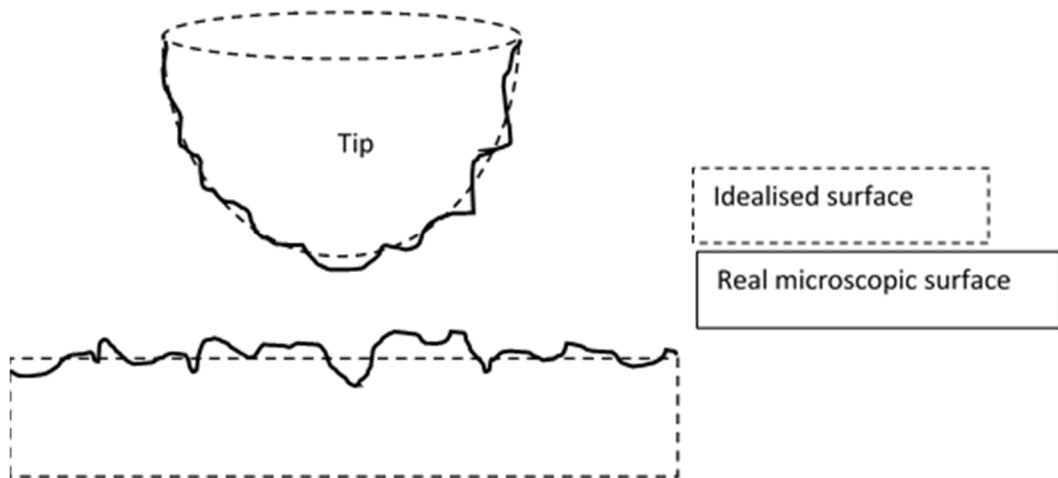


Figure 16: Diagram showing how indenter and surface roughness are approximated when modelled as a perfect sphere and a perfectly flat plane.

The finding that has been echoed across the literature, is that measurements of surface energy were far lower than predicted by JKR or DMT models when measured on “real” surfaces. Even deviations of the surfaces as small as 1 nm would cause these models to fall apart (Rabinovich *et al.*, 2002).

The prediction was that this was due to reduced surface area of contact caused by surface roughness which would result in not one continuous contact area but many smaller areas of contact at the peak of surface asperities, sometimes referred to as multi-asperity contact. Early work found this trend without attempting to fully explain it (Quon, Knarr and Vanderlick, 1999; Sirghi *et al.*, 2000).

The early work of Rabinovich (Rabinovich *et al.*, 2000) suggested the following equation (Equation 7) for contact between a smooth sphere and a rough surface. This is an extension of vdW theory and models the nanoscale roughness as the caps of asperities with their centres located far below the surface, and just their caps exposed to the surface.

$$F_{adh,dry} = \frac{AR}{6a_0^2} \left[\frac{1}{1 + 58.14R \cdot RMS/\lambda^2} + \frac{1}{(1 + 1.817RMS)^2} \right]$$

Equation 7: Empirical equation for adhesion force for rough surfaces (Rabinovich *et al.*, 2000).

where, as before, R is the radius of the contact sphere and A is the Hamaker coefficient; while RMS is the root mean squared roughness of the surface, λ is the average peak-to-peak distance between asperities and a_0 is the minimum separation distance between the adhering particle and asperity.

The same team (Rabinovich *et al.*, 2002) then expanded on this and provided a better analytical solution for surface roughness in the nanoscale regime, suggesting modifications to include a surface energy parameter (as in JKR and DMT theory) in order to capture more of the surface forces.

$$F_{adh,dry} = \frac{3\pi\gamma R\lambda^2}{(\lambda^2 + 58.14R \cdot RMS)} + \frac{AR}{6(a_0 + 1.817RMS)^2}$$

Equation 8: Empirical equation for adhesion force for rough surfaces (Rabinovich *et al.* 2002).

where γ is a surface energy parameter. The first term of Equation 8 is a surface energy term, and the latter a vdW term. This model offered a huge improvement on the previous and work by Kappl and Butt (Kappl and Butt, 2002) reported it to have an accuracy of around 50% compared to previous models which could be up to a factor of 50 out from measured values.

(Ramakrishna *et al.*, 2013) conducted a thorough study into the effect of surface roughness on the validity of JKR and DMT models for surface adhesion. They prepared surfaces with different packing densities of nano spheres and measured pull-off adhesion in each case. At high particle density, they found the JKR type adhesion dominates as the contacting colloidal sphere undergoes large deformations over several nanoparticles. At low particle density however, adhesion is dominated by long-range, DMT-type, noncontact interactions with the surface, as the contacting sphere is suspended by a few particles only, resulting in local deformations of the colloid sphere.

The most sophisticated models (Suresh and Walz, 1996, 1997; Duval, Leermakers and van Leeuwen, 2004; Hoek and Agarwal, 2006; Valtiner *et al.*, 2012; Elzbieciak-Wodka *et al.*, 2014) available show that surface roughness suppresses short range surface forces; specifically they all support the assumption that surface roughness suppresses the impact of vdW forces in the surface measurement. However, they are very mathematically and experimentally expensive, and still are not always correct; for example, in the case of very hydrophobic surfaces (Israelachvili and Adams, 1977; Hansson *et al.*, 2012).

In a review of the literature (Thormann, 2017), Thormann discussed the complexity of including surface roughness in an understanding of adhesion, in particular for Derjaguin, Landau, Verwey, and Overbeek (DLVO) theory, which includes both vdW forces and the electric double layer.

Overall while many theories have been suggested, roughness is still not fully understood. One of the main challenges of producing an experimentally validated analytical solution is that it is difficult to capture all the complexities of surface roughness into one parameter which can be neatly slotted into an equation.

Many works use root mean squared (RMS) roughness, which captures the average deviation of the surface from the mean plane. However, this single term does not contain all the possible information about the surface's topography. It also requires direct measurement of the surface by AFM, SEM or other similar metrology technique which becomes experimentally expensive if you want to model many different surfaces. Persson and Tosatti (Persson and Tosatti, 2001) chose instead to describe surface as a self-affine fractal, but this is still limited in describing the surface in its entirety. They found that adhesion dramatically decreases once the fractal value exceeds 2.5.

As stated above, these reports, while including surface roughness effects, are still for in-vacuum interactions, therefore ignoring capillary layer effects. Once interactions are happening outside of a perfect vacuum, it is necessary to take capillary layer effects into account; these have been neglected in the discussion so far. Initially there will be a discussion of the origin of capillary layer effects and their impact on idealised flat surfaces, and then surface roughness will be reintroduced.

2.2.7 CAPILLARY FORCES

Capillary layer refers to a liquid phase present in surface-surface interactions. In the majority of applicable cases where surfaces are interacting and the adhesion force is of interest, the capillary layer liquid will be atmospheric water which is adsorbed onto the surface of one or both solids, although there has been one notable study into capillary layer effects in non-Newtonian fluids (Bowen *et al.*, 2011).

The behaviour of water on a surface, or in other words, its propensity to either fully wet a surface, or to instead form droplets, is mediated by the so-called capillary force. This is

determined by the balance between the liquid-air, liquid-substrate, and the substrate-air interfacial tensions.

The equilibrium between these interfacial tensions is related to the contact angle via Young's equation:

$$\gamma_{solid-vapour} = \gamma_{solid-liquid} + \gamma_{liquid-vapour} \cos\theta$$

Equation 9

where θ is the contact angle of the liquid on that particular solid substrate. The origin of the contact angle is from the balance of forces between a) the molecules of the liquid (water molecule to adjacent water molecule) and b) the molecules of the liquid and the surface (water molecule to adjacent substrate molecule).

Once the capillary layer is thick enough, during a pull-off event, the capillary layer will form a bridging meniscus which will contribute to the overall adhesion force felt. This can be seen schematically in Figure 17.

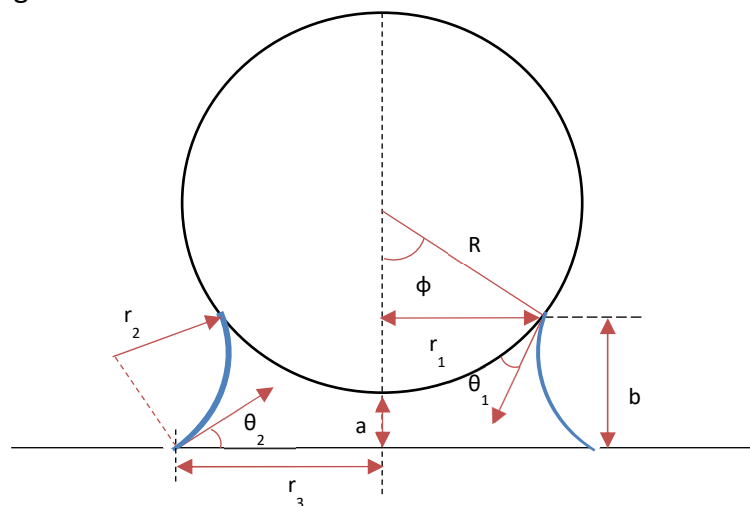


Figure 17: Schematic of sphere on plane contact for a perfectly smooth plane in the presence of a bridging meniscus.

2.2.8 CAPILLARY FORCE MODELLING WITH AFM

As discussed earlier the overall adhesion of the surface interaction can be defined as the sum of the capillary, van der Waals and electrostatic components.

$$F_{adhesion} = F_{capillary} + F_{vdW} + F_{electrostatic}$$

Equation 10.

In an AFM set up, where surfaces are allowed to come to equilibrium, this reduces to

$$F_{adhesion} = F_{capillary} + F_{vdW}$$

Equation 11.

It is believed that above a certain critical capillary layer thickness the $F_{capillary}$ will dominate the adhesion force and the contribution of F_{vdW} will be negligible. This will be discussed in more detail later. The simplest model for calculating capillary force, hereafter denoted F_c , is well established in the literature as:

$$F_c = 4\pi\gamma R\cos\theta$$

Equation 12:

where R (as above) is the radius of the sphere, γ is the surface tension of the liquid, and θ is the contact angle of both the liquid on the surface and the liquid on the sphere. This expression is derived from combining the expressions for the two components of the capillary force, the surface tension component F_s and the pressure differential component F_p , which comes from the Laplace Equation.

This expression only holds under very specific conditions which can be seen in Table 3. Table 3 also outlines the two AFM cases – traditional tip and colloidal tip – and whether these assumptions hold.

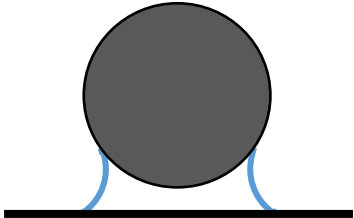
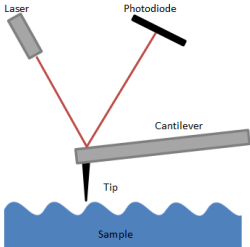
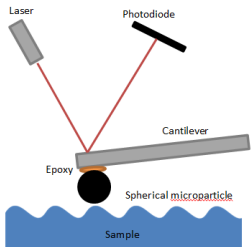
Assumption	Standard AFM Tip	Colloidal Probe AFM Tip
		
1. The radii of the solid-liquid contact lines are much smaller than the radius of sphere R	Does not hold in general as tip narrows to a near atomically sharp point	Can hold as long as the colloidal particle is sufficiently large
2. The radii of the two contact lines are equal	Often does not hold as the contact line is small due to the narrow tip geometry	Holds for most cases as long as humidity is sufficiently low
3. The distance between the sphere surface and the flat surface is very small compared to the radius of the contact line	Often does not hold as the contact line is small due to the narrow tip geometry	Holds for most cases
4. Thickness of the capillary layer is humidity independent	Does not hold	Does not hold
5. The radius of the curvature of the meniscus is much smaller than the radius of the contact lines	Holds for most cases	Holds for most cases
6. θ is the same for both surfaces	Holds only in some rare cases	Holds only in some rare cases
7. Sphere and plane are smooth	Holds only in some rare cases	Holds only in some rare cases
8. Sphere and plane are non-deformable	Holds only in some rare cases	Holds only in some rare cases

Table 3: Summary of assumptions when using standard AFM compared to colloidal probe AFM for a sphere on plane geometry contact event.

As can be seen from table 3 above, for the majority of AFM cases, even the colloidal case, the simplified expression in Equation 12 cannot hold. Instead, a more sophisticated model needs to be developed. The next sections cover the development of the model to exclude some of the assumptions. This yields models which are broadly applicable to a colloidal probe AFM so that experimental and theoretical values can be compared.

As stated in assumption 4, Equation 12 is independent of humidity, which clearly does not hold for 0% relative humidity where there will not be a capillary layer at all. While it has been shown to hold for lots of macroscopic measurements, it is insufficient for micro-scale AFM measurements under ambient conditions.

2.2.9 HUMIDITY DEPENDENT CAPILLARY FORCE

An equation for the humidity dependent capillary force is fairly well agreed upon in the literature. An expression for this was neatly outlined by Xiao and Qian (Xiao and Qian, 2000) and is given below in Equation 13.

As mentioned above, capillary force comes from a combination of the surface tension and the pressure difference between the inside and outside of the meniscus due to its curvature. This model assumes the curvature of the meniscus can be modelled as an arc of a circle.

$$F_{capillary} = F_{pressure} + F_{surface\ tension} = \pi r_1^2 \Delta P + 2\pi \gamma_L r_1 \sin(\theta_1 + \varphi)$$

Equation 13.

And

$$\Delta P = \gamma_L \left(\frac{1}{r_2} - \frac{1}{r_1} \right)$$

Equation 14.

These have been defined within fluid dynamics but require knowledge of the additional term ϕ , the filling angle and the geometrically related r_1 and r_2 , which cannot be determined experimentally. The contact angles ϑ_1 and ϑ_2 are experimentally measured values for the interacting surfaces.

As long as the system is in thermal equilibrium, the relationship between the filling angle and the radii of curvature of the menisci is obtained by using the Kelvin equation (Equation 15 and 16).

$$\frac{kT}{\gamma v_0} \ln \frac{p}{p_s} = \left(\frac{1}{r_1} - \frac{1}{r_2} \right) = \frac{1}{R \sin \phi} - \frac{\cos(\theta_1 + \phi) + \cos \theta_2}{a + R(1 - \cos \phi)}$$

Equation 15.

$$r_2 = \frac{-V\gamma_L}{N_a k T \ln \left(\frac{P}{P_s} \right)}$$

Equation 16.

Where P is the vapour pressure, P_s is the saturated vapour pressure, V is molar volume, T is absolute temperature, and k is the Boltzmann constant

The other term which needs to be defined is a , the separation distance, which must be non-zero and finite. It is almost impossible to determine experimentally but the convention is to use the recommendation of Israelachvili and Adams (Israelachvili and Adams, 1977) who suggest a value of a for the case of van der Waals approximations of $\sim 2 \times 10^{-10}$ m.

This gives a model which allows the calculation of the capillary force at a given humidity, for a given sphere, temperature, liquid, and separation distance. This model is known as the Laplace-Kelvin model. It predicts an increasing capillary force for increasing humidity.

The work of Marmur (Marmur, 1993) expanded on this basic model to include other geometries, environmental conditions and separation distances. De Lazzer, Dreyer and Rath (de Lazzer, Dreyer and Rath, 1999) continued this and incorporated surface tension in their model, discussing capillary adhesion for a variety of probe geometries including spherical, conical and parabolic. Finally, Mantel (Mantel *et al.*, 1995) conducted direct measurements to confirm the predictions of these models, finding decent agreement in trends but a large discrepancy in absolute values.

2.2.10 HUMIDITY DEPENDENT CAPILLARY FORCE AND VDW FORCES

Having established the method for calculating the magnitude of the capillary force, it is now possible to add back in the term for vdW forces. At low relative humidity (RH) F_c tends to zero and the vdW term dominates the adhesion. As relative humidity increases, water will begin to condense in the gap between the plane and the sphere, and the vdW forces will start to decrease. This is because the Hamaker constant in water is lower than in air. As relative humidity continues to rise, F_c will begin to dominate the adhesion value. This introduces the discussion of *critical relative humidity*. This is the RH value where a meniscus can fully form, and F_c will no longer = 0 and will begin to contribute to the overall adhesion.

The critical relative humidity is not simple to determine and often is found experimentally. It has also been found to be related to the hydrophobicity of the surfaces involved (Binggeli and Mate, 1994; Farshchi-Tabrizia, Kappl and Butt, 2008; Çolak *et al.*, 2012). Typical values are anywhere between 10 – 99% RH. Overall, this means that at low values of RH (below critical humidity), a change in RH will have a minimal effect on adhesion, however at RH larger than the critical value, changing RH will have a large effect on adhesion (Kappl and Butt, 2002).

There are at two main approaches which try and predict this value from first principles. The first was suggested by Coelho and Harnby (Coelho and Harnby, 1978). This is based on the idea of thermodynamic equilibrium between the bulk liquid, the liquid meniscus, and water in vapour form. In order to prevent water in the meniscus from boiling, the bulk liquid must be under greater pressure than the vapour; therefore, if the water pressure in the vapour is known, it is possible to predict the minimum pressure and therefore the curvature of a stable meniscus. This leads to values of critical relative humidity of between 70-99%, higher than what is typically found experimentally. It has been suggested that this discrepancy could be because in the nano-regime there would fail to be defects to be the source of boiling initiation, so the initial assumption of this model was flawed.

Rabinovich (Rabinovich et *al.*, 1991) suggested an alternative approach where they proposed that below a certain meniscus dimension, the adsorbed molecules cannot be considered a macroscopic phase. This means that macroscopic phenomena such as surface tension or capillary forces would not apply. Hence the critical humidity is the point at which the adsorbed water molecules could be considered to act macroscopically, which they experimentally determined to be about 1 nm. Therefore, critical relative humidity is at the point where the calculated meniscus for a given material and geometry would exceed this dimension.

Despite all these improvements, the theory is still poor at predicting adhesion, with experiments consistently finding values are lower than predicted. This is because it fails to take surface roughness into account, which will now be re-introduced to the discussion.

2.2.11 CAPILLARY FORCE AND SURFACE ROUGHNESS

The experimental findings of Çolak (Çolak *et al.*, 2012) were that humidity and surface roughness effects are strongly interrelated. For their measurements using a 2 μm colloidal sphere on a surface, they found that adhesion to a roughened surface showed a greater relative increase with increasing RH than for a chemically equivalent smooth surface. This implies that the roughness of a surface affects how the meniscus of the capillary layer will form and behave.

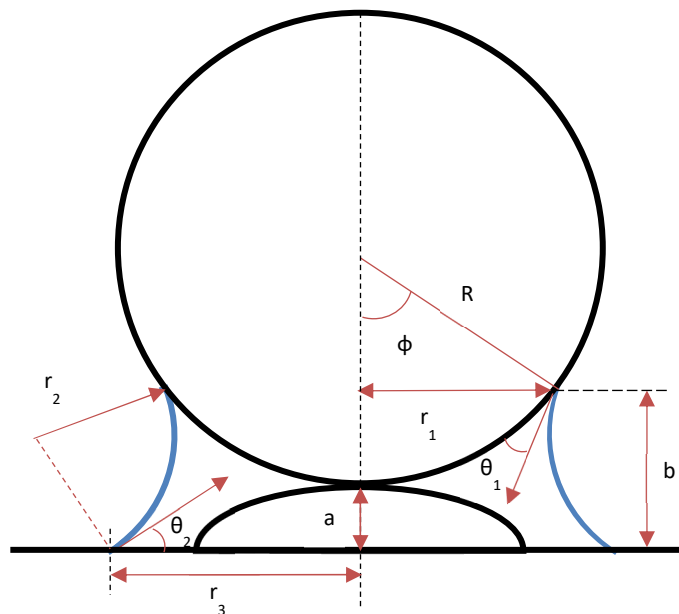


Figure 18: Schematic of sphere-plane contact in the presence of a capillary layer that bridges across surface asperities.

One of the most significant developments in this area came from Rabinovich (Rabinovich *et al.*, 2002). They expanded on the humidity dependent expression to include a factor of surface roughness.

As before, the capillary force arises from a combination of a pressure differential across the meniscus and the contribution of the surface tension. The pressure difference is determined from the Laplace Equation and the equilibrium radius of the meniscus, and therefore the filling

angle, are given by the Kelvin equation. Asperities of nano-scale roughness are introduced into the surface as seen in Figure 18. These are approximated by nanometre sized spherical asperities with their centres located below the average surface plane with the distance from the average surface plane to the tip of the asperity denoted a .

They developed a relationship between a and an experimentally accessible value of roughness (RMS – root mean squared). They find that:

$$a = 1.817.RMS$$

Equation 17

This powerful relationship allows a term for surface roughness to be included in the calculations. From the above expressions it is possible to derive that

$$F_c = 4\pi\gamma_L R \left(\frac{\cos\theta_1 + \cos\theta_2}{2} \right) \left[1 - \frac{a}{2r_2 \left(\frac{\cos\theta_1 + \cos\theta_2}{2} \right)} \right]$$

Equation 18

Using equation 16, 17 and 18, it is therefore possible to calculate the adhesion force for a given humidity and surface roughness.

This will only hold for very large RH such that the meniscus can fully bridge between the surface and the contacting sphere. In a low humidity case, bridging between an asperity and the contacting sphere may occur.

This case of a smaller bridging capillary is shown in Figure 19.

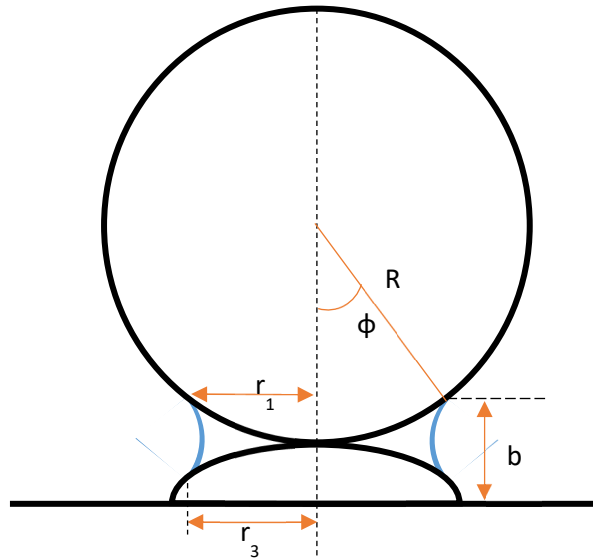


Figure 19: Schematic of sphere-plane contact for a rough surface in a low humidity case where capillary is bridging between an asperity and the contacting sphere.

Here the meniscus is effectively formed between two spheres. For this situation, an effective radius of the interacting particle and asperity, R_{eff} , can be calculated using Equation 19 which is based on the model of (Derjaguin, 1934). This can be fed back into Equation 18 as the R term to obtain the capillary force for this case.

$$R_{eff} = \frac{2R_{sphere}R_{asperity}}{R_{sphere} + R_{asperity}}$$

Equation 19.

The result of this equation is a very small effective radius which predicts a very low capillary adhesion for a low relative humidity regime. The experimental work in the same paper of (Rabinovich *et al.*, 2002), validated this theory. A graph of their work comparing theoretical

modelled data and measured experimental data from surfaces with three differently sized asperities can be found in Figure 20.

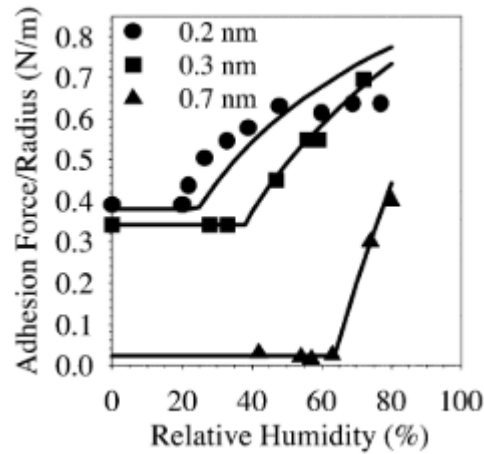


Figure 20: Solid lines are theoretical values of adhesion; solid points are measured adhesion for surfaces with differently sized asperities.

There are three things of note from their results. Firstly, they found that adhesion force decreases with an increase in roughness in the low relative humidity regime, but the adhesion is low for all low humidity cases. Secondly, they found a critical relative humidity at which the force of adhesion begins to increase. And thirdly, that the value of this critical relative humidity increased with increasing roughness.

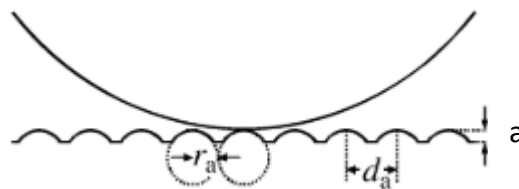


Figure 21: Schematic of sphere-plane contact for a rough surface as modelled by Farshchi-Tabriziam (Kappl and Butt, 2008).

An alternative method of incorporating roughness into a calculation that includes capillary thickness was proposed by (Farshchi-Tabrizia, Kappl and Butt, 2008). Instead of defining a

numerical relationship between RMS and separation distance, they simply took the separation distance, a to be the height of any given asperity. They then expanded this to an array of spherical asperities, as can be seen in Figure 21. This a term can be fed into Equation 18 to get the adhesion force. In addition, they defined a radius, r_{asperity} and spacing factor a so that multiple asperities are defined. The results of this model can be seen in Figure 22. Using this model, they found that the size of the asperities had a dramatic difference on the measured adhesion force at the same humidity. However, the downside of this approach in practice is the challenge of determining a value of a that will be valid across an entire surface.

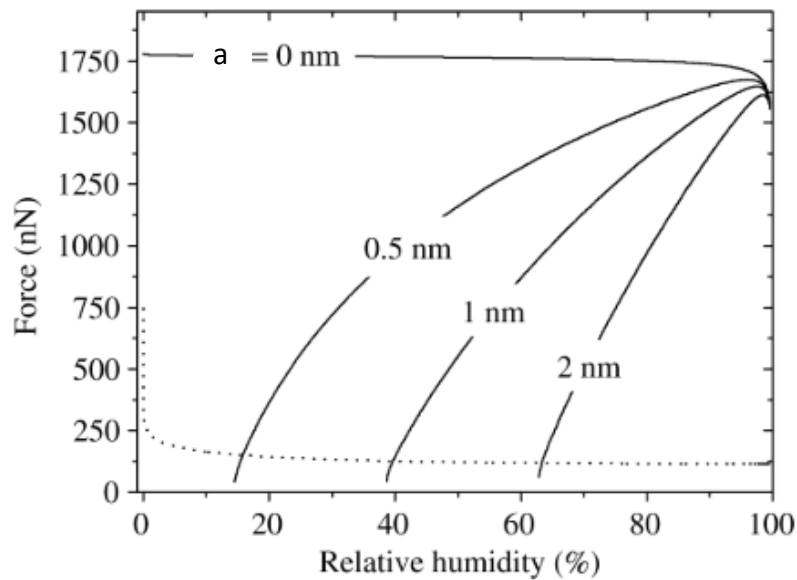


Figure 22: Capillary force between sphere of radius $R = 2 \mu\text{m}$ and a planar surface versus relative humidity for different distances ' a ' of closest approach. The vdW forces are given by the dashed line and were calculated using equation 4 and an a_0 of 0.17nm . The contact angle of both surfaces was set to 10° .

2.2.12 CAPILLARY FORCES, SURFACE ROUGHNESS AND DEFORMATION

In all the models for capillary force and roughness that have been described so far, the surface deformation has been neglected (Hertzian or otherwise). The continuation of the work by

Farshchi-Tabrizia, Kappl and Butt (Farshchi-Tabrizia, Kappl and Butt, 2008) added this back in, but assumed that the tops of all their asperities seen in Figure 21 were elastically deformable according to Hertz theory, defining an indentation term δ where:

$$\delta = \frac{1}{4} \left(\frac{9F_{adh}(1 - \nu^2)^2}{r_{asperity}E^2} \right)^{\frac{1}{3}}$$

Equation 20.

Where F is the meniscus force plus the van der Waals force, E is Young's modulus, and ν is Poisson's ratio. Indentation value of $-\delta$ should then be inserted back into the Kelvin equation in the place of a to re-calculate meniscus radius and subsequently adhesion. Including this term, they found an increase in the meniscus force.

2.2.13 SUMMARY

Over the course of this review, it has been shown that calculating adhesion is very challenging in any system other than one that is completely idealised. There is a lot of disagreement between different researchers about the correct methods to employ and there are substantial discrepancies between calculated and experimental results (Jones *et al.*, 2002).

In addition, the inclusion of surface roughness, capillary layers (and subsequently humidity dependence and critical relative humidity) and surface deformation all complicate the calculation of overall adhesion. These concepts, and the theories proposed for modelling them, have been covered in this review. As has been shown, even the most sophisticated theories in the literature are unable to capture more than an idealised roughness of an isotropic material that deforms elastically in the presence of a Newtonian capillary layer.

In particular, the idealised roughness means these theories are still limited in their applicability to real life surfaces, since a singular term for asperity height, or RMS roughness fails to capture all the nuances of surface topography. This is particular important when a capillary layer is present, as some work has indicated that with a very rough surface, air cavitation and movement of the layer will occur during the contact event (Thormann, 2017).

In conclusion, it is therefore the case that many researchers attempting to determining the surface adhesion of a surface will do so experimentally. This is often done using FMM under carefully controlled experimental conditions. However, the trends of the theories – that adhesion will increase with humidity and with surface area, but decrease when surface roughness increases, are expected to hold true in experimental measurements, even though accurate quantitative values are hard to predict from theory.

3. METHODS AND MATERIALS

A broad range of spectroscopic, microscopic, and surface analysis techniques have been employed throughout this research. The techniques of greatest importance will be discussed in detail while those of lesser significance will be only briefly mentioned.

3.1 CHEMICAL COMPOSITION

3.1.1 FOURIER TRANSFORM INFRARED SPECTROSCOPY

3.1.1.1 *PRINCIPLES OF FTIR*

Fourier Transform Infrared Spectroscopy (FTIR) is a technique for compositional analysis, primarily of organic materials. The sample of interest is bombarded with infrared radiation (IR) and the spectrum collected, usually by examining the radiation that passes through to the other side without absorption (transmission). Absorption intensity is plotted relative to wavelength/frequency of the radiation. Absorption of particular frequencies is characteristic of the presence of particular functional groups (known from a reference database or literature) and hence the spectrum can be used to identify the presence of particular chemicals for functional groups.

3.1.1.2 *INSTRUMENTATION OF FTIR*

FTIR spectra were recorded on a Thermo-Fisher Nicolet is50 equipped with a Di-ATR accessory, spectra were acquired with a resolution of 4 cm^{-1} and an accumulation of 32 scans. The depth into the sample probed is dependent on the wavelength, angle of incidence and refractive index of the sample being probed but is typically of the order of $100\text{ }\mu\text{m}$.

3.1.2 RAMAN SPECTROSCOPY

3.1.2.1 *PRINCIPLES OF RAMAN*

Raman Spectroscopy is a technique for compositional analysis, primarily of organic materials. Using a source of monochromatic light, Raman measured the inelastic scattering of the light as it passes through the sample of interest. From this scattering the vibrationally active modes of molecules can be determined. It is considered a compliment to IR spectroscopy as molecules which are IR active will be Raman inactive and vice versa.

3.1.2.2 *INSTRUMENTATION OF RAMAN*

Raman Spectra were recorded on a Horiba LabRam HR Evolution equipped with a Sincerity CCD. Spectra were acquired using a 633 nm HeNe laser, 100 μm confocal hole, 600 gr/mm grating and an Olympus LMPLFLN 50x, N.A. 0.5 metallurgical objective.

3.1.3 ENERGY DISPERSIVE X-RAY SPECTROSCOPY

3.1.3.1 *PRINCIPLES OF XPS*

Energy Dispersive X-ray Spectroscopy (EDX) is an analytical technique which is primarily used to determine which elements are present in a sample, and their proportions. The guiding principle is that excitation of an atom via electron bombardment can cause an electron in its inner shell to be promoted to an excited state, leaving a hole in the lower energy shell. It is then energetically favourable for a higher energy electron to fill that hole and in the process lose some energy which is ejected from the atom as a photon. Since the energy levels in atom shells are quantised and distinct to the atomic structure of the element, the energy lost will be characteristic of the atom the photon is ejected from. In EDX the sample of interest is bombarded with x-rays and the emitted radiation is measured in an energy dispersive spectrometer. The energies seen on the spectrum and their intensities are compared with the

known literature values for each element, such that the elemental composition of the sample of interest can be determined.

3.1.3.2 *INSTRUMENTATION OF XPS*

EDX measurements were conducted using a Hitachi TM3030 tabletop scanning electron microscope with EDX bolt on.

3.1.4 GAS CHROMATOGRAPHY MASS SPECTROMETRY

3.1.4.1 *PRINCIPLES OF GC-MS*

Gas Chromatography Mass Spectrometry (GC-MS) is an analytical technique used to detect what chemicals/substances are present in a sample. It is highly sensitive even to trace elements and chemicals even in a complex mixture of substances. In the first stage the sample is heated until it enters the gas phase and injected into the column with a carrier gas (usually an inert gas such as helium or nitrogen). The column is coated internally with a thin layer of a specific “stationary phase” – usually a polymer or inert solid. The different chemicals in the substance are separated by chromatography, relying on the chromatographic principle that different chemicals can be separated by their retention times in the column. These retention times are determined by the chemical’s affinity for the stationary phase of the column, chemicals with a high affinity for the stationary phase will take a long time to pass through relative to the mobile phase, and those with a low affinity will travel through at a speed similar to the speed of the mobile phase. In this way the chemicals in the mixture are separated and enter the second stage (the mass spectrometer) at different times. The chemicals are then analysed by the mass spectrometer.

The mass spectrometer analyses the elements by first ionising them, usually by bombarding them with free electrons emitted from a filament via thermionic emission. This both breaks

them down into various fragments and gives them a charge. The fragments produced by a specific starting molecule and a known electron energy are characteristic of the molecule and reproducible. The mass to charge ratio of the fragments are analysed by accelerating them and subjecting them to an electric or magnetic field and measuring their deflection.

GC-MS allows complex mixtures of chemicals to be separated and analysed. The resulting spectrum is compared to literature references and the components of the mixture as well as their proportions determined.

3.1.4.2 INSTRUMENTATION OF GC-MS

GC-MS measurements were conducted on an 820A GC + 7697A Headspace autosampler + 5977A MSD using a DB-Wax (30 m x 0.25 mm x 0.50 μ m) column and a He flow rate of 1.41 ml/min.

3.1.5 ULTRAVIOLET HIGH PRESSURE/PERFORMANCE LIQUID CHROMATOGRAPHY

3.1.5.1 PRINCIPLES OF UV-HPLC

Ultraviolet High Performance Liquid Chromatography (UV-HPLC) is similar in principle to GC-MS in that two techniques, one chromatographic and one analytical, are used in sequence; to first separate and then analyse a mixture of chemicals.

In UV-HPLC the substance of interest is dissolved into an appropriate solvent and injected as the mobile phase into a column which contains a stationary phase. The chemicals in the substance are separated by their affinity for the stationary phase, which is often determined by extent of hydrogen bonding or other dipole interactions. The retention time in the column is therefore specific to each chemical and they elute from the column at different times. Once they emerge from the column the components are analysed by a UV detector. This operates

in a similar manner to FTIR in that a characteristic fingerprint of functional groups present in the chemical are determined by UV absorption at each frequency.

3.1.5.2 *INSTRUMENTATION OF UV-HPLC*

HPLC measurements were conducted on an Agilent 1260 Infinity II HPLC using a Zorbax SB-C18 (150mm x 4.6 mm x 5 μ m) column. Mobile phase A was 0.1% FA in Water and mobile phase B was MeOH. Both used a flow rate of 0.7 ml/min.

3.2 TOPOGRAPHY MEASUREMENT

3.2.1 COHERENCE SCANNING INTERFEROMETRY

3.2.1.1 *PRINCIPLES OF CSI*

Coherence scanning interferometry is a surface metrology technique which was developed in the early 60s (Denisyuk, 1962). Coherence Scanning Interferometry, here after known as CSI, has a resolution limit of approximately 1 μ m. Unlike optical microscopy where the resolution limit is driven by the wavelength of visible light, CSI utilises the wave superposition principle to unlock higher resolution.

The superposition principle states that the total amplitude in a given medium of two (or more) waves is equal to the sum of the individual wave amplitudes that would have been produced by the same waves in isolation. CSI exploits this rule and extracts topographical information about a surface from the phase difference between an incident beam which was reflected off of the sample of interest, and a reference beam.

The two beams of white collimated light are produced by a source. One beam is bounced off a mirror, while the other is shone at the sample surface. While the reference beam remains unchanged, the sample beam will be scattered and reflected according to the topography of

the sample surface. Both beams then combine to form interference pattern which is analysed pixel by pixel. At each x-y position the superposition principle allows for the calculation of the phase different between the two beams, and thus the difference in path length. As long as the difference in path length is less than half the coherence length of the electromagnetic source, the difference in path length allows the height of the surface at that pixel to be determined, and thus a topographical image of the surface can be built up.

Following a topographical image of the surface being obtained, quantitative values for surface roughness can be extracted. Some examples of these values of surface roughness are given in Table 4 below.

Parameter	Description
S_a	The mean deviation of the peaks and troughs from the measured mean average height of the surface
S_q (also known as RMS)	Root mean squared of S_a
S_v	Absolute maximum valley/trough depth below the mean average height of the plane.
S_p	Absolute maximum peak height above the mean average height of the plane.
S_t	Maximum height of the profile ($R_t = R_p - R_v$)
S_{sk}	“skewness” – measure of the asymmetry of the distribution of the deviations from the measured mean average height of the surface
S_{ku}	“kurtosis” – measure of the tailedness of the distributions of the deviations from the measured mean average height of the surface

Table 4: Summary of surface roughness parameters.

In the case of PET films where filler particles have been used, CSI provides information about how fillers permeate the bulk of the film. As Figure 23 shows, the location of filler particles in the PET bulk can significantly affect the surface topography, which can affect the visual appearance of the film (e.g., matt-ness). The surface will be changed in different ways depending upon the depth into the surface that the particle is sitting.

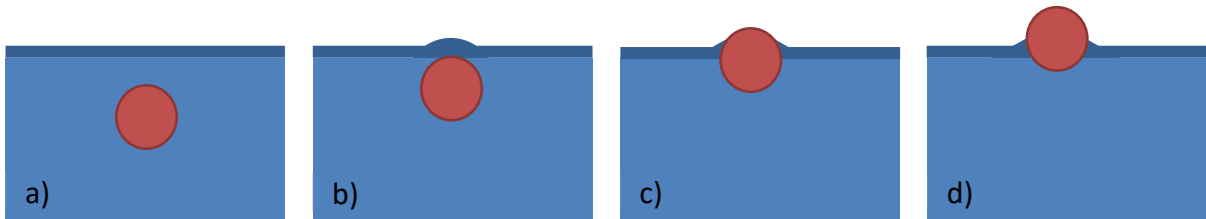


Figure 23: Schematic showing how a filler particle can be located in a PET film. a) particle far below the surface - no surface effect seen. b) particle below the surface, some surface topography effects seen. c) particle at the surface, partially exposed d) part

As CSI is able to measure the surface at a relatively high spatial resolution but at a large field of view, this makes it an ideal tool to assess topography of a film surface.

3.2.1.2 INSTRUMENTATION OF CSI

Coherence scanning interferometry measurements were conducted on a Veeco NT9800 using VSI mode, a magnification aperture of 50x and a variety of stitch sizes.

3.2.2 ATOMIC FORCE MICROSCOPY

3.2.2.1 PRINCIPLES OF AFM

Atomic force microscopy was invented in 1986 by scientists working in partnership with IBM and Stanford University. It was developed as a technique allows surfaces to be imaged in atomic resolution and had been used widely in many fields over the subsequent decades. Atomic force microscopy was an evolution of an earlier development, scanning tunnelling microscope (STM), which was developed at IBM in 1982. STM was the first microscopic technique which could image surfaces at the atomic scale and relies on quantum tunnelling

between a conducting tip, and a semi-conducting or conducting surface. AFM was the natural extension of STM to allow non-conducting surfaces to be imaged.

Instead of relying on quantum tunnelling, AFM derives its sensitivity from the Lennard Jones Potential. The Lennard Jones Potential graphs the potential energy between two atomic bodies versus the distance between them. Across this distance there is both an attractive and a repulsive regime. The minimum energy occurs at the distance at which the atoms would be separated if they were in a chemical bond. An atomic force microscope probes these atomic forces (Binnig, Quate and Gerber, 1986).

3.2.2.2 INSTRUMENTATION OF AFM

In AFM, the sample of interest (which can be a solid surface in air or in liquid medium) is placed on a positioning stage. The sample of interest is scanned by a tip, mounted on a flexible

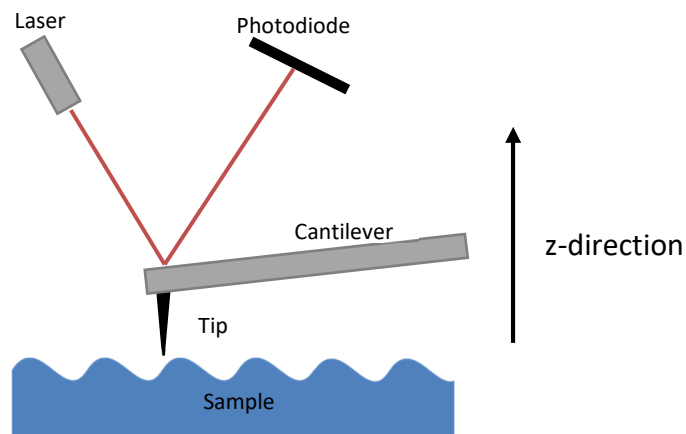


Figure 24: Diagram of typical AFM with atomically sharp tip

cantilever. A highly sensitive piezo controls the z-position of the cantilever and the tip is brought into contact with surface. This is shown schematically in Figure 24.

As the tip scans across the sample, the cantilever is deflected by the atomic forces. A laser beam reflected off of the cantilever, records these deflections on a photodiode. Thus, the

force felt by the cantilever, which corresponds directly to the topography of the sample, is transferred to the photodiode, where it is recorded for each x-y position of the scanned sample.

Cantilevers can have different physical properties (e.g., spring constant) which are determined by width, length, thickness, and material. Different cantilevers are used for different “modes”. The tip at the end of the cantilever can also be altered to improve image quality.

The AFM has many operational modes, including contact mode and tapping mode, which are used for imaging. Force modulation mode is the most relevant to this project and will be discussed in Section 3.3.2. Lateral force microscopy will be discussed in Section 3.4.1

3.3 SURFACE ENERGY/ADHESION MEASUREMENT

3.3.1 CONTACT ANGLE GONIOMETRY

3.3.1.1 PRINCIPLES OF CONTACT ANGLE GONIOMETRY

Contact angle measurement via a goniometer is a quantitative method for measuring surface energy. The contact angle refers to the angle formed between flat substrate for which the surface energy is to be determined and the tangent to the curvature of a liquid droplet at the point of contact with this substrate. A schematic of this is shown in Figure 25.

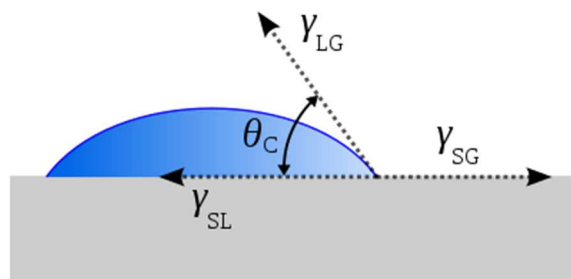


Figure 25: Schematic of the measurement of contact angle (θ_c) for a droplet on a surface.

The water contact angle of a droplet on a surface is determined by the three surface tensions for the three interfaces $\gamma_{\text{solid-liquid}}$, $\gamma_{\text{liquid-gas}}$ and $\gamma_{\text{solid-gas}}$. This is determined by the thermodynamic equilibrium between these three terms, where the shape of the droplet will be such that all are minimised. They are related to work adhesion by the Young-Dupre equation.

$$\bar{\omega}_{\text{adhesion}} = \gamma_{LG} + \gamma_{SG} - \gamma_{SL} = \gamma_{LG}(1 + \cos \theta)$$

Equation 21

$$\text{where } \gamma_{SG} = \gamma_{LG} + \gamma_{LG} \cos \theta$$

Equation 22

In surface goniometry contact angle is measured for two liquids, for which the $\gamma_{\text{liquid-gas}}$ term is well known in the literature. From the measurement of θ_{contact} in the two liquids it is then possible to calculate surface energy by one of two methods: harmonic or geometric.

Harmonic:

$$\gamma_{LG}(1 + \cos \theta) = 4 \left(\frac{\gamma_{LG}^d \gamma_{SG}^d}{\gamma_{LG}^d + \gamma_{SG}^d} + \frac{\gamma_{LG}^p \gamma_{SG}^p}{\gamma_{LG}^p + \gamma_{SG}^p} \right)$$

Equation 23

Geometric

$$\gamma_{LG}(1 + \cos \theta) = 2 \left((\gamma_{LG}^d \gamma_{SG}^d)^{\frac{1}{2}} + (\gamma_{LG}^p \gamma_{SG}^p)^{\frac{1}{2}} \right)$$

Equation 24

Where ^d denotes the dispersive component and ^p denotes the polar component. In either case these construct simultaneous equations which can be solved.

In order to obtain accurate measurements for θ_{contact} , a motorised pipette is programmed to deposit a droplet of water of a known volume onto the surface of interest. An in-built camera captures a photo of the droplet at surface level and the angle determined by the on-board computer.

3.3.1.2 INSTRUMENTATION OF CONTACT ANGLE GONIOMETRY

Contact angle measurements were conducted using VCA Optima XE Goniometer. Two liquids used were de-ionised water and diiodomethane at a volume of 3 μL per droplet. 3 measurements of contact angle were taken, and surface energy calculated using both methods indicated above (harmonic and geometric).

3.3.2 FORCE MODULATION MODE

3.3.2.1 PRINCIPLES OF FMM

AFM is primarily used as a surface imaging technique, but it is also possible to use the technique to measure surface forces. This is done by collecting “force curves”. The AFM tip is sequentially moved towards and then away from the surface at a defined rate, during which time the cantilever movement is measured (Cappella and Dietler, 1999). This is achieved by applying a triangular voltage waveform to the z-piezo, with an amplitude and frequency defined by the user.

A schematic example of a force curve is shown in Figure 26. Section A-B is the region where the cantilever is moving towards the sample but not interacting with any long-range forces. At point B the attractive forces of the surface cause the cantilever to *snap to contact*. The snap to contact is associated with the tip being attracted to the surface by long range forces once it gets close to the sample.

At point C the piezo direction reverses, and the cantilever begins to move away from the surface (or “retract”). Then, between point C – D, the probe is continuing to retract past the original z-position where contact occurred, but remains in contact with the surface due to adhesion forces, until the tip detaches at point D. Information about the surface can be extracted from features of the force curve (Butt, Cappella and Kappl, 2005a), including Young’s modulus, adhesion and diffusivity. This operational mode of AFM is known as force modulation mode.

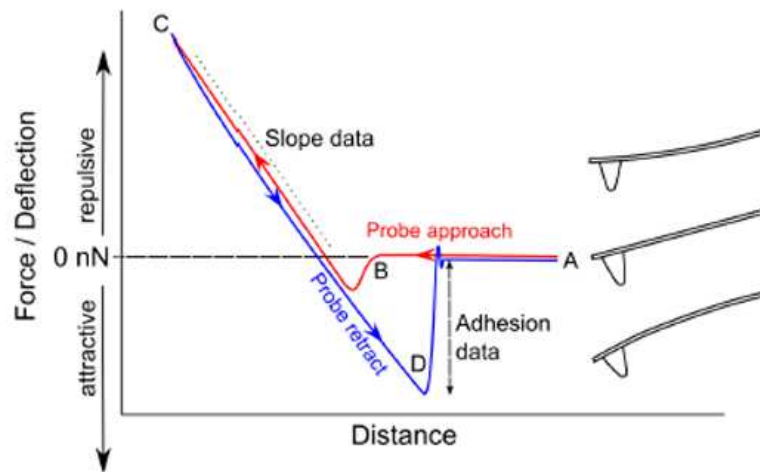


Figure 26: Example of a force curve.

In a situation where there is any deformation occurring during contact, there is not a one-to-one relationship between the deflection of the end cantilever and the deflection of the spot on the photodiode. This relationship is described by the deflection sensitivity.

The deflection sensitivity is determined by measuring the deflection of the cantilever while in contact with a sample of “infinite” hardness – typically a sapphire standard. In this set up the motion of the cantilever by the Z-piezo is assumed to correlate exactly to the deflection of the end of the cantilever and so for a contact region the gradient is extracted – which gives a deflection sensitivity in V/m. Once the spring constant and deflection sensitivity are known, it

is possible to calculate the force felt by the cantilever for a given deflection in volts according to the following equation.

$$Force = Photodiode\ deflection \cdot \frac{1}{deflection\ sensitivity} \cdot spring\ constant$$

Equation 25

3.3.2.2 COLLOIDAL PROBES

An extension of the force modulation AFM mode has been to modify AFM tips, so instead of a sharp imaging AFM tip probing a surface, the surface is probed by a particle of interest – thus the interactions between the two can be investigated. This is shown schematically in Figure 27. The first reported work to do this was that of Ducker, Senden and Pashley (Ducker, Senden and Pashley, 1991). Where a silica microparticle was attached to a tip-less cantilever using epoxy glue and used to probe the surface. Subsequent work by Mantel’s group (Mantel *et al.*, 1995) and Eastman and Zhu (Eastman and Zhu, 1996) repeated this technique with different materials.

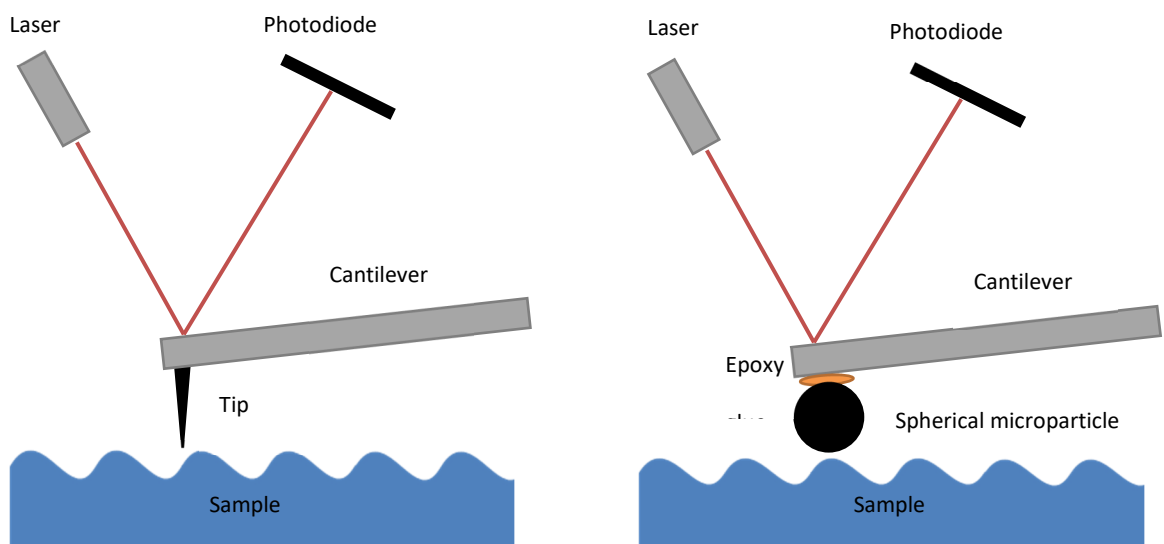


Figure 27: Left: typical AFM set-up with tip mounted on tip. Right: adapted AFM tip with microparticle glued to cantilever (not to scale).

Several years later Ong and Sokolov (Ong and Sokolov, 2007) extended this further by using a nano-particle instead of a microparticle in order to probe a silica surface. Nano-sized particles of cerium oxide were compared to micro-sized ceria particles in this use case.

Adhesion can be calculated from the force curves as in force modulation mode collected using the colloidal probe as long as the contact mechanics are assumed to be Hertzian (Johnson, Kendall and Robert, 1971) and the deflection sensitivity and the spring constant of the cantilever are known.

3.3.2.3 *INSTRUMENTATION OF FMM*

Colloidal probe microscopy was carried out on a Veeco dimension 3100 AFM. Probes were constructed using a MX7630 motorized crossed roller bearing micromanipulator powered by a MC1100e 4-axis push-button control unit. Untipped probes from Apex (Specification AIO-TL) with a spring constant of 0.2 N/m, 2.7 N/m and 7.4 N/m were mounted into the micromanipulator.

The colloids used were Duke standards borosilicate glass microspheres with nominal diameter of 9.7 +/-0.8 μm , and Cospheric PSMS-107 polystyrene microspheres with nominal diameter 10 +/- 1.5 μm .

The deflection sensitivity was found by collecting a force curve on a standard sapphire sample. Force curves were collected with an applied normal force of 50nN unless otherwise stated. Force curves were collected across a 20 x 20 grid with a column and row spacing of 4 μm , at 3 independent locations across the surface. This yielded 1200 force curves per measurement.

3.3.2.4 CONSTRUCTION OF COLLOIDAL PROBES

The cantilever is brought under the optics of an optical microscope at 10x magnification and by moving it using the micromanipulator is brought into focus (Figure 28)

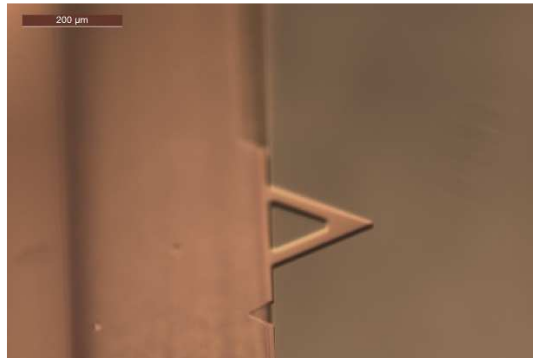


Figure 28: View down optical microscope of AFM probe held by micromanipulator in plane of focus.

Then the cantilever is then raised using the micromanipulator above the plane of focus. Some epoxy is smeared onto a glass slide and placed onto the bed of the optical microscope and brought into the plane of focus below the cantilever.

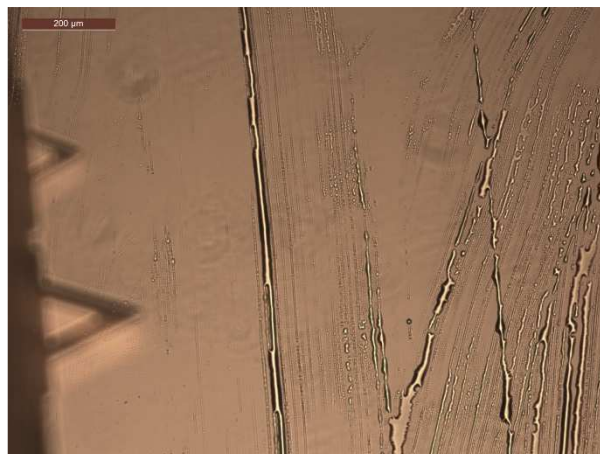


Figure 29: View down optical microscope of AFM probe held by micromanipulator above plane of focus and surface with epoxy glue in plane of focus.

Using the micromanipulator, the cantilever is lowered down to the surface, so the very tip connects with the epoxy, it is then moved laterally to remove any excess before being moved up away from the surface again.

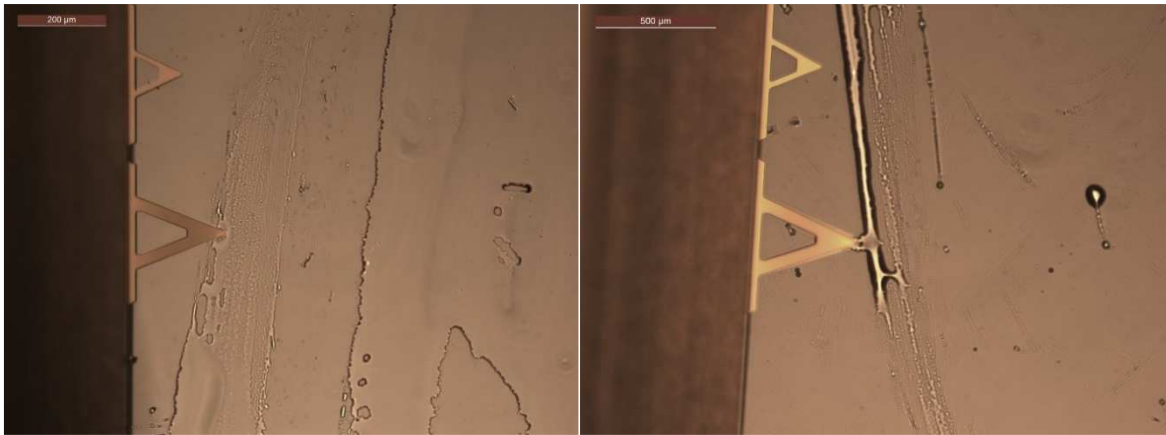


Figure 30: View down optical microscope. Left: AFM probe held by micromanipulator making contact with epoxy glue. Right: AFM probe being moved using micromanipulator to remove excess epoxy.

A small amount beads of the desired size are placed on a different glass slide under the optical microscope and brought into the plane of focus under the cantilever.

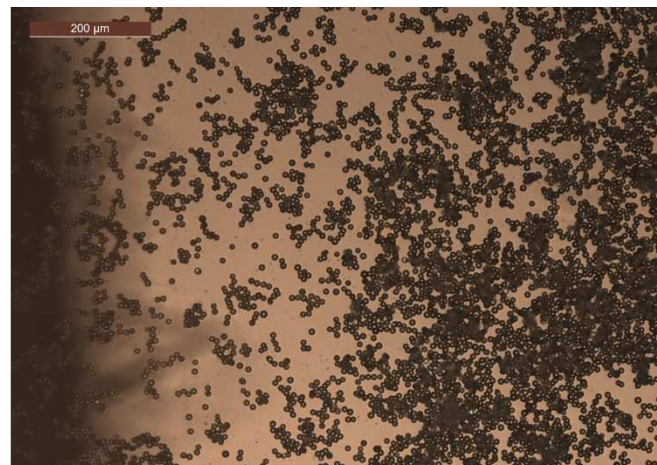


Figure 31: View down optical microscope of the beads on a glass slide in the plane of focus. Shadow of AFM probe held above the plane of focus can be seen in the bottom left

The cantilever is lowered onto one of the beads until the tip of the cantilever is seen to be deflecting indicating contact with the bead. Then it is immediately raised up and successful attachment will be indicated by the target bead no longer being visible on the surface.

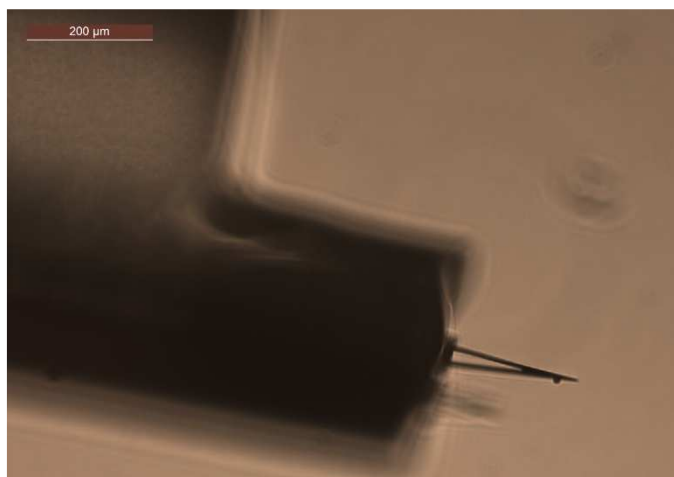


Figure 32: Side-on view of AFM probe after successful colloidal probe attachment viewed through optical microscope.

The colloidal probe is assessed with optical microscopy to ensure good silica bead placement and then left to fully cure for 24 hours before use. Probes where the bead was placed more than 15μm off the centre line of the probe were automatically rejected and for each probe the deflection sensitivity, as this changed depending upon the exact silica bead placement.

3.3.2.5 OPTIMISATION OF SPRING CONSTANT

In order to set the normal force applied to an appropriate value the spring constant of the AFM probe need to be optimised. There are several interconnected issues at play that make this a surprisingly complicated question. The spring constant of the cantilever affects both the range of forces that can be applied, but also the range of forces which can be “felt”.

A high spring constant means that the applied force must also be necessarily high. This is due to the fact that in order to collect a valid force curve, a deviation from the baseline of the non-

contact zone must be sufficiently large as to be distinct from the noise in the measurements. Attempting to apply too small a force with a stiff probe would result in such a small displacement that it would be indistinguishable from the background noise and the collection would fail. Hence a larger deflection is required, which inherently means a larger force applied to the sample, which is sometimes unfavourable.

In order to lower the applied force, the spring constant should be decreased, however this then introduces an issue when retracting from the surface and measuring adhesion. This is due to the fact that the photodiode which measures the cantilever deflection has a finite range over which it can “see” the cantilever. On the Veeco 3100 the range is 10 V and the relationship between cantilever deflection and photodiode response is given by deflection sensitivity as described above. This is demonstrated in Figure 33.

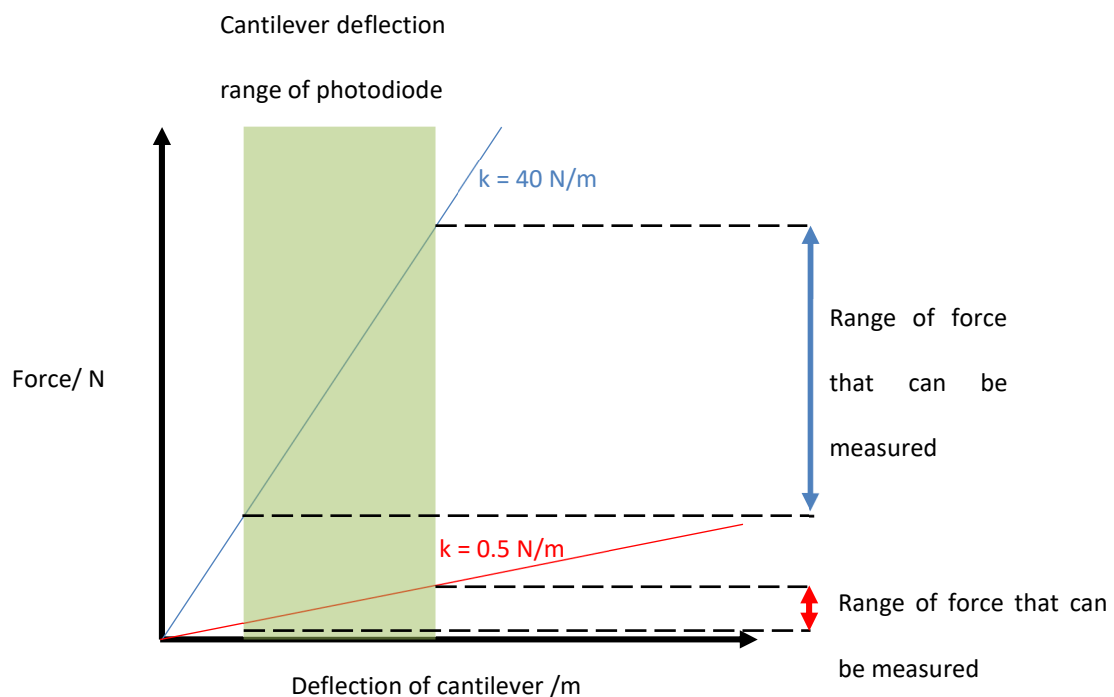


Figure 33: Example graph of the relationship between force on cantilever and cantilever deflection for probes of different forces with the range of the photodiode highlighted.

As shown, for two probes with the same deflection sensitivity, but different spring constants, the range of forces that can be measured is dependent on the spring constant. Therefore, in order to ensure the adhesion force can be measured, a spring constant high enough that the deflection that occurs during the adhesion hysteresis of the force curve does not exceed the photodiode range is required. However, a high spring constant reduces the sensitivity of the measurement, as a slight change in adhesion only has a very small effect on cantilever deflection such that it might not be able to be distinguished on the photodiode.

It was found to be the case in this study that the cantilever spring constant was indeed a delicate balance, too low and probe didn't fully detach from surface during the retraction before photodiode signal was lost; too high, and sensitivity between samples suffered and the applied force moved further from the desired value.

Through trial and error, it was found that probes with spring constants between 1 and 10 N/m were the best for this work.

3.4 FRICTION MEASUREMENTS

3.4.1 LATERAL FORCE MICROSCOPY

3.4.1.1 *PRINCIPLES OF LFM*

Lateral force mode is an operational mode of atomic force microscopy that is a derivation of contact mode. In lateral force mode the tip is engaged with the surface in contact mode with a known contact force. This is defined by the deflection setpoint applied and the deflection sensitivity of the cantilever.

In normal imaging mode the vertical deflection on the photodiode is most important, but in this mode, it is the side-to-side movement of the laser spot on the photodiode that is of interest.

On an atomically flat surface, the lateral deflection will be caused only by frictional forces. For materials which are not flat however, the flexing of the cantilever in the lateral plane will also be contributed to by topographical interactions (similarly lateral forces may contribute to the measured vertical deflection). To extract just the lateral movement caused by frictional force and eliminate the lateral deflection caused by topographical movement the trace signal minus the retrace signal of each sequential line is observed (Bhushan, 1998). The forwards and reverse direction components of the loop are subtracted from each other. As the direction of forces arising from topographical effects will be the same no matter the direction of the motion of the tip, while friction forces always oppose the tip motion, the resulting signal is proportional to twice the frictional force. In theory this frictional measurement is therefore independent of topography and contributed to only by surface energy.

3.4.1.2 INSTRUMENTATION OF LFM

Lateral force microscopy was performed on a Veeco Dimension 3100 AFM using Bruker CONTV probe with estimated (vertical) spring constant of 0.2 N/m, in contact mode. Trace minus retrace (TMR) values are taken for an applied normal force at a range of 10 nN to 80 nN and TMR/2 vs. normal applied force plotted on a graph and the gradient extracted.

3.5 SCRATCH MODELLING USING AFM

Initially scratch modelling was tested by engaging with the surface in contact mode, as though imaging the surface, and then scanning a few lines at a set deflection setpoint before

withdrawing from the surface. This is analogous to methods used in the literature mentioned above where they would scan a single line using an AFM tip.

In the standard imaging set up, and a scan area of 10 μ m by 10 μ m, the image is comprised of 512 columns and 512 rows per image, this is shown schematically in Figure 34.

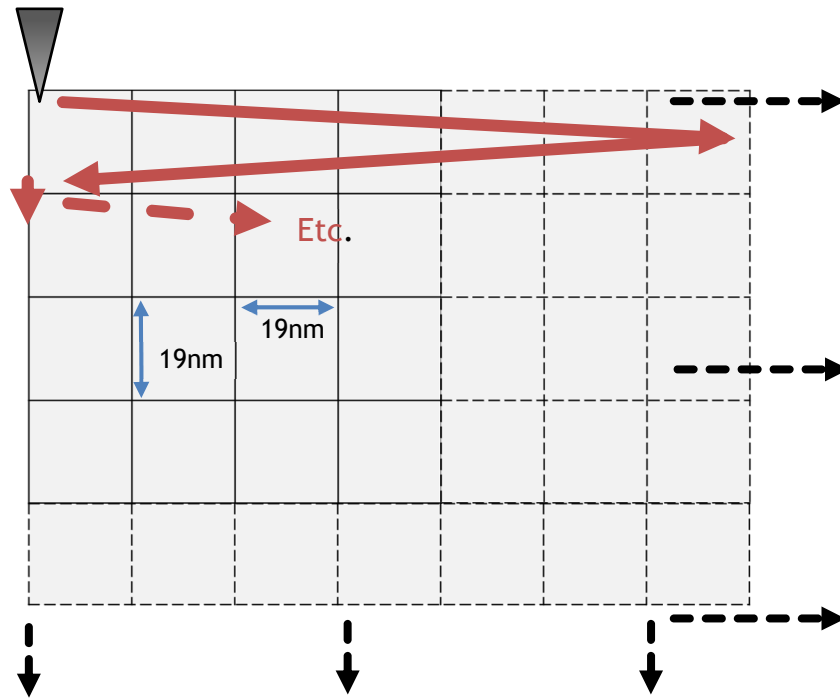


Figure 34: Schematic of a portion of the scan area of AFM image. The grid represents a part of the total pixels in a typical 512 x 512 pixel image and the red line represents the path of the AFM tip across those pixels.

This means that each pixel \approx 19 nm as shown in Figure 34. 19 nm in the x-y plane is smaller than the microscope can easily resolve laterally which essentially means the tip goes back on itself for each line. As a result, in this configuration each 'line' is scanned twice (trace and retrace) so scratch morphology is impossible to analyse.

To overcome this, a method was used where the standard imaging set up was changed. A schematic of this can be seen in Figure 35. The imaging dimension remained at 10 μ m. Lines (columns) remained at 512, but rows were reduced to 8. This meant that the space between

trace and retrace was 1.25 μm instead of 19 nm. This allows the trace and retrace scan to be resolved and the scratch morphology to be interpreted.

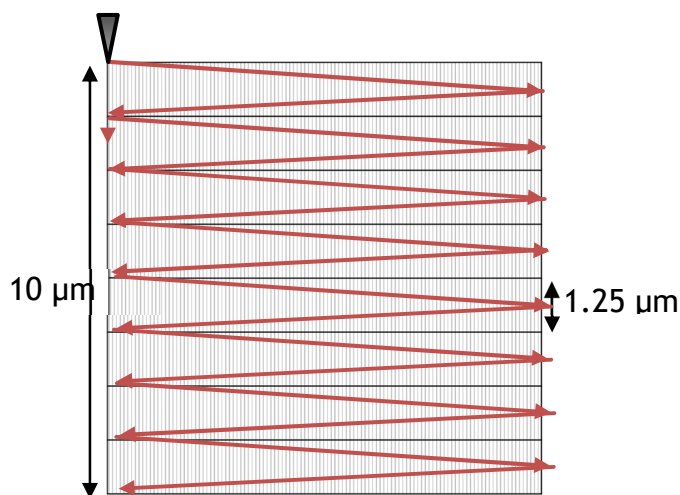


Figure 35: Schematic of AFM tip path across entire scan area in reduced line indentation method.

In all cases samples were heated using a hot plate and indented with a RFESP-75 probe with spring constant $k \approx 3 \text{ N/m}$ using the above methodology on a Veeco Dimension 3100 AFM at a range of deflection setpoints. Samples were then immediately imaged in tapping mode using RFESP-190 probe. A tip speed of 2 $\mu\text{m/s}$ was used in all cases.

3.6 MATERIALS UTILISED FOR MEASUREMENTS

3.6.1 PET FILM

Unless otherwise specified, whenever film samples are referred to in this work this denotes the following:

Cast: Unfilled, uncoated film collected from the D52 production line in fall 2018 taken immediately after quenching on the casting drum

FWD: Unfilled, uncoated film collected from the D52 production line in fall 2018 taken immediately after drawing in the forward draw at a draw ratio of 2

Finished: Unfilled, uncoated film collected from the D52 production line in fall 2018 taken from the end of the production line after winding and slitting.

3.6.2 ROLLER SURFACES

Unless otherwise specified whenever a roller sample is referred to in this work, it refers to 2 cm square samples of roller surface. These were cut from an old 1st cooling roll that was no longer in service.

3.6.3 CLEANING PADS

Unless otherwise specified, whenever a pad sample is referred to in this work it refers to a sample of the cleaning pads used by DTF on the automatic cleaners installed on the D52 production line. These pads consist of an epoxy resin in which abrasive particles of aluminium oxide are trapped.

4. ANALYSIS OF THE COMPOSITION OF CONTAMINATION FOUND ON PET PRODUCTION LINES

4.1 HYPOTHESES OF DEBRIS GENERATION

The majority of surface damage of concern in this project occurs in the forward draw on the D52 unit. Surface quality decreases with time from one clean to the next indicating that contamination is contributing to surface damage. However, it is important to stress that the contamination is not visible to the human eye, its presence is only inferred by the impact of cleaning and from historical reports.

It is important to understand the origin and composition of this contamination, as this understanding leads naturally to many other questions of concern:

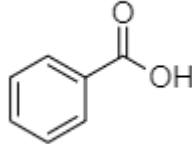
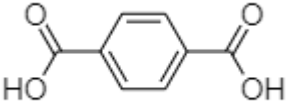
- Does the contamination form coherent particles?
- What are the mechanical implications of the contamination on the line?
- Can the contamination be prevented at the source?
- What cleaning methods can be employed given the form/solubility/adhesion/physical properties of the contamination?

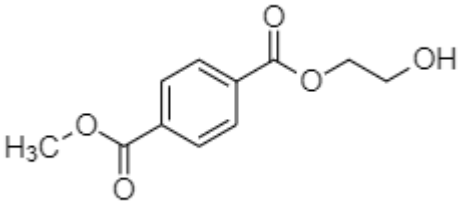
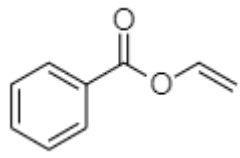
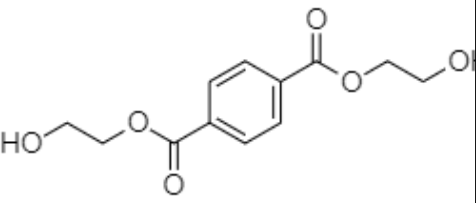
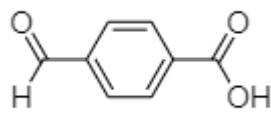
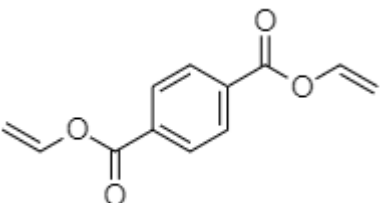
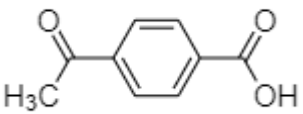
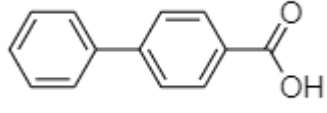
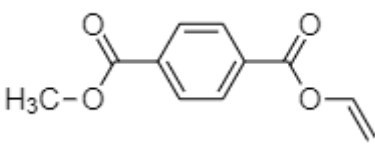
Having examined the historical work done in this area (see Appendix 9.1) it is clear that contamination of various kinds has been an ongoing problem on various units of the production line throughout the last 60 years. Based on this work the contamination present in the stenter and the casting drum is known to come from one of two origins, and it is reasonable to hypothesise that the debris in the forward draw might be from one of these origins also. Some historical work has been done on the composition of forward draw contamination, but reports have had conflicting results.

4.1.1 SUBLIMATION-CONDENSATION MECHANISM

Much of the historical internal literature found contamination (sometimes referred to as “white powder”) was derived from products of the decomposition of PET. Decomposition mechanisms of PET were detailed in Section 2.1. No matter the exact mechanism (thermal/oxidative/hydrolytic), the degradation products of PET are small organic molecules, which are often highly volatile. When the PET film is heated, these products can sublime out of the PET matrix. The volatilised products can then condense on the cooled film surface or on surfaces on the production line such as the edges of the casting drum. This process of sublimation and then condensation of volatile products of PET degradation will henceforth be referred to as the *sublimation-condensation* mechanism. Degradation products include terephthalic acid, half esters, cyclic trimer, dimers and other short chain oligomers.

The most likely products of degradation that might be found in the forward draw according to this theory are the products shown in Table 5. This gives the structure of these products and their sublimation temperatures known from the literature, as well as which degradation route they originate from based on the understanding of the literature covered in Section 2.1.

Product	Melting Point Boiling point	Structure	Degradation route
Benzoic acid	122.3°C 249.2°C		Thermal & Oxidative
Terephthalic acid	Sublimates 276- 373°C		Thermal & Oxidative

Hydroxyethyl methyl terephthalate	82-83°C 370.4°C		Thermal
Vinyl benzoate	95 – 96°C 203°C		Thermal
Terephthalic acid-bis(2-hydroxyethyl ester)	106°C 300°C +/-50		Thermal, Hydrolytic
4-Formylbenzoic Acid	249-255°C 330 +/-25°C		Thermal
Divinyl terephthalate	83 – 84°C 340 +/-38°C		Thermal
4 – acetyl benzoic acid	208 – 210°C ~250°C		Oxidative
4-Biphenylcarboxylic acid	228°C 370 +/-25°C		Oxidative
Methyl- vinyl- terephthalate	150 – 250°C 315 +/-35°C		Oxidative

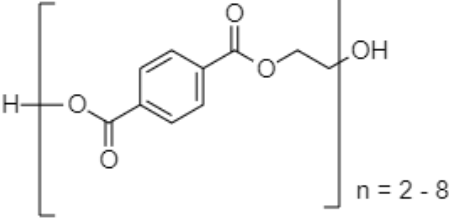
Oligomers of PET	106°C + > 350°C		Hydrolytic
------------------	--------------------	--	------------

Table 5: Summary of solid phase degradation products of PET from literature studies.

It is important to note in particular that while the degradation processes detailed in Section 2.1 result in many different products, the only ones that can plausibly be found in the forward draw are those which are solid phase at room temperature, and gas phase at extrusion temperatures (typically 265 – 315°C). For this reason, some of the most common degradation products discussed in Section 2.1, e.g., acetaldehyde, benzaldehyde, CO and CO₂, have been excluded from this list as they will not be solid phase at room temperature.

This sublimation-condensation process is visually seen occurring on the casting drum on the D52 production line, where contamination builds up extensively over a production cycle, as can be seen in Figure 37.



Figure 36: Photos of the casting drum from D52 production line with white powder build up at the edges and the centre portion obscured by condensation. Samples of powder have been removed leaving clean areas of the mirror-finish exposed.

While visual contamination of this severity is not detectable by human eye in the forward draw unit, there are some anecdotal reports that alternating rolls in the preheat and cooling section of the FWD become slightly more matt looking over the course of a production campaign.

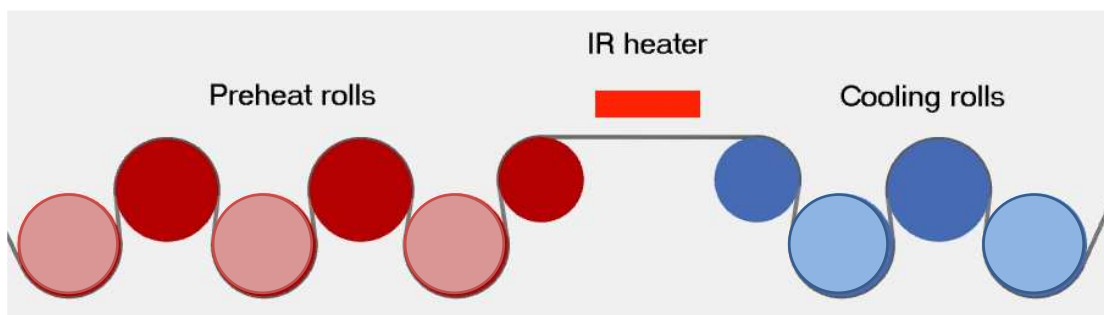


Figure 37: Example schematic of the forward draw showing alternate rolls (shown pale) where powder builds up where the drum side of the film lands.

The rolls that appear more matt are where the drum side of the film lands. This is believed to be because degradation products can get trapped in the PET matrix on the drum side, which is cooled very rapidly during casting, and then subsequently are able to escape once heated on the preheat (PH) rolls. The air side of the film however, being cooled slightly more slowly as contact with the cooled casting drum is not direct, allows more sublimation-condensation earlier in the production line around the casting drum, so there is less remaining to escape in the subsequent preheat rolls. This theory is backed up by the data found in a 2007 study into scratch density on film from D52 (Cooper, 2007) which found a far higher instance of scratches on the drum side than the air side of the film indicating a higher level of contamination on the drum side rollers.

Overall this *sublimation-condensation* mechanism is known to occur around the extruder/casting drum and in the stenter (Pemberton and Stening, 1966; Mackenzie, 1982; Donnellan, 1989c) and there is some evidence this type contamination is also present in the forward draw (MacDonald, 1995; Beattie and Cooper, 2006; Cooper, 2007; Coles, 2009a). If chemical analysis of the contamination from the forward draw reveals this type of *sublimation – condensation* contamination is present, it means that either it is carried down from the casting drum or is generated in situ, or both.

4.1.2 ABRASION MECHANISM

Other historic work (von Morgen, 2011) also found evidence of debris containing inorganic compounds and undegraded PET which cannot come from the *sublimation-condensation* mechanism.

It is hypothesised that this comes from an abrasive mechanism - abrasion of the PET web (including fillers) by the rollers and cleaning pads, and abrasion of the rollers by the web and

cleaning pads. Previous work had found debris samples taken from the FWD to contain components such as chrome, iron, aluminium and steel, (roller and other metalwork surfaces), as well as silicon, titanium, barium, sulphur and phosphorus, (fillers used in other products) and un-degraded PET (von Morgen, 2011). However, these conclusions were somewhat unsubstantiated by available data. As a result, the expectation is that the chemical composition of contamination is different in this mechanism as compared to the sublimation-condensation mechanism.

4.2 DEPOSITION OF CONTAMINATION DURING PET FILM PRODUCTION

This chapter aims to determine if either of the routes above can explain the presence and build-up of contamination in the forward draw. In order to do this samples of contamination were collected and analysed using a variety of techniques.

However, the premise of the problem does present a challenge in this regard. As mentioned above, the contamination in the forward draw is imperceptible to the human eye and as a result it is challenging to collect a sizable sample. A number of collection methods were trialed across many production cycles (occurring about once every 2 months), including using a solvent, using a brush, using transfer tapes, and using a sterile scalpel. The only methodology which had success without the results being impossible to interpret was the sterile scalpel.

Given the limited size of the sample collected directly from the forward draw a number of other samples were collected in the hope that information could be inferred. These include a sample collected from metal work adjacent to the forward draw rolls, and samples of the cleaning pads used to clean the forward draw rolls.

In all the following samples have been measured:

- Forward draw: Cooling roll 1 (small sample)
- Forward draw: Metal work adjacent to cooling roll 1
- Forward draw: Clean and dirtied cleaning pads from cooling roll 1
- Casting drum: White powder debris

Initially the results of the casting drum will be shown, as this shows what is typical of sublimation-condensation type debris. Then the results from the forward draw will be discussed.

All samples were collected in the down time during a clear product campaign on the D52 unit. This line produces a range of filled and unfilled products with cleaning regimens in place between different product campaigns. The clear products contain no fillers or dyes, and all samples were collected upstream of the coating unit so theoretically should be free of inorganic components in terms of their formulation – assuming cleaning is completely perfect at removing all contamination between product runs.

4.3 ANALYSIS OF CONTAMINATION

4.3.1 ANALYSIS OF CASTING DRUM SAMPLE

Casting drum sample was collected on 13th July 2018 from the edge of the casting drum using a sterile scalpel and were analysed using EDX, XPS, FTIR, Raman, UV-HPLC and GC-MS. The hypothesis is that this sample is comprised entirely of the products of PET degradation, short chain, volatile organic molecules. The area at the edge of the casting drum where debris can collect is dependent on the width of the polymer melt curtain. The width of the melt curtain is dependent on the specification being manufactured, the thinner the product, the thinner the melt curtain and the more the curtain necks in. As a result, the edges of the casting drum can be from either in or outside of the film path, depending on the product in question.

4.3.1.1 EDX ANALYSIS OF CASTING DRUM SAMPLE

EDX analysis of the contamination found on the casting drum can be seen in Figure 38 and showed the presence of majority carbon and oxygen, with trace amounts of phosphorus and silicon. The phosphorus is derived from phosphoric acid that is added after the esterification step as a stabiliser during the PET synthesis. The silicon is likely contamination from a previous product ran on the line which contains SiO₂ fillers. The bulk being carbon and oxygen is aligned with the hypothesis that this sample will be comprised of products of PET degradation.

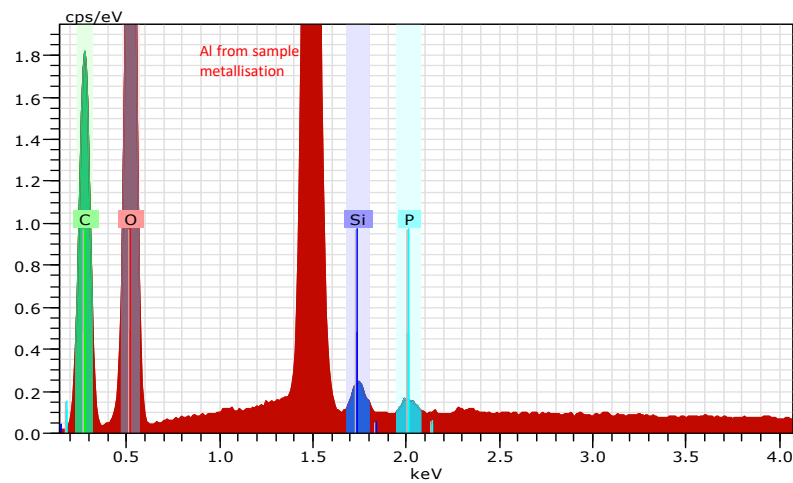


Figure 38: EDX analysis of casting drum sample. Sample metallised in Al to improve sampling quality. Al peak appears in red.

4.3.1.2 XPS ANALYSIS OF CASTING DRUM SAMPLE

XPS analysis of the contamination showed the presence of majority carbon and oxygen with no trace signals detected (inset of Figure 39). This implies that, since this measurement was done on a different section of the sample than the EDX, that the distribution of P and Si is not consistent across the contamination.

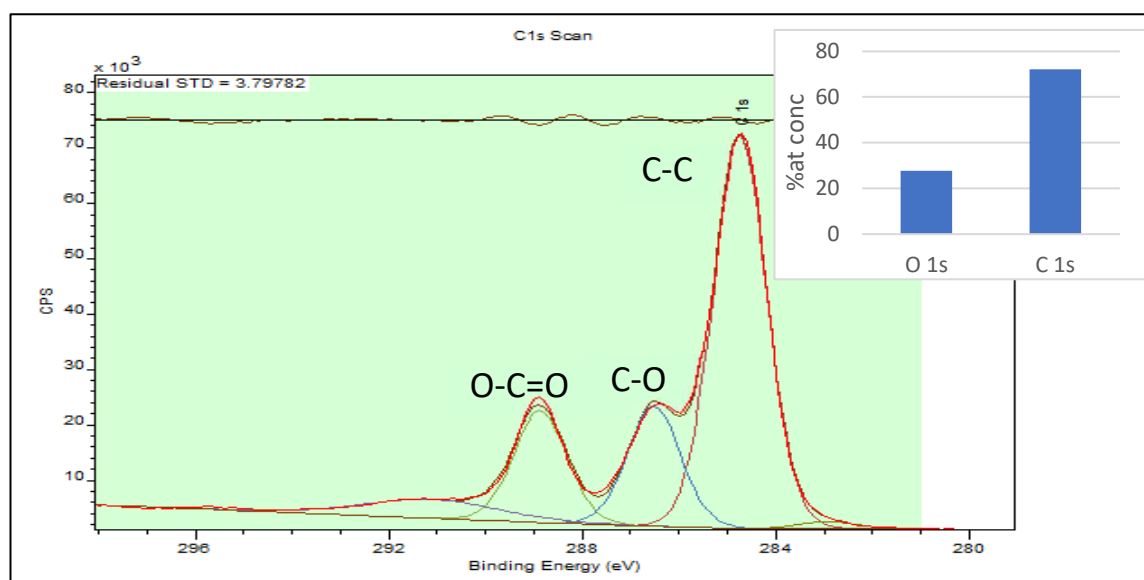


Figure 39: XPS analysis of casting drum sample, Carbon environments. Inset: Major elements present by percentage concentration.

Figure 39 shows the carbon environments present in the XPS carbon peak. The carbon environments show the presence of characteristic binding energies of carbon in C-C and C-O bond and O-C=O ester linkages. These bonds are typical of those found in the degradation products of PET, and PET itself, see Table 5.

Using these chemo-analyses it has been established that, as expected, the sample from the casting drum is organic in nature. In order to better understand the exact composition, other spectroscopic techniques need to be employed to further probe the organic functionalisation present.

4.3.1.3 FTIR ANALYSIS OF CASTING DRUM SAMPLE

FTIR analysis was completed on the sample of powder from the casting drum; 4 measurements were taken, as shown in Figure 40. Traces show nearly identical FTIR spectra suggesting that the material is homogenous on a macroscopic scale.

Figure 42 shows a comparison of a typical spectrum of the deposits compared against TA, a terephthalic acid/ethylene glycol ester dimer [terephthalic acid -bis(-2hydroxyethyl ester)] (BHET) and PET cyclic trimer. The spectra are all dominated by the presence of terephthalic acid (TA), however comparison against a library reference spectrum of TA shows that the spectra of the deposits contain an additional carbonyl absorption at $\sim 1717\text{ cm}^{-1}$ which is indicative for the presence of terephthalate ester e.g., PET, PET derivatives or PET oligomers.

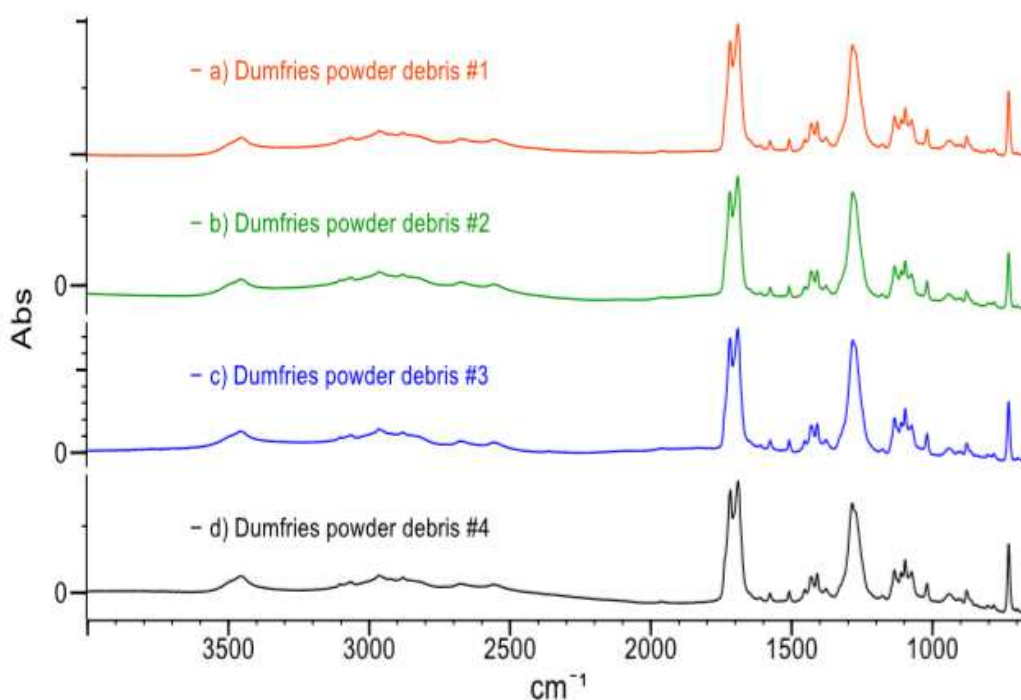


Figure 40: FTIR analysis of casting drum sample; measurement repeated 4 times (1, 2, 3, 4) to check homogeneity.

Although the spectra of the deposits show clear evidence of a carbonyl consistent with a terephthalate ester e.g., PET oligomers, there is no clear evidence of PET cyclic trimer. The spectra show similarities with library reference data of the type of TA/ethylene glycol dimer shown in Figure 41 but the carbonyl position for PET cyclic trimer occurs at a slightly higher frequency ($\sim 1727\text{cm}^{-1}$) than PET or the TA/EG dimer, suggesting that any PET oligomers or derivatives present are not cyclic trimer.

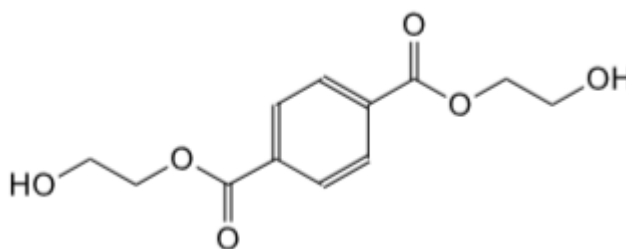


Figure 41: Terephthalic acid-bis(2-hydroxyethyl ester).

Interestingly there does not appear to be strong evidence of carbonyl bonds. ($\text{C}=\text{C}$, expected around 1650 cm^{-1}) which rules out the presence of several vinyl degradation products theorised in Table 5. Additionally the presence of benzoic acid can be ruled out as there is an absence of a strong signal at 1000 cm^{-1} which would be due to one of the benzene carbons (Kwon *et al.*, 1994). Overall analysis of a sample of powder/debris by FTIR spectroscopy shows that the powder is dominated by the presence of terephthalic acid. There is evidence for the presence of PET oligomer present but no clear evidence of PET cyclic trimer.

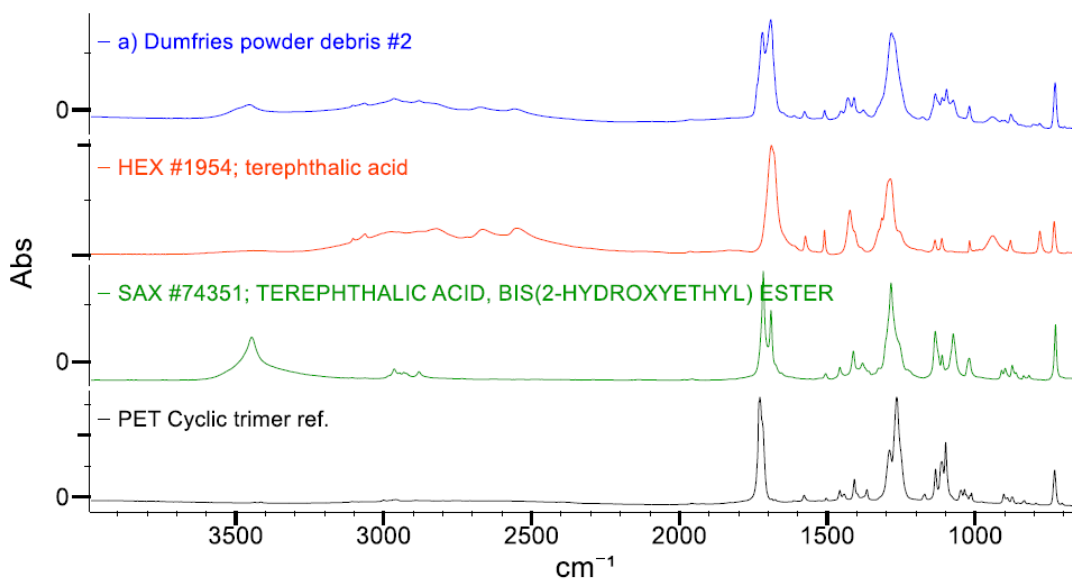


Figure 42: FTIR of casting drum powder (blue - Dumfries powder debris) and compared to literature samples of b) terephthalic acid, c) terephthalic acid, bis(2-hydroxyethyl)ester, d) PET cyclic trimer.

4.3.1.4 RAMAN ANALYSIS OF CASTING DRUM SAMPLE

Raman analysis of the casting drum powder was also conducted and compared to literature traces for both terephthalic acid and amorphous PET, the results are shown in Figure 43. It was found that there was extremely strong correlation between the powder and terephthalic acid.

Where deviations are seen, for example the peak at $\sim 1700\text{ cm}^{-1}$ which is characteristic of the carbonyl position for TA/ethylene glycol dimer, this is confirmation of the presence of the ethylene glycol, terephthalic acid dimer or other oligomers of PET. As with the FTIR data above there is no strong evidence for the presence of carbon-carbon double bonds, ruling out the presence of some of the vinyl products listed in Table 5. This is expected from the literature (MacDonald, 2002). Additionally, the lack of a strong peak at 1000 cm^{-1} rules out the presence of large amounts of benzoic acid in the sample.

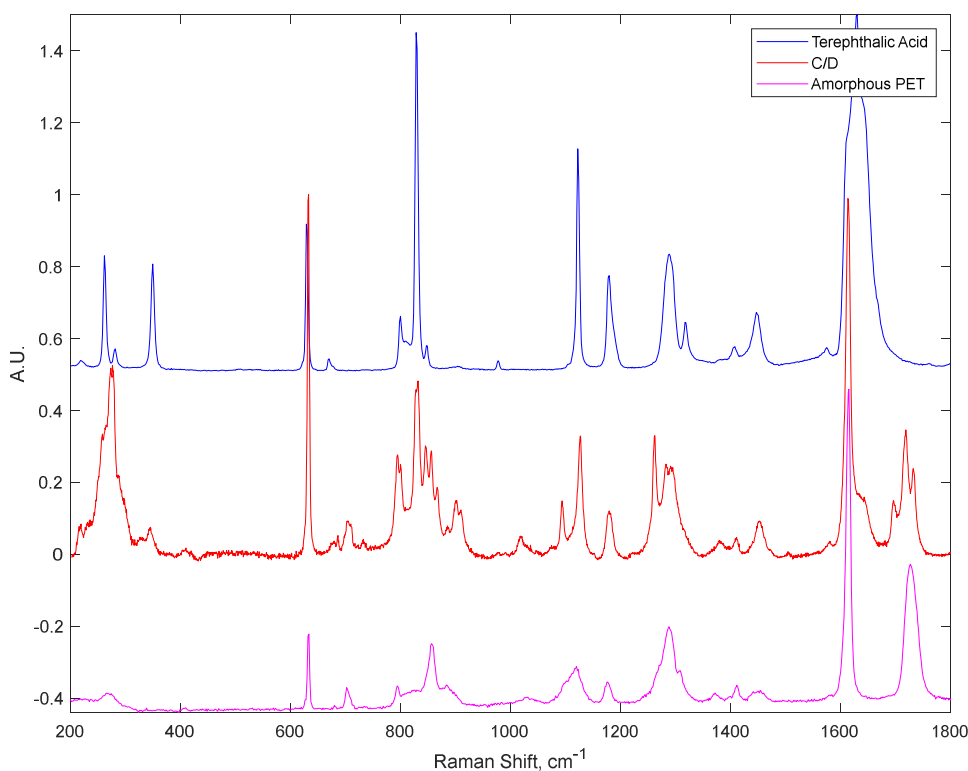


Figure 43: Raman analysis of casting drum sample (red) compared to literature traces for terephthalic acid (blue) and amorphous PET (pink).

Overall, the casting drum powder trace has a great deal in common with both library traces displayed in Figure 43, but it is impossible to determine the exact composition of the mixture as it contains peaks characteristic of both and hence of the other degradation products of PET.

4.3.1.5 *GS-MS ANALYSIS OF CASTING DRUM SAMPLE*

GC-MS of a casting drum sample was conducted. The purpose of this experiment was to confirm that TA was present in the casting drum powder. The predicted sublimation temperature is a range of 263-373°C as reported by (Kimyonok and Uluturk, 2016) so it is possible that no TA could be present. The PET melt in the extrusion system reaches a typical maximum temperature of 285°C +/- 10°C and the data from FTIR and Raman seemed to support the presence of TA, however many of the functional groups present in terephthalic acid are also present in many of the other degradation products listed in Table 5. GS-MS was attempted in order to quantify the proportion of TA present.

A blank chromatogram was run, followed by a sample of pure terephthalic acid, and finally a sample of casting drum debris was run. Unfortunately, the headspace GC-MS was unable to detect the pure sample of TA as distinct from the background. This does not mean TA is not present in the sample but merely cannot be detected by the instrument.

The casting drum sample was run through the headspace GC-MS and compared against a blank background, which can be seen in Figure 44. There were a large number of peaks in the chromatogram, but only peaks with an area percentage greater than 1% and a percentage match to the literature database of greater than 85% were processed. A summary is shown in Table 6.

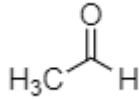
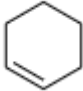
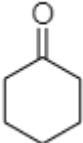
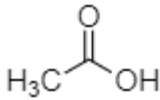
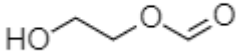
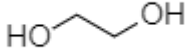
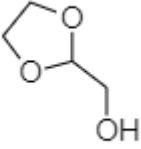
Retention time / min.	NIST Database match	Structure	% Match to NIST	Peak area %
1.96	Acetaldehyde		97.6	8.17
2.49	Cyclohexene		87.3	1.24
7.92	Cyclohexanone		90.8	4.03
8.94	Acetic acid		96.4	3.93
10.11	1,2-ethanediol, monoformate		86.6	6.14
10.17	Ethylene glycol		93.0	43.49
10.27	1,3-dioxolane-2-methanol		88.9	2.76

Table 6: Summary of components present in GC-MS analysis of casting drum powder.

A large proportion of the sample is comprised of ethylene glycol at a retention time of 10.17 minutes, one of the two base components of the PET monomer. Acetaldehyde, and acetic acid are expected degradation products of PET (Turnbull, 2013). However, as neither of these is solid at room temperature, they are not expected in the sample powder and so their presence in the GC-MS is slightly surprising. The remainder of the products listed in Table 6 do not overlap with the expected degradation products listed in Table 5.

It seems likely that it is a result of further degradation of the powder during GC-MS measurement, so yields little information about the starting products. However, one useful piece of information can be resolved from the high proportion of Ethelene glycol. This indicates that at least 40%+ of the sample is not comprised of TA, as they do not contain ethylene glycol fragments. Instead, this must be comprised of Hydroxyethyl methyl terephthalate, BHET or other PET oligomers.

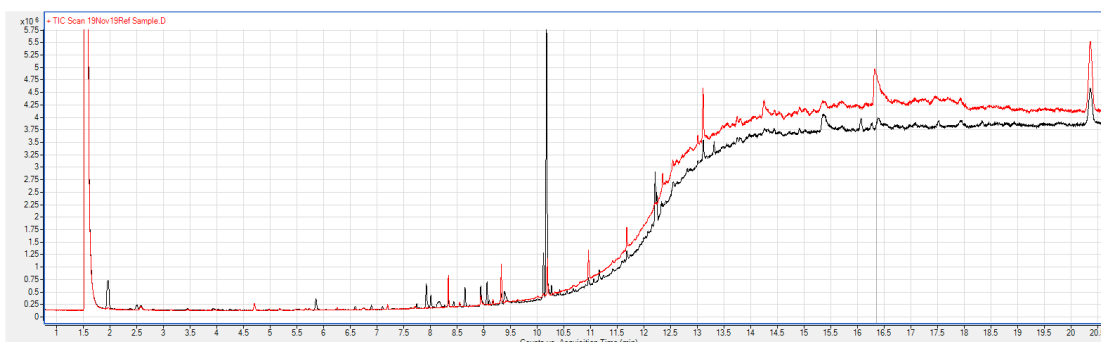


Figure 44: GC-MS trace of casting drum powder (red). Black line is blank spectrum.

4.3.1.6 UV-HPLC ANALYSIS OF CASTING DRUM SAMPLE

High-performance liquid chromatography is a technique in analytical chemistry used to separate, identify, and quantify each component in a mixture.

Two samples were submitted – a sample of pure TA and a sample of casting drum powder.

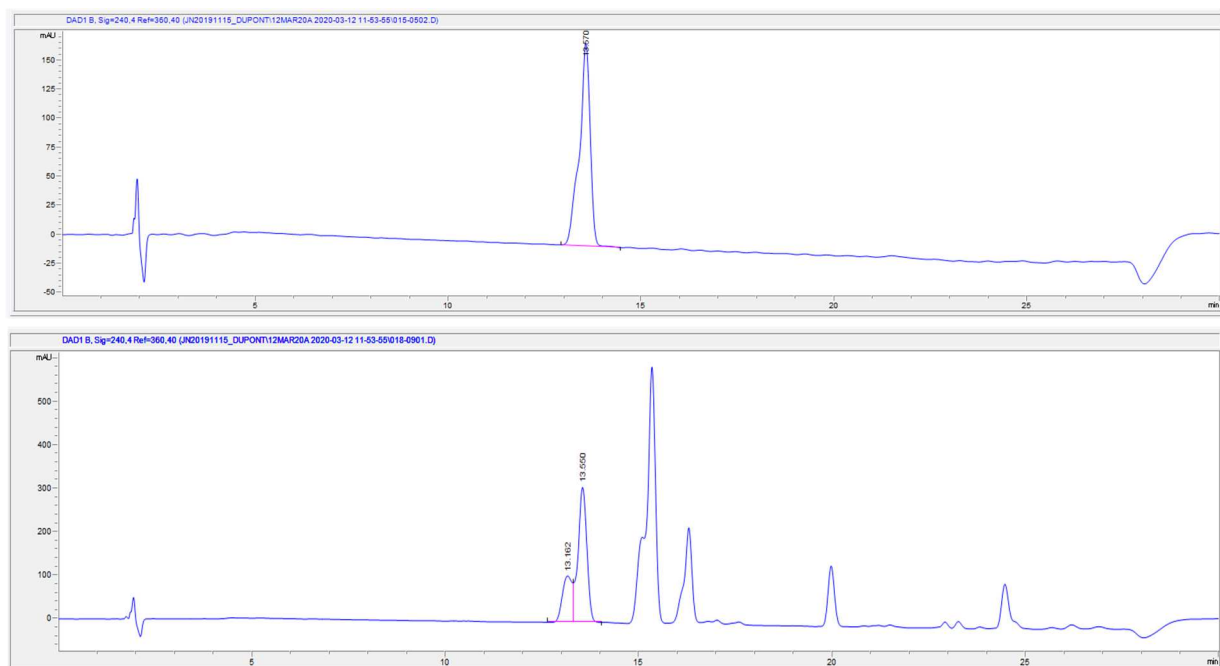


Figure 45: UV-HPLC analysis of casting drum powder. Top: Pure TA sample. Bottom: Casting drum sample.

They were run in sequence in order to determine if TA was present in the casting drum sample.

The results are shown in Figure 45. The TA samples shows one characteristic peak at ~13.50 minutes. The casting drum sample shows more peaks but does show one at the same retention time ~13.5 minutes, confirming that the casting drum sample does contain some TA in addition to other components.

4.3.1.7 CONCLUSIONS FROM CASTING DRUM SAMPLE ANALYSIS

Overall, the analysis of casting drum samples has revealed much of what was expected by the theory described in Section 2.1 of the literature review. One of the main challenges of this analysis is that many of the degradation products of PET are exceptionally chemically similar, see Table 5. This makes distinguishing them in organic analyses far more challenging.

EDX and XPS confirmed that the composition of the powder is almost entirely organic in nature, and XPS confirmed a quantitative split of 27.7% Oxygen and 72.2% Carbon, a ratio of

approximately 2:5. This is approximately the split of carbon to oxygen in PET (28.5% Oxygen and 71.5%) which strongly indicates that the contamination is made up of components of thermal degradation of PET. This is because products of oxidative and hydrolytic degradation have a higher proportion of oxygen due to H₂O and O₂ inclusion in the reactants than products of thermal degradation, where PET is the only reactant.

This implies that the current polymerisation process and melt system cannot easily be altered to improve on the degradation products, since O₂ and H₂O have been sufficiently excluded as to rate limit these degradation pathways and the only degradation route left is thermal degradation. This is impossible to rate limit since the activation energy is lower than the melt temperature of PET.

The presence of TA in the contamination, which was called into question by its sublimation temperatures, was definitively confirmed by UV-HPLC analysis to be present on the casting drum. In addition to this, FTIR and Raman analysis revealed a strong correlation between BHET and the casting drum sample.

The results of GC-MS provided strong evidence that the casting drum sample is at least partially oligomeric due to the presence of ethylene glycol fragments. Thermodynamically the smaller oligomers of PET are more likely than larger ones due to their relative boiling points.

Finally, neither the FTIR nor the Raman provided evidence of vinyl products as the characteristic absorption energy for carbon-carbon double bonds was absent in both cases. This is expected from the literature where it was found by (MacDonald, 2002) that vinyl products are not found in degradation products of PET formed at extrusion temperatures.

They also both ruled out the presence of large amounts of benzoic acid due to the lack of a peak at 1000 cm^{-1} . Additionally, the FTIR was able to rule out the presence of cyclic trimers.

Overall, it can be concluded that the casting drum powder has a large proportion of terephthalic acid, with another significant portion of oligomeric material, with the rest being made up of other degradation components that do not contain carbon – carbon double bonds.

A final note that this study shows why it is sometimes critical to perform analysis in multiple ways on the same sample. This is shown by the fact that EDX and XPS disagreed about trace components, and that GC-MS was unable to confirm the presence of TA, while UV-HPLC was.

4.3.2 ANALYSIS OF FORWARD DRAW SAMPLE

Despite over a dozen attempts to collect a sample directly from the rolls, only one sample of debris direct from the rollers in the draw was successfully collected.

4.3.2.1 *EDX ANALYSIS OF FORWARD DRAW SAMPLE*

This sample was collected from the 1st cooling roll in October of 2019; it was collected during a full line stop that occurred due to a need to clean the line, mid-way through a clear production campaign.

The minimal amount meant only two techniques could be employed. In order to try and determine which of the two proposed routes to contamination are taking place, EDX was selected as it can identify inorganics if present. Raman was also conducted as this would provide comparison to the casting drum samples.

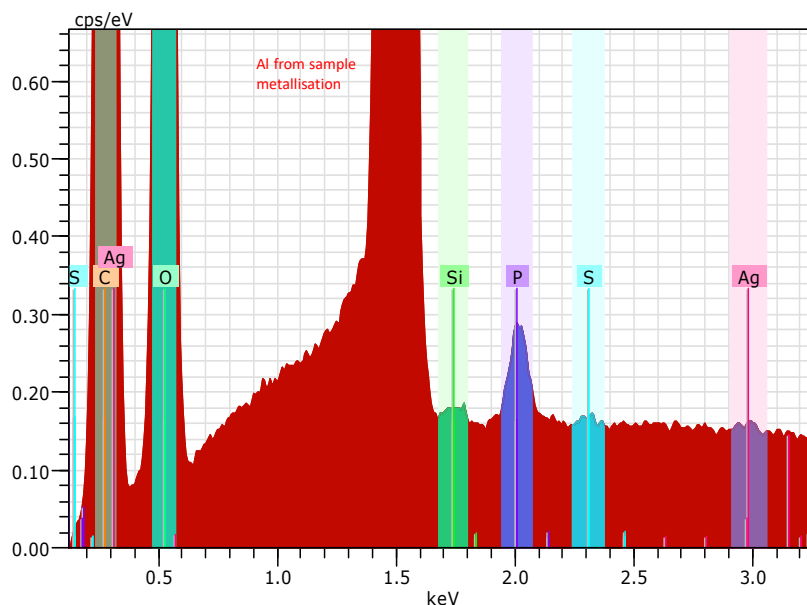


Figure 46: EDX analysis of forward draw sample. Sample was metallised in Al which appears as a background peak in red.

EDX analysis, shown in Figure 46, shows that the sample is almost entirely organic in composition, dominated by carbon and oxygen. There is a minor amount of phosphorus present – this was also seen in the EDX of casting drum powder, and it is known to originate from the phosphoric acid catalyst used in the synthesis of PET. This domination of oxygen and carbon with strong signals also from phosphorus indicates strongly that the debris coating the rollers in the forward draw could be similar in composition to the debris found on the casting drum. There are trace amounts of silicon, sulphur and silver that have been detected. These will originate from the fillers used in other products made on the same production line, such as SiO_2 and BaSO_4 which are used as opacifying agents.

4.3.2.2 RAMAN ANALYSIS OF FORWARD DRAW SAMPLE

The sample was analysed using Raman spectroscopy and the trace compared to library reference spectra. The results are shown in Figure 47.

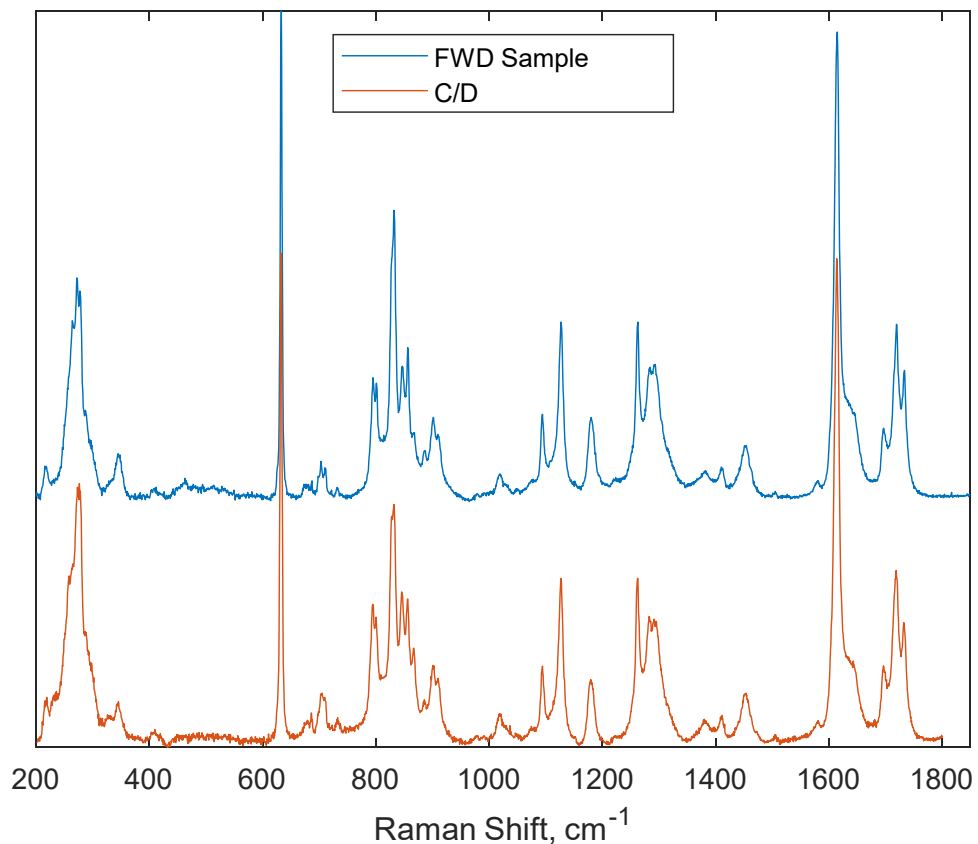


Figure 47: Raman analysis of FED sample (blue) compared to sample from casting drum (red)

The organic portion of the debris shows strong agreement with the sample from the casting drum, showing the same peaks characteristic of the benzene rings in PET derivatives. Such close agreement strongly implies that the contamination present in the forward draw is the same as is found on the casting drum, which may have been carried down the line by the film web.

4.3.2.3 CONCLUSIONS FROM FORWARD DRAW SAMPLE

Data from EDX analysis strongly indicates a contamination that is almost entirely organic in nature. The Raman analysis then confirms that this contamination is indistinguishable from the debris found on the casting drum. This strongly implies that debris is carried by the film

web down from the casting drum to the forward draw, though it does not entirely eliminate the possibility that some sublimation-condensation contamination is being generated in situ at the forward draw.

4.3.3 ANALYSIS OF FORWARD-DRAW-ADJACENT SAMPLE

In order to try to determine if sublimation-condensation debris is being generated in situ, a sample of contamination was taken from a section of metal work adjacent to the 1st cooling roll which can be seen in photos in Figure 48. This sample was analysed by EDX and FTIR.

The hypothesis is that if this sample contains PET degradation products, then this strongly indicates the presence of sublimation-condensation debris that is being generated in-situ, as volatilised products are condensing on this metal work, so will also be condensing on the rollers.

4.3.3.1 EDX ANALYSIS OF FORWARD-DRAW ADJACENT SAMPLE



Figure 48: Photos of D52 forward draw. Area where FWD adjacent sample collected from metal work shown in red.

EDX analysis of contamination collected from metal work adjacent to cooling roll 1 shows a majority amount of, Silicon, and Oxygen, with smaller amounts of Carbon, Sulphur, Titanium, Calcium, Potassium, and Iron.

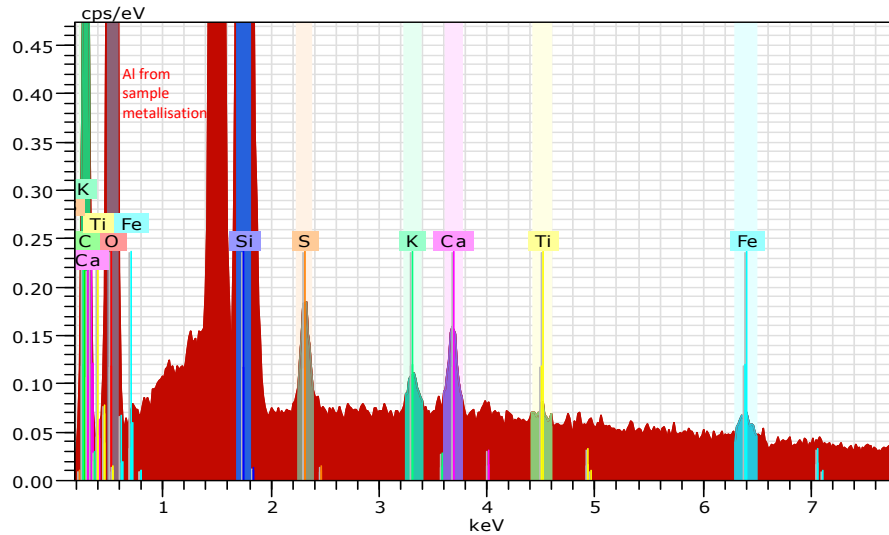


Figure 49: EDX analysis of FWD adjacent sample. Sample was metallised in Al which appears as a background peak in red.

EDX analysis in Figure 49 shows a spectrum that appears to be rich in a typical kaolin type clay and close inspection by SEM confirms the presence of round platy particles typical of a kaolin clay. These are clays that are typically used in cleaning products.

It was strongly suspected that this was leftover Silvo cleaner that had dried down without being fully removed. In order to confirm this a sample of Silvo was submitted for EDX analysis. It was deposited on an SEM stub and left to dry to a powder at room temperature overnight before analysis.

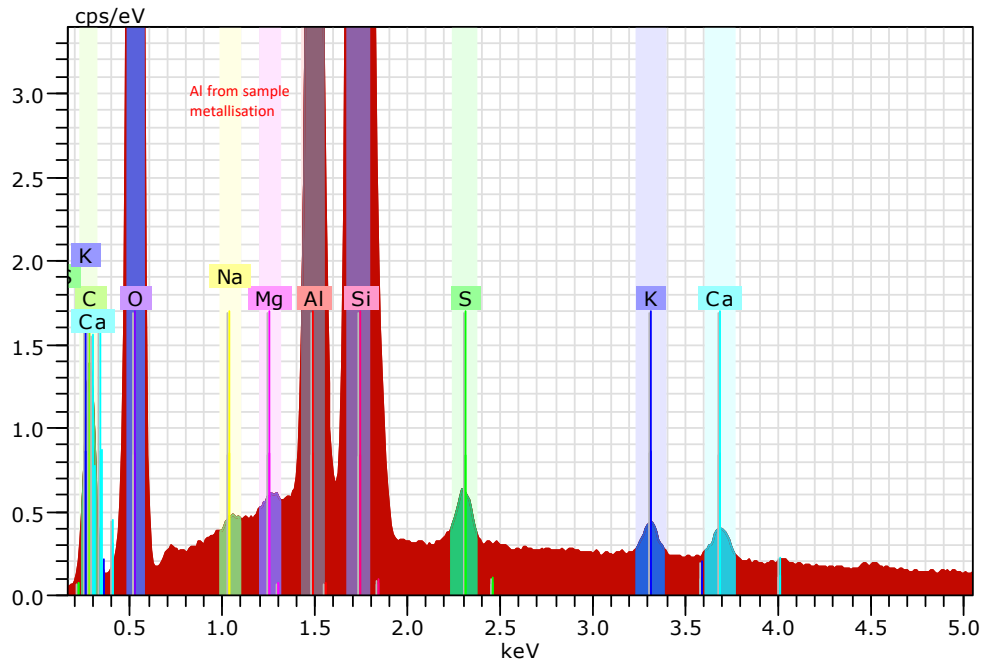


Figure 50: EDX analysis of Silvo cleaner. Sample was metallised in Al which appears as a background peak in red

EDX analysis of pure Silvo cleaner shown in Figure 50 shows a majority, of Silicon and Oxygen, consistent with the sample from the metal work. There are also trace amounts of Carbon, Sulphur, Calcium, Potassium, Magnesium, and Sodium.

Element	Metal work	Pure Silvo
Oxygen	X	X
Silicon	X	X
Carbon	X	X
Sulphur	X	X
Calcium	X	X
Potassium	X	X
Magnesium		X
Iron	X	
Titanium	X	
Sodium		X

Table 7: Comparison of elements detected by EDX in metal work sample compared with pure silvo sample

Table 7 shown a comparison of the FWD adjacent sample and the pure Silvo EDX analysis. The presence of Fe in the metal-work sample is not unexpected as the metal in question is steel so a trace amount of iron is not irregular. The Mg and Na present in the pure sample may derive from the Silvo itself but are very minor components so were not detectable in the metal work sample.

4.3.3.2 RAMAN ANALYSIS OF FORWARD-DRAW ADJACENT SAMPLE

Raman analysis was conducted also comparing the metal work sample, also with a pure Silvo sample for comparison. The results are shown in Figure 51.

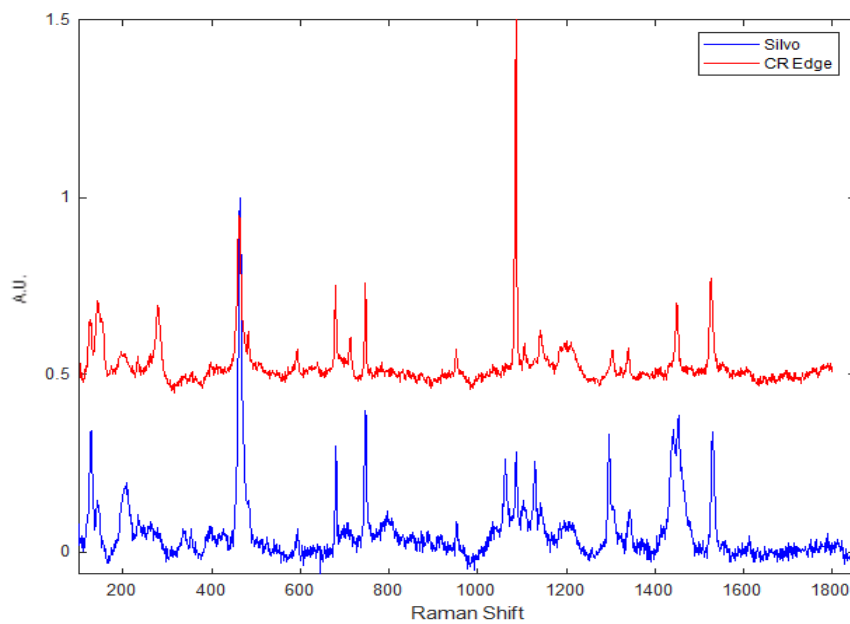


Figure 51: Raman analysis of FWD adjacent sample (red) compared to pure Silvo cleaner sample (blue).

Overall, the two samples correlate strongly on several key shift numbers, indicating the sample is majority Silvo cleaner. However, there is one key peak which is obviously not from the Silvo located at around 300 cm^{-1} . This peak is difficult to assign to any particular functional group.

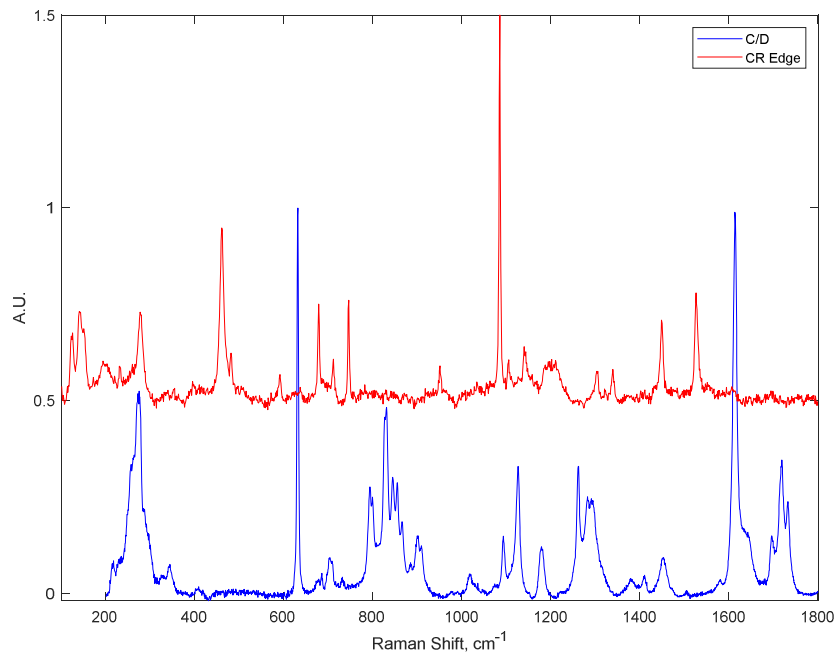


Figure 52: Raman analysis of FWD adjacent sample (red) and casting drum sample (blue).

The sample was compared to the casting drum sample described previously. The results are shown in Figure 52. Here it can be seen that 300 cm^{-1} peak is also present in this casting drum sample.

Additionally, it should be noted that the intensity of the peak in Figure 52 at 1100 cm^{-1} is dissimilar to the Silvo and may be characteristic of a benzene ring. This indicates that there may be some organic component of the metal work sample that is PET degrade products, similar to what was found in the casting drum sample.

4.3.3.3 CONCLUSIONS FROM ANALYSIS OF FORWARD-DRAW ADJACENT SAMPLE

The results from the cooling roll adjacent sample collected from the metal work are unfortunately not as illuminating as originally hoped.

The sample is majority Silvo cleaner residue, with additional components of Ti and Fe, which likely derive from the metal work and from filler particles. The Raman analysis confirms the similarity to Silvo but contains two peaks which indicate the presence of an additional organic aspect that may be derived from PET. This indicates that there may be volatile products of PET degradation that are being generated in the forward draw itself and condensing on the metal work – and therefore also on the rollers, however their proportion is small in this sample.

4.3.4 ANALYSIS OF CLEANING PAD SAMPLES

Finally, samples of the cleaning pads that are used in the forward draw were analysed before and after use. Samples of cleaning pads that had been used for a period of 8 hours on the line during a clear campaign were analysed by EDX, XPS and FTIR. In each case a clean pad was also measured for comparison. Coherence scanning interferometry topographical analysis of the pad texture in the clean and dirty state was also conducted.

4.3.4.1 *COHERENCE SCANNING INTERFEROMETRY OF CLEANING PAD SAMPLES*

Coherence scanning interferometric analysis was conducted on a clean pad and a visibly contaminated area of a used cleaning pad. The clean area showed a rough surface, with a topography characterised by disparate, discrete height features typically 100 µm high. These are the abrasive particles which are trapped in a surrounding organic resin matrix.

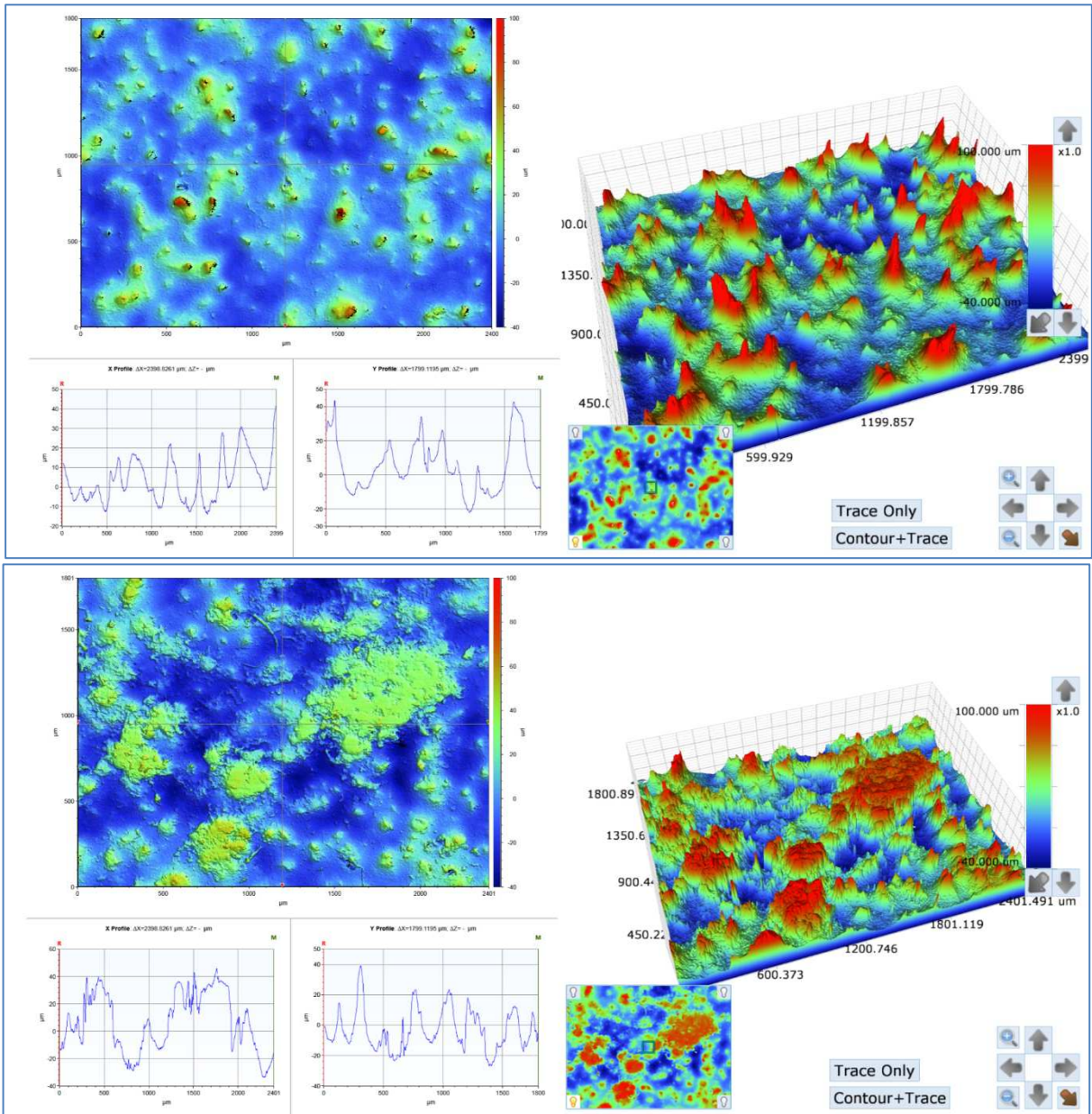


Figure 53: Top: Topographical analysis by CSI of a visually clean area of D52 FWD automatic cleaning pads. Bottom: Topographical analysis by CSI of a visually contaminated area of D52 FWD automatic cleaning pads

The clean area is visualised in Figure 53 (top), and the contaminated area in Figure 53 (bottom). The contaminated area is very dramatically different from the clean, with large islands of higher topography as well as a few more discrete height features. The islands are

large irregular areas with a consistent height and a flat top, as opposed to peaked/mountainous features.

This seems to imply that contamination collecting on the pads has been caught between the features seen in the clean image. This clearly indicates that the cleaning pads are collecting material from the rolls during use and so are effective in removing at least some of the contamination. What continues to be of concern however is that despite their ongoing use and apparent ability to collect some material, full line stops are still required to return the line to an absolute “pristine” condition, which means there is some contamination the pads are not collecting.

4.3.4.2 EDX ANALYSIS OF CLEANING PAD SAMPLES

EDX measurements of clean and contaminated pad samples were completed; the results are shown in Figure 54. These revealed a critical difference between the samples.

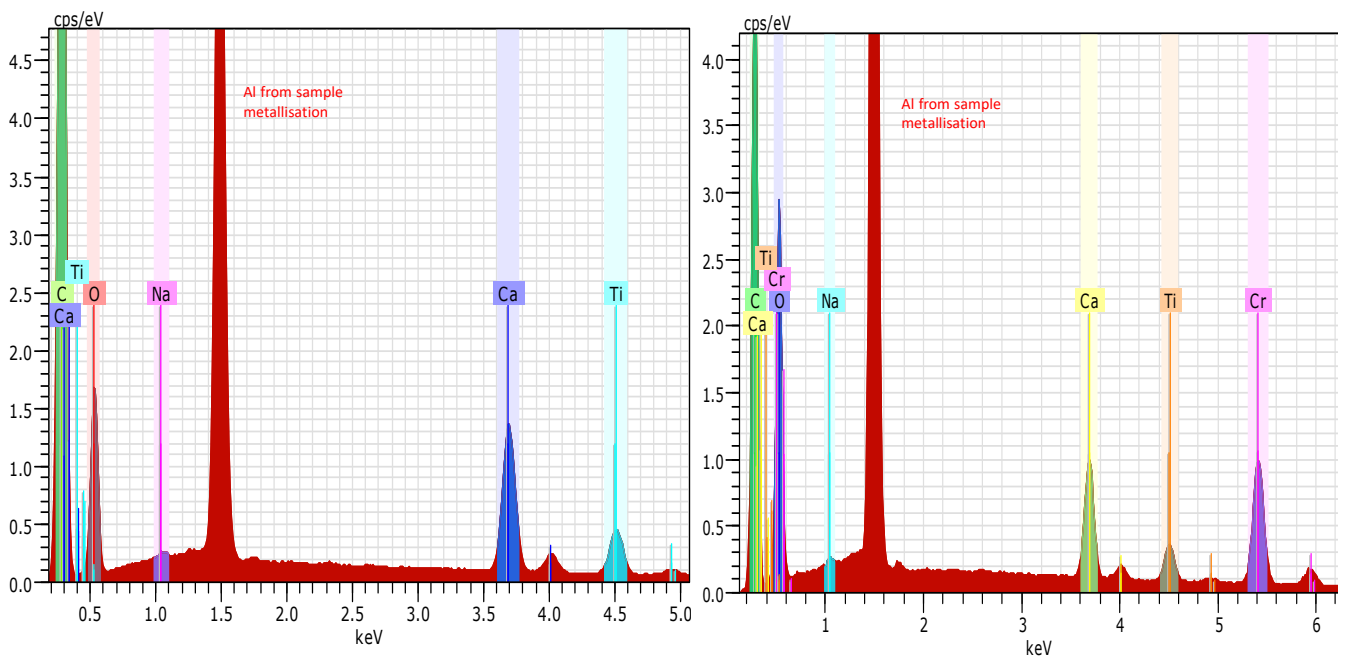


Figure 54: EDX elemental analysis of left: clean automatic cleaning pad, right: contaminated automatic cleaning pad. Samples were metallised in Aluminium thus its presence in the starting sample cannot be detected.

The pads are characterised by the presence of calcium, titanium, carbon and oxygen, as well as trace amounts of sodium. In the contaminated pad the presence of chromium is also seen. This implies that the pads are possibly abrading the rollers during use (the rollers are made of chrome oxide).

4.3.4.3 XPS ANALYSIS OF CLEANING PAD SAMPLES

XPS analysis of the clean and dirty pads is shown in Figure 55. The clean sample contained binding energies for carbon, oxygen, calcium and sodium. The dirty sample contained the same binding energies but also ones for chromium, iron and aluminium. The EDX inorganic analysis also saw the additional chrome in the dirty sample, however, did not detect the iron or aluminium. The absence of the Al can be explained since to conduct the EDX analysis, the sample was metallised in aluminium. The iron may have been missed as it is in such a low amount (less than 1%) that it may be below the limit of detection of the EDX instrument. As mentioned above, the chrome will originate from the rollers, meaning the cleaning pads could be abrading the surface of the rollers during use. The aluminium and silicon will likely derive from residual Silvo cleaner as was seen in the metal-work adjacent sample in Section 4.3.3.

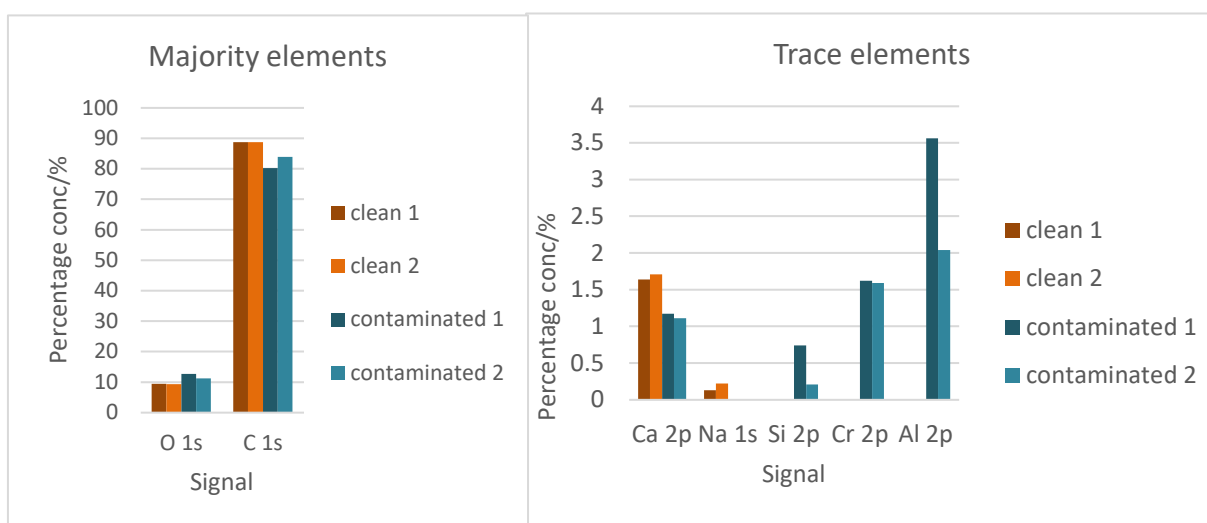


Figure 55: XPS elemental analysis of clean and contaminated automatic cleaning pads. Each measurement was repeated twice (labelled 1 and 2). Left: Majority elements, Right: Trace elements.

The analysis showed the presence of majority carbon and oxygen in both the dirty and clean samples. Critically, comparing clean to dirty, there is proportionally more oxygen, and less carbon. This could be for a number of reasons. The first, from the EDX dataset in Figure 54 above, the pads are picking up chrome which derives from the roller surface. The roller is made from chrome oxide so the additional oxygen on the dirty pad may originate from this. Secondly, mentioned above, the trace elemental analysis strongly indicated that the pads were collecting residual Silvo.

Silvo, as was revealed by the EDX conducted in Section 4.3.3, is majority Kaolin clay, chemical formula $\text{Al}_2(\text{OH})_4\text{Si}_2\text{O}_5$, so if the pads are collecting Si and Al associated with this cleaner, it makes sense that there would be a corresponding increase in oxygen proportion in the dirty sample. The corresponding decrease in carbon is due to the increase in other elements.

Taking a closer look at the carbon environments present in the XPS binding energies in Figure 56, there is no significant difference in the carbon bonds present for the clean and contaminated samples, with only a strong signal for carbon – carbon bonds present.

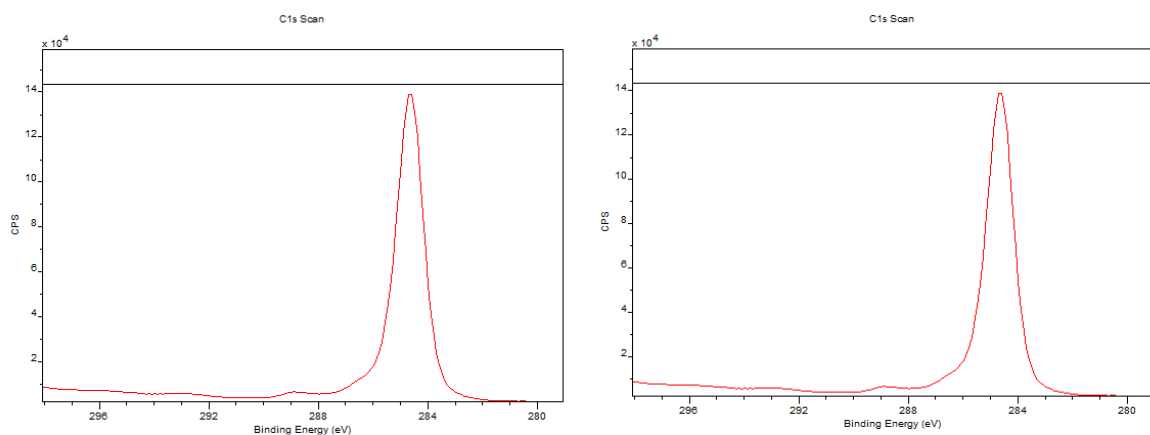


Figure 56: Carbon 1s scan from XPS analysis of left: clean automatic cleaning pad, right: dirty automatic cleaning pad

This is of note because it is known from Sections 4.3.1-4.3.3 above that the contamination contains a large proportion of organic components that are similar in nature to the debris found on the casting drum. This contamination contains a large number of carbon single bonded oxygen and carbon double bonded oxygen functionalisation, as this is what was clearly seen in the XPS data for the casting drum sample. These bonds being absent in the pads means that if this type of contamination is present on the rollers, the pads are not collecting it.

4.3.4.4 FTIR ANALYSIS OF CLEANING PAD SAMPLES

FTIR of the clean and dirty pads was conducted to further probe changes in the organic composition of any contamination collected by the pads. The analysis can be seen in Figure 57. The analysis returned spectra which are characterised by majority aliphatic carbon environments. The spectrum of the clean pad contains peaks characteristic of CH₂/CH₃ components. For example, the CH₂ Bending at 1456 cm⁻¹, Gauche CH₂ Wagging at 1376 cm⁻¹, symmetrical CH₂ vibrations at 2848 cm⁻¹ and asymmetrical vibrations of CH₂ at 2916 and 2955 cm⁻¹. These aliphatic hydrocarbons make up the bulk of the signal; this can be deduced because less polar bonds tend to have lower absorption coefficients than very polar bonds. There is also there is a broad peak at 3300 cm⁻¹ which is due to an O-H bond, most likely from an alcohol due to the lack of a strong carbonyl peak.

The dirty spectrum is broadly similar to the clean one, however there are two additional peaks in the dirty trace at ~1250 cm⁻¹, which corresponds to a C-O vibration, and ~1720 cm⁻¹ which corresponds to a C=O vibration. These share a similarity with PET/PET oligomers, although the peaks here are quite weak, especially for polar bonds. Therefore, if PET derivatives are present then they are in very small quantities.

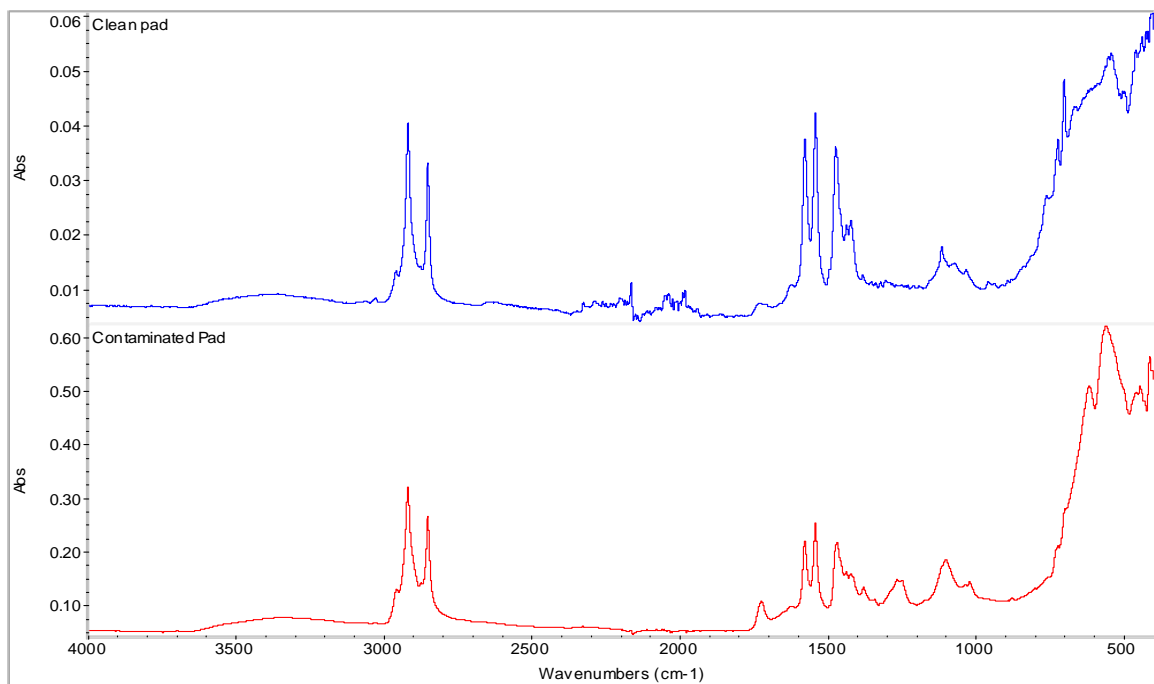


Figure 57: FTIR analysis of top: clean automatic cleaning pad, bottom: contaminated cleaning pad from D52.

4.4 CONCLUSIONS FROM ANALYSIS OF CONTAMINATION

The purpose of the work described in this chapter was to understand the composition of the contamination that causes surface damage on the D52 line forward draw unit. The presence of this contamination is inferred by the fact that from a fully pristine “clean” state, surface quality decreases over time, with the frequency, length and severity of surface scuffs and scratches increasing over the course of the production cycle. Eventually the line is stopped to be fully cleaned at which point surface quality is restored.

Initially powder from the casting drum was analysed as a comparison as the archetype of “white powder” that appears on the line. This same contamination is theorised to be the main culprit of the contamination causing problems in the forward draw – either after being carried down from the casting drum in/on the film, or generated in situ at the forward draw, or both. Therefore, a good understanding of its composition was required.

Analysis by EDX and XPS found that the powder, as expected, was nearly all carbon and oxygen, with a C:O ratio consistent with products of thermal degradation of PET. Evidence from FTIR and Raman confirmed the presence of PET derivatives such as TA, BHET, and other oligomers, but ruled out the presence of any significant vinyl products and benzoic acid. Raman analysis was able to rule out the presence of amorphous PET. UV-HPLC was able to conclusively prove the presence of TA, and GC-MS confirmed the presence of PET oligomers/BHET.

Analysis of a single small sample from the forward draw by EDX found that this sample too was mainly organic (C/O) with trace amounts of silicon, phosphorus and sulphur. Raman analysis then revealed this organic portion was indistinguishable in composition from the debris found on the casting drum. This suggests the possibility that the majority of the contamination of concern was travelling down the line from the casting drum to the forward draw.

A sample collected from metal work adjacent to the cooling rolls in the forward draw was analysed in the hope it could rule out the in-situ generation of sublimation-condensation contamination. This sample proved to be majority Silvo cleaner. However, Raman analysis suggested it also contained a small amount of evidence for other PET derivatives that do not originate from Silvo. This would indicate that at least some in-situ sublimation-condensation contamination is occurring in the forward draw.

Finally, samples of the automatic cleaning pads from the D52 forward draw were analysed. Coherence scanning interferometry revealed that the cleaning pads are collecting contamination. EDX and XPS analysis showed this contamination is primarily made kaolin clay from the Silvo cleaner which is used on the line, with strong signals for Al and Si. EDX and XPS

analysis also found that the contaminated pads contained chrome indicating the pads are picking up abraded roller material over time.

FTIR analysis of the contaminated pads found evidence of the ester linkage associated with PET derivatives (carbon-oxygen and carbon=oxyg en bonds), which indicates a small amount of organic material is present on the rolls. However, it will be in very small quantities since not only were the signals in the FTIR analysis very weak for polar bonds. In addition, no evidence of carbonyl functionalisation for the PET ester linkage was found in the carbon bond environments of the XPS analysis.

Overall, the following can be concluded about the contamination in the forward draw:

- Majority of the contamination is organic and is identical to the contamination found on the casting drum – indicating it may be travelling down the line with the film web.
- Some in-situ sublimation-condensation debris generation is also occurring, however.
- Since a very minor proportion of the forward draw sample is inorganics, it can be inferred that the abrasion route is playing a minor role compared to the sublimation-condensation route in terms of the proportion of material.
- Residual Silvo is left on the rollers after cleaning and is gradually removed by the cleaning pads.
- Current cleaning pads accumulate abraded roller surface material.

This understanding sets the scene for the rest of this report which aims to understand how this contamination exacerbates film surface damage.

5. USING ATOMIC FORCE MICROSCOPY TO UNDERSTAND ADHESION OF CONTAMINATION TO SURFACES ON PET PRODUCTION LINE

5.1 MOTIVATION

The overall motivation of this project was to understand how contamination present on the D52 production line causes the rate and severity of surface defects to increase. Armed with this knowledge, this study aims to then establish an improved cleaning method for the D52 production line based on the understanding developed. One part of this understanding is to measure and quantify the adhesion of the surfaces in this complex process.

Adhesion is critical to understand for several reasons. First, adhesion impacts the extent to which contamination will adhere to the rolls, which dictates how easily it can be cleaned and removed. Secondly, measuring adhesion will aid in understanding the propensity of contamination to attach to the PET film vs. the rollers which dictates how readily it will migrate down the line, carried by the film. Finally, the extent of relative movement on the line is friction moderated, and therefore measuring adhesion of the roller in a clean and contaminated state might yield more information about how roller-to-film contact is changing over time.

For all of these reasons it is within the scope of this project to measure adhesion to the PET and roller surfaces at a variety of conditions that mirror process conditions (chemistry, temperature, humidity). Adhesion of surfaces is highly sensitive to all of these factors, so by varying each in turn, understanding about the overall system can be gained. In particular humidity was of interest to study since humidity is kept deliberately elevated on the DTF

production lines (50-60%) to aid in other processing aspects. Humidity is known to greatly affect adhesion due to capillary layer effects that were detailed in Section 2.2.7 onwards of the literature review.

5.2 TECHNIQUE SELECTION

Surface adhesion can be measured and modelled in a variety of ways – of which details are presented in Section 2.2. In this work the intention was to not use theory to predict trends but to measure adhesion directly using an experimental method.

AFM colloidal probe force modulation mode (FMM) (See Section 3.3.2) was selected as the ideal technique. This is because AFM force modulation mode allows for direct measurement of the adhesive force to the surface. It also allows for precise control of the duration, speed, geometry, chemistry, and magnitude of the applied normal force during a contact event. With the correct choice of samples and conditions therefore, it is possible to measure adhesion in experimental conditions that closely model that of surface conditions during the PET film production process.

The major difference between force modulation mode with a normal tip and a colloidal tip (assuming the same material chemistry), is the size of the contact region. Increasing contact area from a nanometre-scale sharp imaging tip (typically 5-20 nm radius) to a colloidal tip (typically 1-50 μm radius) will increase the adhesion value measured by several orders of magnitude. However, in theory, assuming identical chemistry in both the sharp and colloidal case, the trend of adhesion of the compared surfaces will not change. It is therefore generally believed to be better to measure adhesion with a colloidal tip to allow better differentiation between surfaces in adhesion measurements. This is because, when using a colloidal tip, the increase in magnitude of the adhesion value will also increase the difference between

compared samples such that they can be distinguished apart, above the baseline noise of the measurement.

There has been a wealth of literature that has used force modulation mode AFM to measure adhesion in complex systems including polymeric coatings (Giesbers *et al.*, 1998; Braithwaite, Luckham and Howe, 1999), floatation (Butt, 1994; Fielden, Hayes and Ralston, 1996; Preuss and Butt, 1998), conductive surface coatings (Bele *et al.*, 2000) , paper making (Holmberg *et al.*, 1997; Alfano *et al.*, 2000; Zauscher and Klingenberg, 2000), printing (Jenkins *et al.*, 1999), and biological applications (Hassan *et al.*, 1998; Iyer *et al.*, 2009).

5.3 EXPERIMENTAL DESIGN

The intention of this work was to measure the adhesion on 5 samples:

- Cast film
- Forward drawn film
- Finished film
- Clean roller
- Pseudo dirty roller (see Section 6.10)
- Mica standard

Measurements were intended to be taken at conditions that mirror processing conditions for the final preheat roll and the first cooling roll of D52's forward draw. These conditions can be seen in Table 8.

Parameter	Final preheat roll	First cooling roll
<i>Pressure of roll-on web/web on roll /kPa (THOR Oxford)</i>	202.6	202.8
<i>Pressure of roll-on web/web on roll /kPa (THOR Clifford)</i>	210.5	210.8
Average pressure/ kPa	206.6	206.8
Dwell time of contact event/s	0.67	0.26
Temperature of roll/°C	81	42
Temperature of film/°C	80	44
Air temperature/°C	21	21
Humidity/ g/m ³	10-11	10-11
Relative humidity/ %	53-59	53-59
Entrained air layer thickness/nm	2.6	5.8

Table 8: Summary of processing conditions on final preheat and first cooling roll.

Tension around the forward draw is difficult to determine and various methods yield slightly different results. Two methods used here are named Oxford and Clifford and are correlations defined from empirical measurements made on DTF production lines. An average pressure from these models is taken as a good ballpark figure for the force felt by the web/roll on each roller during a contact event. The resulting force that should be used in the contact event is calculated by multiplying the predicted contact area of the probe on the surface by the pressure, to get a force in N.

For reference the average approximate roughness of the surfaces of interest can be seen in Table 9.

	Mica	PET	Roller
RMS /nm	0.5	2	Much larger

Table 9: Average roughness of surfaces of interest measured by CSI. Roller surface omitted due to proprietary restrictions.

Across a 3-year period, a total of 56 experiments were conducted. These are summarised in a table which can be found in Appendix 9.4. Experiments were performed using different tips,

with different spring constants, on different machines, by different users, and at different environmental conditions.

Based on the literature on this topic it was expected that there would be a clear relationship in these measurements between surface temperature and humidity, and measured adhesion. While humidity is not varying on the line macroscopically, the film and cooling roll experience a wide range of temperatures in the forward draw which will dramatically affect the humidity local to the surface. Exactly the nature of the relationship between the factors was hypothesised to be linked to the surface in question (PET vs. roller), as the surfaces have both different chemistries (hydrophobic/hydrophilic) and surface textures. Trends were predicted to follow patterns seen in the literature:

- Adhesion will be larger if the area of contact is larger
- Adhesion will be higher on hydrophilic surfaces compared to hydrophobic ones.
- The capillary force ($F_{\text{capillary}}$) becomes the biggest contribution to adhesion forces once the meniscus radius is $\approx 1 \text{ nm}$ + (Ouyang, Ishida and Okada, 2001; Butt, Cappella and Kappl, 2005b)
- This point is called the *critical relative humidity*. It is widely accepted that adhesion will increase with relative humidity after this point.
- The value of this critical relative humidity, and the magnitude of $F_{\text{capillary}}$, is inversely proportional to hydrophobicity of surfaces. (Fuji *et al.*, 1999; Bhushan and Dandavate, 2000; Sirghi *et al.*, 2000; Xiao and Qian, 2000; Garoff and Zauscher, 2002; Jones *et al.*, 2002; Kaibara *et al.*, 2003; Yoon *et al.*, 2003)

- Critical relative humidity is interrelated with surface roughness and asperity density on the surface (Bocquet and Barrat, 1993; Jones *et al.*, 2002; Rabinovich *et al.*, 2002). Though exactly how is not fully understood.
- Introduction of surface roughness to otherwise flat surfaces rapidly eliminate surface capillary forces (Rabinovich *et al.*, 2000, 2002). The length scale of roughness required to do this is believed to be at the length scale where capillary bridge length and asperity height are the same order of magnitude (Lehr and Kietzig, 2015).

Therefore, it was expected that PET would have a higher adhesion overall than the roller surface, and that its dependence on humidity (critical relative humidity) would occur at a lower humidity due to easier formation of bridging menisci compared to the relatively rougher roller surface. Similarly, the mica standard should have a higher adhesion than PET above its critical relative humidity due to the very flat surface, but below this point will have a lower value than PET due to being more hydrophobic.

While the intention was to measure adhesion on the samples listed above, at a variety of conditions mirroring those experienced by those surfaces during film production, early experiments yielded very inconsistent results. Many subsequent experiments were then performed to attempt to understand why this was the case. For the remainder of this discussion, the focus will be on the adhesion measurements of PET and mica as they provide the best basis upon which to compare experimental results to theory and to demonstrate the inconsistencies seen during this work.

5.4 RESULTS OF ADHESION MEASUREMENTS

5.4.1 SUMMARY OF ALL ADHESION EXPERIMENTS

A summary of adhesion values for PET and mica across many experiments is given in Figure 58. The adhesion values are plotted against relative humidity which was always monitored and recorded in the room during experimentation.

In all the data sets shown, the colloidal probe was made of borosilicate and the applied force was 50 nN +/- 10%. Each value represents the average of approximately 1200 repeats on a sample and the error bars represent the standard deviation of those 1200 repeats. A model for predicting adhesion according to the statements above is also plotted for comparison. The full mathematical theory of this model is described in appendix 9.5.

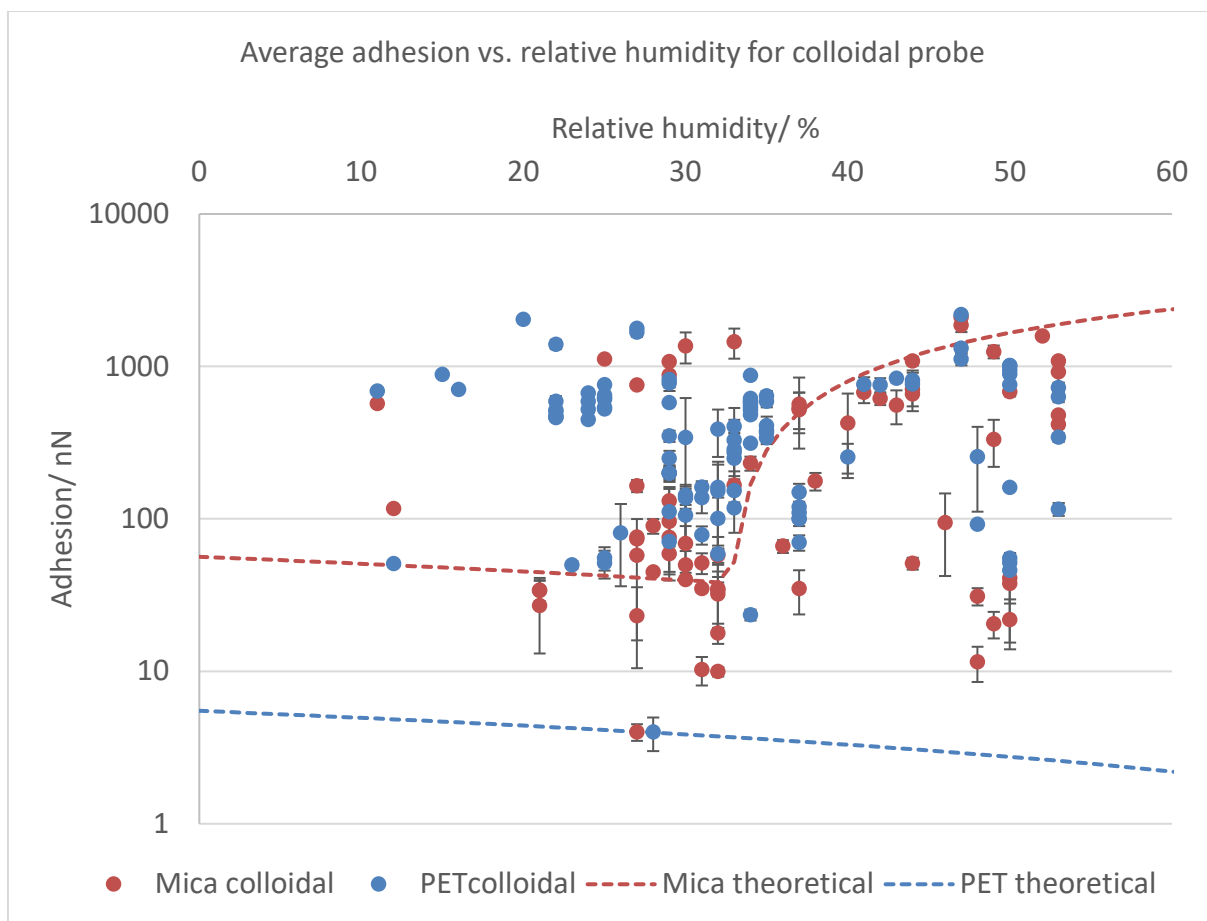


Figure 58: Graph of adhesion vs. relative humidity for experimental measurements of mica and PET using a colloidal tip and compared to the modelled data for the same systems. Each point represents an average of 1200 independent measurements (see section 3.3.2.3 for explanation of collection method) and standard deviations of those repeats is given by the error bars.

Figure 58 shows data with a high degree of variability. The range of adhesion values measured for mica range from ~4 to ~1800 nN, and for PET from ~4 to ~2200 nN. The values of adhesion measured with the colloidal tip do not appear to trend with the predictions, with the values for PET in particular being especially far from the expectation. There does appear to be a clustering of values around 30% r.h. which is due to the fact the greatest number of experiments were done at this value (as this was the typical ambient humidity of the room).

From the modelling work shown in appendix 9.5 it was found that above 7% relative humidity (which all of these experiments are), mica adhesion always exceeds PET adhesion due to its greater hydrophilicity and flatter surface. Figure 59 below shows the split of experiments where mica and PET were both measured and shows that which sample was measured to have higher adhesion.

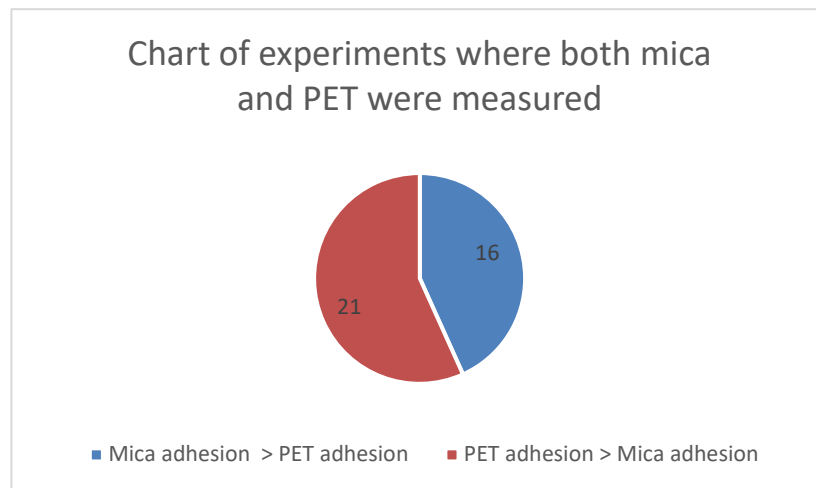


Figure 59: Pie chart showing the split of experiments where both adhesion to mica and adhesion to PET were measured via colloidal probe force modulation AFM indicating the number of experiments where PET adhesion exceeded mica adhesion vs. the number where mica adhesion exceeded PET adhesion.

Figure 60 shows similar data for experiments where an atomically sharp tip was used to measure adhesion on mica and PET, and the results plotted against relative humidity.

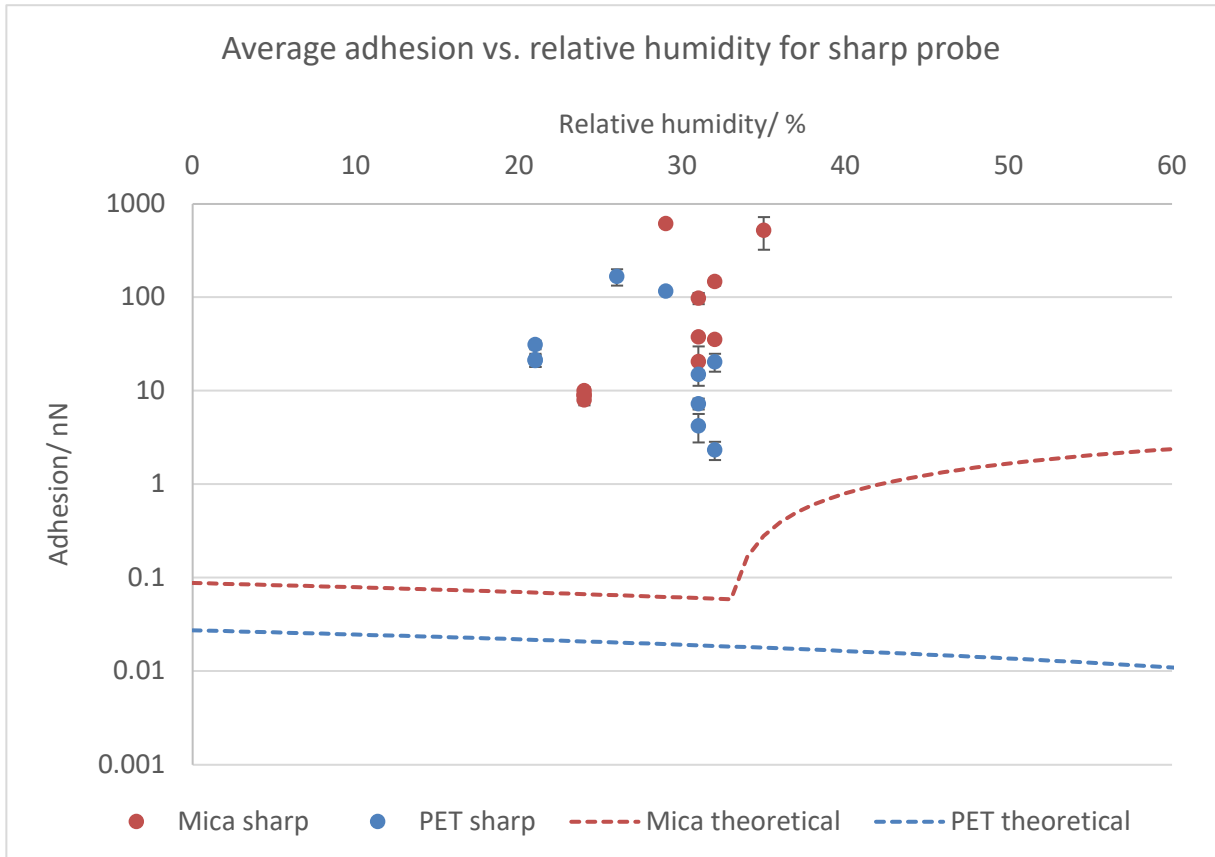


Figure 60: Graph of adhesion vs. relative humidity for experimental measurements of mica and PET using a sharp AFM tip and compared to the modelled data for the same systems. Each point represents an average of 1200 independent measurements (see section 3.3.2.3 for explanation of collection method) and the standard deviation of those repeats is given by the error bars.

These results show average adhesion values that are 2 or 3 orders of magnitude bigger than the predicted values. The values of measured adhesion for PET vary from ~2 to ~170 nN and for mica from ~8 to ~620 nN.

The first hypothesis for this was an error in experimental design which was introducing variability. Many factors are already controlled in the experimental design and are outlined in Table 10.

Factor that may be changing	Control measure
Chemistry between tip and the substrate being measured	Same probe used for entire experiment
Humidity: The thickness of capillary layer affects magnitude of capillary force but is mediated by the hydrophilicity of the surfaces	Temperature and humidity monitored and recorded during experiment
Contact area during contact event: Affected by radius of tip and the roughness of surface	Same probe used throughout the experiment Adhesion measured across a large area This means experiments will not always have the same precise absolute values but should show the same trends
Deformation of the surface: softer materials will deform during contact increasing the contact area	Low normal force is used so indentation into the surface is small
Chemistry of the interaction due to pick-up on the tip/contamination	Probes are cleaned using UV ozone

Table 10: Summary of factors that can affect adhesion and the control measures used during experimentation.

Over the course of this extensive experimental work a number of possible causes for the inconsistency were suggested:

- Colloidal probe was in some way introducing variation due to faulty construction.
 - To test this a probe was bought direct from manufactures and compared also to a sharp imaging probe. See Section 5.4.2
- User was in some way introducing error
 - User was changed to check for experimental error (refer to appendix 9.4)
- Wilton machine was in some way faulty

- Machine at University of Birmingham was used in a series of experiments to test this. See Section 5.4.3
- Applied force was too high
 - Applied force was varied in a series of measurements. See Section 5.4.4
- Borosilicate probe was introducing variation via electrostatic effects
 - Probe material was switched to polystyrene. See Section 5.4.5.

Overall, the force-distance curves seen across these experiments were characteristic of a typical contact event, with minimal hysteresis in the contact zone and sharp snap-to-contact events, examples of which can be seen in Figure 61. These curves have very similar characteristics, but the z-scale varies significantly, which accounts for the difference in adhesion force measured.

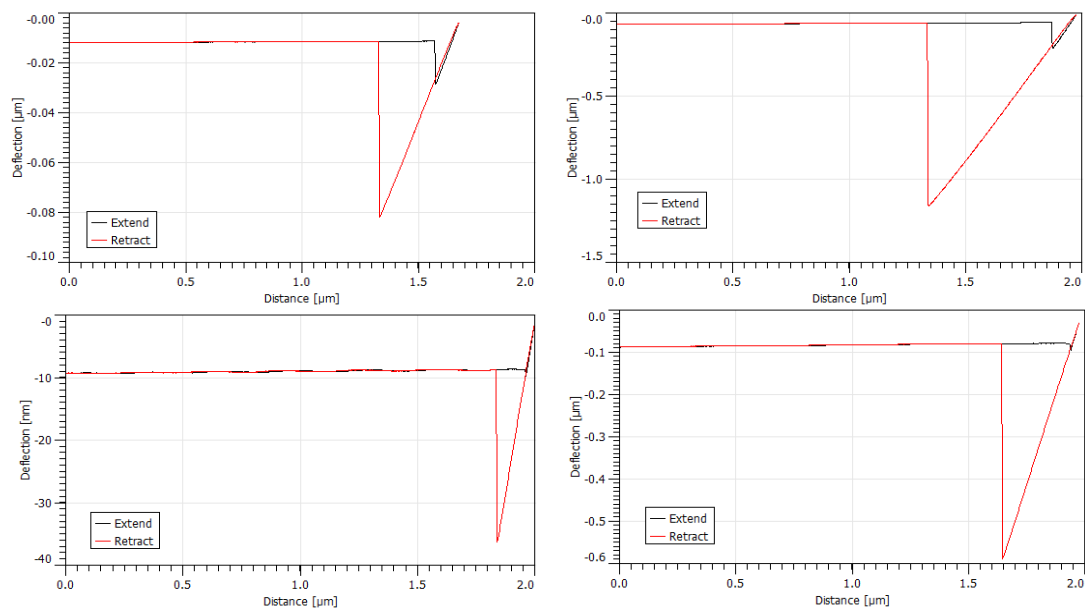


Figure 61: A selection of force-distance curves collected across the experiments shown in Figure __.

When the curves were returning a very small adhesion, the noise in the baseline could become disruptive to the setting of the zero-point of the baseline of the curve. An example of this is

shown in Figure 62. These curves made analysis slower and more manual, but were included in the analysis shown above.

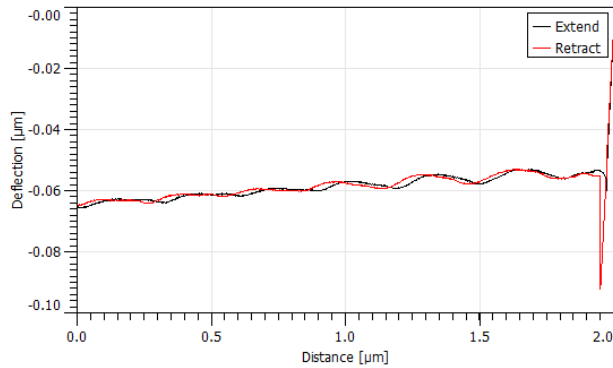


Figure 62: Typical example of a force-distance curve of very low adhesion where the noise in the baseline of the non-contact region can be seen

Occasionally, especially early in this work, curves with very curved baselines were collected – examples of which can be seen in Figure 63. This typically occurred when the AFM cantilever was too “soft” and as a result was bending towards the surface. These measurements were eliminated from the analysis shown above.

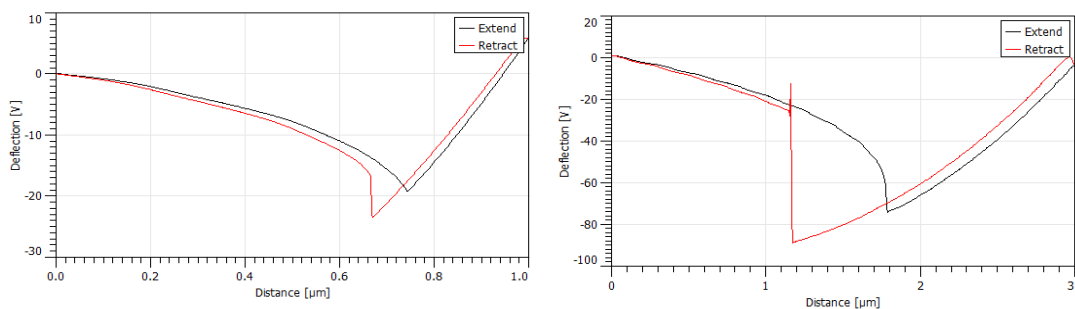


Figure 63: Typical examples of force-distance curves where the baseline was curved, even in the non-contact region, causing the curves to be eliminated from the analysis

Throughout the analysis there was no strong evidence for notable viscoelastic behavior, and thus the focus moved to uncovering other possible sources of the inconsistency, which are discussed in the sections below.

5.4.2 COMPARING DIFFERENT TIP GEOMETRY

A series of experiments (31-35 in the table in appendix 9.4) was conducted to measure the adhesion of mica and PET finished film with two different tips. The experiment was conducted 4 times on four consecutive days and the same probes used throughout with cleaning procedures in place.

The relative humidity varied between 30 – 32% across this time period with the ambient temperature varying between 20-22°C. The expectation was that the sharp tip would give lower absolute values, and that at those environmental conditions, mica would have a higher adhesion than PET.

The results are shown in Figures 64 and 65. Variability within a measurement is shown by the standard deviation (error bars).

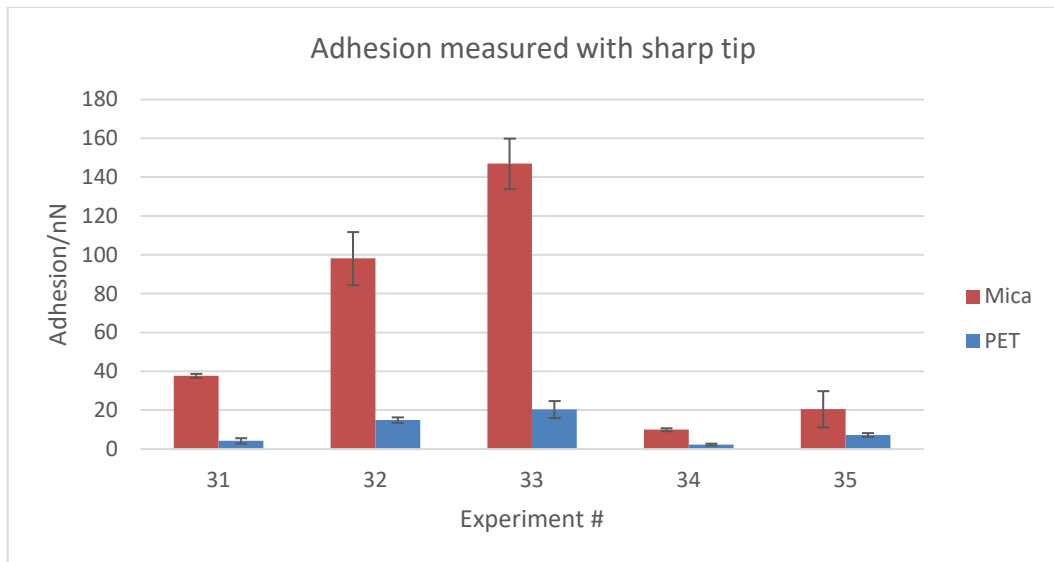


Figure 64: Average adhesion of mica and pet measured using a sharp tip across five experiments using the same set-up and environmental conditions. Each bar represents average of 1200 independent measurements (see section 3.3.2.3 for explanation of collection method) and standard deviation of those repeats is given by the error bars.

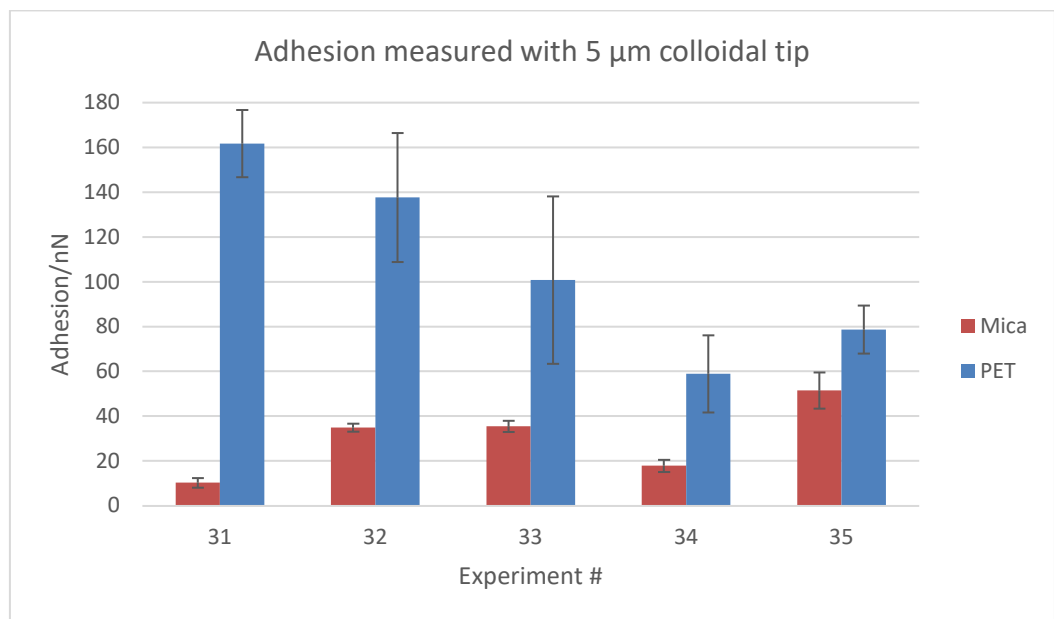


Figure 65: Average adhesion of mica and pet measured using a colloidal tip across five experiments using the same set-up and environmental conditions. Each bar represents average of 1200 independent measurements (see section 3.3.2.3 for explanation of collection method) and standard deviation of those repeats is given by the error bars.

The sharp tip consistently measured mica to be more adhesive than PET, whereas the colloidal tip found the opposite to be true. They both measured values of approximately the same order of magnitude which is also contrary to expectation as the sharp tip should give far smaller adhesion values due to its reduced contact area.

There is also a significant amount of experiment – to – experiment variability for the same sample and tip, especially for the sharp AFM tip.

5.4.3 COMPARING DIFFERENT MACHINES

It was suggested that the source of the variability was the Wilton Veeco machine, so work was conducted in Wilton and Birmingham. Across a number of experiments using probes from the same box, adhesion was measured on mica and PET samples.

In Figures 66 and 67 below, adhesion is plotted for the two machine locations with the error bars representing standard deviation within that data set. Relative humidity is plotted on the secondary y axis.

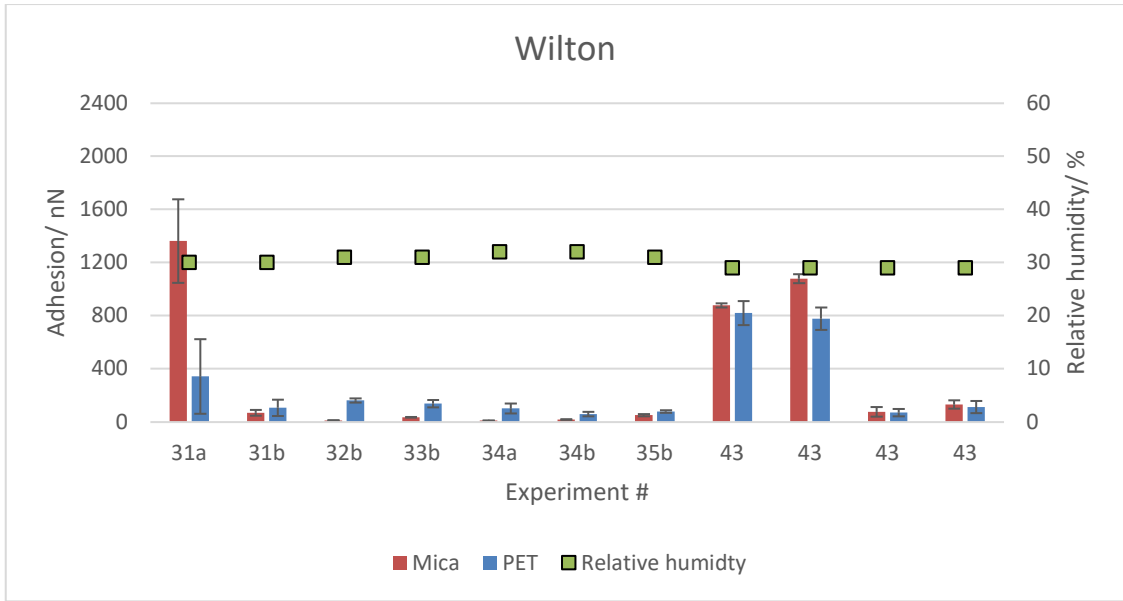


Figure 66: Average adhesion of mica and PET measured using a colloidal probe across experiments conducted in Wilton using the same procedure. Each bar represents average of 1000 independent measurements (see section 3.3.2.3 for explanation of collection method) and standard deviation of those repeats is given by the error bars.

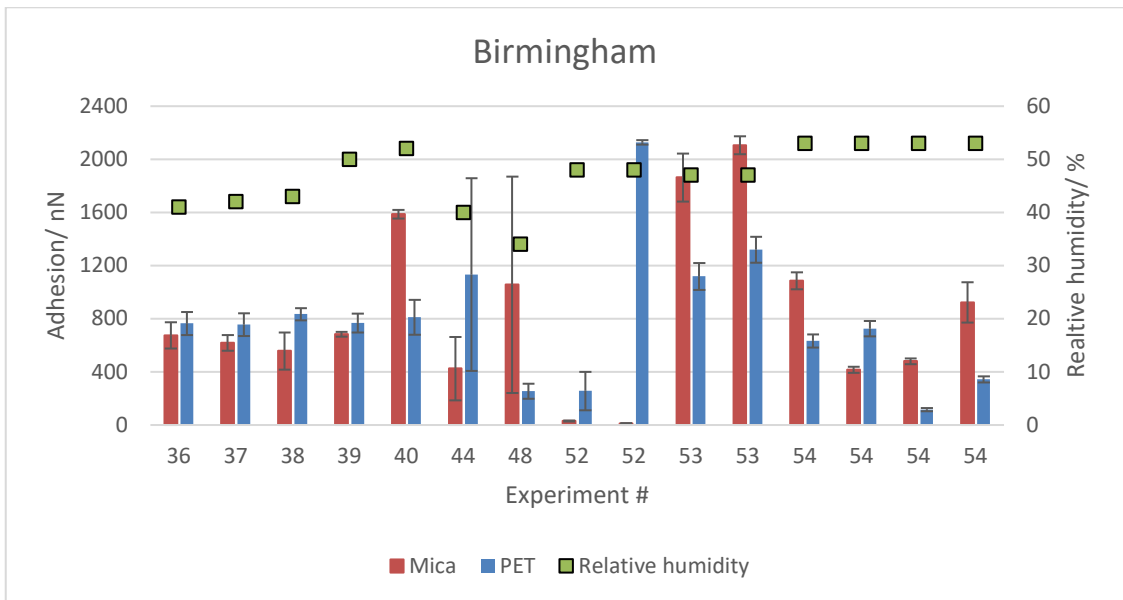


Figure 67: Average adhesion of mica and PET measured using a colloidal probe across experiments conducted in Birmingham using the same procedure. Each bar represents average of 1000 independent measurements (see section 3.3.2.3 for explanation of collection method) and standard deviation of those repeats is given by the error bars.

Displaying the results in this way shows that the variability does not seem to be exclusive to the Wilton instrument. The values are on average higher in Birmingham, and this may be due to the higher relative humidity across these experiments, as it predicted by the literature. However, this trend is not seen elsewhere in the results and the Birmingham results still show a great deal of internal variability not tracking with humidity. For example, comparing experiment 48 and 52 shows an adhesion value to mica of 1050 nN at 34% relative humidity but an adhesion value of 30 nN at 52% relative humidity.

5.4.4 COMPARING DIFFERENT APPLIED FORCES

It was also suggested that a source of the variability was the impact of the deformation of PET. This would explain why PET values are larger than expected as deformation increases the contact area available for capillary bridging. In order to test this an experiment was done where normal applied force was varied and adhesion on PET and mica was measured. The results are shown in Figure 68. The expectation was that adhesion would increase with applied force.

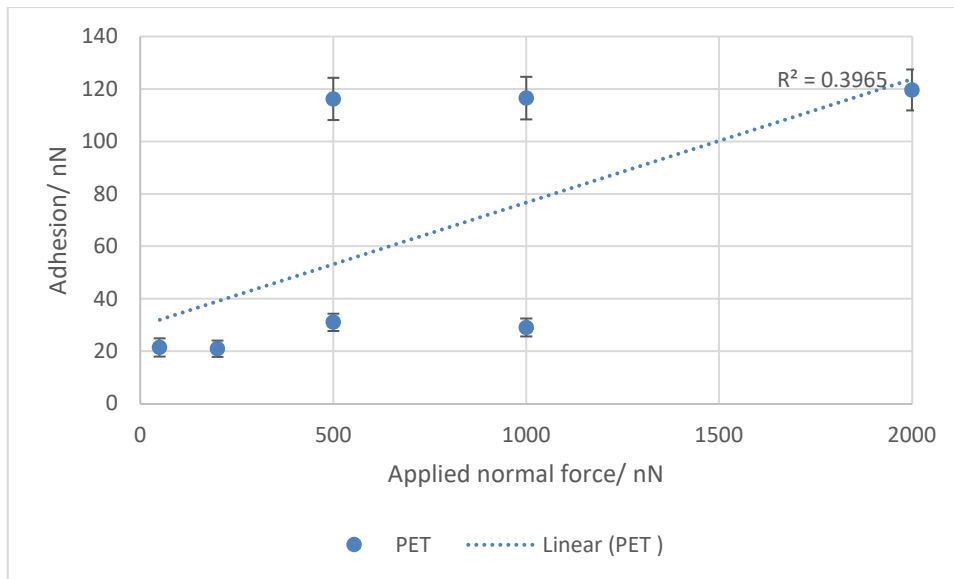


Figure 68: Average adhesion to PET using the same sharp AFM tip and varying the applied normal force. Each point represents the average of 1200 independent measurements (see section 3.3.2.3 for explanation of collection method) and standard deviation of those repeats is given by the error bars.

It is clear from the data in Figure 65 that there is not a strong correlation between applied normal force and adhesion. It should be noted also that compared to other values of adhesion measured across all the experiments, these are on the lower side for this particular study.

5.4.5 COMPARING DIFFERENT COLLOIDAL MATERIALS

Finally, in order to check if the variability was due to the probe material – perhaps some electrostatic effects – the colloidal probe material was changed from borosilicate to polystyrene (PS). PS is less polar than borosilicate so if electrostatic effects were present, they should be reduced.

Experiments were run over 4 days with the same tip being cleaned and used for each case. Mica and PET surfaces were replicated several times in each case, with each measurement displayed in Figure 69 being the average of ~1200 repeats and the error bars being the standard deviation of those repeats. Each of the 1200 measurements were taken at a different

location on the sample surface. Full details of the measurement methodology can be found in section 3.3.2.3.

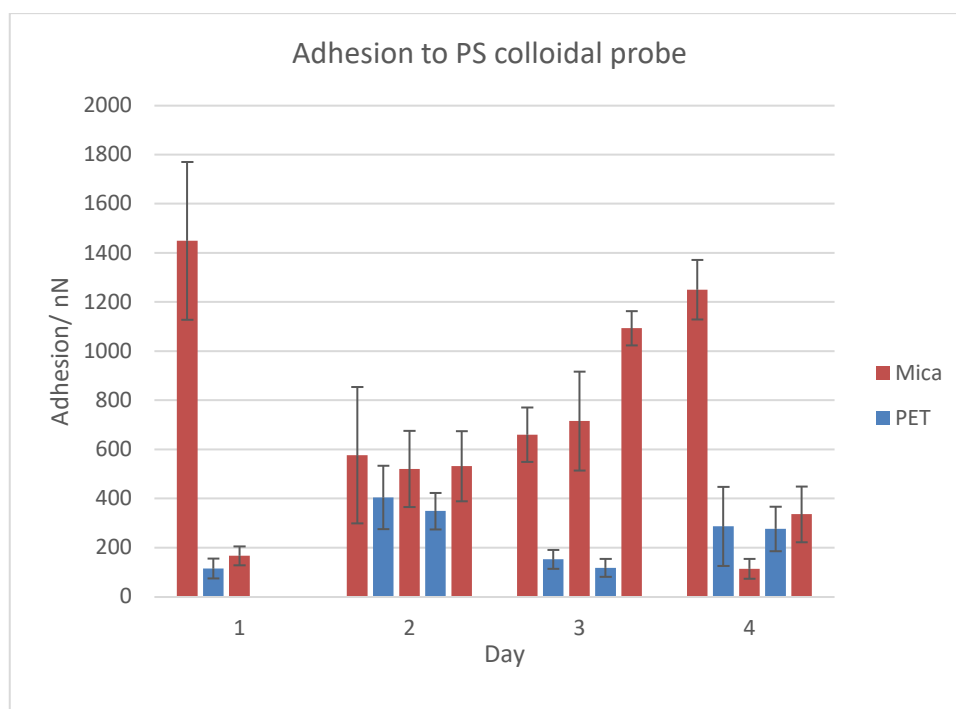


Figure 69: Adhesion of a PS probe to Mica and PET across 4 days of experiments and multiple repeats of each surface with the same experimental procedure. Each bar represents an average of 1200 independent measurements (see section 3.3.2.3 for explanation of collection method) and standard deviation of those repeats is given by the error bars.

Across at least these four experiments, the PS colloidal probe finds mica to be more adhesive than PET. However, there are also significant inconsistencies between the times when the surfaces were measured. On day two and day three the repeats of mica and PET are fairly consistent, but on day 1 and 4 this is not the case. Given nothing in the procedure changed and the room was kept environmentally controlled across this period, it is unclear what is causing the inconsistency. At the very least it can be said that changing the colloidal material does not seem to have changed day to day repeatability of the adhesion measurement.

Examination of a typical force-distance curve from this analysis is shown in Figure 70. An increase in viscoelastic behaviour might have been expected given the change in material from borosilicate to polystyrene and would manifest in hysteresis in the contact region or an irregular detachment event. However as both are absent in these curves it indicates minimal visco-elastic behaviour of the contact event.

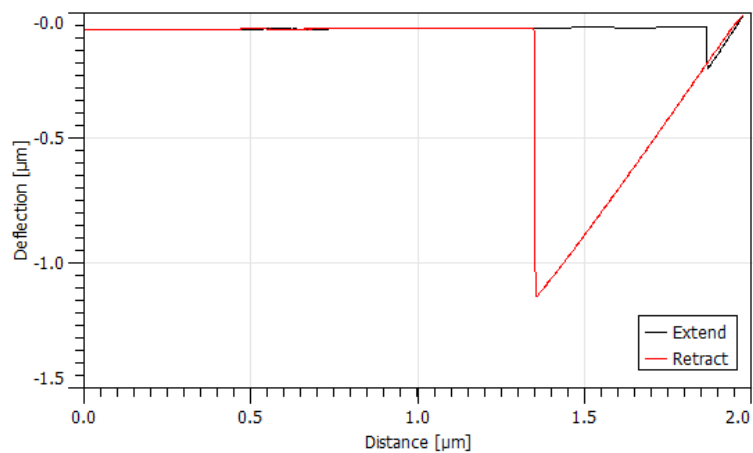


Figure 70: Force-distance curve collected on mica surface using a polystyrene colloidal probe

5.5 DISCUSSION OF ADHESION RESULTS

Having eliminated many sources of experimental error, a hypothesis was formed based on 3 unexplained observations.

- Adhesion to mica and PET varies dramatically across all experiments, both in trends and in absolute values, while individual measurements (of 1200 repeats) are often reasonably consistent.
- Adhesion to mica and PET does not appear to trend with
 - Humidity
 - Probe radius
 - Applied normal force

- Adhesion to mica and PET does not always correlate with modelled values

A possible hypothesis for these inconsistencies is that the surfaces in question have irregular surface roughness location to location which has an impact on local capillary layer effects. This is because the surface roughness of the measured surface causes a variable dependence on humidity due to the variation in behaviour of the bridging capillary. This is described well in the work of Rabinovich in 2002. (Rabinovich *et al.*, 2002). The group validated their proposed model by measuring adhesion of a silica sphere to regularly shaped roughened surfaces ranging from 0.2 to 0.7 nm RMS and found a decrease in adhesion with increasing roughness, and an increasing critical relative humidity with increasing roughness. It would follow from this that if roughness were not the same across the surface, adhesion would also be varying, even at the same relative humidity.

Using this work a model was developed to test the hypothesis. The theory behind the model is described in appendix 9.5. Taking case of a colloidal SiO₂ probe (5 µm radius) contacting a PET surface at 21 °C, the terms for surface roughness were varied and the resulting adhesion plotted against relative humidity, which can be seen in Figure 67. The assumptions of this model can be found in appendix 9.5.3.

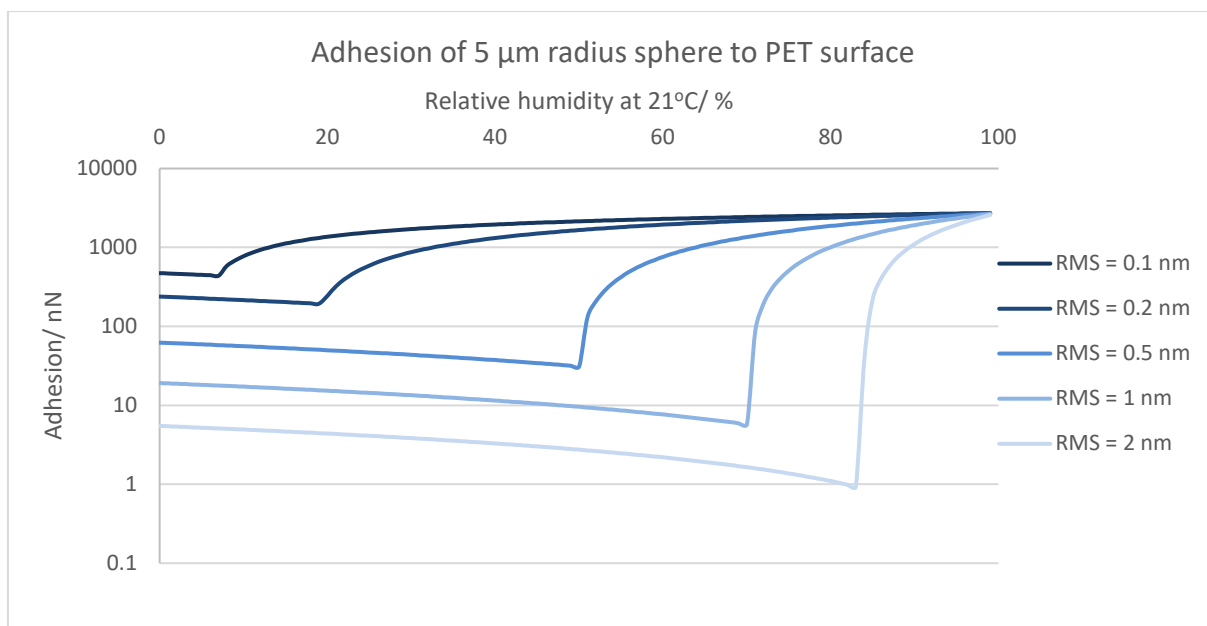


Figure 71: Modelled adhesion of a 5 μm radius colloidal sphere to a PET surface vs relative humidity on surfaces with different RMS values.

This model shows is that even within a relatively small range of relative humidity, e.g., between 20 and 30%, is that adhesion is predicted at values of vastly different orders of magnitude depending upon the RMS roughness. For example, a change from 0.1 to 0.2 nm RMS at 20% RH increases adhesion from 240 nN to 1370 nN. Most critically, the increase in RMS roughness changes the critical relative humidity for the onset of capillary forces.

This could go some way to explain why measurements have been so variable, as RMS roughness values of the surfaces of interest will easily vary on this scale. In a sense, rougher surfaces, which are not well modelled by the equations according to the authors, would cause less of an issue in this regard, as an increase in RMS from 100 nm – 200 nm would cause far less of an effect on adhesion than the increase from 0.1 – 0.2 nm, as at this scale of roughness, capillary effects would be so reduced already. According to the model, in a system such as the one measured experimentally in this work, small changes in relative humidity and roughness have disproportionately large impact on the value of adhesion.

PET finished film can vary in location-to-location roughness. Figure 72 below shows two images taken using AFM tapping mode measurements of a finished film surface in locations directly adjacent to each other. Even though the surfaces are only subtly different, in the case of a colloidal probe contacting this area, the sphere to surface contact areas, and the capillary layer interactions will not be identical, and thus the measured adhesion will differ.

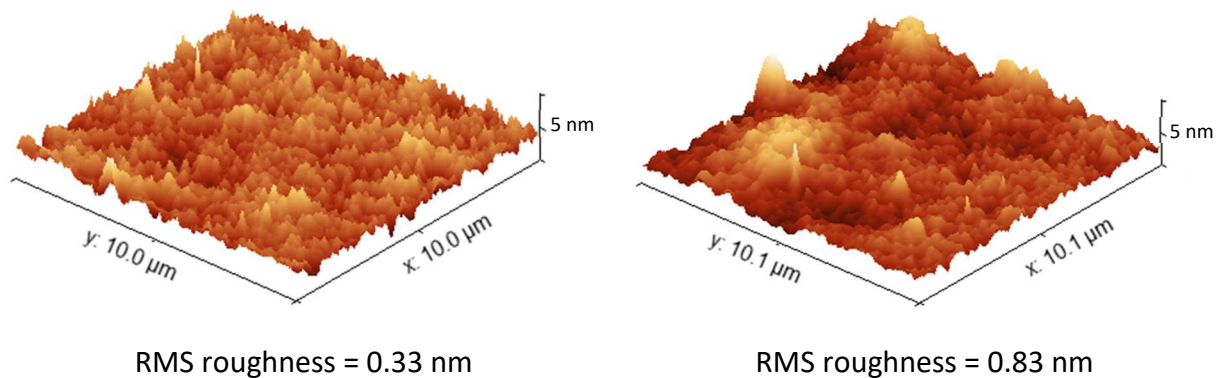


Figure 72: AFM tapping mode images of a DTF BoPET finished film uncoated surface. Images have been scaled such that their z-axes are identical to show difference in topography.

In literature studies where roughness has been investigated using FFM, researchers have often artificially created surfaces with defined roughness of exact RMS and λ values. These were found to give consistent results that aligned with the theory used (see Section 2.2.11). However, one paper of note which analysed irregularly rough surfaces is that of Lehr and Kietzig (Lehr and Kietzig, 2015). They measured adhesion at humidity at 0, 50 and 70% on titanium sheet which had been laser etched to either a “rippled” or “bumpy” texture. They collected 100 force curves per substrate per RH level and used a 10s dwell time to ensure equilibrium was reached. They were unable to elucidate any consistent trends, despite

extensive surface analysis of the samples via AFM, SEM and EDS. Their data also contained large statistical error such that samples could not be distinguished with confidence.

Additionally, in the work of Zarate (Zarate *et al.*, 2013) the adhesion of stainless steel and Perspex were measured between relative humidity values of 15 – 65% following extensive surface roughness characterisation. They used a colloidal probe to take 1200 force curves at independent locations on each surface at each humidity level. They found Perspex, which is relatively hydrophobic, had an adhesion which was independent of RH. Stainless steel adhesion was found to first increase at 25%, then decrease at 50% and finally increase slightly again at 65%. They could not satisfactorily completely explain this trend.

Further to this, in a review paper by Harrison, Corti and Beaudoin (Harrison, Corti and Beaudoin, 2015) they comment upon the inconsistencies across the field for the trends of adhesion with relative humidity in general, grouping the papers by the systems studied. For one system, of silicon nitride AFM tip contacting a mica surface, there was reported an independent relationship (Eastman and Zhu, 1996), a step-wise increase between 20–60% RH (Sedin and Rowlen, 2000), or a trend where adhesion has a maximum between 20–40% RH (Farshchi-Tabrizia, Kappl and Butt, 2008). This shows that even in simple systems, slight variations in sample between different groups work can result in wide variations in conclusions.

This supports the hypothesis that the inconsistencies seen in this work are due to surface roughness effects causing a variable dependence on humidity. To prove this hypothesis would require repeating the measurements with far more emphasis on specific surface roughness characterisation of both the surface and the colloidal tip. This would require additional measurement using SEM or an equivalent technique. Re-measurement of the colloid and

surface at regular intervals during experimentation might also be required if there was concern about it changing shape over the course of the measurement. The contact area of each individual contact event could then be found and an adhesion value proportional to contact area determined.

To build on this, additional location to location variation in chemistry may also be contributing to this effect. A paper by Christenson and Thomson (Christenson and Thomson, 2016), discusses the nature of the surface chemistry of freshly cleaved mica. In a thorough review of the literature, they showed that when mica is cleaved in ambient air, atmospheric water and carbon dioxide react with the surface, forming a layer of K_2CO_3 . This layer is crystalline under dry conditions, but mobile under humid ones, with a transition region in-between the two extremes where the mobility of the ions can vary depending on the exact surface structure. They suggest that because of this mica is not, in fact, an ideal choice as an AFM standard for surface adhesion measurements, as the surface chemistry can vary significantly and the structure of adsorbed water on mica surface, is more complex than most models currently presume. This understanding of the mica surface may go some way to explain the variation in measurement seen in this work.

Finally, these above effects may also be compounded by the fact that an insufficiently large area of the surface was examined. As was also pointed out by Harrison, Corti and Beaudoin (Harrison, Corti and Beaudoin, 2015) even if force curves are taken across a $100\ \mu\text{m}$ by $100\ \mu\text{m}$ area, this is only 0.00032% of a 1 cm diameter circular sample. In this report 1200 independent locations on the surface were recorded, but this could be increased to possibly improve the measurement.

5.6 CONCLUSIONS FROM ADHESION MEASUREMENTS

The intention of this chapter was to measure adhesion for the surfaces of interest to this industry problem using colloidal probe AFM. It proved to be impossible to obtain consistent values for adhesion via this method in this case.

PET and mica substrates became the focus to uncover the source of these inconsistencies and sources of error were sequentially examined. Machine, user, tip chemistry, probe diameter, applied force and local humidity were varied and no resolution to the inconsistency or trend with conditions was found. The one factor that was not varied was surface roughness, as the whole purpose of this work was to understand adhesion of the samples of interest in their current surface state that results from processing. This was hypothesised to be a possible root cause of the inconsistencies.

The impact of roughness was examined more closely using a literature model. It was determined that for “real” surfaces, according to the model, RMS values have an enormous impact on dry adhesion forces, but more critically, on the critical humidity value predicted for the onset of capillary forces. To model adhesion, surface roughness parameters (RMS and λ) would need to be determined by experimental methods. These methods will necessarily yield values which are affected by field of view and lateral resolution used to sample them, and even though these changes are small (scale of nanometres), they are predicted to have an enormous impact on adhesion values. This means that for irregularly rough surfaces with local location-to-location roughness variation, even on the same sample, the surface texture may be sufficient to derail experimental repeatability, with variation of many orders of magnitude being introduced due to the variability in local onset of capillary adhesion. This would explain

why these measurements under ambient conditions were unable to capture reliable adhesion values for the surfaces of interest.

To answer the question of contamination adhering to rollers and PET surfaces, an alternative method to understand contamination adhesion should be explored. In the case of understanding the adhesion of PET to roller adhesion a possible method for this would be to conduct a more macro-scale measurements on the production line. The forward draw could be environmentally isolated, and the humidity varied within this chamber to see if this greatly affected either debris adhesion or relative movement. This could be measured by monitoring average scratch length across many production cycles at different conditions.

6. UNDERSTANDING THE CONTRIBUTION OF CONTAMINATION TO SURFACE DEFECT FORMATION

6.1 SCRATCH FORMATION DURING PET FILM PRODUCTION

The aim of this chapter is to understand the ways in which the presence of contamination contributes to surface defect formation during PET processing. In the Chapter 4, the chemical composition of the contamination was investigated. Armed with this knowledge it is now possible to answer one of the key questions surrounding this problem: is the contamination itself acting as an intender and causing scratches, or is it modifying the surfaces such that it promotes scratch formation?

To cover this complex topic this chapter will first present the types of defects which are seen most frequently based on records of line faults and customer complaints to give a grounding to the scope and scale of the problem. Next, in order to attempt to model scratch formation on PET films surfaces and understand the factors which affect their appearance, a method for modelling scratching using atomic force microscopy will be described. The results of comparing cast and finished film at different temperatures will be shown.

The next stage in developing understanding is to measure the surface roughness of the rollers on the production line under clean and “contaminated” conditions to understand their role in scratch formation. This will be done using imprint tapes in-line, lab-based samples, and coherence scanning interferometry.

Finally, to understand the role of relative movement on scratch formation the possible sources of relative movement derived from the production process will be described including

their link to frictional properties. Using lateral force microscopy and force board measurements the frictional properties of the roller surfaces of interest are shown and linked back to the types of scratches seen.

6.2 CLASSIFICATION OF SCRATCH TYPES

Polymeric materials are prone to scratching at all stages of the production, including stretching, coating, handling and use. Some of the mechanics governing scratching are covered in appendix 9.2.

Scratches are just one type of defect that can be found on the BoPET surfaces. Defects can occur in the film surface itself or in the coatings that are applied to the surface. Coating defects include coating misses, air bubbles, and streaks associated with the coating. These will not be discussed in detail here. However, coatings can sometimes serve to highlight defects in the underlying surface, making problems more visible to the human eye.

Other defects such as gauge profile, MD lines, stretch lanes, TD thickness, holes, or issues related to winding will also not be discussed here. However, it is useful to identify the different types of scratching defects which are commonly seen on the D52 production line.

Scratches are single, isolated defects that occur on the PET film due to an impinging asperity damaging the film. Scratches are distinguished by the fact that they are produced by tangential motion between contacting surfaces. They can be caused either by a fixed or a rolling asperity. The difference between these two types of scratches is shown in Figure 73.

In either case three things are required:

- An impinging asperity

- A normal force/scratching force acting on this particle sufficient to overcome the yield stress of the material being scratched
- A lateral movement

In the case of scratching occurring during the PET film production process, all of these components are present. The lateral movement (referred to subsequently as relative movement) and will be discussed further in Section 6.5.

The normal force will be derived from the tension in the film. The tension is a process parameter which can be changed a little by the production team but generally needs to be high enough to stretch the film in the draw zone to the desired stretch ratio. This tension forces the film onto the rollers at a calculable normal force, which in the presence of the other factors can cause surface damage/scratching. This can occur at any stage of the production process from casting to winding but the focus of this report is to discuss scratches formed in the forward draw unit of the production line.

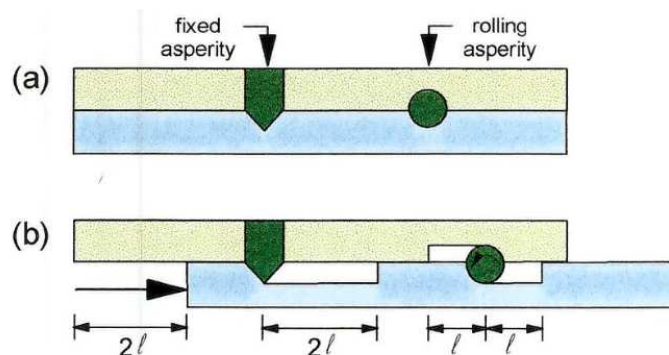


Figure 73:(a) Two deformable planes in contact containing a fixed and rolling asperity. (b) The scratch produced for both the fixed and rolling asperity after a lateral movement of $2l$ (Smyth et al., 1998).

Examples of rolling asperities could include:

- Dislodged filler particles (from filled films)

- Abraded roller particulates
- Aluminium oxide particles from cleaning pads
- Particles of contamination

Fixed asperities could include:

- Features on the roller surface which are proud of the surface
- Any of the rolling asperities listed above which have become fixed in the roller surface

6.2.1 REPLICATION MARKS

'Replication marks' is a term given to scratches caused by a single fixed asperity on one roll, an example is shown in Figure 74. This asperity is usually caused by a temporary particle that can be removed by a manual clean, or by a topographical feature on the roller surface caused by damage to that roller. These types of scratches are identified because they are deep and long and occur at a regular repeat distance along the length of the finished film that corresponds with the circumference of the roller.



Figure 74: Replication scratches found on D52 film. Scratches appear identical in shape and form and were found at a specific separation distance.

If such a repeat surface marking is discovered during a quality check, then candidates for the culprit roller can be determined by measuring the length of the repeat distance of the fault and then cross-checking vs the circumference of the relevant rollers. A manual clean as described in Section 1.6.7.3. is often sufficient to remove the incidental particle.

Incidental scratches without a replication distance are referred to simply as scratches. These occur without a discernible pattern so are more likely to be due to non-fixed asperities. These may only be present for a short period of time before they are removed either by the mechanical action of the rollers and film, or the automatic cleaners.

6.2.2 NEEDLES

Needles are a specific type of scratch that are commonly seen on the D52 production line. Needles are characterised by their hooked shape at one end, which gives them their name. An example of this characteristic scratch can be seen in Figure 75. These can be found as replication marks, or as incidental scratches.

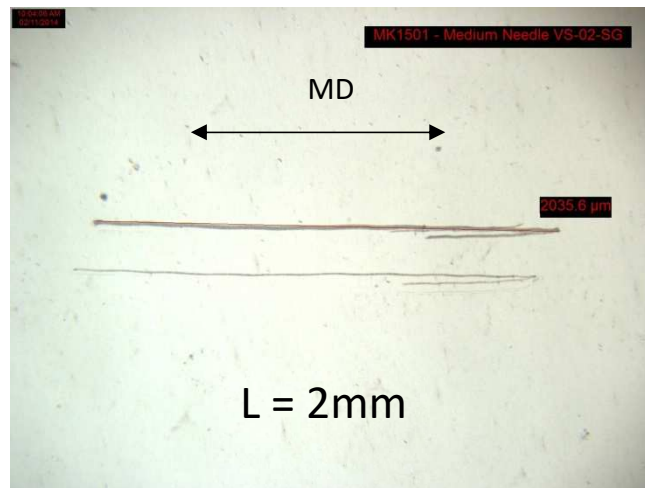


Figure 75: Image of a needle captured by Zeiss light microscope.

They are typically found aligned just off from the machine direction and are more commonly found on filled films, indicating they are caused by mobile filler particles that have detached

from the film surface. Scratches without this characteristic hooked end are referred to simply as scratches, an example is shown in Figure 76.

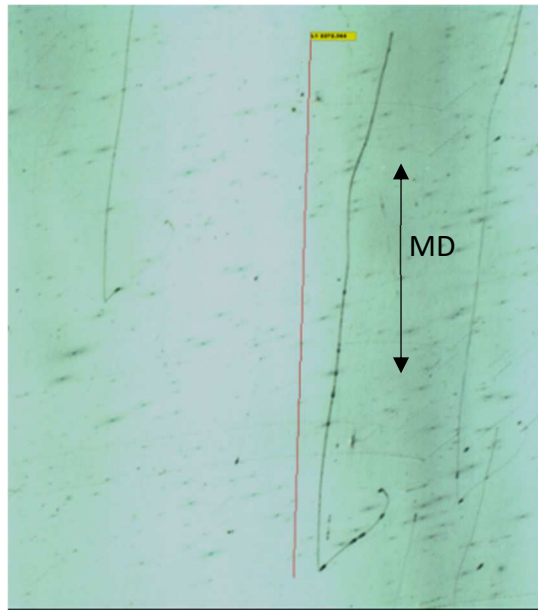


Figure 76: Image of scratch caused by CR2 on D52 captured by Zeiss light microscope. Length measurement reads 2.3 mm. Double headed arrow indicates machine direction axis.

Scratches can vary in length from a few μm to many mm and in “severity” by how easily they can be perceived by human eye or how much they impact the function of the film surface. During film production the distinction of “severity” is made qualitatively by line operators based on user experience of the possible range of scratch severity.

Coherence scanning interferometry analysis of some scratches defined as “light”, “medium” or “heavy” was conducted internally in 2014 (Kupferman *et al.*, 2014).

They found that scratches have heights (protrusion from surface), caused by displaced material. Critically they found that perceived severity of a scratch by eye is correlated more closely with this height, and not length and width.

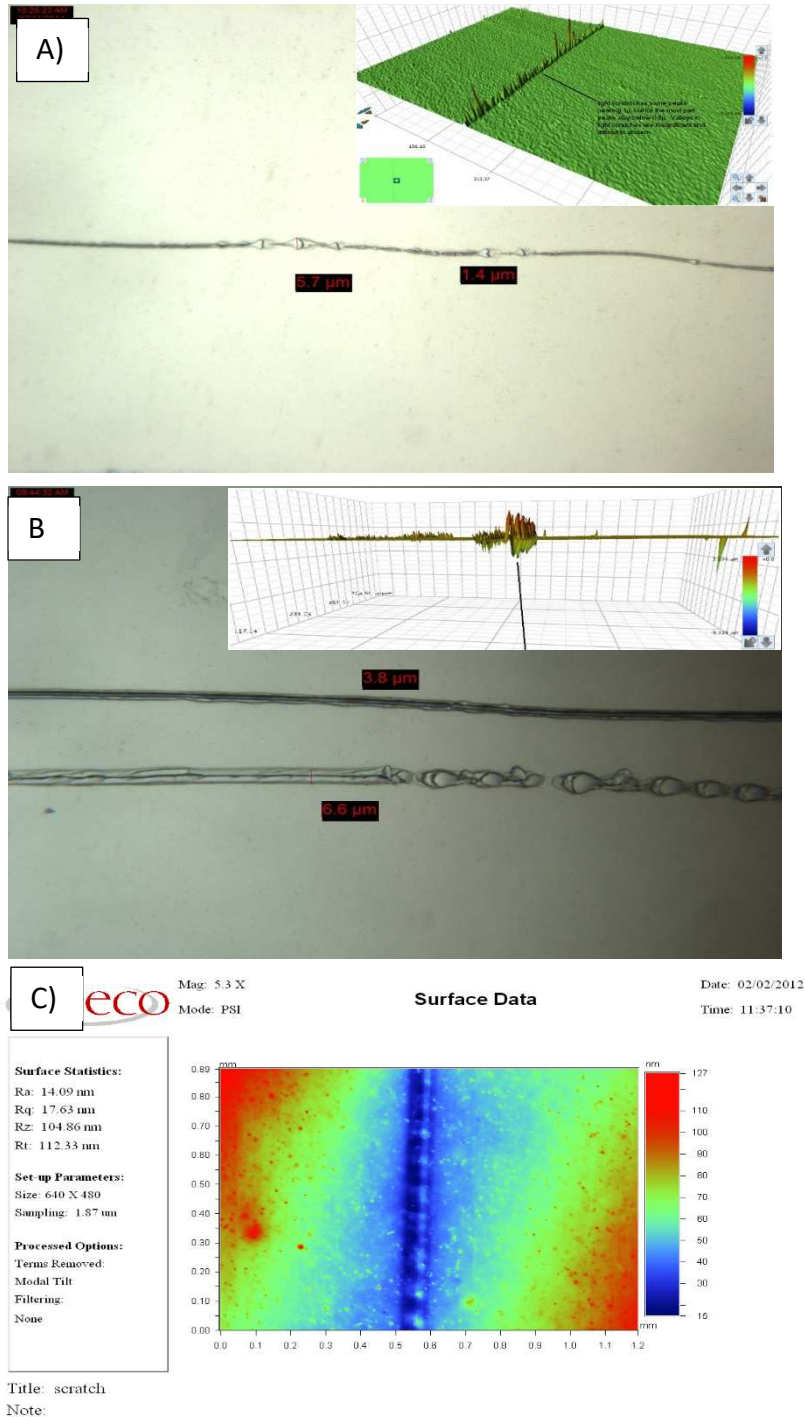


Figure 77: Zeiss microscope and CSI images showing height of protrusions of two scratches. A): "Light" scratch with range of width 1.5 - 5.7 μm . B) "Heavy" scratch of width 3.8 – 6.6 μm . C) CSI image of scratch track with typical "ribbing" formations.

Images from their work can be seen in Figure 77. All scratches observed have “a string of pearls”, or “ribbed” track feature consistent with the hypothesis of a hard pinpointed object digging into the PET surface associated with stick-slip type behaviour. For a description of stick-slip motion see Appendix 9.3.

6.2.3 SCUFF MARKS

While one isolated scratch does present a problem, especially if “heavy” or severe, many scratches even if only “light” and shorter than 1 mm in length present a greater problem to the end user of the film if the frequency and density is at a high enough level.

When this occurs, the convention internal to DTF is to refer to the scratches collectively as one defect called a “scuff mark”. This is by far the most common type of defect of concern on the D52 production line, and nothing except a full line clean is found to be able to resolve the issue.

Scuffing most commonly appears at the extreme edges of the film web and is generally categorised by numerous small scratches that are individually invisible to the human eye but when packed densely on the film surface, produce an effect which is visible overall. They give the film a “speckled” or “hazy” appearance to the which becomes worse over time. This is best visualised using microscopy or coherence scanning interferometry, an example of which can be seen in Figure 78.



Figure 78: Optical Microscopy image of Scuffing defect taken with Zeiss light microscope. Length labels read 0.1 mm, 0.1 mm and 0.2 mm respectively left to right. Marker pen at top right is to help the surface focus.

6.3 SCRATCH MODELLING USING ATOMIC FORCE MICROSCOPY

In the previous section a number of the key scratch types seen on the D52 film production line were described. In all cases an indenter (or indenters) is needed to propagate the scratch. It is hypothesised that the necessary force required will be affected by factors including the crystallinity of the film and the temperature of the polymer.

Micro manipulators have been used extensively as micro indenters in the literature to model deformation and scratch behaviour (Akhtar, 2010; Zhang *et al.*, 2019). Building on this, a few previous studies have used AFM tips as micro indenters. This work is discussed in Appendix 9.2.7.

In order to investigate scratch morphology of BoPET in this case, it was proposed that the AFM could be used as a micro-indenter. This required the development of a new methodology compared to traditional imaging (described in Section 3.5) where the AFM tip was utilised as

a micro- indenter. This was inspired by the work of Hamada and Kaneko, Han, Schmitt and Friedrich, and Du (Hamada and Kaneko, 1992; Han, Schmitt and Friedrich, 1999; Du *et al.*, 2001). This method allows precise control of the applied force and speed of the indenter on a micron-scale. This allowed for exploration of the impact of surface temperature, crystallinity, and applied force on the visual appearance of scratches.

As mentioned previously, the work of Kupferman (Kupferman *et al.*, 2014) found that the visual perception of the severity of scratches on a PET surface is dictated by how high the surface protrusions are, rather than the depth of the scratch. Surface protrusions from stick-slip behaviour during scratch formation are on average higher than from constant motion due to the way that material is displaced irregularly, rather than in consistent tracks either side of the scratch valley. Therefore, of particular interest in these measurements is the impact of changing a factor on the visual appearance of stick-slip like scratch morphology, as the more visual a scratch is, the more significant it is to the overall perceived surface quality of the film, which may cause it to fail quality checks during production.

6.3.1 IMPACT OF CHANGING NORMAL FORCE

Three samples of finished film were scratched at increasing force. The normal force is altered by changing the deflection setpoint. This can then be converted to a force in Newtons by multiplication with the deflection sensitivity and the intrinsic spring constant of the cantilever. The results can be seen in Table 11.

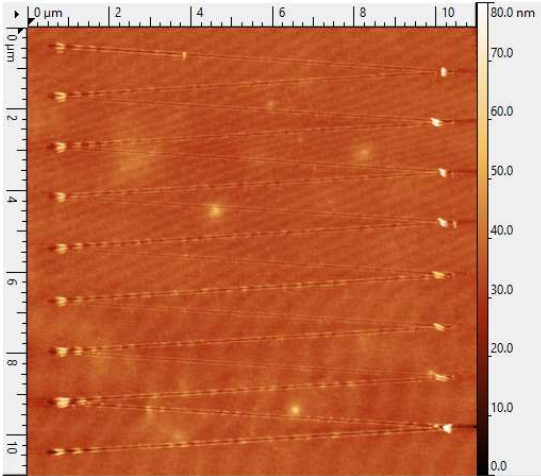
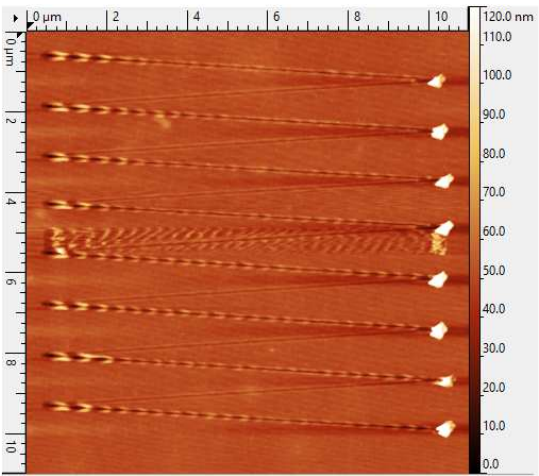
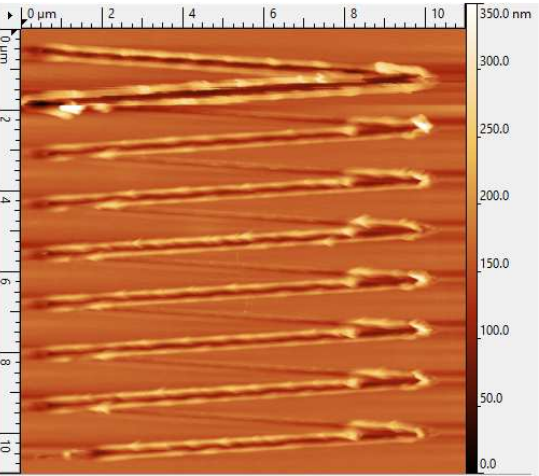
			
Deflection setpoint (V)	0.5 V	1 V	4 V
Force	159 nN	318 nN	1272 nN
Notes	Light scratch seen with slight evidence of ribbing in the scratch track	Medium scratch seen with strong evidence of ribbing in the scratch track	Deep scratch seen with little/no evidence of ribbing in the scratch track

Table 11: AFM images of finished film scratched using AFM as micro-indenter at a three of deflection setpoints.

These images offer a qualitative look at how altering normal forces affects scratching mechanisms. In all three cases it appears the film has undergone ductile deformation as there is no evidence of tensile fracture which would be characterised by crazing or cracking radiating away from the point of indentation. As force is increased there is a change in scratch track morphology from more stick-slip ribbing, to less. It is worth noting also that the scratches have asymmetry in the ribbing track, this is derived from the inverse pyramidal geometry of the AFM probe.

6.3.2 IMPACT OF CHANGING FILM PROCESSING STAGE

Samples of cast, forward drawn and finished film were also scratched and imaged at a deflection setpoint of 1 V. The images are shown in Table 12. It can be seen that at the same setpoint of normal applied force, the visibility of the scratch is strongly affected by the underlying roughness of the starting surface. Cast film has far more surface features than finished film and as such the scratch is more difficult to distinguish. This is particularly notable on the 3D projections.

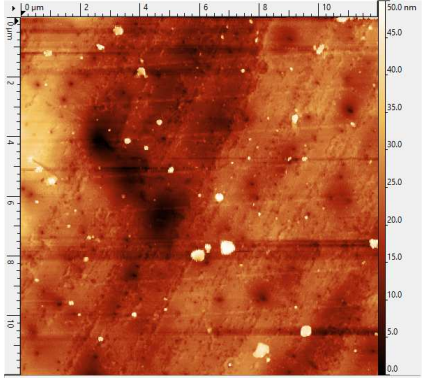
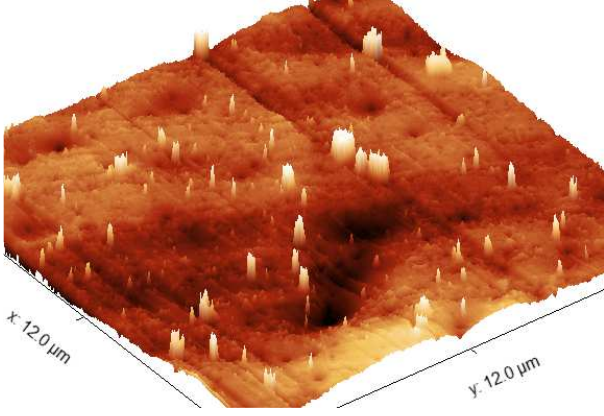
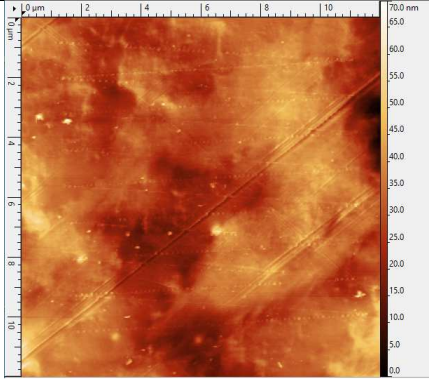
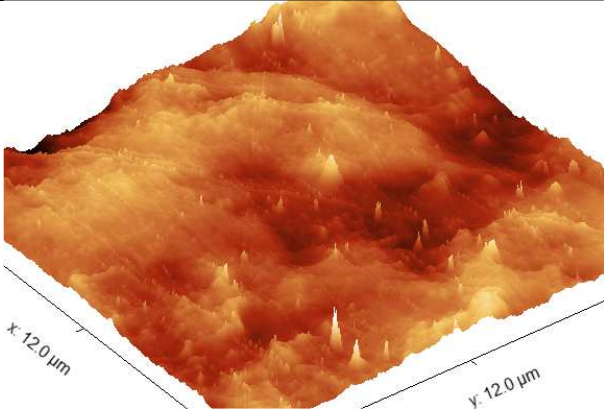
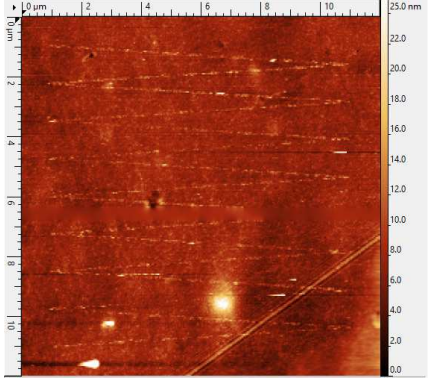
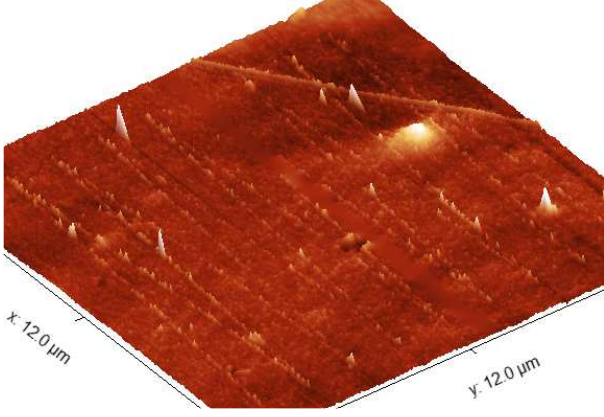
	2D image	3D projection
Cast film		
Forward drawn film		
Finished film		

Table 12: 2D and 3D AFM images of cast, forward draw and finished film scratched using the same deflection setpoint.

This implies that perhaps the perceived visibility of scratches to the human eye could depend partly on where in the production line the scratch forms, with later in the line being more detrimental to overall appearance. This could be due to changes in morphology as you orientate and crystallise the film. It was expected that cast film, as the least crystalline would deform more easily than finished film, leading to a more visible scratch on cast film, compared to scratch made at the same applied force on finished film. However, this cannot be proved as any impact of the surface crystallinity on the scratch is hidden by the vast difference in starting surface roughness.

6.3.3 IMPACT OF CHANGING TEMPERATURE

In a subsequent experiment, a sample of finished film was scratched at room temperature, and then heated to above glass transition temperature and scratched in an adjacent location. This was to investigate the impact of changing temperature and polymeric phase on the morphology of the scratch formed. The results can be seen in Table 13.

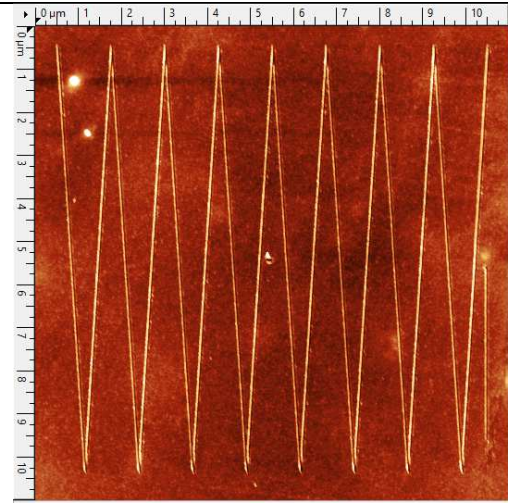
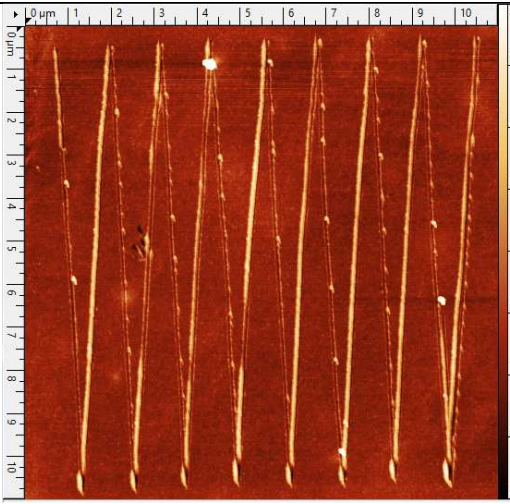
		
Temp	21 °C	80 °C
D.S.	1 V	1 V
Force	330 nN	330 nN

Table 13: 2D AFM images of finished film scratched with the same force at two different temperatures.

In the low temperature case, the scratch appears to have a consistent depth throughout with little-to-no evidence of ribbing in the scratch path. However, in the case of the heated film. The scratch shows far more characteristics of stick-slip ribbing in the scratch path with displaced material being more noticeable. From analysis of the cross section of the scratch path at ambient conditions compared with elevated temperatures in Figure 79 it can be seen that the depth profile is slightly deeper for the trace at elevated temperatures, and that the profile is slightly less symmetrical, resulting in a slightly higher peak of displaced material on one side.

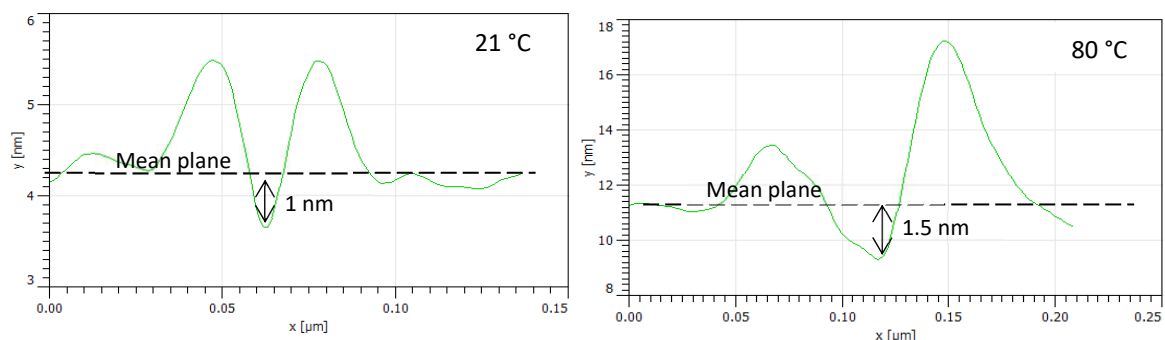


Figure 79: Cross-section profiles of scratches in PET surface formed at ambient and elevated temperatures utilising 1V deflection

6.3.4 CONCLUSIONS FROM SCRATCH MODELLING EXPERIMENTS

Overall, using AFM as a micro-scale scratch modeller proved partially successful. The AFM set-up including heating stage allows for very precise control of many factors including normal force, speed, size and temperature.

It is, however, no easy task to collect such images. A lengthy process of finding an appropriate location on the surface (free from as many defects as possible), then switching to the scratching tip (without losing the place on the surface), and then switching back to the imaging tip and finding the scratch on the surface, is required. This is time consuming and

frequently fails, especially when changing temperatures, as thermal expansion effects it is easy to lose the correct place on the surface.

Nevertheless, some interesting insights were obtained through this work. Scratching cast, forward drawn, and finished films revealed that scratches were more noticeable the more processed the film, possibly due to the roughness of the starting surface impacting the visibility of the scratches, or some other effect of the increasing crystallinity of the surface. Missing from this assessment however was the resulting scratch after subsequent stretching in the case of the cast and forward drawn films.

More critical to the topic of this report, it was seen that changing the applied normal force saw the scratch morphology change from more stick-slip motion at lower force, to less at higher forces. As expected, the average indentation depth increased with increasing force. Finally, it was seen that higher surface temperatures on both cast and finished films led to more stick-slip motion during scratching. This leads to the understanding that scratches which are more noticeable to the human eye (those with stick-slip) morphology occur when temperatures are elevated.

Having now discussed the types of defects seen on BoPET surfaces and modelled scratching using AFM, it appears that for scratches to be most visible to the human eye, they require elevated temperatures and an impinging feature which is mechanically strong to provide a high enough normal force to overcome the shear strength of the PET.

Linking this back to the contamination of interest – which was shown in the previous chapter to be made up mostly of components of PET degradation – it unlikely that it is the contamination itself that is acting as the indenter in scratch formation. Instead, it must be

promoting scratching another way. It is known that relative movement is required to provide the tangential motion for scratch formation. The logical hypothesis therefore that contamination promotes relative movement in some way. Relative movement is of greatest prevalence in the forward draw unit, where temperatures are also elevated, which was shown by the AFM modelling to also result in more noticeable scratches. The forward draw unit will now be described in more detail, followed by the major sources of relative movement, which will allow this hypothesis to be more fully explored.

6.4 THE FORWARD DRAW UNIT

The location of concern in this project is the forward draw (FWD) unit. This is where the majority of surface damage occurs during film processing. Here the film is oriented by stretching (or drawing) it along the direction of film travel. A schematic for the forward draw unit is shown in Figure 80. First, driven nip or capstan rollers isolate the cast film from the forward draw tension; this is known as the slow nip. From the slow nip the film passes over a series of heated rollers ('preheat rolls' or PHR) typically heated to temperatures below 80°C – 85°C to avoid sticking to the rollers and surface damage to the film. The final preheat roll(s) before the point of draw, may be heated to a higher temperature. For thick films, like those made on D52, infra-red heat is required to boost the film temperature to above its glass transition temperature and to localise the draw region. The actual draw region occurs at the point where the film reaches its highest temperatures which is between the last and hottest preheat roll, and before the first cooling roll.

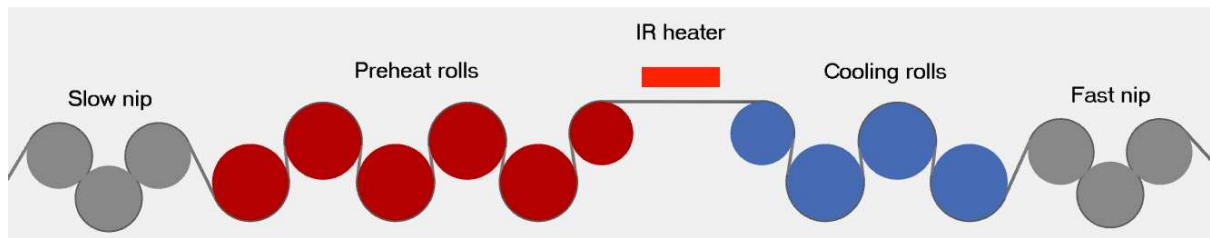


Figure 80: Schematic of a typical forward draw unit

After drawing, the film is rapidly cooled over a series of cold rollers to arrest the draw and halt crystallisation, prevent relaxation of the orientation, and also prepare the film surface for coating (if applicable) before transport to the stenter

Finally, a second set of nip rollers, known as the fast nip, are located at the outlet of the forward draw and are driven at a higher speed. These provide the drawing force which stretches the film. The nips are sometimes rubber covered and not temperature controlled. The speed of the fast nip relative to that of the slow nip determines the amount of draw or draw ratio. The preheat and cooling rolls are often un-driven and will run at a speed determined by that of the film passing over them. Being unconstrained, the film will neck-in slightly during the draw process, reducing in width by a small percentage as it emerges from the draw zone, resulting in some relative movement as will be discussed in the next section.

6.5 FILM TO ROLLER RELATIVE MOVEMENT DURING PET FILM PRODUCTION

There are several possible sources of relative movement between the film web and the FWD rollers. This relative movement is a possible source of lateral movement for surface defect formation and should be eliminated wherever possible. There are different causes of this relative movement which have different degrees of impact as well as different speed and length scales.

6.5.1 JUDDER

Judder is the name given to the micro and macro vibrations that occur in a production line as a result of the high speeds and tensions at play across all the units. These include any environmental controls, the casting, coating, and stretching units as well as the ambient vibrations of the building. Judder will occur at locations of the production process, in any direction and is hard both to measure and account for. All efforts are made to ensure the system is running as smoothly as possible with as minimal vibrational disturbance as possible, this is even considered in the construction phase when building the foundations of production plants.

The base level of judder in the D52 line is not of concern. In the instance where there is a fault which increases this base level such that it begins to affect surface quality, there are often multiple faults in addition to merely surface defects - for example with coat quality or gauge thickness. This will prompt a line shutdown to address or repair whatever fault is causing the problem.

6.5.2 PRE AND POST DRAW

Pre and post drawing of the film also causes relative movement between the web and (typically) the last preheat roll (pre draw) or the first cooling roll (post draw). In a FWD machine, the objective is for the MD stretch of the web ("the draw") to be localised between the last preheat roll and first cooling roll, in the "draw zone". Pre draw refers to the situation where the hot web starts to stretch (draw) before leaving the last preheat roller – in other words, the web runs faster than the roller and so is "sliding" on it. Post draw refers to a similar situation in which, instead of the draw being arrested at touchdown on the first cooling roll, the web continues to stretch part way into the web wrap contact region on this roll; this

situation can occur for different reasons, for example inadequate quench (e.g., from poor heat transfer) on this roll.

Post draw can cause both MD and TD relative movement as the film will both be lengthening in the MD direction, but also correspondingly narrowing in the TD direction due to Poisson forces (it will also be thinning in the film thickness direction, but this does not have an impact on relative movement). The scale of the MD relative movement due to this effect typically greatly exceeds the TD scale. If there is significant post draw, relative movement and hence size of defects, can be large. Much of the work done in the 90s, as described in Appendix 9.1.4 - 9.1.5, was involved in eliminating this as much as possible. This is done by ensuring an excellent quench on cooling roll 1 and by optimising the position and power of the IR heater.

6.5.3 THERMAL EXPANSION

Thermal expansion refers the tendency of matter, in response to a change in temperature, to increase its linear dimensions, and hence change its shape, area, volume, and density, not including changes occurring due to phase transitions. Since temperature is a function of the kinetic energy of the molecules of a substance, this means that as the substance is heated, the molecules move faster, increasing the average distance between them, thus decreasing density and increasing volume. The inverse of this is thermal contraction in response to a decrease in temperature.

In the case of polymeric materials films, over a particular temperature range, a coefficient of thermal expansion can be defined. Expansion of the film will occur in all directions during heating and can be different in each direction. For the purposes of understanding relative movement's impact during production of BoPET film, only the expansion in the machine direction and in the transverse direction are important.

As it leaves the last preheat roll, the film is above the glass transition temperature of PET polymer (~80 °C) so the film can be drawn/stretched in the MD. Often, to aid this drawing process, the final preheat roll is warmer than the preceding rolls; there is often also an infrared heater in the draw zone. During heating on preheat rolls, the zero tension dimensions of the web will increase due to thermal expansion. If the forces associated with these changes exceed the constraint from roll to film friction, then relative movement can occur. This relative movement often occurs close to the web leaving the roller as any dimensional changes in the web must be complete by the time the web leaves the roll. The change would be an increase in MD length (manifests as a speed increase in the moving web). The TD change in width will be a combination of an increase due to thermal expansion, and potentially a decrease due to Poisson ratio effects. As a result, there can be a combination of MD and TD relative movement during the last part of the wrap on the roll. The TD changes will be greater towards the edge of the web, and zero in the web centre, by symmetry. Therefore, in the event that a defect forms via a fixed asperity on the rolls during these movements, the scratch will be orientated at an angle direction of travel with the end pointing away from the centre of the film.

At the end of the draw zone, the film touches down on the first cooling roll, which is typically cooled to around 10 - 25°C. For thinner films, the majority of cooling takes place on the first cooling roll, whereas for thicker grades, due to slow through thickness conduction (PET has a low thermal conductivity), a significant amount of cooling also happens on the second cooling roll. During this period, stresses in the film will change due to a number of phenomena, including thermal contraction effects. As seen on the preheats, these stresses are not usually large enough to break the frictional hold between film and roll, until the last part of the wrap

when relative movement will occur as the web on the roll moves to equalise tensions with the part of the web after the roller exit. During this period of relative movement, thermal contraction effects alone would produce a tendency for the web to contract in the MD (a speed decrease) and a width loss in the TD. In the event that a defect forms via a fixed asperity on the roll during this expansion, the scratch resulting from the relative movement between the web and the roll will be orientated at an angle to the direction of travel with the end pointing towards the centre of the film.

As stated above, both MD and TD thermal contraction effects are friction moderated, meaning that the higher the coefficient of friction between the film and the roll, the shorter the region of relative movement at the end of the web contact with a given roller. Before this “slip” region, film will be effectively “stuck” to the rolls and the thermal contraction and expansion effects will cause an increase in internal stress of the film, changes of which will be released when the film leaves the roll with a therefore reduced risk of defect formation.

6.5.4 STRESS RELAXATION

Stress relaxation is a phenomenon seen with viscoelastic materials (such as PET). When the material is held at a specific temperature under constant strain/dimension, there is an observable decrease in stress over time. The timescales involved are shorter at higher temperatures. Stress relaxation is often talked about in conjunction with creep, but they are very much two sides of the same coin, related, but distinct. Creep is the dimensional increase seen over time if a viscoelastic material/polymer is held at a constant tension at a specific temperature. Here, the timescales decrease with temperature. Both stress relaxation and creep occur as molecules move to a more relaxed (lower energy) state.

This effect comes into play on the film production line, depending upon how the web tension is controlled. Throughout the FWD, the web will be at a high MD stress as this is needed for the web to draw. In a typical FWD, the rolls in between the slow and fast nips are all idling rolls. Therefore, the tension before and after each roll must be the same (neglecting bearing friction). During the main part of the web wrap on a roller the film is held by friction in contact with the roll and hence the web is held to a “fixed dimension”. Over the course of its travel on the roller, the web will experience stress relaxation, which will result in a decrease in tension in the web.

However, when the web leaves the roll, the tension needs to equal the pre-roll tension, and therefore the loss in tension from stress relaxation must be reversed. Therefore (as for thermal effects), in the final part of the web wrap on the roll, there is a region of slip where the web speeds up very slightly to regain the lost tension. In a higher friction scenario, this region of slip will be shorter and relative movement will be less. Indeed, in a theoretical infinite friction case, only as film leaves the roll would the tension be restored, and the film would speed up to restore the tension in an infinitely short period of time with zero slip. This case is impossible in reality. In the region of slip, the film leaving the roll will speed up and will be moving slightly faster than the idling roll. This will result in relative movement between the film and the roller and is therefore a possible source of defect formation.

The time dependence of this decrease in tension around the roller wrap is dictated by the mobility of the polymer chains. Therefore, a hotter film will have experienced a larger decrease in tension over the same wrap angle than a cooler one.

For thinner films with the majority of cooling on the first cooling roll, relative movement due to stress relaxation will also be predominantly on the first cooling roll. The longer the web

remains hot, the greater the degree of stress relaxation. This is another reason (as for post draw) why a good quench on cooling rolls is critical.

Figure 81 below shown how tension in the film changes with distance across an idling cooling roll for both an isothermal case, and a case where the film is quenched.

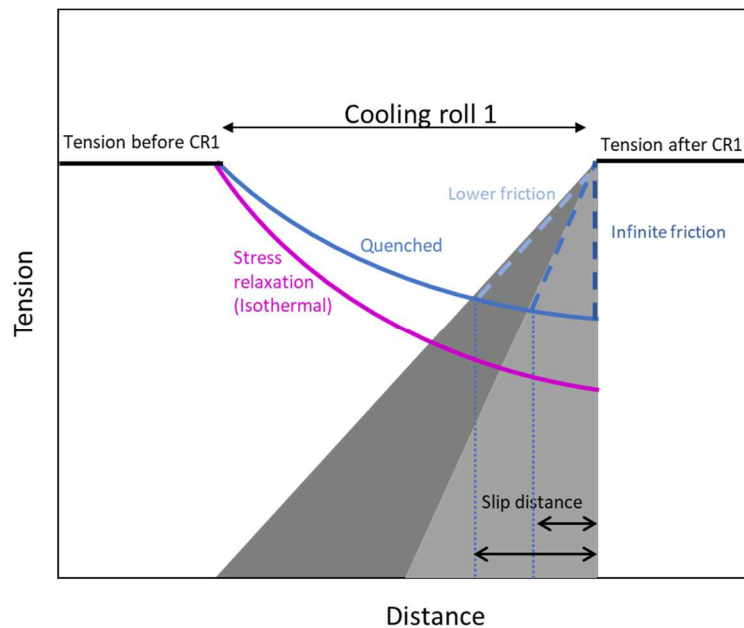


Figure 81: Diagram showing how tension changes against distance for an idling cooling roll.

Extensive in-house experiments and modelling have derived some proprietary equations for the relationship between temperature, film thickness, tension, friction, polymer properties, and movement due to stress relaxation. These can then be correlated with scratch length to make predictions about how changing processing conditions can affect scratch length.

A notable internal model for this is an internal heat transfer model termed THOR (Transfer Of Heat on Rolls) which can estimate web temperature through a FWD machine, but also has an approximate means of quantifying the relative movement associated with stress relaxation. For example, for the case of a 125 μm thickness film being produced on D52 it predicts MD scratch lengths of the order of around 100 microns could be seen, with an increase predicted

for reduced coefficients of friction. This represents the scratch length at creation, not the final length after subsequent transverse direction stretching in the stenter. The model is only simple and does not account for thermal expansion/contraction effects or TD relative movement, and therefore does not predict the orientation of a scratch. It is nevertheless a useful order of magnitude guide for these effects.

Since the MD relative movement originates from tension equalisation following MD stress changes such as stress relaxation on a roll, then a reduction in this tension change would reduce relative movement. One way to do this would be to add a drive to the roller such that the web tension after the roller would not have to be the same as that before it. The tension following the roller could then be modified to reduce the tension change needed. In the case of stress relaxation, a slight reduction in the post roller web tension would mean less slip and shorter scratches.

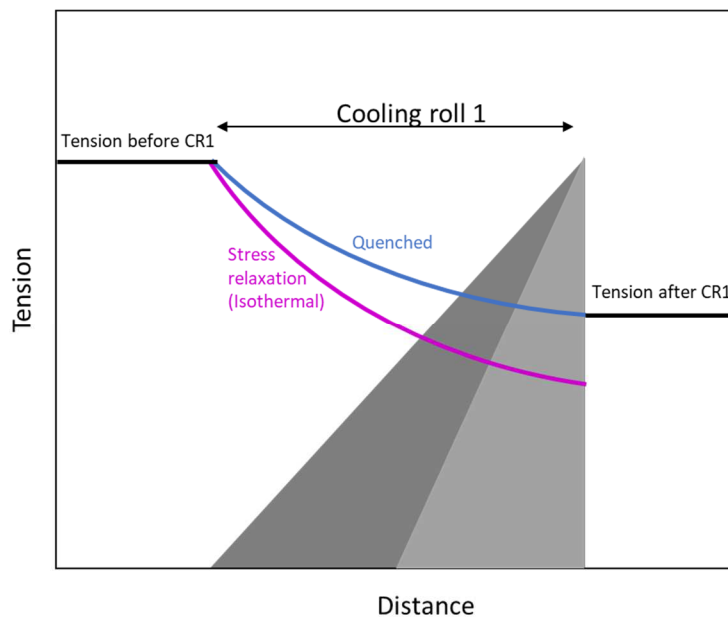


Figure 82: Diagram showing how tension changes against distance for a driven cooling roll

The effect of this is shown schematically in Figure 82. In this case the torque applied to the driven roller is set so that the post web tension matches the reduced web tension from stress

relaxation and other effects. This means that there is no change in speed as the film leaves the roll, and no slip. Figure 82 also illustrates how an improved quench (cooling rate) on the cooling roll results in less stress relaxation and hence less tension drop.

As with thermal expansion/contraction, stress relaxation is friction moderated, with the higher the friction between the film and the rollers, the closer to the theoretical infinite friction case.

6.6 SCRATCH ORIENTATION

The above discussion of the origins of relative movement have talked extensively about the axes in which these effects take place. However, it is worth mentioning in more detail at this stage the convolution of scratch orientation by the BoPET production process.

Scratches are analysed after film is finished being processed (finished film, FF). The orientation and form of scratches between when they form and when they are analysed is not necessarily easy to understand. Scratches that form after the stretching process is completed, on the transport rolls or during winding, will undergo no changes between formation and analysis. Scratches that form on the cooling rolls of the forward draw will undergo subsequent stretching in the sideways direction during the second drawing, so will change between formation and analysis. Finally, scratches formed prior to the first draw e.g.,

on the preheat rolls, will undergo a stretch in both the forwards and sideways direction between formation and analysis.

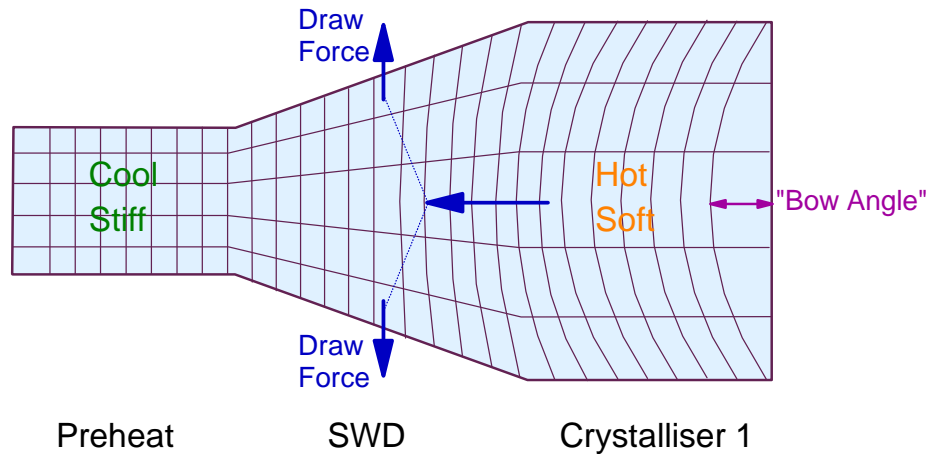


Figure 83: Diagram of film web as it travels through the stenter

Additionally, the sideways stretch will not occur equally in all locations due to bowing effects. Bowing effects originate from TD forces also causing MD forces, which pull the hot, soft film in the crystalliser back towards the sideways draw as shown in Figure 83. The MD forces are due to Poisson ratio effects.

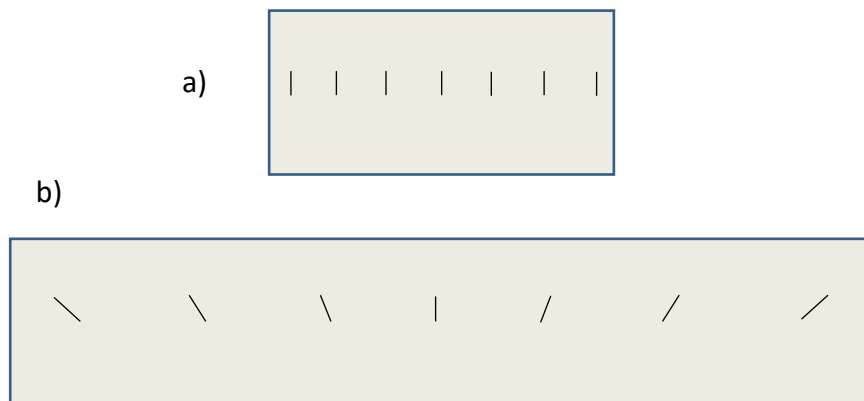


Figure 84: a) Film as it enters the stenter with scratches across the web aligned in the MD. b) The same film after exit from the stenter after undergoing sideways draw and the resulting angle of the original scratches

The edges of the film therefore stretch more than the middle meaning scratches towards the film edges will change orientation more than those in the centre of the web.

Take for example a film which enters the stenter with scratches across the full width all aligned perfectly with the MD, shown in Figure 84a; after the sideways draw in the stenter, the scratches will be aligned as shown in Figure 84b. This makes deconvoluting the exact origin of scratches challenging as the orientation may be caused by the relative movement itself or by down-line stretching alterations. If the contamination of interest is indeed promoting scratch formation by increasing relative movement, it is likely that this is derived from the contamination changing the frictional properties of the rollers.

6.7 SUITABILITY OF ROLLER DESIGN.

The rollers in the forward draw are designed to optimise the friction between the film and the roller such that the relative movement effects described above are minimised, and the film will remain “stuck” to the roll for as long as possible during its time in contact with this roller. In addition to this the rollers need to be made from material that has high durability and excellent thermal conductivity to allow the heating and cooling that occur in the preheat and cooling zones to be effective. In particular the importance of a good quench has already been mentioned.

The desire to increase friction to minimise relative movement would favour a roller surface with a higher roughness. However, this is mediated by the fact that a higher roughness would result in imprint defects. This is where, especially when the film is above glass transition, the film would be effectively “stamped” by the rollers and the roughness imprinted into them, therefore limiting the minimum surface roughness the end product film could achieve and resulting in hazy or damaged films.

As such there is a delicate balance to strike in optimising the roughness such that the lay down of the film to the roll occurs with as little relative movement as possible but without leaving

an impression. The predicted optimum range for surface roughness has been determined through experience over many decades to a value that strikes the right balance but is orders of magnitude larger than the film roughness.

Therefore, cooling rolls have a precisely defined roughness that needs to be achieved during manufacture. The rollers are made of chrome oxide which is covered by an epoxy coating. This coating is etched until it is the desired roughness, typically the rollers are delivered slightly rougher than ideal, as Figure 85 shows.

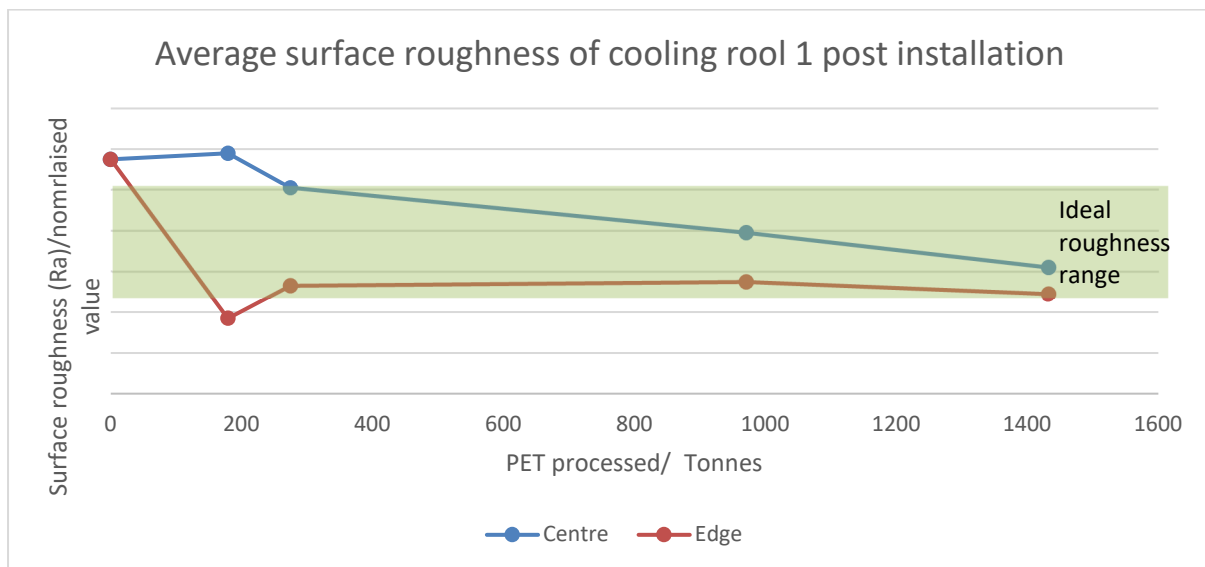


Figure 85: Graph of average surface roughness in micrometers of cooling roll 1 measured via line profile vs tonnes of PET processed from installation onwards.

The study above shows that the roller roughness decreases over time during the lifetime of their use on the production line. This is due to abrasion by the film web, and also may be contributed to by the automatic cleaners as the finding in Chapter 4 was that they were collecting chrome over time implying they could be abrading away the roller surface. As such the typical lifetime of a cooling roller is around 1 – 2 years of full-time use.

Taking it to be true that the designed roller roughness is the optimum to achieve minimal relative movement in their “clean” state, it can be hypothesised that the contamination is providing an effective “smoothing” to the rollers and altering their surface roughness. In order to prove this, in-line measurements of the rollers in their clean and contaminated state needed to be made.

6.8 CHALLENGES OF IN-LINE MEASUREMENTS

One of the main challenges of understanding the impact of contamination on roller-film dynamics is the challenge of making reliable in-line measurements. Many of the techniques that would ideally be selected (AFM, SEM, Raman, coherence scanning interferometry) to measure the roller roughness in-line cannot be done, partly because the rollers are not very easy to access but also because of the curvature of the rollers, the speed of rotation, and the temperature of the mobile surfaces.

Much of the understanding of in-line surface roughness in-house has historically been achieved via line profile measurements which are limited in their validity. Line profile measurements use a microneedle to take a single 2D trace of the roller surface along a single line. While useful for large dramatic changes, for the scale of change discussed here – that is – the impact of a few micro-grams of degradation products, they are far less useful. Assuming you were able to take a profile along the exact same line twice, one might get an indication of a change in surface roughness, however this is impossible to achieve in reality.

6.9 IN-LINE MEASUREMENTS OF SURFACE ROUGHNESS

In order to overcome the drawbacks of profile measurements, measurement of rollers in-line were made using replication tapes. Their validity was first tested on known surfaces before clean and dirty rollers were measured and compared.

6.9.1 VALIDITY OF REPLICATION TAPES

Measurements were made using imprint tapes provided from Testex Tapes International. All of the tapes consist of 2 layers – a 2 mm of clear mylar coated with different thicknesses of Press-O-Film foam. The foam conforms to a test surface to make a replica. The tape used was medium/fine grade which has a 2 mm layer of Mylar and a 0.5 mm layer of foam and is graded to replicate features of 0.1 μm to 2 μm . In order to test their validity, these tapes were first used to replicate surfaces of known surface topography and measurement. Two surfaces with known roughness were sampled.

One was a sample of roller and the other a sample of Melinex 383. These surfaces were replicated using the tapes and the result measured using coherence scanning interferometry and the results compared to the “true” surface. The results are displayed in Figure 86 and 87.

5.8.1.1 REPLICATION OF ROLLER SURFACE

Qualitatively, the roller sample replication is not perfect, as the “true” surface contains far greater micro-texture than the imprint was able to capture.

If the measured Sa value of the true surface is 1, the replicated surface was found to have a normalised value of 0.851, so quantitatively the surfaces are reasonably similar. This is because the largest contributions to the surface average roughness term are the largest valleys and peaks which are replicated well by the tape.

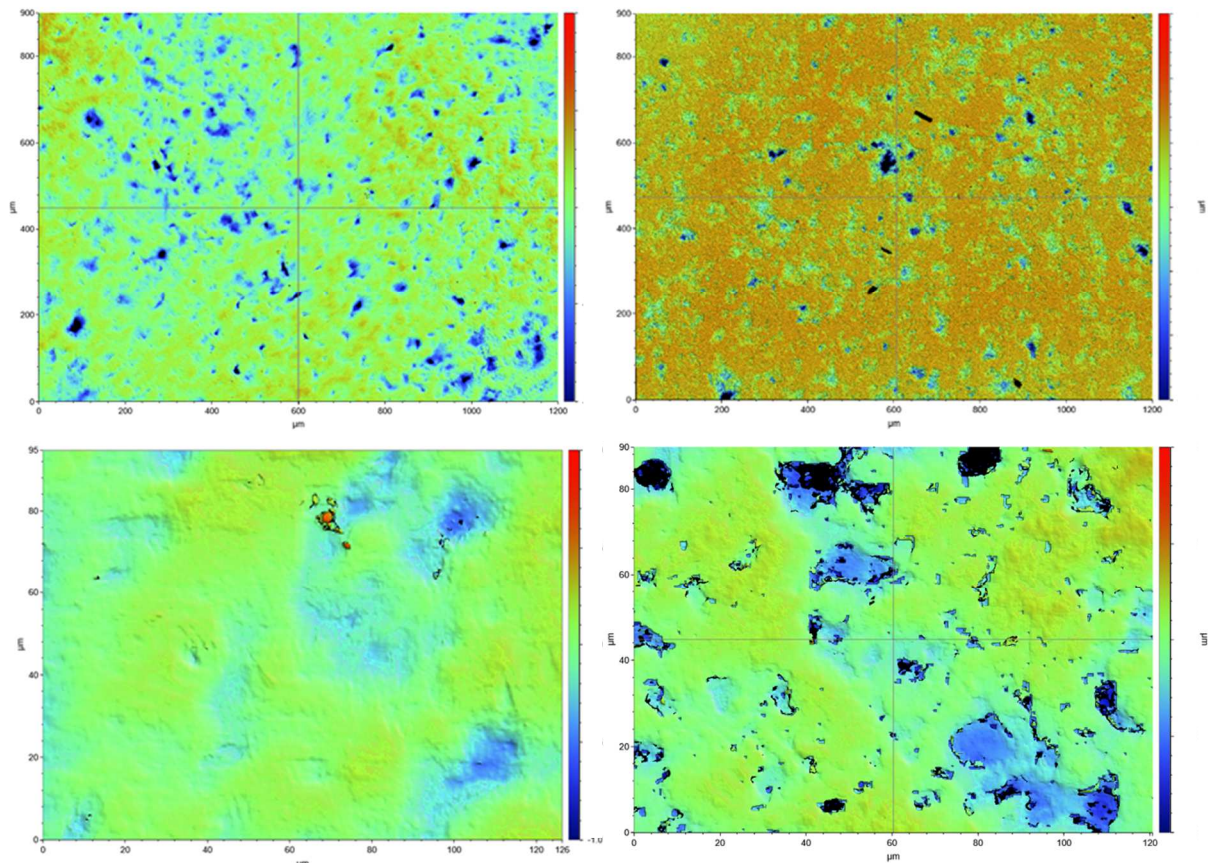


Figure 86: Comparison of true and replicated surfaces of roller surface. Top Left: Replicated surface at large field of view. Bottom Left: Replicated surface at small field of view. Top right: Real surface at large field of view. Bottom right: Real surface at small field of view.

5.8.1.2. REPLICATION OF MELINEX 383 SURFACE

The replication of the Melinex 383 surface is qualitatively good, showing a clear imprint of the expected filler particles distributed evenly across the surface.

In particular, the images at a smaller field of view show an excellent surface replication. The S_a value for the true surface is 107 nm and the replicated surface had a value of S_a of 106 nm showing a good quantitative correlation also.

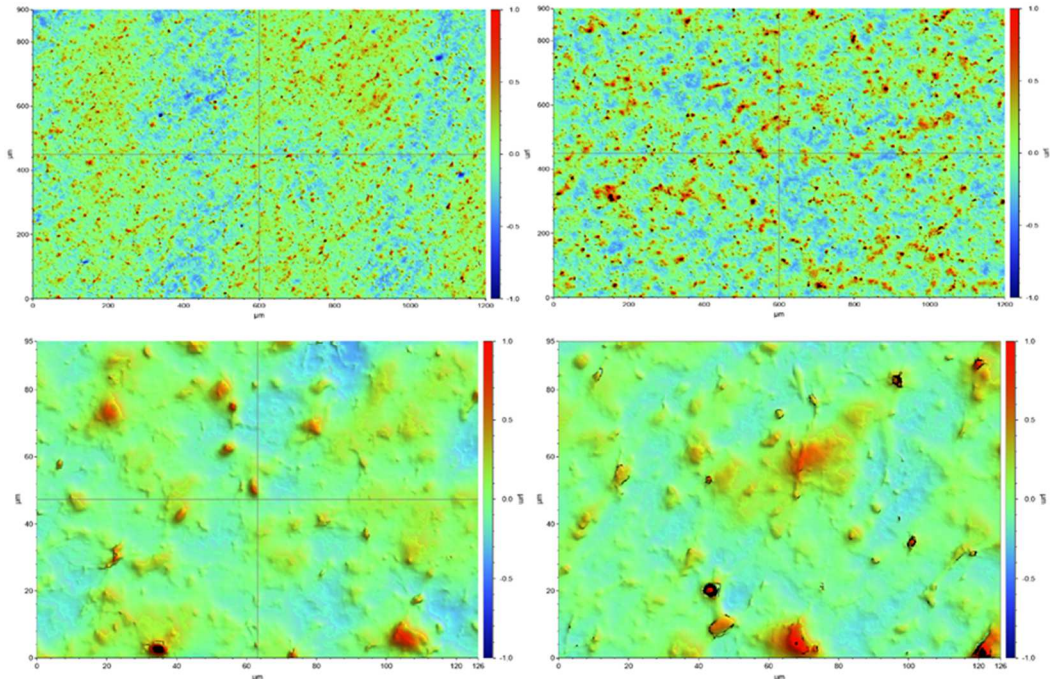


Figure 87: Comparison of real and replicated surfaces of Melinex 383. Top left: Replicated surface at large field of view. Bottom left: Replicated surface at small field of view. Top right: Real surface at large field of view. Bottom right: Real surface at small field of view.

6.9.2 REPLICA TAPES ON THE PRODUCTION LINE

Having established that the replica tapes were producing reasonably valid replications of the surface, they were used to make replicas of cooling roll 1 at three positions across the web from feed edge to blank edge. This was done once at a full line stop after the line had been running continuously on clear PET film production for 4 days, and once again immediately after a full clean. Measurements were taken at the feed edge, centre and blank edge of the roller and 5 repeats of each measurement was made. The graphs below show the average surface skewness, average surface roughness, and average surface pit depth which quantitatively help elucidate the findings of the replication tapes.

S_{sk} or average surface skew gives an indication of the distribution of deviations from the mean plane across the whole surface. A graph of the values is shown in Figure 88. An S_{sk} equal to zero would indicate a surface which has an entirely symmetrical distribution of deviations from the surface. A negative number indicates a skew below the mean plane, and a positive number a skew towards features above the mean plane. In the graph both the clean and dirty surfaces show a negative skew, indicating the surfaces are dominated by valleys. However, the clean surface shows a more symmetrical distribution than the dirty surface indicating the dirty surface is *more* dominated by valleys.

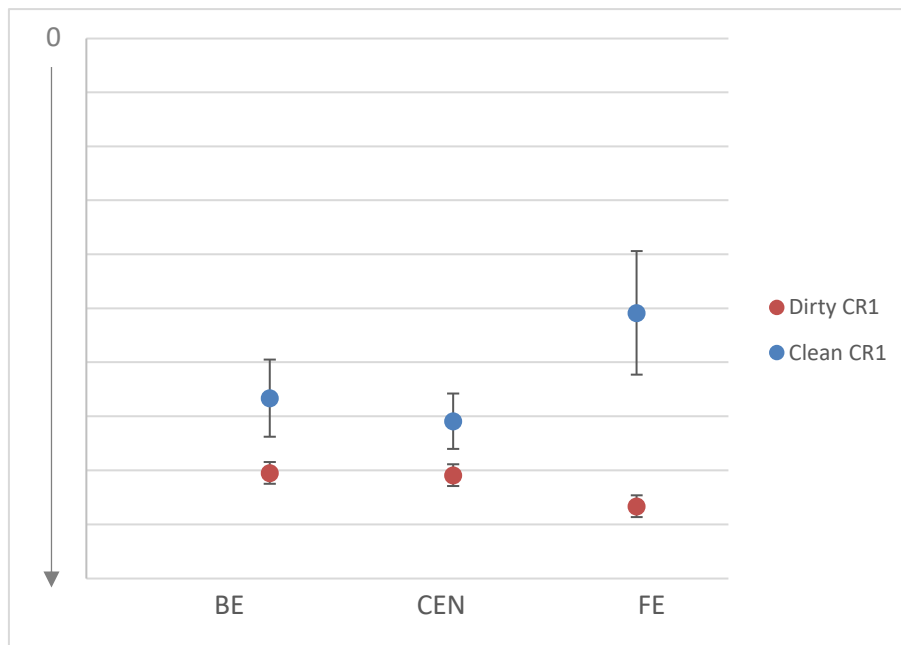


Figure 88: Graph of the S_{sk} values as measured by CSI of CR1 replica tapes taken when line was dirty and clean. Z-axis scale has been removed for proprietary reasons.

The average valley depth, (S_v) of the surface gives the average depth of any valley on the surface. Figure 89 shows that average valley depth decreases when the surface is dirty.

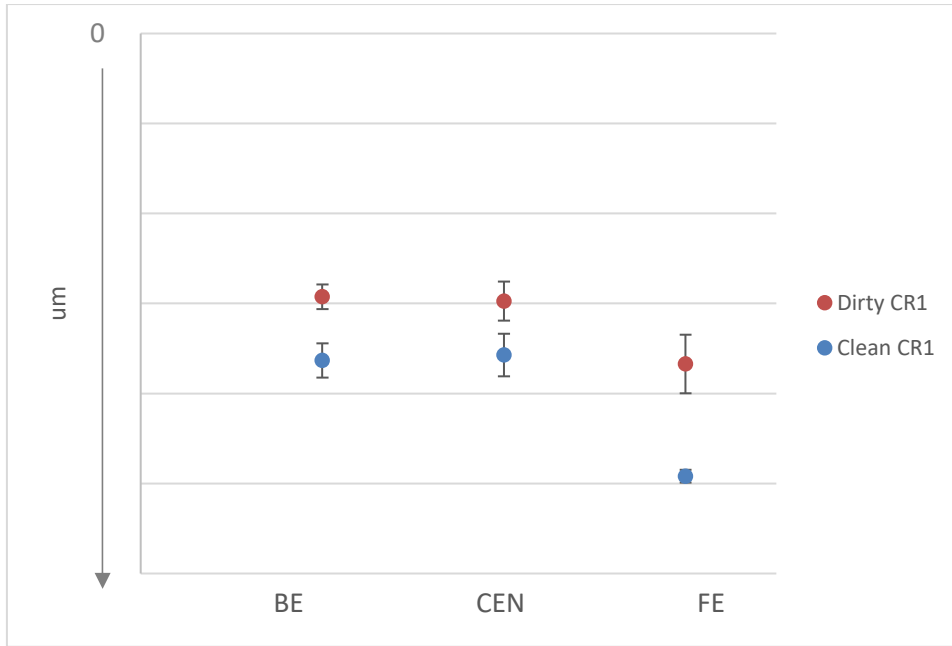


Figure 89: Graph of S_v values measured by CSI of CR1 replica tapes taken when the line was dirty and clean.

Z-axis scale has been removed for proprietary reasons

These two factors can be understood best in combination. Imagining a surface with a perfectly symmetrical distribution of peaks and valleys (shown schematically in Figure 90) the average plane will be directly in the middle. If half of the valleys decrease in depth, then the average plane will move “upwards”. This results in the same number of peaks, but at a lower height, and the same number of valleys, but with some deeper and some shallower than before. Therefore, it follows that the distribution of the height features is more skewed below the mean plane.

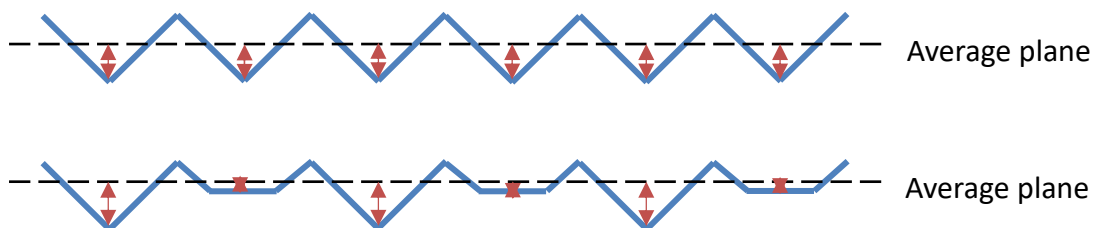


Figure 90: Schematic of an idealised surface versus a surface where half the valleys are halved in depth and how the average plane and average valley depth changes.

Finally, the average surface roughness is a term which expresses, as an absolute value, the difference in height of each point compared to the arithmetical mean of the surface, across the entire field of view. The result is shown in Figure 91. The graph below shows that Sa decreases when the surface is dirty, with the effect being more pronounced at the roll edges.

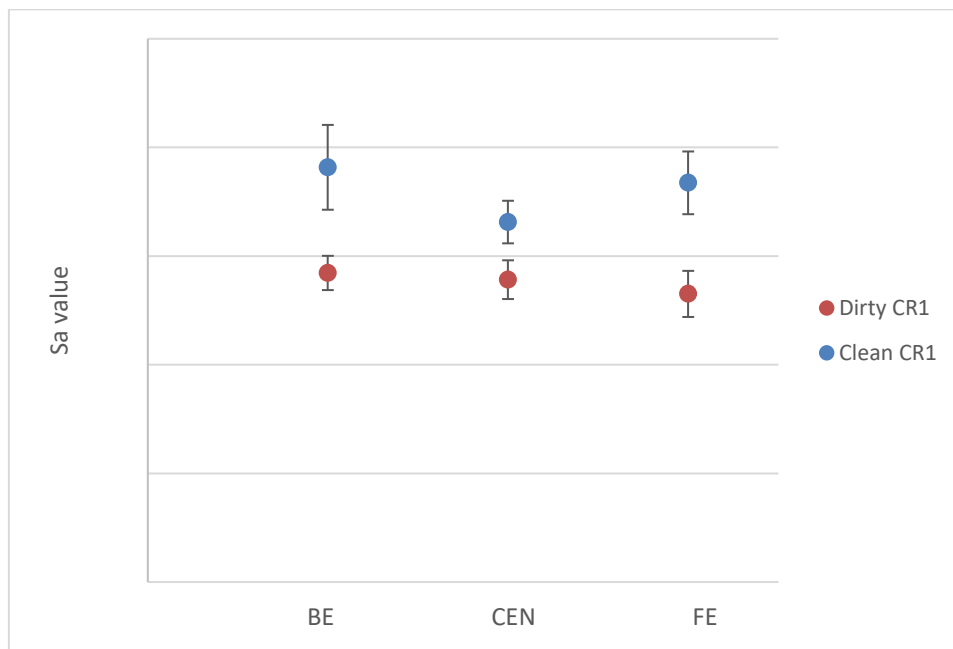


Figure 91: Graph of Sa values measured by CSI of CR1 replica tapes taken when the line was dirty and clean.

Z-axis scale has been removed for proprietary reasons

This shows clearly that the dirty rolls have a smoother surface overall than the clean rolls. It can be concluded therefore that over the course of the production, the valleys of the rollers intrinsic roughness are being gradually filled in, causing the effective smoothing of the rollers.

6.10 LABORATORY MODEL FOR SURFACE ROUGHNESS

6.10.1 EXPERIMENTAL SET-UP

Having established via in line measurements with the replication tapes that surfaces are experiencing an effective smoothing over time as the micro-roughness is filled in with

contamination, it would be useful to recreate this in the lab so measurements can be made that are not possible in-line.

This contamination was found in the previous chapter to be majority organic, and Raman analysis implied it to be mostly derivatives of PET degradation.

In order to be able to measure the frictional properties of the surface in both the “clean” and “dirty” state, a laboratory model of a *pseudo* dirty roller was needed. To obtain frictional measurements, the pseudo dirty roller should match the in-line rollers in construction and should be “dirtied” with contamination similar in composition to that found on the line.

A rig was created to capture the volatiles from molten PET degradation – in line with the findings from Chapter 4. First a sample of roller was cleaned with Silvo in a method identical to the manner in which the rolls are cleaned on the line.

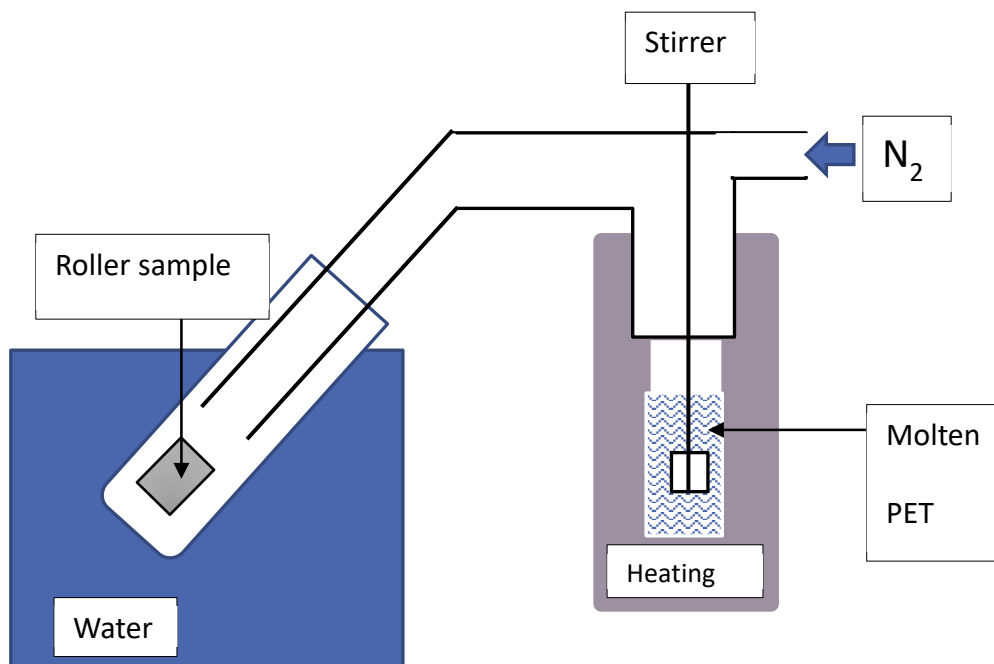


Figure 92: Schematic illustration of laboratory rig for generating contamination on roller sample.

The roller sample was then placed inside the rig, which is displayed schematically in Figure 92. PET base chip is heated to 280°C inside a sealed glass tube while being continuously stirred. A side arm tube connected to a glass sample tube is held in a cooled water bath. The roller sample is positioned in this glass tube held such that the volatiles flowing from molten PET condense on the cooled roller. A flow of continuous air is pushed through the tubes to encourage the volatiles to progress along the side arm of the glassware. The rig is left for 6 – 8 hours to allow PET degradation to proceed before the sample is removed. After this the sample is rubbed with PET film for 10-15 minutes to simulate the contact of PET film during production. This yields a roller sample which is designed to mimic the roller in the forward draw where contamination is compressed into the microroughness by the motion of the film on the roller. Hereafter it is referred to as pseudo-dirty roller.

6.4.1 RAMAN ANALYSIS OF LABORATORY MODEL

In order to confirm that the lab rig had produced contamination which is similar in composition to that found on the line, a sample of clean and dirty roller were submitted for Raman analysis. The dirty sample was analysed in two locations and compared to the Raman analysis of the casting drum contamination previously shown in Section 4.3.1.4. The results are shown in Figure 93 with the blue line showing the trace of the contamination collected from the casting drum and the red and orange traces being two measurements of the contaminated roller at different locations.

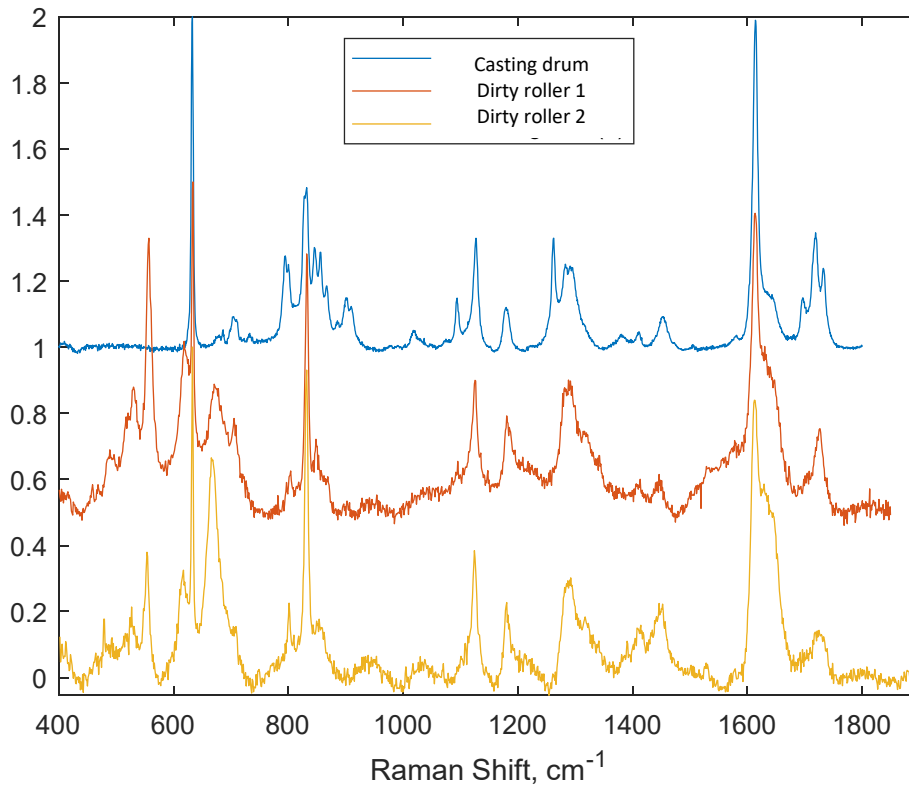


Figure 93: Raman spectra of pseudo dirty roller compared to casting drum sample.

Comparison of the traces finds good agreement between many of the characteristic peaks of the casting drum contamination and the lab-dirtied roller. The roller sample contains far more noise than the casting drum sample – this is likely a substrate effect of the roller sample scattering and reflecting the Raman incident beam. Scattering in this manner will also be responsible for the effective broadening of the characteristic peaks in the roller spectra. The most notable differences are two peaks in the fingerprint region at $\sim 575\text{ cm}^{-1}$ and $\sim 640\text{ cm}^{-1}$. The two peaks are of different intensities for the two different spectra, implying they may derive from the underlying substrate with their intensity being affected by the thickness of the deposited layer of contamination at the particular location that has been measured.

In order to confirm this, a sample of the clean roller was analysed (Figure 94) and compared to the dirty spectra. This same characteristic peaks at $\sim 575\text{ cm}^{-1}$ and $\sim 640\text{ cm}^{-1}$ can be clearly seen in the clean roller, confirming that this is the origin. These are energies typical of aliphatic carbons and so likely derives from the rollers' epoxy coating.

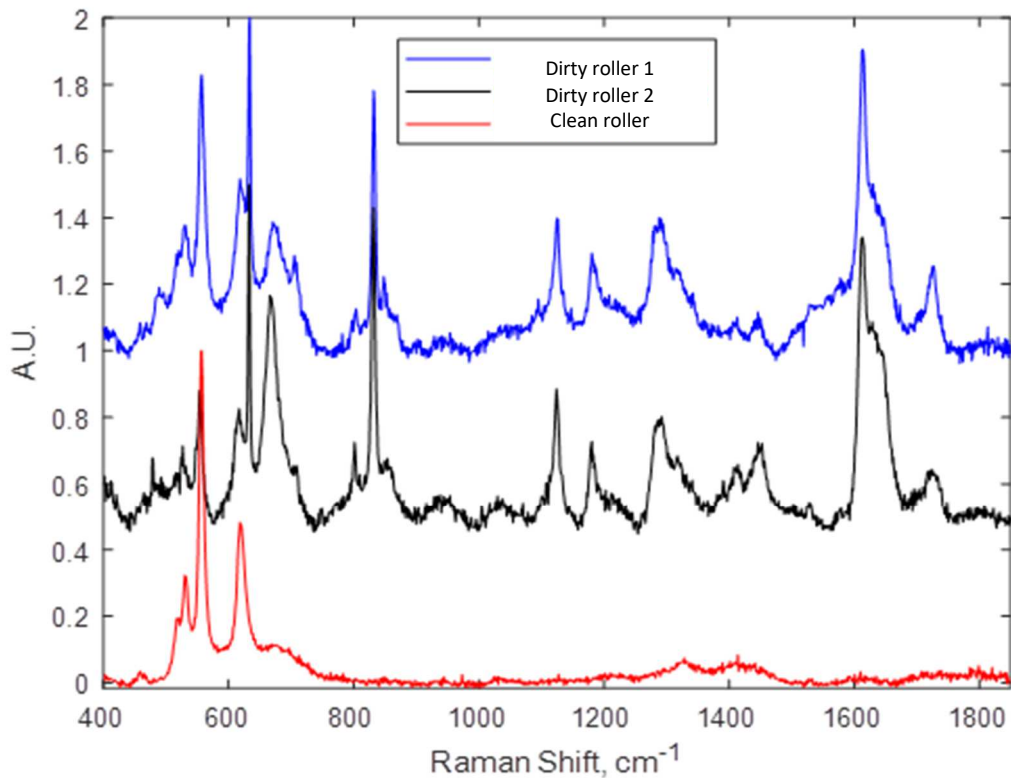


Figure 94: Raman spectra of pseudo dirty roller sample compared to a clean roller.

6.4.2 COHERENCE SCANNING INTERFEROMETRY ANALYSIS OF LABORATORY MODEL

Having confirmed the contamination laid down was of the expected contaminant composition, the roller surfaces before and after contamination were analysed using CSI. In order to make the comparison as useful as possible, the same location was imaged for the freshly dirtied sample, the same sample following abrasion with PET and the sample after cleaning thoroughly with Silvo and ammonium hydroxide. The results can be seen in Figure 95.

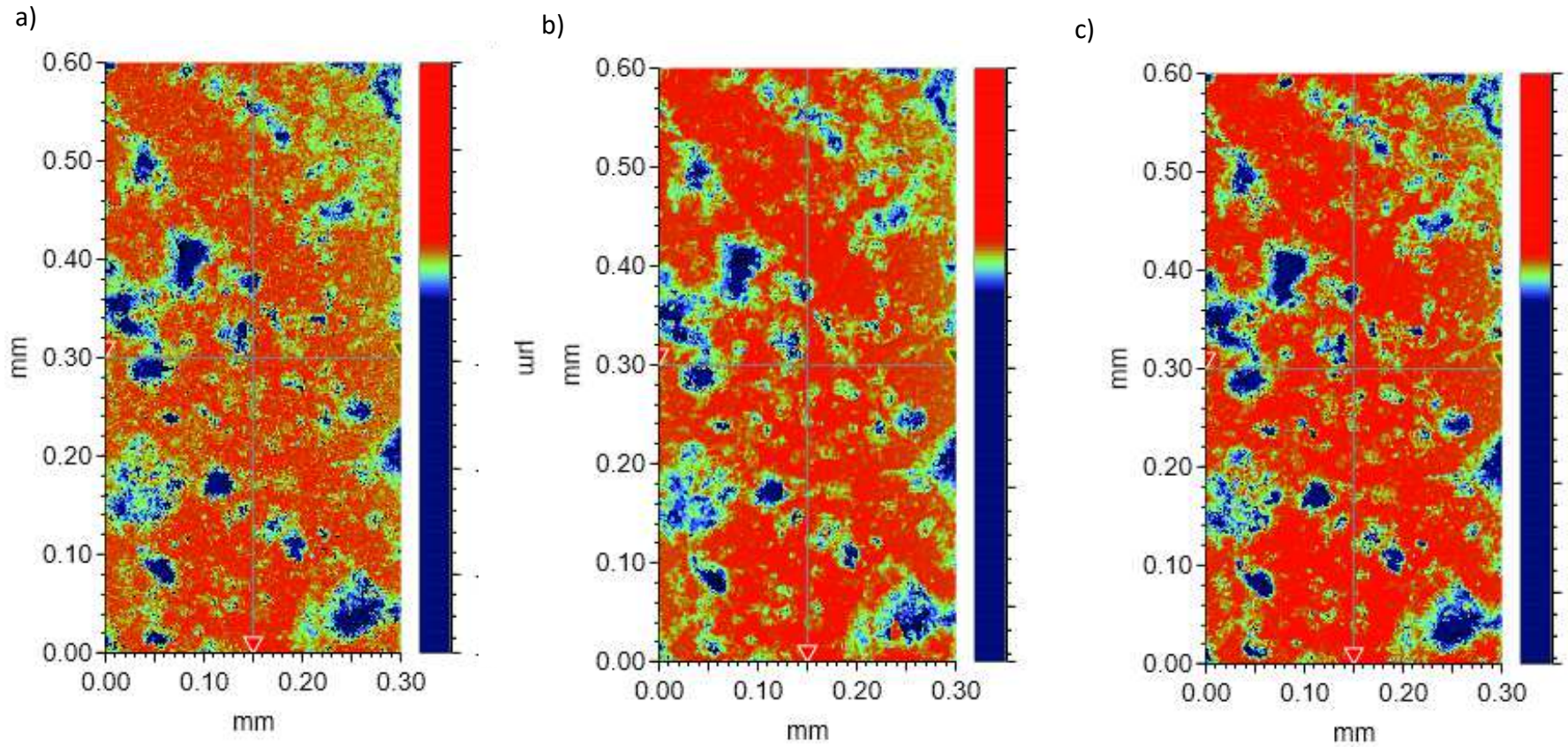


Figure 95: Images of roller surface in 3 different states imaged using CSI. a) Roller sample dirtied by exposure to molten PET vapours for 6 hours. b) Sample after subsequent rubbing with PET film (Pseudo dirty). c) Sample after cleaning with Silvo and ammonia hydroxide. Numerical z-scale has been omitted for proprietary reasons

A qualitative look at the images shows the same area of the surface undergoing subtle changes. The contaminated sample which had not been altered (a) is characterised by the valleys typical of the roller surface, but with additional small-scale peaks which are presumably accumulations of the degradation components. Comparing this with the pseudo dirty roller (b) there is an absence of the small-scale peaks, and the surface is characterised by an average plane with relatively few peaks and large number of valleys. Finally, comparison to the fully cleaned sample shows the same overall characteristic surface as the pseudo-dirty sample but the valleys appear on average slightly larger and deeper. This difference between the pseudo-dirty and clean sample is also reflected in the quantitative analysis of the surface shown in Table 14.

Roughness parameter	Pseudo-dirty	Cleaned
S_a (um)	0.874	1
S_v (um)	-31.2	-32.9

Table 14: Summary of surface roughness parameters of pseudo dirty and cleaned roller samples measured by CSI (relative to S_a value of cleaned roller).

From these data it can be seen that the average surface roughness (S_a) is lower for the “rubbed” sample than for the cleaned sample – mirroring the findings of the replica tapes, that the surface is smoothed by contamination. It is also seen that the average peak depth for the clean sample is larger than for the dirty – suggesting full cleaning removes hard-to-remove contamination from the depths of valleys. This laboratory model of the roller surface appears to show the same approximate surface roughness characteristics as the in-line measurements, implying it is a good model to take forward into friction measurements.

6.11 FRICTION MEASUREMENTS OF ROLLER SURFACES

As discussed in Section 6.5 of this chapter, the majority of relative movement which can occur in the forward draw is friction mediated. It is therefore prudent to measure the rollers in their clean and dirty state to see if the change in surface roughness or chemical composition of the surface (and hence surface energy) is having a noticeable effect on coefficient of friction.

In-line measurements of friction, which are relatively crude and at length scales of centimetres, are not sensitive enough to detect a difference as subtle as has been shown in the surface analysis so far. Friction will be measured in two ways, at two different scales. First via lateral force microscopy at length scales around 10 μm , and using friction rig at length scales of around 10 mm.

6.11.1 FORCE BOARD FRICTION MEASUREMENTS

Force board measurements were conducted in the University of Birmingham by Katlego Balemoge. The friction rig required a modification before use for this project.

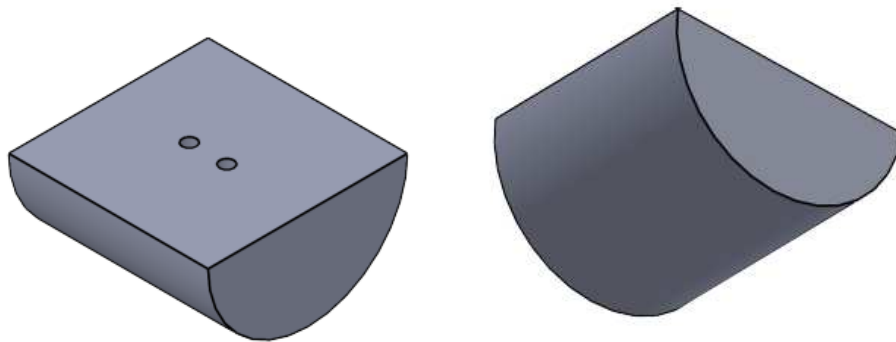


Figure 96: CAD design for component for force board friction measurements to allow intimate contact between PET film and roller surface.

Using computer aided design (CAD) a new component piece was designed (Figure 96) which could be used within the device to allow friction to be measured between a sheet of PET film and the roller surface. PET finished film was wrapped around the curved side of the

component and fixed in place at the corners. The piece was then screwed to the force board arm which applied the tangential motion between the film and the roller surface, which was fixed to the lab bench below the arm. A normal force was applied by placing weights on the arm as shown in Figure 97. The coefficient of friction is expected to be dependent on applied normal force according to Amontons-Coulomb Friction Law.

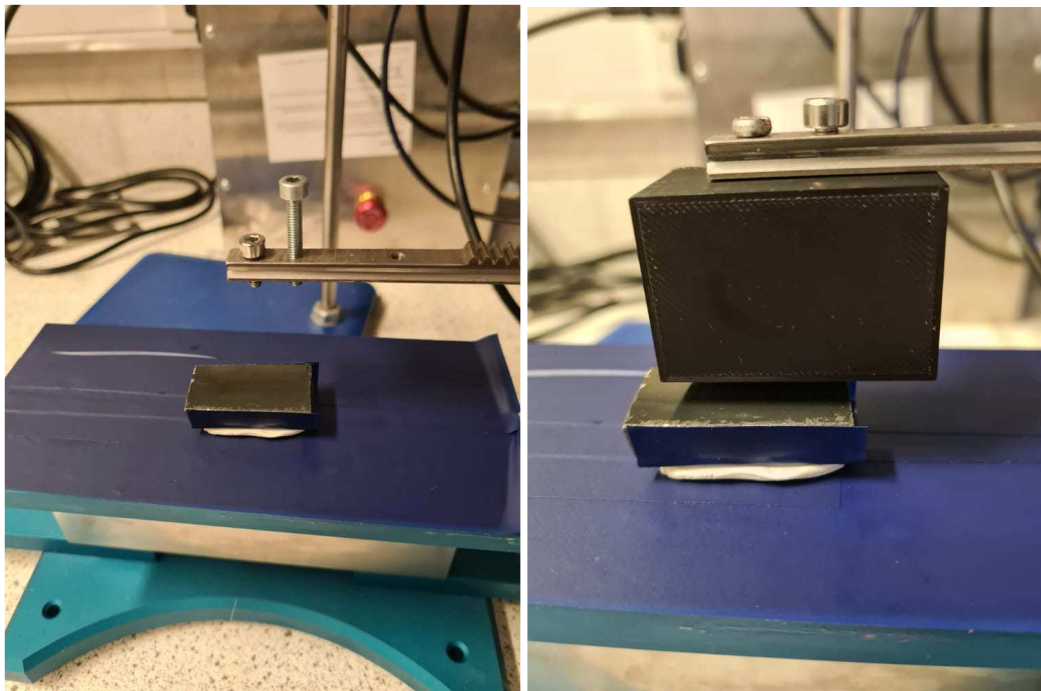


Figure 97: Force board stage. Left: with no attachment on arm and roller sample fixed beneath. Right: with 3D printed head attached (head not from this work and is provided to show an example for clarity).

Measurements of friction were made on a clean roller and a pseudo dirty roller, and the coefficient of friction measured in each case. The results are displayed in Figure 98.

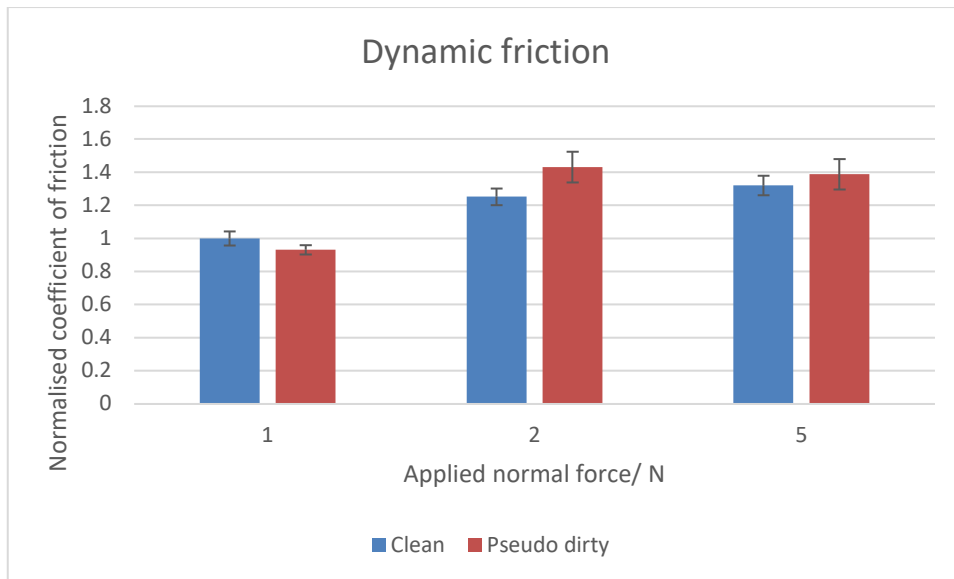


Figure 98: Graph showing average coefficient of dynamic friction from 1000 measurements for a clean and dirty roller as measured by force board during tangential motion. Error bars represent the standard deviation of the data set.

Despite the fact that at this length scale there does not appear to be a statistically significant difference between these samples, these data reveal several interesting results. The first is that the error in the measurement of pseudo dirty roller is larger than the clean sample, indicating a less homogeneous surface in terms of its dynamic behaviour.

A closer examination of the pseudo dirty data (Figure 99) in fact shows a bimodal distribution of coefficient of friction values, indicating there are areas on the surface of higher and lower dynamic friction.

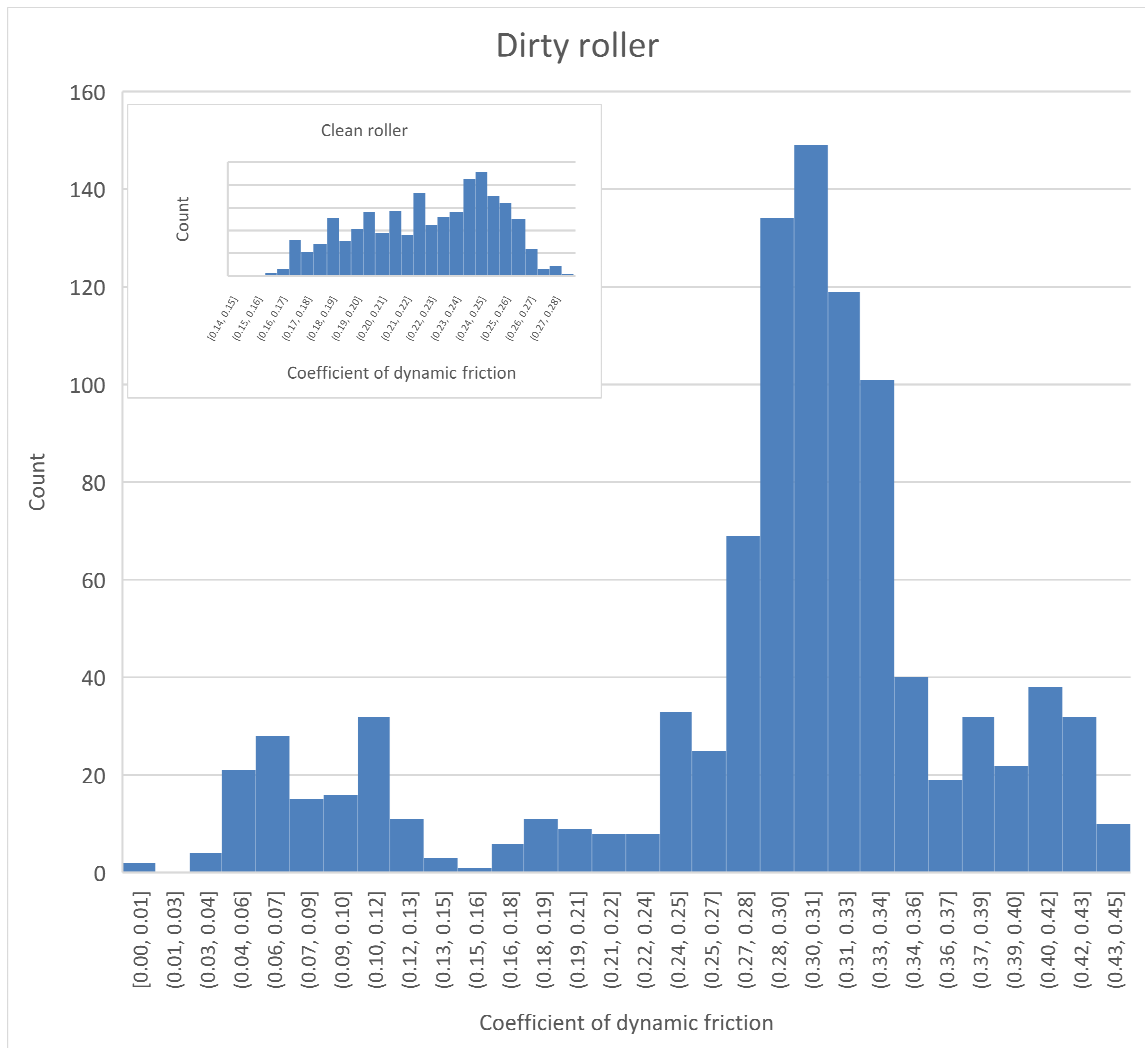


Figure 99: Histogram of coefficient of friction for pseudo dirty roller surface measured at 2 N applied force.

Inset: Histogram of coefficient of friction for clean roller surface measured at 2 N applied force

This same distribution is not seen for the clean surface (see inset graph). Plotting the average from each distribution, seen in Figure 99, it can be clearly seen that the two regimes have vastly different dynamic friction coefficients. These are then shown in figure 100. It could be hypothesised that the heterogeneous nature of this surface may result in more stick-slip type behaviour, where movement is arrested by areas of high friction and is able to again initiate in areas of lower friction.

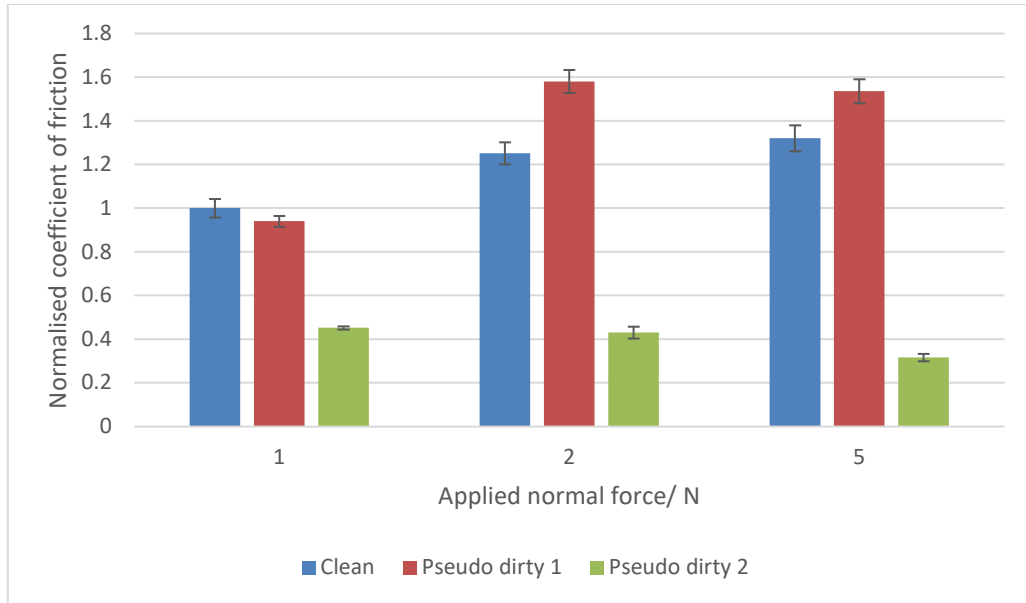


Figure 100: Graph showing average coefficient of dynamic friction for a clean and dirty roller as measured by force board during tangential motion, with dirty results split according to the bimodal distribution of the data. Error bars represent the standard deviation of the data set.

If just the measurements from the first 0.1 seconds of motion in each case are taken, these give an indication of the surface static friction. Results can be seen in Figure 101.

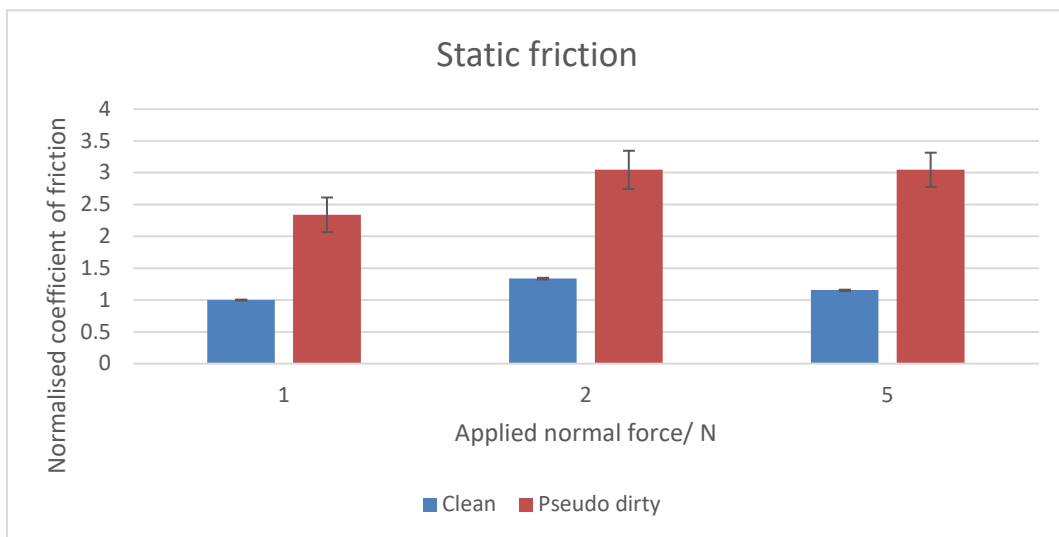


Figure 101: Graph showing average coefficient of static friction for a clean and dirty roller as measured by force board during tangential motion. Error bars represent the standard deviation of the data set.

This shows that while dynamic friction of the overall average surface is unchanged overall by the contamination, static friction increases. While counter intuitive at first, as it might have been expected that sliding would initiate more easily under the hypothesis of surface smoothing by contamination lay-down; this could actually inform why more scratching occurs in contaminated conditions. If there is a higher static friction in a contaminated case, this might mean that the system requires a higher shearing force to initiate movement, this higher shear force is more likely than a lower force to cause plastic (rather than elastic) deformation of the surface during the movement. Contrastingly, while in a “clean” state, relative movement may initiate more easily due to lower static friction but proceed without surface damage.

6.11.2 LATERAL FORCE MICROSCOPY FRICTION MEASUREMENTS

Measuring friction via lateral force mode (LFM) AFM was described in detail in Section 3.4.1. and is a way of using AFM to measure the dynamic frictional force independent of surface topography at a scale of nm – μm . Frictional force was measured on a clean and pseudo dirty roller. The results are shown in Figure 102.

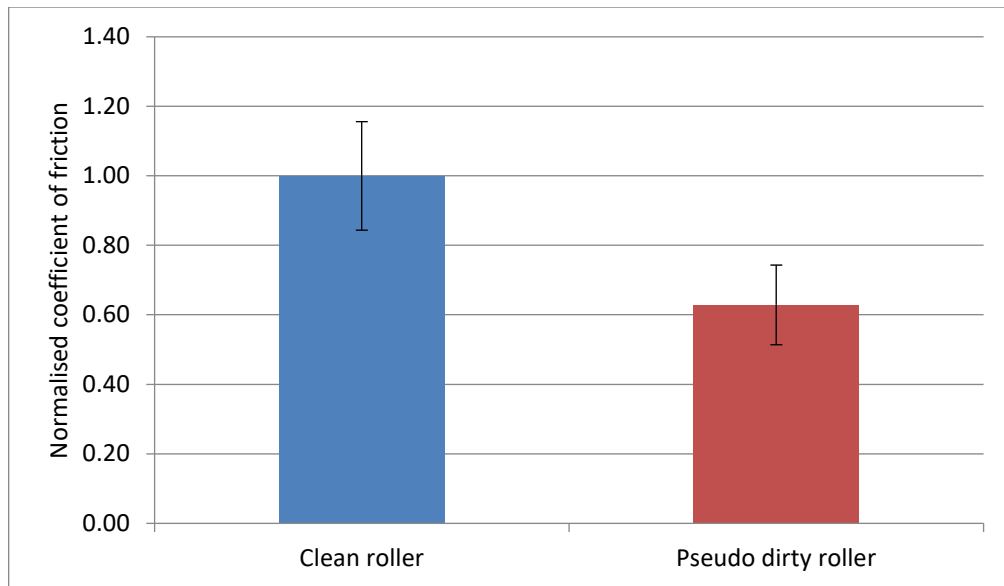


Figure 102: Graph showing average coefficient of dynamic friction for a clean and dirty roller as measured by lateral force microscopy with a 5 μm scan area and 1 Hz scan rate. Error bars represent the standard deviation of the data set.

Coefficient of friction as measured by LFM is lower than measured by force board. This is expected since surface roughness effects are eliminated by the nature of the technique. Results show a lower dynamic coefficient of friction for the pseudo dirty roller as compared to the clean roll. This indicates less resistance to sliding due to a lower surface energy in the contaminated state.

An additional study into the impact of Silvo residue on the rollers was also conducted (shown in Figure 103) and it was found that Silvo residue on a roller surface increased dynamic frictional force of the surface by a small amount.

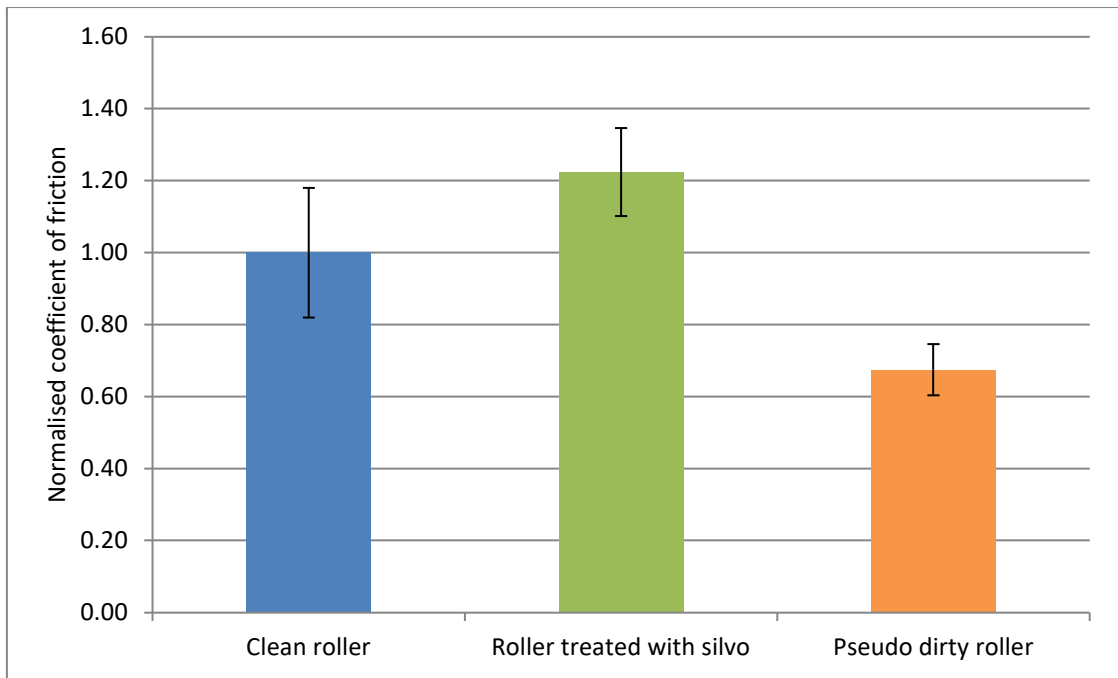


Figure 103: Graph showing average coefficient of dynamic friction for a clean, dirty, and Silvo treated roller as measured by lateral force microscopy with a 5 μm scan area and 1 Hz scan rate. Error bars represent the standard deviation of the data set.

This offers some insight into why Silvo has been found to be a good cleaner for the rollers – not only does it restore surface roughness as seen in Section 6.10 of this chapter – but it also offers a temporary (it is known that the pads gradually remove the Silvo residue (Section 4.4)) increase in dynamic friction coefficient to the rollers, decreasing the likelihood of scratch formation.

6.11.3 CONCLUSIONS OF FRICTIONAL STUDIES

The two selected techniques provide vastly different insights into the frictional impact of contamination on the rollers.

Friction rig measurement offers a macroscopic measurement of friction, both static and dynamic, including effects of surface topography and surface energy, which cannot be deconvoluted. The measurement has been made directly between PET film and a roller

surface. By contrast LFM offers a microscopic measurement of dynamic friction only considering effects of surface energy. The measurement is made between an inert tip and the surface of interest.

Force board data revealed a homogenous frictional surface for the clean roller, and a heterogenous surface for the contaminated one. This heterogenous surface contained regions of very low dynamic friction and very high dynamic friction. Perhaps suggesting areas where contamination has accumulated, such as in surface valleys. Lateral force microscopy saw a decrease in dynamic friction for the pseudo dirty roller compared to the clean one, indicating a decrease in surface energy caused by the presence of contamination.

These two results can be considered complimentary as they both suggest that contamination decreases dynamic friction. Force board reveals this effect is happening in isolated regions across the surface, and LFM reveals it is a surface energy moderated effect as well as potentially a topographical one.

Indications of static friction from friction rig measurements show a higher static friction for the contaminated surface, which means a higher shearing force is required to initiate movement. This higher shear force means that plastic rather than elastic deformation may be favoured for the case of the contaminated roll.

Overall, this leads to a picture where, as the roll becomes dirty, higher shear forces build up before relative movement begins, but once initiated, sliding is favoured compared to the clean case. This overall leads to surfaces which are more prone to forming scratches.

6.12 CONCLUSIONS OF ANALYSIS OF SCRATCH FORMATION AND FRICTION

This chapter has aimed to cover many of the complex aspects of scratch formation during PET film processing in the forward draw. Initially some of the most common scratch types were shown from historical records, with scuffing – that is, small dimension, closely packed scratches, being considered the main issue facing the line today.

Given the small scale of such scratches, a novel method of using a reduced line contact mode on AFM to utilise the tip as a nano-indenter was developed. This allowed certain information about scratching at this scale on PET films to be elucidated. In particular that higher forces result in deeper scratches, but that higher temperatures, lower forces, and flatter starting surfaces all independently result in scratches that show more stick-slip motion, which has been reported to make them more noticeable to the human eye.

Some thought was then given to the sources of the lateral movement needed for scratch formation (relative movement), and the fact that many are friction moderated mentioned in particular. In-line measurements of surface roughness of the rollers to understand how contamination might be changing the frictional properties of the rollers was attempted using replication tapes. Although these were not perfect for the surface, they are considered a big improvement on line-profile measurements of the rollers used previously. Some evidence was found that effective smoothing of the rollers was occurring as they become contaminated.

In order to understand this, and the impact on friction further, a laboratory model for modelling a “pseudo” dirty roller state was developed and tested with Raman analysis and coherence scanning interferometry. A good relationship between the contamination produced in the lab, and the suspected contamination in the forward draw, and the impact

this has on surface roughness was reflected in this model. This model was then used for in-lab measurements of surface roughness via LFM and friction rig.

It was seen that the dirty surface was more heterogeneous in its friction characteristic and had a lower coefficient of dynamic friction. LFM showed that is at least partially due to surface energy effects, rather than being purely topographical. It was also shown that the dirty surface may have a higher coefficient of static friction. Overall, this means that on the dirty surface it is more difficult to instigate movement, and a higher shearing stress will build up, potentially leading to more plastic deformation. Once movement has begun, the sliding is favoured (compared with a clean case), and the resulting scratch will be longer on average. This then goes some way to explain why scratches become more severe as the line becomes more contaminated.

7. CONCLUSIONS AND FUTURE WORK

7.1 CONCLUSIONS

Overall, this work has aimed to explore the ways in which the manufacturing process can affect the surface quality of PET optical films on the DTF D52 unit. This work has drawn on many different disciplines.

In Chapter 4 work began by attempting to analyse the composition of contamination in the forward draw where surface damage has been the most problematic. Contamination in the forward draw was found to be majority organic in nature, dominated by carbon and oxygen, and was shown by Raman analysis to be comparable in composition to the white powder found on the casting drum. The white powder found on the casting drum was found to be comprised of the degradation products of PET, most notably terephthalic acid. Therefore, it is possible that most of the contamination in the forward draw has been transported from the casting drum to the forward draw by the film web. However, analysis of powder on adjacent metal work suggested some may also be generated in situ. The chemical route of this degradation is found to be both thermal and hydrolytic degradation based on the products that were found.

Analysis of the cleaning pads revealed the unsuitability of current cleaning practices. EDX found chrome deposits, meaning the pads are possibly abrading the rollers over time, as well as Silvo residue which is lingering on the forward draw rolls.

In Chapter 6, current scratch examples were described, with small scale (<1 mm) scratches which are densely packed on the film surface – known as scuffing, being the cause of the most down time on the D52 production line.

A microscale method of modelling scratch formation using AFM as an indenter was developed and tested on PET films. It was found that stick-slip motion, which has been noted by previous work internally at DTF to make scratches more visible to the human eye, was more favoured at higher temperatures and lower forces. It was noted that scratches were also more visible on flatter starting surfaces.

Scratches originate from complex relative movement effects in the forward draw which have been modelled and understood by DTF over the decades and have been mitigated as much as possible with processing changes. These effects are all friction moderated so it became crucial for this work to measure friction of the rollers.

One hypothesis was that contamination impacts the friction of the rollers by filling in the microroughness of the roller surface, though this has been challenging to prove in previous studies. Replication tapes, a significant improvement on line-profile measurements, were used to take imprints of the rollers in-line and found some evidence of effective smoothing over time as contamination builds up.

A laboratory model for “dirtying” a roller sample was developed and friction measurements at micro and macro scale were taken. These determined that dirty rollers have a lower dynamic friction than clean rollers, but a higher static friction. The change in dynamic friction was found by LFM to be at least partially surface energy moderated. Measurements also found a more heterogenous friction characteristic to the dirty rollers compared to the clean at a macro scale.

This indicates that the presence of debris on the rollers, may not only be having an impact on topographically induced friction, but also on surface energy induced friction. In combination,

the increase in static but decrease in dynamic friction mean scratches forming on dirty rollers will initiate at higher forces, but motion will be favoured once begun. This means scratches on dirty rollers will be deeper, longer and favour the stick slip motion, making them more noticeable to the human eye.

Finally, despite extensive efforts and experimentation, experimental colloidal probe force modulation mode AFM was not able to collect reliable data from which understanding of adhesion of the surface could be used to inform a new cleaning method. It is hypothesised this is due to an interwoven relationship between relative humidity and surface roughness of the surfaces in this system.

Overall, the learnings vs. the industry problem can be summarised by Table 15 below.

Question	Answer
What is the debris?	Degradation products of PET
How does it appear on the line?	Though sublimation during the hot parts of the PET process, and then sublimation on the cooler parts of the line. It can linger where it initially condenses, or can subsequently be carried down the line by the motion of the film
How does it impact the rollers?	It clogs the micro-roughness of the roller surface
Why does this increase scratch formation?	Resulting film-roller frictional relationship has an increased static friction (relative movement initiates at higher temperatures) and lower dynamic friction (movement continues once initiated)
Why do currently in-line cleaning methods not work?	Cleaning pads do not remove the debris from the roller microroughness - this is only achieved through full-line clean.

Table 15: Summary of the questioned posed and answered as part of this research versus this industry problem posed.

7.2 FUTURE WORK

The future of exploring this problem is, as this project has been, multi-faceted, drawing on many different disciplines.

First, a new method for measuring adhesion, possibly at a more macro-scale should be explored, as this may still provide useful insights into debris accumulation that this work was not able to offer.

On the matter of AFM force modulation mode, it may be possible to use the vast array of roughened PET films made by DTF to develop a model for adhesion that is far away from the realm of low RMS where the adhesion is so sensitive to small changes in RMS and RH. Using these films as an example of “real” surfaces but ones where surface roughness is on the order of 100s of nanometres, where critical relative humidity will be far higher than ambient conditions, may provide a way to develop an in-house empirical model for adhesion vs. roughness that would be a valuable addition to the understanding of adhesion in the literature. In particular, it would be good to explore parameters of surface roughness beyond RMS, for example S_a , S_{ku} or similar. Perhaps in combination with each other they would be able to provide a better solution to the problem of capturing surface roughness in an empirical equation.

The AFM indentation method developed should be used further to test more parameters such as lateral speed, humidity and indenter geometry. Scratching velocity in particular would be useful to explore to understand scratch formation in different locations in the filming process.

The laboratory model for creating pseudo dirty rollers should be used further to test alternative in-line cleaning methods in order improve the performance of the current cleaning

pads. A promising cleaning solution could be an in-line UV-ozone cleaner which could remove organic contamination without contacting the roll. This would come with its own challenges in terms of safety and operation but could first be explored thoroughly in the lab using coherence scanning interferometry and AFM analysis.

A possible means of further enhancing understanding of adhesion more generally would be to conduct a more macro-scale measurement on the production line. The forward draw could be environmentally isolated during a clear optical production campaign, and the humidity varied within this chamber to see if this greatly affected either debris adhesion or relative movement. This could be measured by monitoring average scratch length across many production cycles at different conditions.

Finally, since it is now known that the frictional effects which contribute to relative movement and thus cause surface damage are surface energy moderated, alternative roller materials could be investigated. The exact chemistry of the etched epoxy coating the rollers is not well known to DFT and alternatives that have a higher surface energy could be explored.

8. BIBLIOGRAPHY

Adams, J. F. A. and Gerber, K. G. (1957) 'Process for the production of biaxially orientated polyethylene terephthalate film'. Welwyn Garden City: United States Patent Office, p. 5.

Akhtar, N. R. (2010) *The Fundamental Interactions between Deposits and Surfaces at Nanoscale using Atomic Force Microscopy*.

Alfano, J. *et al.* (2000) 'Polyelectrolyte-Induced Aggregation of Microcrystalline Cellulose: Reversibility and Shear Effects', *Journal of colloid and interface science*, 223(2), pp. 244–254.

Allen, N. S. *et al.* (1993) 'UV and thermal hydrolytic degradation of poly(ethylene terephthalate): importance of hydroperoxides and benzophenone end groups', *Polymer Degradation and Stability*. Elsevier, 41(2), pp. 191–196.

Allen, N. S. *et al.* (1994) 'Physicochemical aspects of the environmental degradation of poly(ethylene terephthalate)', *Polymer Degradation and Stability*. Elsevier, 43(2), pp. 229–237.

Attard, P. and Parker, J. L. (1992) 'Deformation and adhesion of elastic bodies in contact', *Physical Review A*, 46(12), pp. 7959–7971.

Ballara, A. and Verdu, J. (1989) 'Physical aspects of the hydrolysis of polyethylene terephthalate', *Polymer Degradation and Stability*. Elsevier, 26(4), pp. 361–374.

Bamford, C. H. and Tipper, C. F. H. (1975) *Comprehensive Chemical Kinetics: Degradation of Polymers*. UK: Elsevier Scientific Publishing.

Beake, B. D. and Leggett, G. J. (2002) 'Nanoindentation and nanoscratch testing of uniaxially and biaxially drawn poly(ethylene terephthalate) film', *Polymer*.

Beamson, G. *et al.* (1996) 'High-resolution X-ray photoelectron spectroscopy of crystalline and amorphous poly(ethylene terephthalate): A study of biaxially oriented film, spin cast film and polymer melt', *Polymer*, 37(3), pp. 379–385.

Beattie, I. and Cooper, B. (2006) *MDO Roll Cleaning Tests*. Redcar.

Bele, M. *et al.* (2000) 'Substrate-induced deposition: Molecular bridging between dispersed particles and gelatine-modified surfaces', *Progress in Colloid and Polymer Science*, 115, pp. 97–99.

Bergstrom, L. and Ennart (1997) 'Hamaker constants of inorganic materials', *Advances in Colloid and Interface Science*, 70, pp. 125–169.

Berman, A. D., Ducker, W. A. and Israelachvili, J. (1996) 'Origin and Characterization of Different Stick-Slip Friction Mechanisms†', *Langmuir*. American Chemical Society, 12(19), pp. 4559–4562.

Bhushan, B. (1998) 'Micro/nanotribology using atomic force microscopy/friction force microscopy: State of the art', *Proceedings of the Institution of Mechanical Engineers, Part J: Journal of Engineering Tribology*, 212(1), pp. 1–18.

Bhushan, B. and Dandavate, C. (2000) 'Thin-film friction and adhesion studies using atomic force microscopy', *Journal of Applied Physics*. American Institute of Physics AIP, 87(3), p. 1201.

Biggs, S. and Spinks, G. (1998) 'Atomic force microscopy investigation of the adhesion between a single polymer sphere and a flat surface', *Journal of Adhesion Science and Technology*, 12(5), pp. 461–478.

Bikiaris, D. N. and Karayannidis, G. P. (1999) 'Effect of carboxylic end groups on

thermooxidative stability of PET and PBT', *Polymer Degradation and Stability*. Elsevier Ltd, 63(2), pp. 213–218.

Binggeli, M. and Mate, C. M. (1994) 'Influence of capillary condensation of water on nanotribology studied by force microscopy', *Applied Physics Letters*, 65(4), pp. 415–417.

Binnig, G., Quate, C. F. and Gerber, C. (1986) 'Atomic Force Microscope', *Physical Review Letters*. American Physical Society, 56(9), p. 930.

Bocquet, L. and Barrat, J.-L. (1993) 'Hydrodynamic boundary conditions and correlation functions of confined fluids', *Physical Review Letters*. American Physical Society, 70(18), p. 2726.

Bolland, J. L. and Gee, G. (1946) 'Kinetic studies in the chemistry of rubber and related materials. III. Thermochemistry and mechanisms of olefin oxidation', *Transactions of the Faraday Society*. The Royal Society of Chemistry, 42(0), pp. 244–252.

Botelho, G. *et al.* (2001) 'Studies on thermal and thermo-oxidative degradation of poly(ethylene terephthalate) and poly(butylene terephthalate)', *Polymer Degradation and Stability*. Elsevier, 74(1), pp. 39–48.

Bowen, J. *et al.* (2011) 'Application of colloid probe atomic force microscopy to the adhesion of thin films of viscous and viscoelastic silicone fluids', *Langmuir*, 27(18), pp. 11489–11500.

Braithwaite, G. J. C., Luckham, P. F. and Howe, A. M. (1999) 'Study of a Solvated Adsorbed Gelatin Layer Using a Modified Force Microscope', *Journal of Colloid and Interface Science*. Academic Press, 213(2), pp. 525–545.

Briscoe, B. J. *et al.* (1998) 'Scratch deformation of methanol plasticized

poly(methylmethacrylate) surfaces', *Polymer*. Elsevier, 39(11), pp. 2161–2168.

Briscoe, B. J., Delfino, A. and Pelillo, E. (1999) 'Single-pass pendulum scratching of poly(styrene) and poly(methylmethacrylate)', *Wear*, 225(229), pp. 319–328.

Briscoe, B. J., Sebastian, K. S. and Adams, M. J. (1994) 'The effect of indenter geometry on the elastic response to indentation', *Journal of Physics D: Applied Physics*. IOP Publishing, 27(6), p. 1156.

Butt, H.-J. *et al.* (1999) 'Steric forces measured with the atomic force microscope at various temperatures', *Langmuir*, 15, pp. 2559–2565.

Butt, H. J., Cappella, B. and Kappl, M. (2005a) 'Force measurements with the atomic force microscope: Technique, interpretation and applications', *Surface Science Reports*. Elsevier, pp. 1–152.

Butt, H. J., Cappella, B. and Kappl, M. (2005b) 'Force measurements with the atomic force microscope: Technique, interpretation and applications', *Surface Science Reports*, 59(1–6), pp. 1–152.

Butt, H. J., Jaschke, M. and Ducker, W. (1995) 'Measuring surface forces in aqueous electrolyte solution with the atomic force microscope', *Bioelectrochemistry and Bioenergetics*. Elsevier, 38(1), pp. 191–201.

Butt, H. J. (1994) 'A Technique for Measuring the Force between a Colloidal Particle in Water and a Bubble', *Journal of Colloid and Interface Science*. Academic Press, 166(1), pp. 109–117.

Buxbaum, L. H. (1968) 'The Degradation of Poly(ethylene terephthalate)', *Angewandte Chemie*, 7(3), pp. 182–190.

Cappella, B. and Dietler, G. (1999) 'Force-distance curves by atomic force microscopy', *Surface Science Reports*, 34, pp. 1–104.

Carpick, R. W., Ogletree, D. F. and Salmeron, M. (1999) 'A General Equation for Fitting Contact Area and Friction vs Load Measurements', *Journal of Colloid and Interface Science*. *J Colloid Interface Sci*, 211(2), pp. 395–400.

Chanda, A. *et al.* (1997) 'A new parameter for measuring wear of materials', *Journal of Materials Science*, 16, pp. 1647–1651.

Chiu, S. J. and Cheng, W. H. (1999) 'Thermal degradation and catalytic cracking of poly(ethylene terephthalate)', *Polymer Degradation and Stability*. Elsevier, 63(3), pp. 407–412.

Christenson, H. and Thomson, N. (2016) 'The nature of the air-cleaved mica surface', *Surface Science Reports*, 71(2), pp. 367–390.

Chu, J. *et al.* (2000) 'Scratch resistance of mineral-filled polypropylene materials', *Polymer Engineering & Science*, 40(4), pp. 944–955.

Chu, J., Rumao, L. and Coleman, B. (1997) 'Scratch and Mar Resistance of Mineral-Filled Polypropylene Materials', *Journal of Materials and Manufacturing*, 106(5), pp. 565–573.

Çolak, A. *et al.* (2012) 'Surface adhesion and its dependence on surface roughness and humidity measured with a flat tip', *Applied Surface Science*, 258(1), pp. 6938–6942.

Coles, J. (2009a) *D52 FWD CR Auto-Cleaner Assessment*. Redcar.

Coles, J. (2009b) *Film Surface Quality Analysis September 2009 Clear Campaign*. Redcar.

- Cooper, B. (2007) *D52 CLEAR FILM SURFACE QUALITY*. Redcar.
- De, R. *et al.* (1954) 'The crystal structure of polyethylene terephthalate', *Proceedings of the Royal Society of London. Series A. Mathematical and Physical Sciences*. The Royal Society London, 226(1167), pp. 531–542.
- Debye, P. (1920) 'Die van der Waals'schen Kohäsionskräfte', *Mathematisch-Physikalische Klasse*, pp. 55–73.
- Denisyuk, Y. (1962) 'Photographic Reconstruction of the Optical Properties of an Object in Its Own Scattered Radiation Field', *Soviet physics-Doklady*, p. 543.
- Derjaguin, B. (1934) 'Untersuchungen über die Reibung und Adhäsion, IV - Theorie des Anhaftens kleiner Teilchen', *Kolloid-Zeitschrift*. Springer, 69(2), pp. 155–164.
- Derjaguin, B. V., Muller, V. M. and Toporov, Y. P. (1975) 'Effect of contact deformation on the adhesion of elastic solids', *Journal of Colloid and Interface Science*, 53(2), pp. 314–326.
- Donnellan, J. (1989a) *Installation of DASH catalyst in 51 unit*. Redcar.
- Donnellan, J. (1989b) *Installation of DASH catalyst in 71 unit*. Redcar.
- Donnellan, J. (1989c) *The catalytic control of white powder on 16 unit*. Redcar.
- Donnellan, J. and Cook, R. (1990) *Catalytic control of White Powder on 17 Unit*. Redcar.
- Du, B *et al.* (2001) 'Direct measurement of plowing friction and wear of a polymer thin film using the atomic force microscope', *Journal of Materials Research*, 16(1), pp. 1487–1492.
- Ducker WA, Senden TJ and Pashley PA (1991) 'Direct measurement of colloidal forces using an atomic force microscope', *Nature*, 353(353), p. 2239.

Duval, J. F., Leermakers, F. A. M. and van Leeuwen, H. P. (2004) 'Electrostatic interactions between double layers: influence of surface roughness, regulation, and chemical heterogeneities', *Langmuir*, 20(12), pp. 5052–5065.

Dzięcioł, M. and Trzecznyński, J. (1998) 'Studies of temperature influence on volatile thermal degradation products of poly(ethylene terephthalate)', *Journal of Applied Polymer Science*, 69(12), pp. 2377–2381.

Dzięcioł, M. and Trzecznyński, J. (2000) 'Volatile products of poly(ethylene terephthalate) thermal degradation in nitrogen atmosphere', *Journal of Applied Polymer Science*, 77(9), pp. 1894–1901.

Eastman, T. and Zhu, D.-M. (1996) 'Adhesion Forces between Surface-Modified AFM Tips and a Mica Surface', *Langmuir*. American Chemical Society, 12(11), pp. 2859–2862.

Ecke, S. *et al.* (2001) 'Measuring normal and friction forces acting on individual fine particles', *Review of Scientific Instruments*, 72(11), p. 4164.

Ellison, M. S. *et al.* (1982) 'Physical properties of polyester fibers degraded by aminolysis and by alkaline hydrolysis', *Journal of Applied Polymer Science*. John Wiley & Sons, Ltd, 27(1), pp. 247–257.

Elzbieciak-Wodka, M. *et al.* (2014) 'Measurements of dispersion forces between colloidal latex particles with the atomic force microscope and comparison with Lifshitz theory', *The Journal of Chemical Physics*. American Institute of Physics, 140(10), p. 104906.

Farshchi-Tabrizia, M., Kappl, M. and Butt, H. J. (2008) 'Influence of humidity on adhesion: An atomic force microscope study', *Journal of Adhesion Science and Technology*, 22(2), pp. 181–

203.

Fielden, M. L., Hayes, R. A. and Ralston, J. (1996) 'Surface and Capillary Forces Affecting Air Bubble-Particle Interactions in Aqueous Electrolyte', *Langmuir*. American Chemical Society, 12(15), pp. 3721-3727.

Fuji, M. *et al.* (1999) 'Effect of wettability on adhesion force between silica particles evaluated by atomic force microscopy measurement as a function of relative humidity', *Langmuir*, 15(13), pp. 4584-4589.

Gady, B. *et al.* (1998) 'Particle Adhesion to Elastomeric Substrates and Elastomeric Substrates with Semi-Rigid Coatings', *The Journal of Adhesion*, 67(1-4), pp. 19-36.

Garoff, N. and Zauscher, S. (2002) 'The influence of fatty acids and humidity on friction and adhesion of hydrophilic polymer surfaces', *Langmuir*, 18(18), pp. 6921-6927.

Gauthier, C. and Schirrer, R. (2000) 'Time and temperature dependence of the scratch properties of poly(methylmethacrylate) surfaces', *Journal of Materials Science*. Springer, 35(9), pp. 2121-2130.

Geng, Y. *et al.* (2019) 'Influence of tip adhesion on nanoindentation and scratching', *Modelling and Simulation in Materials Science and Engineering*. IOP Publishing, 27(6), pp. 1-17.

Giesbers, M. *et al.* (1998) 'Forces between polymer-covered surfaces: a colloidal probe study.', *Colloids and Surfaces. A: Physicochemical and Engineering Aspects*. Elsevier, 142(2-3), pp. 343-353.

Grassie, N. (1984) *Developments in Polymer Degradation : Volume 5*. UK: Applied Science Publications.

Grassie, N. and Scott, G. (1985) *Polymer Degradation and Stabilisation*. Cambridge: Cambridge University Press.

Guevin, P. R. . (1995) 'State-of-the-Art Instruments to Measure Coating Hardness', *Journal of Coatings Technology*, 67(No. 840), p. 61.

Hamada, E. and Kaneko, R. (1992) 'Micro-tribological evaluations of a polymer surface by atomic force microscopes', *Ultramicroscopy*. North-Holland, 42–44, pp. 184–190.

Hamaker, H. C. (1937a) 'The London-van der Waals attraction between spherical particles', *Physica*, 4(10), pp. 1058–1072.

Hamaker, H. C. (1937b) 'The London—van der Waals attraction between spherical particles', *Physica*. North-Holland, 4(10), pp. 1058–1072.

Han, Y., Schmitt, S. and Friedrich, K. (1999) 'Nanoscale Indentation and Scratch of Short Carbon Fiber Reinforced PEEK/PTFE Composite Blend by Atomic Force Microscope Lithography', *Applied Composite Materials*, 6, pp. 1–18.

Hansson, P. M. *et al.* (2012) 'Effect of Surface Depressions on Wetting and Interactions between Hydrophobic Pore Array Surfaces', *Langmuir*. American Chemical Society, 28(30), pp. 11121–11130.

Hao, H. W. (1991) 'Electrostatic and contact forces in force microscopy', *Journal of Vacuum Science & Technology B: Microelectronics and Nanometer Structures*, 9(2), p. 1323.

Harrison, A. J., Corti, D. S. and Beaudoin, S. P. (2015) 'Capillary Forces in Nanoparticle Adhesion: A Review of AFM Methods', *Particulate Science and Technology*, 33(5), pp. 526–538.

Hassan, E. *et al.* (1998) 'Relative microelastic mapping of living cells by atomic force microscopy.', *Biophysical Journal*. The Biophysical Society, 74(3), p. 1564.

Heim, L.-O. *et al.* (1999) 'Adhesion and Friction Forces between Spherical Micrometer-Sized Particles', *Physical Review Letters*. American Physical Society, 83(16), p. 3328.

Heim, L. O. *et al.* (2002) 'Adhesion forces between individual gold and polystyrene particles', *Journal of Adhesion Science and Technology*. Taylor & Francis Group, 16(7), pp. 829–843.

Hertz, H. (1878) 'Die lieber die Berührung fester elastischer Körper', *J. Reine Angew. Math*, 92, pp. 156–171.

Hewitt, J. (1992) *Assessment of The Effectiveness of Catalyst Bricks Installed on Melinex's 34 Unit*. Redcar.

Heyer, D. (2011) *Tuesdays Surface Global R Conference (email exchange)*. Redcar.

Hoek, E. M. V. and Agarwal, G. K. (2006) 'Extended DLVO interactions between spherical particles and rough surfaces', *Journal of Colloid and Interface Science*. Academic Press, 298(1), pp. 50–58.

Holmberg, M. *et al.* (1997) 'Interactions between cellulose and colloidal silica in the presence of polyelectrolytes', *Colloids and Surfaces A: Physicochemical and Engineering Aspects*, 129(130), pp. 175–183.

Hosseini, S. S. *et al.* (2007) 'Hydrolytic Degradation of Poly(ethylene terephthalate)', *Journal of Applied Polymer Science*, 103, pp. 2304–2309.

Israelachvili, J. N. and Adams, G. E. (1977) 'Measurement of Forces between Two Mica Surfaces in Aqueous Electrolyte Solutions in the Range 0-100 nm', *Journal of the Chemical*

Society, Faraday Transactions, 74, pp. 975–1001.

Iyer, S. *et al.* (2009) 'Atomic force microscopy detects differences in the surface brush of normal and cancerous cells', *Nature nanotechnology*, 4(6), pp. 389–393.

Jabarin, S. A. and Lofgren, E. A. (1986) 'Effects of water absorption on physical properties and degree of molecular orientation of poly (ethylene terephthalate)', *Polymer Engineering & Science*. John Wiley & Sons, Ltd, 26(9), pp. 620–625.

Jenkins, P. *et al.* (1999) 'Copper Phthalocyanine-Mica Interactions in Nonaqueous Media', *Journal of colloid and interface science*, 211(1), pp. 11–17.

Johnson, J. E. (1959) 'X-ray diffraction studies of the crystallinity in polyethylene terephthalate', *Journal of Applied Polymer Science*. John Wiley & Sons, Ltd, 2(5), pp. 205–209.

Johnson, K. L. (1985) *Contact Mechanics*. Cambridge: Cambridge University Press.

Johnson, K. L., Kendall, K. and Robert, A. D. (1971) 'Surface Energy and the Contact of Elastic Solids', *Proceedings of the Royal Society of London. Series A, Mathematical and Physical Sciences*, 324(1), pp. 301–313.

Jones, A. (2007) *FWD Cooling Roll Cleaning*. Redcar.

Jones, R. *et al.* (2002) 'Adhesion forces between glass and silicon surfaces in air studied by AFM: Effects of relative humidity, particle size, roughness, and surface treatment', *Langmuir*, 18(21), pp. 8045–8055.

Kaibara, Y. *et al.* (2003) 'Control wettability of the hydrogen-terminated diamond surface and the oxidized diamond surface using an atomic force microscope', *Diamond and Related Materials*, 12(3–7), pp. 560–564.

Kappl, M. and Butt, H. J. (2002) 'The Colloidal Probe Techniques and its Application to Adhesion Force Measurements', *Particle & Particle Systems Characterization*, 19, pp. 129–143.

Keesom, W. H. (1915) 'The second virial coefficient for rigid spherical molecules, whose mutual attraction is equivalent to that of a quadruplet placed at their centre', in *KNAW Proceedings*, pp. 636–646.

Kelen, T. (1983) *Polymer degradation*. New York: Van Nostrand Reinhold Co.

Khemani, K. C. (2000) 'A novel approach for studying the thermal degradation, and for estimating the rate of acetaldehyde generation by the chain scission mechanism in ethylene glycol based polyesters and copolyesters', *Polymer Degradation and Stability*. Elsevier, 67(1), pp. 91–99.

Kimyonok, A. B. E. and Uluturk, M. (2016) 'Determination of the Thermal Decomposition Products of Terephthalic Acid by Using Curie-Point Pyrolyzer', *Journal of Energetic Materials*, 34(2), pp. 113–122.

Kint, D. and Muñoz-Guerra, S. (1999) 'A review on the potential biodegradability of poly(ethylene terephthalate)', *Polymer International*, 48(5), pp. 346–352.

Kody, R. S. and Martin, D. C. (1996) 'Quantitative characterization of surface deformation in polymer composites using digital image analysis', *Polymer Engineering & Science*. John Wiley & Sons, Ltd, 36(2), pp. 298–304.

Krupička, A., Johansson, M. and Hult, A. (2003) 'Use and interpretation of scratch tests on ductile polymer coatings', *Progress in Organic Coatings*. Elsevier, 46(1), pp. 32–48.

Kupferman, M. *et al.* (2014) *Grading of Needles on HSTCH11/500ga Carestream*. Redcar.

Kwon, Y. J. *et al.* (1994) 'Vibrational Spectroscopic Investigation of Benzoic Acid Adsorbed on Silver', *Journal of Physical Chemistry*, 98, pp. 8481–8487.

Laitinen, O. *et al.* (2013) 'Validity of the Rumpf and the Rabinovich adhesion force models for alumina substrates with nanoscale roughness', *Powder Technology*, 246, pp. 545–552.

Lamy, B. (1984) 'Effect of brittleness index and sliding speed on the morphology of surface scratching in abrasive or erosive processes', *Tribology International*. Elsevier, 17(1), pp. 35–38.

Launay, A., ThomINETTE, F. and Verdu, J. (1999) 'Hydrolysis of poly(ethylene terephthalate). A steric exclusion chromatography study', *Polymer Degradation and Stability*, 63(3), pp. 385–389.

de Lazzer, A., Dreyer, M. and Rath, H. J. (1999) 'Particle–Surface Capillary Forces', *Langmuir*, 15(13), pp. 4551–4559.

Lehr, J. and Kietzig, A. M. (2015) 'Dependence of capillary forces on relative humidity and the surface properties of femtosecond laser micromachined titanium', *Journal of Colloid and Interface Science*. Academic Press, 448, pp. 356–366.

Leite, F. L. *et al.* (2012) *Theoretical models for surface forces and adhesion and their measurement using atomic force microscopy*, *International Journal of Molecular Sciences*.

Liang, Y. N. *et al.* (1996) 'Some developments for single-pass pendulum scratching', *Wear*, 199(1), pp. 66–73.

Lifshitz, E. M. (1956) 'The theory of molecular attractive forces between solids', *Journal of Experimental and Theoretical Physics*, 2, pp. 73–83.

Lim, G. T. *et al.* (2005) 'An integrated approach towards the study of scratch damage of polymer', *Journal of Coatings Technology and Research*. Springer, 2(5), pp. 361–369.

Lim, G. T. (2005) *SCRATCH BEHAVIOR OF POLYMERS*. Texas A&M University.

London, F. (1930) 'Zur Theorie und Systematik der Molekularkräfte', *Zeitschrift für Physik*. Springer, 63(3), pp. 245–279.

Lu, C. J., Bogy, D. and Kaneko, R. (1994) 'Nanoindentation Hardness Tests Using a Point Contact Microscope', *Journal of Tribology*. American Society of Mechanical Engineers Digital Collection, 116(1), pp. 175–180.

MacDonald, W. A. (1995) *White Powder (email exchange)*. Redcar.

MacDonald, W. A. (2002) 'New advances in poly(ethylene terephthalate) polymerization and degradation', *Polymer International*, 51(10), pp. 923–930.

Mackenzie, C. (1982) *White Powder*. Welwyn Garden City.

Mantel, M. *et al.* (1995) 'A Study of Hydrophobic Interactions between Stainless Steel and Silanated Glass Surface Using Atomic Force Microscopy', *Journal of Colloid and Interface Science*, 170(1), pp. 203–214.

Marmur, A. (1993) 'Tip-surface capillary interactions', *Langmuir*. American Chemical Society, 9(7), pp. 1922–1926.

Marsh, P. (2007) *Characterisation of D52 D744 film scratches and pad debris*. Redcar.

Maugis, D. (1992) 'Adhesion of spheres: The JKR-DMT transition using a dugdale model', *Journal of Colloid And Interface Science*, 150(1), pp. 243–269.

Maugis, D. and Pollock, H. M. (1984) 'Surface forces, deformation and adherence at metal microcontacts', *Acta Metallurgica*, 32(9), p. 1323.

McNeill, I. C. and Bounekhel, M. (1991) 'Thermal degradation studies of terephthalate polyesters: 1. Poly(alkylene terephthalates)', *Polymer Degradation and Stability*. Elsevier, 34(1–3), pp. 187–204.

Montaudo, G., Puglisi, C. and Samperi, F. (1993) 'Primary thermal degradation mechanisms of PET and PBT', *Polymer Degradation and Stability*. Elsevier, 42(1), pp. 13–28.

Mordor Intelligence (2021) *Flexible Electronics Market | 2021 - 26 | Industry Share, Size, Growth*. Hyderabad.

von Morgen, V. (2011) *Characterisation of swab tapes in relation to TD needles investigation*. Redcar.

Muller, V. M., Derjaguin, B. V. and Toporov, Y. P. (1983) 'On two methods of calculation of the force of sticking of an elastic sphere to a rigid plane', *Colloids and Surfaces*, 7(3), pp. 251–259.

Notbohm, J., Poon, B. and Ravichandran, G. (2012) 'Analysis of nanoindentation of soft materials with an atomic force microscope', *Journal of Materials Research*, 27(1), pp. 229–237.

Ong, Q. K. and Sokolov, I. (2007) 'Attachment of nanoparticles to the AFM tips for direct measurements of interaction between a single nanoparticle and surfaces', *Journal of Colloid and Interface Science*, 310(2), pp. 385–390.

Ouyang, Q., Ishida, K. and Okada, K. (2001) 'Investigation of micro-adhesion by atomic force microscopy', *Applied Surface Science*. , 169–170, pp. 644–648.

- Oxborough, R. J. and Bowden, P. B. (2006) 'A general critical-strain criterion for crazing in amorphous glassy polymers', *The Philosophical Magazine: A Journal of Theoretical Experimental and Applied Physics*. Taylor & Francis Group, 28(3), pp. 547–559.
- Pemberton, M. W. and Stening, T. C. (1966) *MELINEX FOR RECORDING TAPES: The White Powder Problem - The present position*. Welwyn Garden City.
- Persson, B. N. J. and Tosatti, E. (2001) 'The effect of surface roughness on the adhesion of elastic solids', *Journal of Chemical Physics*, 115(12), pp. 5597–5610.
- Pirzadeh, E., Zadhoush, A. and Haghghat, M. (2007) 'Hydrolytic and thermal degradation of PET fibers and PET granule: The effects of crystallization, temperature, and humidity', *Journal of Applied Polymer Science*, 106(3), pp. 1544–1549.
- Pohl, H. A. (2002) 'The Thermal Degradation of Polyesters', *Journal of the American Chemical Society*. American Chemical Society, 73(12), pp. 5660–5661.
- Preuss, M. and Butt, H.-J. (1998) 'Direct Measurement of Particle–Bubble Interactions in Aqueous Electrolyte: Dependence on Surfactant', *Langmuir*. American Chemical Society, 14(12), pp. 3164–3174.
- Quon, R. A., Knarr, R. F. and Vanderlick, T. K. (1999) 'Measurement of the Deformation and Adhesion of Rough Solids in Contact', *Journal of Physical Chemistry B*. American Chemical Society, 103(25), pp. 5320–5327.
- Rabinovich, Y. I. *et al.* (2000) 'Adhesion between Nanoscale Rough Surfaces', *Journal of Colloid and Interface Science*. J Colloid Interface Sci, 232(1), pp. 10–16.
- Rabinovich, Y. I. *et al.* (2002) 'Capillary forces between surfaces with nanoscale roughness',

Advances in Colloid and Interface Science.

Ramakrishna, S. N. *et al.* (2013) 'Study of adhesion and friction properties on a nanoparticle gradient surface: Transition from JKR to DMT contact mechanics', *Langmuir*, 29(1), pp. 175–182.

Ramsteiner, F. *et al.* (2003) 'Scratch resistance and embrittlement of coated polymers', *Polymer Testing*. Elsevier, 22(4), pp. 439–451.

Reitsma, M., Craig, V. and Biggs, S. (2000) 'Elasto-plastic and visco-elastic deformations of a polymer sphere measured using colloid probe and scanning electron microscopy', *International Journal of Adhesion and Adhesives*. Elsevier Science Ltd, 20(6), pp. 445–448.

Reitsma, M., Craig, V. S. J. and Biggs, S. (2000) 'Measurement of the Adhesion of a Viscoelastic Sphere to a Flat Non-Compliant Substrate', *The Journal of Adhesion*, 74(1–4), pp. 125–142.

Rumpf, H. (1953) 'Über das Ansetzen fein verteilter Stoffe an den Wänden von Strömungskanälen', *Chemie Ingenieur Technik*. John Wiley & Sons, Ltd, 25(6), pp. 317–327.

Sakata, Y. *et al.* (1996) 'Thermal degradation of polyethylene mixed with poly(vinyl chloride) and poly(ethyleneterephthalate)', *Polymer Degradation and Stability*. Elsevier, 53(1), pp. 111–117.

Sammon, C., Yarwood, J. and Everall, N. (2000) 'FT-IR study of the effect of hydrolytic degradation on the structure of thin PET films', *Polymer Degradation and Stability*. Elsevier Science Ltd, 67(1), pp. 149–158.

Samperi, F. *et al.* (2004) 'Thermal degradation of poly(ethylene terephthalate) at the processing temperature', *Polymer Degradation and Stability*. Elsevier, 83(1), pp. 3–10.

- Schaefer, D. M. *et al.* (1994) 'Surface force interactions between micrometer-size polystyrene spheres and silicon substrates using atomic force techniques', *Journal of Adhesion Science and Technology*. Taylor & Francis Group, 8(3), pp. 197–210.
- Sedin, D. L. and Rowlen, K. L. (2000) 'Adhesion forces measured by atomic force microscopy in humid air', *Analytical Chemistry*. Anal Chem, 72(10), pp. 2183–2189.
- Seo, K. S. and Cloyd, J. D. (1991) 'Kinetics of hydrolysis and thermal degradation of polyester melts', *Journal of Applied Polymer Science*. John Wiley & Sons, Ltd, 42(3), pp. 845–850.
- Shulha, H. *et al.* (2004) 'Some aspects of AFM nanomechanical probing of surface polymer films', *European Polymer Journal*, 40(5), pp. 949–956.
- Sirghi, L. *et al.* (2000) 'Effect of Sample Topography on Adhesive Force in Atomic Force Spectroscopy Measurements in Air', *Langmuir*. American Chemical Society, 16(20), pp. 7796–7800.
- Smyth, G. *et al.* (1998) *The Scratching of Polymer Surfaces-Part 2: Scratching of Filled PET Films*.
- Sneddon, I. N. (1965) 'The relation between load and penetration in the axisymmetric boussinesq problem for a punch of arbitrary profile', *International Journal of Engineering Science*, 3(1), pp. 47–57.
- Sun, Y., Akhremitchev, B. and Walker, G. C. (2004) 'Using the adhesive interaction between atomic force microscopy tips and polymer surfaces to measure the elastic modulus of compliant samples', *Langmuir*, 20(14), pp. 5837–5845.
- Suresh, L. and Walz, J. Y. (1996) 'Effect of Surface Roughness on the Interaction Energy

between a Colloidal Sphere and a Flat Plate', *Journal of Colloid and Interface Science*. Academic Press, 183(1), pp. 199–213.

Suresh, L. and Walz, J. Y. (1997) 'Direct Measurement of the Effect of Surface Roughness on the Colloidal Forces between a Particle and Flat Plate', *Journal of Colloid and Interface Science*. Academic Press, 196(2), pp. 177–190.

Tabor, D. (1977) 'Surface forces and surface interactions', *Journal of Colloid and Interface Science*. Academic Press, 58(1), pp. 2–13.

Thompson, A. B. and Woods, D. W. (1956) 'The transitions of polyethylene terephthalate', *Transactions of the Faraday Society*. The Royal Society of Chemistry, 52(0), pp. 1383–1397.

Thormann, E. (2017) 'Surface forces between rough and topographically structured interfaces', *Current Opinion in Colloid and Interface Science*.

Timoshenko, S. and Goodier, J. . (1951) *Theory of Elasticity*. New York: McGraw-Hill.

Toikka, G., Spinks, G. M. and Brown, H. R. (2001) 'Fine particle adhesion measured at elevated temperatures using a dedicated force rig', *Langmuir*, 17(20), pp. 6207–6212.

Tomas, J. (2003) 'Mechanics of nanoparticle adhesion—a continuum approach', *Particles on Surfaces*, 8, pp. 183–229.

Turnbull, L. (2013) *Thermal, Oxidative and Hydrolytic Degradation Studies of Poly(Ethylene Naphthalate)*.

Vakarelski, I. U. *et al.* (2001) 'Deformation and adhesion of elastomer microparticles evaluated by AFM', *Langmuir*, 17(16), pp. 4739–4745.

Vakarelski, I. U. and Higashitani, K. (2001) 'Dynamic features of short-range interaction force and adhesion in solutions', *Journal of Colloid and Interface Science*. Elsevier, 242(1), pp. 110–120.

Vakarelski, I. U., Ishimura, K. and Higashitani, K. (2000) 'Adhesion between Silica Particle and Mica Surfaces in Water and Electrolyte Solutions', *Journal of Colloid and Interface Science*. Academic Press, 227(1), pp. 111–118.

Valtiner, M. *et al.* (2012) 'The Electrochemical Surface Forces Apparatus: The Effect of Surface Roughness, Electrostatic Surface Potentials, and Anodic Oxide Growth on Interaction Forces, and Friction between Dissimilar Surfaces in Aqueous Solutions', *Langmuir*. American Chemical Society, 28(36), pp. 13080–13093.

Various (2010) *Highlights of D52 Surface Quality Improvement Work*. Redcar.

Vingsbo, O. and Hogmark, S. (1984) 'Single-pass pendulum grooving — a technique for abrasive testing', *Wear*. Elsevier, 100(1–3), pp. 489–502.

Wang, C. qing *et al.* (2015) 'Interfacial interactions between plastic particles in plastics flotation', *Waste Management*. Elsevier Ltd, 46, pp. 56–61.

Williams, J. (2005) *Analysis of pad residue*. Redcar.

Williams, J. A. (1996) 'Analytical models of scratch hardness', *Tribology International*. Elsevier, 29(8), pp. 675–694.

Xiao, X. and Qian, L. (2000) 'Investigation of humidity-dependent capillary force', *Langmuir*, 16(21), pp. 8153–8158.

Yan, Y. *et al.* (2019) 'Scratch on Polymer Materials Using AFM Tip-Based Approach: A Review',

Polymers. Multidisciplinary Digital Publishing Institute (MDPI), 11(10).

Yokohata, T. and Kato, K. (1993) 'Mechanism of nanoscale indentation', *Wear*. Elsevier, 168(1–2), pp. 109–114.

Yoon, E. S. *et al.* (2003) 'An experimental study on the adhesion at a nano-contact', *Wear*. Elsevier, 254(10), pp. 974–980.

Yu, W. and Blanchard, J. P. (1996) 'An elastic-plastic indentation model and its solutions', *Journal of Materials Research*. Cambridge University Press, 11(9), pp. 2358–2367.

Zarate, N. V. *et al.* (2013) 'Effect of relative humidity on onset of capillary forces for rough surfaces', *Journal of Colloid and Interface Science*. Academic Press, 411, pp. 265–272.

Zauscher, S. and Klingenberg, D. (2000) 'Normal Forces between Cellulose Surfaces Measured with Colloidal Probe Microscopy', *Journal of colloid and interface science*. J Colloid Interface Sci, 229(2), pp. 497–510.

Zhang, Z. *et al.* (2019) 'Robotic Micromanipulation: Fundamentals and Applications', *Annual Review of Control, Robotics, and Autonomous Systems*. Annual Reviews, 2(1), pp. 181–203.

Zimmerman, H. and Kim, N. T. (1980) 'Investigations on thermal and hydrolytic degradation of poly(ethylene terephthalate)', *Polymer Engineering & Science*, 20(10), pp. 680–683.

9. APPENDICES

9.1 HISTORIC DTF REPORTING ON THE “PROBLEM OF WHITE POWDER”

9.1.1 1966

The earliest discoverable report into debris production on a DTF PET production line is from 1966. A report by Pemberton and Stening (Pemberton and Stening, 1966), was published on the so-called “white powder” that was being produced on the (then) ICI Melinex lines. It was being seen on the surface of PET films, particularly those used for recording tapes, causing problems with coating adhesion. At the time the belief was that this white powder (WP) was produced in the stenter ovens. This report challenged this assumption by postulating that there are two routes to WP.

1. Sublimation – condensation: Melinex was heated to high temperatures (270-285 °C) and the weight loss due to sublimation was recorded. Some of this sublimated material was collected and found to contain terephthalic acid, terephthalic acid diethylene glycol esters and cyclic trimers.
2. Abrasion: Material can also be physically abraded from the surface. This was tested, and it was found that (depending on the abrasion resistance of the PET) high molecular weight polymer was removed from the surface.

Despite this report the belief remained that the major cause of “white powder” was due to sublimation of small molecules (TA, cyclic trimers etc.) in the hot parts of the process and then condensing in the cooler parts of the process.

9.1.2 1982

In pursuit of this C. Mackenzie conducted a thorough investigation into the factors affecting the white powder sublimation process in the stenter (Mackenzie, 1982). Mackenzie's work exposed PET chip to a range of temperatures (265 – 320 °C) and atmospheres, both pre-wetted and dry and measured the evolution of WP. He concluded evolution depended on the presence of moisture (indicating the process is hydrolytic), the PET type, the di-ethylene-glycol and carboxylic end group concentration and oxygen concentration (indicating the process is also oxidative).

9.1.3 1980s-1990s

In the subsequent decades there were many reports and trials to attempt to eliminate the WP produced by the *sublimation-condensation* route, particularly around the stenter. This was done by looking at stenter air flows and introducing a DASH/brick catalyst in the stenter.

This was proposed to be used in several lines including 16, 17, 51 and 71 (Mackenzie, 1982; Donnellan, 1989a, 1989b, 1989c; Donnellan and Cook, 1990) and was found to be “extremely effective” in reducing the volume of WP produced on the line (Hewitt, 1992).

By the end of the 1990s, the implementation of these systems, in combination with improved polymer quality that was less susceptible to hydrolytic degradation, and better air flows within the stenter meant that the contamination issue was under control and thus the focus of work into white powder shifted to the forward draw where the issue was surface quality.

9.1.4 1995

Further work on the “white powder problem” identified that the build-up of white powder was occurring in three key places: On the edges of the casting drum, in the forward draw

(FWD) and in the stenter. It was believed that the white powder was almost entirely the mono glycol ester of TA and TA (MacDonald, 1995). It was observed that the build-up in the FWD was worse on the rolls which are in contact with the drum side, and worst on the cooling rolls after the draw. The extent of white powder was also seen to be dependent on the polymer used.

A FEA model of the 1st cooling roll after the draw zone recommended driving the roll to reduce scratch length and further modelling also showed lowering the second cooling roll's coefficient of friction increased scratch length. Overall, this report outlines a belief that a lower coefficient of friction of the rollers could improve scratching, which is the opposite of what is believed today.

9.1.5 1998-1999

Between 1998 and 1999 the IR heater position in the forward draw in D52 was optimised to reduce post-drawing on the first cooling roll, which at the time was the origin of longer scratches. The physics of post drawing are outlined in Section 6.5.2

Another piece of work used 3D modelling of different contact conditions on cooling roll 1 on other production lines to predict scratch length and orientation. This work found scratch lengths associated with scuffing were consistent with those predicted by modelling for stress relaxation effects.

9.1.6 2002

Work in 2002 built upon the work from the late 90s by continuing to improve on the quench at cooling roll 1 to prevent effects such as post draw and stress relaxation. Optimised heating in the draw zone reduced the impact of stress relaxation effects.

9.1.7 2005

After several years of the focus being on the mechanics of sources of relative movement in the forward draw, 2005 saw a shift back to wanting to understand the impacts of white powder.

A cleaning pad used on the line was analysed using optical microscopy (Williams, 2005):

“Examination of the abrasive cloth shows what appear to be green deposits on a macro view but microscopically they are transparent green crystalline deposits which have been 'polished' onto the surface and appear to congregate around more prominent areas of the abrasive surface.

The material can be easily removed, shows minor optical activity in crossed polarised light and easily melts on the micro-slide.”

This work concluded, based on qualitative observations and refractive index measurements, that much of the material was abraded polyester film with a small proportion of terephthalic acid and terephthalic acid esters. That some of the material is TA or TA esters was shown by treating the surface with low concentration solutions of sodium hydroxide – causing some of the material to dissolve - but equally left, or exposed, tiny fragments of film debris.

9.1.8 2006

An extensive piece of work by Bret Cooper and Ian Beattie into roll cleaning was conducted in 2006. This work (Beattie and Cooper, 2006) identified from historic experience the smoothing issues with rolls on lines 51, 52 and 53 and looked at ways to clean them.

“D52: If CR1 is too smooth [...], causes needles/scratches on clear film”

They investigated how effective a variety of cleaning methods were at restoring the surface roughness of a roller by taking single line profiles of the rollers in a “clean” and “dirty” state.

They suggested that rollers became smoother due to white powder embedded in the ceramic surface rather than ceramic wear that had previously been suggested. They found that current cleaning methods (see Section 1.6.7) clean the worst of the contamination in the surface roughness but not on the edges where a smooth edge bead remains.

They found that the most effective method of restoring surface roughness was using ammonia solution. A peel away clean using caustic paste was also effective but subsequently was found to have issues of leaving debris on the roller surface.

9.1.9 2007

A report by Bret Cooper into the characterisation of film scratches and pad debris (Light microscopy, SEM and SEM-EDX) was conducted on his behalf by Paul Marsh (Marsh, 2007).

Examination of scratches concluded that the majority seen on film samples were in a direction slightly off from MD. This report also suggested that there were slightly fewer scratches on the drumside of the film, although this was not confirmed with statistically significant data.

Samples of dirtied cleaning pads were submitted for EDX analysis, and it was found that the majority of debris was an unidentified C based material (PET/TA/oligomer). It was impossible to be more specific about the organic nature from EDX analysis alone. Samples also contained significant amount of metal fragments including Cr, Ni, Fe and Al.

A separate report by Bret Cooper (Cooper, 2007) outlined clearly the current position at that time. He analysed clear film samples obtained from each D52 winder from 12 production runs (Mar-Aug 2006). For each run, film was analysed at 4 locations across film width (2B, 3B, 3F, 1F) (see Figure 104) using an Olympus microscope.

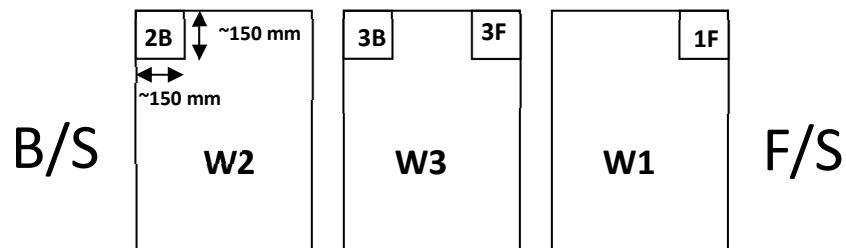


Figure 104: Sampling locations for Bret Cooper's work 2007

Scratch location, length & number density were determined for each of the forty-eight samples. The results are displayed in Figures 105 – 107.

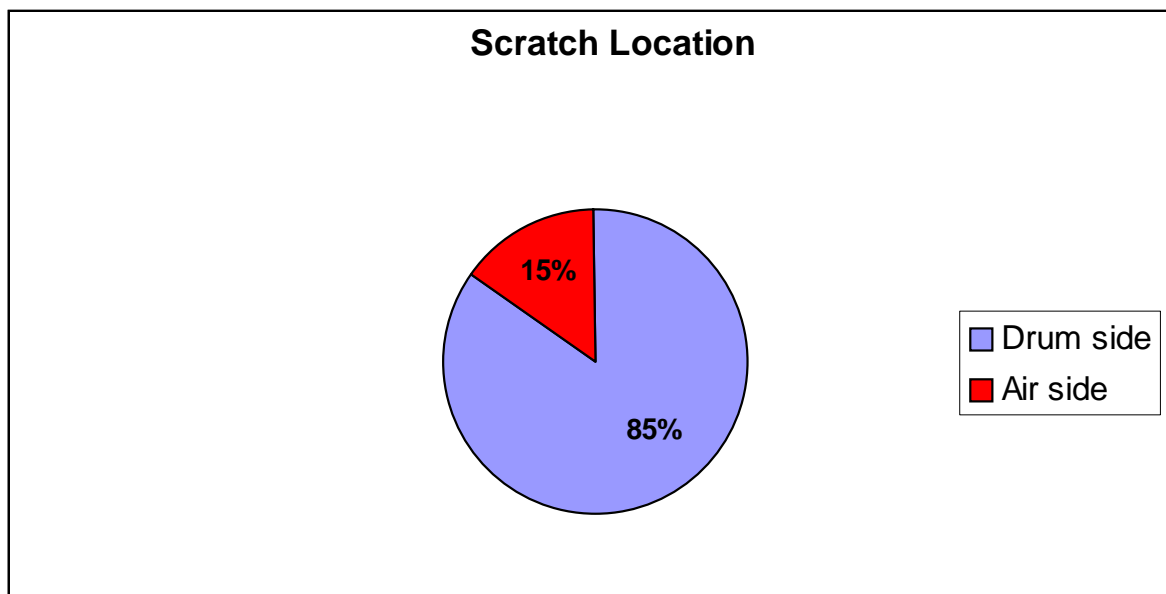


Figure 105: Percentage of scratches found on the air and drumside of film samples analysed.

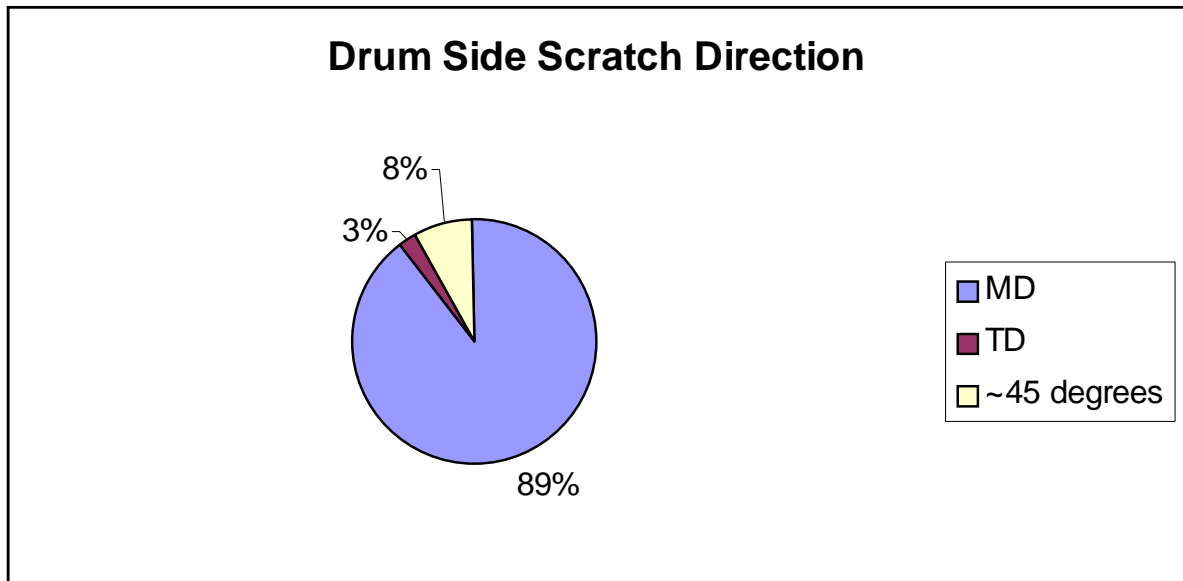


Figure 106: Average direction of scratches found on drumside of film samples analysed.

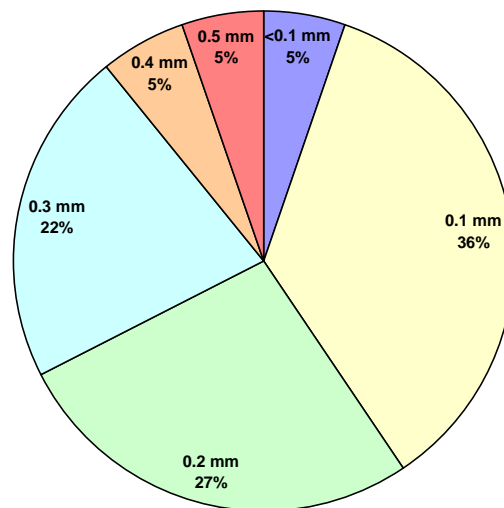


Figure 107: D52 drumside scratch length.

He concluded that web/roll movement with debris present causes scratches and that the debris was principally ‘white powder’. Scratches occurred mainly (85%) on the drum side of the film. He suggested a possible explanation for this is that on the drum side of the film, oligomer is unable to evaporate from hot web on the casting drum, so escapes from the PET matrix in draw zone.

He also noted that scratches are not usually found across the entire sample, suggesting localised areas of debris (white powder) build-up, and that a good surface quality with minimal scratches is only (re)established by a full line clean.

He made a number of recommendations including:

- Reduce generation of white powder:
 - Extract white powder at the die and /or at IR heaters
 - Reduce melt temperatures
- Automate in-line cleaning on CR2, CR4 & possibly on some other rolls.

While thorough and extensive, this piece of work relied a lot on profile measurements to quantify surface roughness, which is known to not be the most accurate of measurements.

9.1.10 2008

A fault in the cooling roll (FDFD9) created an opportunity in 2008 for more learning about the impact of surface roughness on surface quality. A report by (Jones, 2007) describes how shortly after the installation of a new cooling roll 1, the surface quality of the film being produced took a nosedive.

The roller was discovered to be decreasing in roughness in a matter of days (normally months), causing severe deterioration in surface quality. This was found to be caused by a fault in the automatic cleaning system that was causing the cleaning pads to wear away and degrade the roll surface. This supported the understanding that film damage was dependent on roller roughness.

9.1.11 2009 - 2010

In 2009 a team of researchers (Coles, 2009b) investigated the cause of needles on D52. This summary report concluded needles occurred both due to web/roller speed difference and debris present but could not demonstrably probe why, although they theorised it was because cleaning restores roughness. They found that the air side had fewer scratches than the drum side which they attributed to the automatic cleaner on cooling roll 1. They were also able to rule out scratches being caused by the transport rolls since cleaning here had no impact on amount of surface damage. They quantified the extent of the link between roll cleaning of CR1 and scratches (see Figure 108).

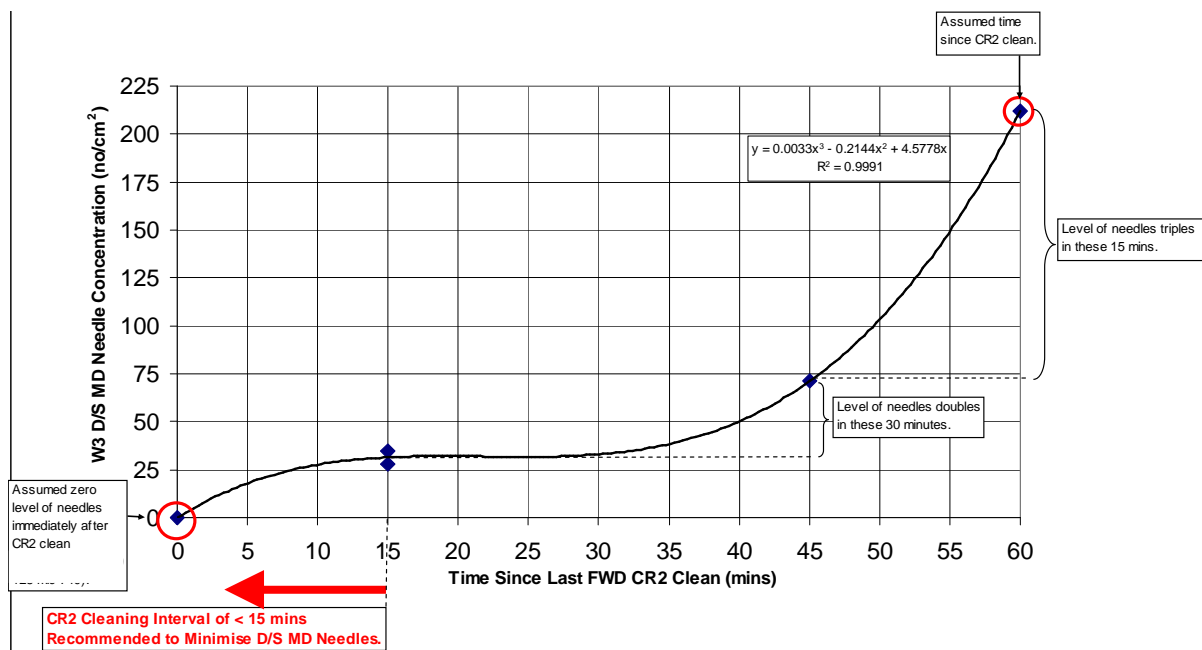


Figure 108: Graph showing the number of needle scratches vs. time in mins since last CR2 clean during clear film production.

The report subsequently made recommendations to improve surface quality. These included:

- Modify CR2 auto-cleaner at the next opportunity to match more effective CR1 auto-cleaner.

- Continue thoroughly cleaning CR1 (with ammonia solution/cleaning pad) at Clear Film entry and at every back to tray (restore surface roughness up to original).
- Assess alternative abrasive pad materials (improved cleaning/low grit shedding).
- Continue changing CR1/CR2 auto-cleaner pads at defined regular frequency.
- If necessary, increase CR1 auto-cleaner frequency for certain films

A second piece of work in 2009 by the same team (Coles, 2009a) reiterated these findings and concluded the improvements to the CR2 cleaner had improved surface quality. However, the data still implied that automatic cleaners were not sufficient to slow the decline in surface quality seen in Figure 104 above. While manual cleans were more effective in reducing scratch/needle density, the time scale over which surface quality declines (~30 mins) is not practical to implement regular manual cleans, as each time the coating heads must be removed.

This led a 2010 team (Anon, 2010) to suggest a redesign of FWD rollers in order to reduce web/roller speed difference/idling (reduces dynamic friction by 33%), having identified a link between low FWD zone tension and surface quality. They also sourced new cleaning pads for the auto cleaners which they hoped would offer a more thorough clean without too much grit shedding.

9.1.12 2011

In 2011, David Heyer published a document (Heyer, 2011) summarising what was and wasn't known about the white powder problem. This is outlined in the bullet points below:

- Scratches form mostly in the approximate MD direction, though not perfectly aligned meaning as the scratch is formed there is some movement in the direction

perpendicular to the movement of the film. This might be due to shrinkage or expansion of the film as it changes temperature.

- Damage of the film and presence of white powder is worst on the drum side and on D52, worst on the 1st and 2nd cooling rolls.
- More frequent cleaning improves surface quality – this is the primary evidence that debris is the major cause of scratching.
- However, the mechanism by which scratching occurs is still unclear. Scratch analysis by an external company showed scratches contain no remnants of debris in the scratches implying it's not the debris itself causing scratching.
- Based on roller surface analysis which showed that cleaning of rollers restores surface roughness, an alternative theory was suggested therefore that debris promotes scratching by changing surface roughness.
- Characterisation of swab tapes from CR1 found grey/green particulates of metal – mostly Al metal and Cr plus low levels of unidentifiable white powder
- Characterisation of swab tapes from CR2 found grey/green metal deposits of chrome steel and Ni plus low levels of same white powder.

9.1.13 2012

The most comprehensive debris powder analysis completed so far was conducted by (von Morgen, 2011). Debris was collected from FWD using scalpels and was found to contain some evidence of Si/Al/Ti/Ba/S – probably due to filler residues. The majority was identified to be carbon based – “white powder”. NMR showed resonances consistent with PET. Cyclic trimers/oligomers were eliminated as major components on solubility grounds and there was

no conclusive evidence of the presence of TA. MALDI showed no evidence of PET oligomers or higher mass polymer and the GPC analysis showed evidence of undegraded PET.

9.2 MECHANISMS OF SCRATCHING

Whenever a pair of contacting bodies are moved relative to each other, there is a chance that permanent plastic deformation, fracture, or material transfer could occur at the contact interface. The conditions required to produce scratches and the theoretical mechanisms which underpin scratch formation will be discussed in this section. The likelihood of any material to scratch is linked not only to the material's own intrinsic properties but also is a function of the properties of the opposing body, the relative velocity of the contact event, the load in the normal direction, the type and geometry of the contacting asperity and the tractions created by friction.

In fact, the material science and mechanics of scratching is a topic complex enough that it could be a project in its own right. The many considerations at play are displayed in Figure 109 (Lim, 2005).

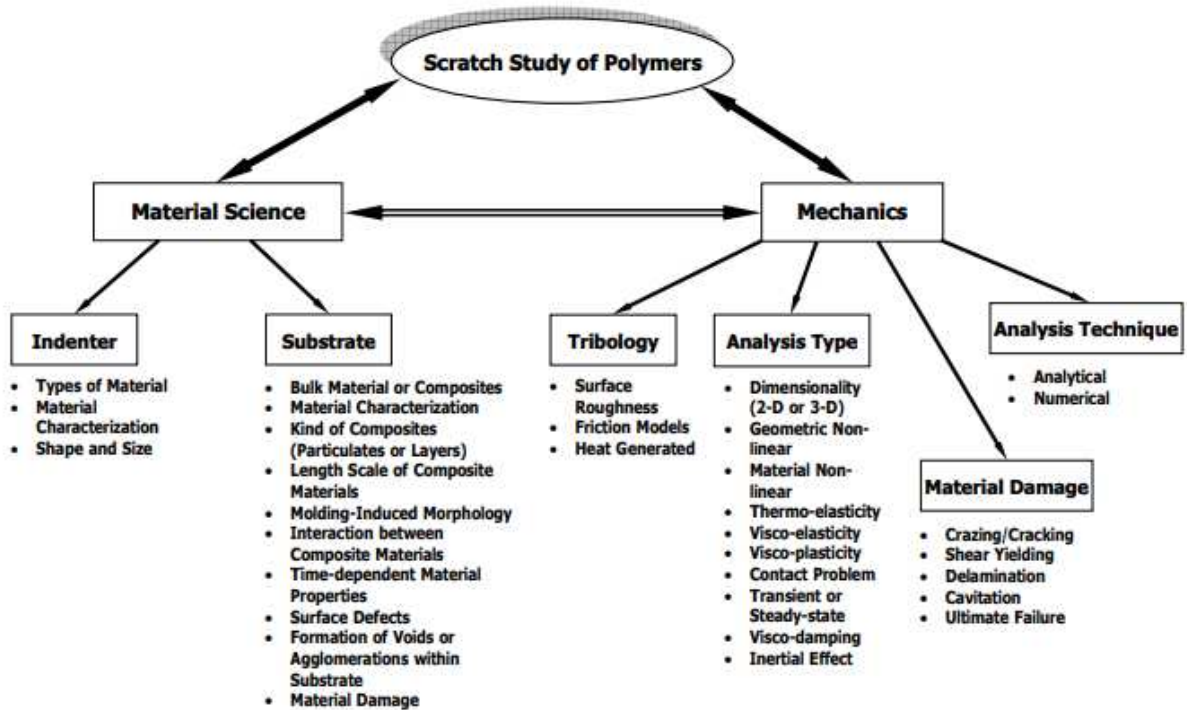


Figure 109: Summary of the material science and mechanical considerations while studying the scratching behaviour of polymers (Lim, 2005).

The result of all these factors is that the problem of understanding scratching is highly complex, such that a complete exploration is outside of the scope of this thesis. Much of the existing literature in this area is concerned with the determination of the “scratch-ability” of a material from a theoretical (Yu and Blanchard, 1996; Lim, 2005) and experimental viewpoint (Lim *et al.*, 2005). To stay relevant to the problem in question, this discussion will focus on the case of an infinitely hard surface (hereafter known as the indenter) abrading a polymer surface.

It is worth noting also that the scope of this research is to understand the line conditions which exacerbate surface scratching and defect formation. This section in the fundamentals of scratching mechanics is therefore helpful mostly for scene setting for the general principles surrounding polymer deformation.

The two halves of this problem that are most important to cover are the tribology of polymer scratching and the deformation mechanics of polymers. Understanding of these two theoretical areas provides a good grounding in scratching phenomena to inform the work of this project. Deformation mechanics will be covered first, followed by tribology.

9.2.1 DEFORMATION REGIMES

The simplest starting point for understanding scratching and wear phenomena is to understand the difference between elastic and plastic deformation regimes for a material. A material which is deforming elastically is one where, as the material is stressed, there is a proportional strain response. This means that after the stress is removed, the material returns exactly to its original shape without any permanent change. Young's modulus is defined as the gradient of the stress vs. strain curve of a material during elastic deformation.

A material which is deforming plastically is one where, as the material is stressed, the strain is not constant. In plastic behaviour the material's shape is being permanently changed by the applied stress. Plastic deformation requires a loss in energy during the applied stress, usually released as heat or noise.

Overall, a material will deform in one of four ways:

- Elastic contact deformation: reversible and independent of rate/time
- Plastic contact deformation: irreversible and independent on rate/time
- Viscoelastic deformation: reversible and dependent of rate/time
- Viscoplastic deformation: irreversible and dependent on rate/time

9.2.2 ELASTIC TO PLASTIC INDENTATION

The theory of elastic indentation as developed by Hertz and others, is discussed in section 2.3.5. These theories can be applied up until the point at which yielding occurs. It may therefore be used to predict the conditions for stress initiation.

No matter the shape of the indenter, the mechanisms for scratch formation can be generalised. In a theoretical case where an indenter approaches the surface and there are no adhesive forces, the initial contact would be a single infinitely small point. However, the presence of adhesive forces (discussed more in Section 2.2), cause the polymer to deform around the tip creating a defined contact area. During a contact event:

- First, as the normal load is increased, elastic deformation of the surface begins as the indenter penetrates below the surface level. This will continue until the yield strength of the material is reached.
- Next, the deformation will become elastic-plastic and a region of plastically deformed material will form surrounding the indenter. The remainder of the polymer continues to be in an elastic regime. If at this stage the indenter was removed, there would be an indentation but no pile-up of material.
- As normal force continues to increase, the remaining matrix can no longer remain in the elastic regime as the stress is too high and the plastic region breaks out to the free surface. This results in a pile-up forming around the indenter tip. The elastic-plastic zone boundary moves further and further from the indenter.
- Once the load is removed, the elastic and any viscoelastic deformations start to relax leaving just the plastic deformations to be imaged. For the majority of polymeric

materials, the viscoelastic relaxation time is such that it does not make any difference to an end user of a product observing a defect in a surface.

In many cases when a scratch profiler or apparatus is used to create an indent or scratch, the depression distance will be recorded. If the resulting indent is then analysed via microscopy techniques, the depth of it will be less than the recorded depression distance due to elastic and viscoelastic behaviour. This was elegantly shown in the work of Du in 2001 (Du *et al.*, 2001).

As a result of the various elastic, viscoelastic and plastic effects, the stress field around the indentation point is generally complex to determine and depends on the geometry of the indenter. In general, the stress field will be directly proportional to the normal load applied and inversely proportional to the square of the distance from the load point.

Pile-up of material during scratching is an important part of this mechanical process and is generally mediated by the ratio between Young's Modulus and material hardness. An excellent review of the various factors affecting pile up in nano-scratching by Yan *et al.* discussed the impact of factors of normal load, scratching velocity, friction between the tip and the sample, elastic recovery of the polymer material and probe geometry (Yan *et al.*, 2019). It was also found by (Geng *et al.*, 2019) that the adhesion between the tip and the sample could also influence the amount of material pile-up.

9.2.3 HARDNESS

In order for scratching to occur, the applied load must be sufficient to overcome the yield strength. This requires a high enough normal load, but also an indenter of sufficient hardness.

Beyond the elastic deformation associated with Hertz and other models (see Section 2.2), indentation with a high enough loading force results in the development of a ductile zone beneath the indenter – even in brittle materials. This zone is almost universally hemispherical in shape no matter the shape of the indenter. In a fully developed ductile contact zone the average stress exerted by the material is known as the indentation hardness. Often a more qualitative scale known as Moh's hardness scale is used to understand hardness. Moh's hardness scale ranks materials sequentially in order of hardness so that any given material will be scratched by those above it in the sequence but will not be able to scratch them in return. Therefore, the definition of an infinitely hard indenter, is one where it will deform the other surface, while itself not becoming permanently deformed in any way. Critically however, these definitions of hardness refer to an indentation hardness, which has been related to, but is not necessarily equivalent to a scratching hardness.

A scratching or ploughing hardness was first proposed by (Williams, 1996), in the context of metal scratching. This was added to subsequently by (Briscoe, Delfino and Pelillo, 1999), who referred to scratch hardness as tangential hardness, and then also by (Liang *et al.*, 1996) who referred to it as specific grooving hardness.

Indentation hardness is affected by temperature, especially at a critical threshold which is termed the glass transition temperature (T_g). The T_g represents the transition from a glass-like to rubber-like state, which is a point of change in the physical properties, such as hardness and elasticity as well as volume, percent elongation to break and Young's modulus of the polymer in question. The value of T_g is affected by the mobility of the polymer chains. The T_g of PET is typically between 70°C and 85°C.

Overall yielding of a material (the force at which it occurs, and the manner in which it occurs), is mediated by ratio of material hardness to Young's modulus. When yielding does occur it can be via tensile or ductile fracture.

9.2.4 TENSILE VS. DUCTILE FRACTURE

The majority of polymeric materials will deform elastically under low loads but will deform plastically above a critical load threshold. This threshold is referred to as the yield strength.

Despite being generally ductile materials, which fail via ductile plastic flow (deformation), polymeric materials can also fail via a tensile fracture mode. This type of failure is referred to as cracking and crazing.

Whether a polymer will deform via ductile plastic flow or fail by tensile fracture depends on the material properties at that temperature and the local distribution of stress. As long as there is asymmetry in the stress field it means yielding will occur.

As a rule of thumb, polymers may yield in shear via ductile mechanics or undergo fracture via crazing or cracking in compression. Predicting which type of damage is complex as often they can coexist. Even during a scratching process, the stress flow in the material can change from tension to compression which could induce a change from one failure mode to another.

The work of (Johnson, 1985) is still some of the most dominant in this field. Johnson states that yielding will occur at the point where maximum shear stress exceeds the yield stress in simple shear.

$$\tau_{max} = \frac{\max\{|\sigma_i - \sigma_j|\}}{2} \geq \tau_y = 2\sigma_y$$

Equation 26.

Where the proportionally related material properties τ_y and σ_y are the yield stress and tension respectively and σ_i ($i = 1-3$) are the principal stress components.

The simplest case for fracture is that tensile fracture will occur when the stress in the material exceeds the tensile fracture stress of the material σ_T , (Oxborough and Bowden, 2006)

$$\max\{\sigma_i\} \geq \sigma_T$$

Equation 27.

More sophisticated approaches to determining brittle fracture criteria take account of the influence of flaws and the role of stress concentration within the framework of fracture mechanics.

9.2.5 BRITTLE VS. DUCTILE MATERIALS

Intrinsically brittle materials are those for which the tensile yield stress greatly exceeds the tensile fracture stress. This means yielding can only be induced under special loading arrangements which avoid the development of tensile stresses. On the other hand, intrinsically ductile materials are those for which the tensile yield stress greatly exceeds the tensile fracture stress.

This work is concerned with exclusively polymeric materials which are generally ductile, especially at temperatures above glass transition. In general, a value of elastic modulus is used to describe polymeric materials. This is a measure of an object or substance's resistance to being deformed elastically when a stress is applied to it. The higher this elastic modulus the less the material is likely to scratch under the same stress since it can resist more stress before any permanent plastic change occurs.

9.2.6 UNDERSTANDING SCRATCHING MECHANICS

The goal of research is to be able to understand all the factors which affect scratch resistance of materials and morphology of scratches under different conditions. In order to achieve this an appropriate testing procedure using a reliable scratch test device needs to be developed. A test device and method need to be able to produce consistent and reproducible results and have the capability to adapt to a variety of test conditions, while reasonably controlling those factors which are not of interest. This includes environmental controls, precise force control and measurement, variation in length scales and velocity of movement, and variable indenter geometry.

Some examples of such methods at the macroscopic scales include the pencil hardness test (Guevin, 1995), scratching machine (Briscoe, Sebastian and Adams, 1994; Briscoe *et al.*, 1998; Briscoe, Delfino and Pelillo, 1999), Taber test (Kody and Martin, 1996), pin-on-disc machine (Chanda *et al.*, 1997), Ford five-finger test (Chu, Ruma and Coleman, 1997; Chu *et al.*, 2000), single-pass pendulum sclerometer (Lamy, 1984; Vingsbo and Hogmark, 1984; Liang *et al.*, 1996), scratch apparatus (Gauthier and Schirrer, 2000), Revetest scratch tester (Krupička, Johansson and Hult, 2003), and the needle test (Ramsteiner *et al.*, 2003).

After performing scratch tests in one of the above devices, the resulting scratches are analysed. This is done using one or more of various microscopy techniques such as optical, scanning electron, atomic force, or laser confocal microscopy, or other metrology techniques such as coherence scanning interferometry or ellipsometry.

9.2.7 NANOTRIBOLOGY AND ATOMIC FORCE MICROSCOPY

In a few studies, atomic force microscopy has been used to directly investigate scratching and wear. This includes the work of (Hamada and Kaneko, 1992) who used point contact

microscopy to deliberately indent polymethyl methacrylate and polycarbonate films and measure the indentation depth. They also used contact mode to “scan-scratch” the films with a tip of large radius (280 nm). While novel in their approach to nano-tribological measurements, their results and data are somewhat convoluted by the fact that imaging of the resulting indented or scratches surfaces was also done by necessity at an applied normal load using contact mode.

Other work in this area was exclusively qualitative (Yokohata and Kato, 1993; Lu, Bogy and Kaneko, 1994; Bhushan, 1998) until the work of (Han, Schmitt and Friedrich, 1999). In their work they first imaged a surface with tapping mode, then induced a scratch using contact mode and then imaged the result deformation with a subsequent tapping mode image. This methodology represents an improvement over the work of (Hamada and Kaneko, 1992) as the scratch image will theoretically not be altered by the imaging process since tapping mode is non-destructive to the sample surface. This allowed them to make quantitative measurements of their scratches with some confidence including depths and volume of pile up material.

Finally the work of (Du *et al.*, 2001) used AFM to measure ploughing friction and wear of polycarbonate films. They examined particularly the differences seen using scan angles of 0° as compared to 90°, both qualitatively but also considering the validity of quantitative conclusions based on the ease of assessing the relevant spring constant (bending in the 0° case and torsional in the 90° case). They found a directly proportional relationship between frictional force and normal applied force allowing the friction coefficient to be determined.

9.2.8 FRICTIONAL PROPERTIES OF PET

It is understood that during scratching, unless the surface is atomically flat and frictionless, the scratching contact produces friction and thus also heat. It is therefore necessary to adopt

a model for friction. The majority of work in the literature uses the Coulomb model for friction, where the friction force is given by the product of the normal force (P) and adhesive friction coefficient of the surface μ .

$$Force = \mu P$$

Equation 28.

The frictional properties of any surface depend on the intrinsic material properties and surface roughness. Surface roughness is one of the key levers pulled by materials scientists to affect material properties and performance. Often fillers are added to polymer films to induce surface roughness which can affect properties such as optical appearance and handleability.

However, this model is limited in its scope as, during the traverse of the surface during scratching, the surface that the indenter is in contact with is continually changing as it penetrates the surface into the bulk. Therefore, the frictional interactions taking place cannot be captured by equation 28 alone. The logical expectation is that as the material deforms around the indenter, the effective surface roughness and corresponding friction will increase.

9.2.9 BULK PROPERTIES OF PET

The final part of polymer scratching which introduces yet more complexity, is that PET is not isotropic or homogenous. PET is known to contain regions of amorphous matrix, where the polymer chains are randomly positioned, and areas of crystallinity where the chains are aligned with each other. (De *et al.*, 1954; Thompson and Woods, 1956; Johnson, 1959; Beamson *et al.*, 1996).

The biaxial orientation process employed by DTF that is described in Section 1.5 increases the crystallinity of the PET film by several orders (Adams and Gerber, 1957) making crystallinity

even more pertinent to this report. In response to an indenter, crystalline regions are more likely to deform by tensile fracture, whereas amorphous regions are more likely to fail by plastic ductile flow.

However, when examining indentation hardness of DTF films at a nano-scale, (Beake and Leggett, 2002) found that an additive law applied; the indentation hardness was found to be the sum of the hardness of the volume fractions of amorphous and crystalline material:

$$H = w_c H_c + (1 - w_c) H_a$$

Equation 29.

Where H_c and H_a are the microhardness of crystalline and amorphous phases respectively. As a result, the surface can be considered homogeneous for indentation hardness. Whether this holds true for scratching hardness is not known in the literature.

The work of this same report also found a critical difference in the elastic modulus of films of different crystallinity. It was found that more crystalline films exhibited higher hardness and higher elastic modulus, as well as being less susceptible to creep deformation than the films of lower crystallinity. They also found that the plasticity index, the ratio of the dissipated energy to the total indentation energy is greater on the more amorphous films, indicating that they exhibit less plastic deformation than the more crystalline films.

9.3 STICK-SLIP BEHAVIOUR

Stick-slip motion is defined as relative movement where the traction forces and speed are constantly changing as motion is continually arrested and re-initiated. It is clear during scratch formation on the DTF production line the nature of the motion occurring during scratch formation will affect the resulting morphology of scratches. This was well reviewed by (Berman, Ducker and Israelachvili, 1996). The general condition for stick-slip motion is that the static friction coefficient is greater than the dynamic friction coefficient. This relationship can be affected by surface adhesion, surface topography, strain hardening of the polymer and the loading arrangement.

Observations of scratching phenomena on PET films by Smyth (Smyth et al., 1998) found that the propensity for stick-slip motion was strongly affected by surface adhesion, as examination of “sticking” spots was associated with small, well-defined adhering contact spots. These spots were able to sustain large shearing traction loads before motion could be re-initiated.

9.4 ALL ADHESION EXPERIMENTS

#	Location	Tip shape	Tip Material	Tip origin	k (N/m)	User	Condition	Samples	Notes	Mica > PET?
1	Wilton	Colloidal	borosilicate	In-house	2.6	A	Ambient	PET: various thicknesses	Low variability	
2	Wilton	Colloidal	borosilicate	In-house	7	A	Ambient	PET: various thicknesses	Curved baselines	
3	Wilton	Colloidal	borosilicate	In-house	2.6	A	Ambient	PET: various thicknesses	Curved baselines	
4	Wilton	Colloidal	borosilicate	In-house	0.2	A	Ambient	PET: various thicknesses	Curved baselines	
5	Wilton	Colloidal	borosilicate	In-house	4.2	A	Ambient	PET: various thicknesses	High variability between locations	
6	Wilton	Colloidal	borosilicate	In-house	4.2	A	Ambient	PET: Cast and FF	Low variability, samples distinct	
7	Wilton	Colloidal	borosilicate	In-house	4.2	A	Ambient	PET: Cast and FF	Ok variability, samples indistinct	
8	Wilton	Sharp	Si ₃ N ₄	Purchased	1	A	Ambient	Graphite	High variability between locations	
9	Wilton	Colloidal	borosilicate	In-house	0.32	A	Ambient	PET FF, Roller, Mica	Low variability, samples distinct	Yes
10	Wilton	Colloidal	borosilicate	In-house	7.6	A	Ambient	PET: FF & Cast, Roller, Mica	Noticed change over time effects	No
11	Wilton	Colloidal	borosilicate	In-house	7.6	A	Ambient	PET	Examining effect of collection rate	No
12	Wilton	Sharp	Si ₃ N ₄	Purchased	0.06	A	Ambient	Mica	Examining effect of collection rate	
13	Wilton	Colloidal	borosilicate	In-house	2.6	A	Ambient	Mica	Examining change over time at same location	
14	Wilton	Colloidal	borosilicate	In-house	0.2	A	Ambient	PET FF, Mica	Examining effect of collection rate	No
15	Wilton	Undefined	Debris	In-house	0.2	A	Ambient	Mica	Examining change over time at same location	
16	Wilton	Undefined	Debris	In-house	7.6	A	Ambient	PET FF, Roller, Mica	Surfaces could not be distinguished	=
17	Wilton	Sharp	Si ₃ N ₄	Purchased	9	A	Ambient	PET FF, Roller, Mica	Samples could be distinguished	No
18	Wilton	Sharp	Si ₃ N ₄	Purchased	9	A	Ambient	PET FF, Roller, Mica	Curved baselines	No
19	Wilton	Colloidal	borosilicate	In-house	2.8	A	Ambient	PET FF, Roller, Mica	High variability between locations	Yes

20	Wilton	Colloidal	borosilicate	In-house	9	A	Ambient	Mica	Good consistency	
21	Wilton	Colloidal	borosilicate	In-house	2.8	A	High temps	PET FF, Roller, Mica	Large variability, couldn't get measurements on PET surface	No
22	Wilton	Colloidal	borosilicate	In-house	7.6	A	High temps	Mica	High variability depending on trigger threshold	
23a	Wilton	Colloidal	borosilicate	In-house	2.4	A	Ambient	PET: FF rough and smooth	Surfaces distinguishable, roughness increases standard deviation	
23b	Wilton	Sharp	Si ₃ N ₄	Purchased	3	A	Ambient	PET: FF rough and smooth	Surfaces indistinguishable, roughness increases standard deviation	
24	Wilton	Colloidal	borosilicate	In-house	3	A	Ambient	PET: FF, FWD & Cast, Roller, Mica	Good consistency	=
25	Wilton	Colloidal	borosilicate	In-house	2.7	A	High temps	PET: FF, FWD & Cast, Roller, Mica	Adhesion increases with temperature, error increases with temperature	No
26	Wilton	Colloidal	borosilicate	In-house	2.7	A	High temps	PET: FF, FWD & Cast, Mica	Temperature dependence is crystallinity moderated	No
27	Wilton	Colloidal	borosilicate	In-house	2.7	A	High temps	PET: FF, FWD & Cast, Mica	Temperature dependence is crystallinity moderated	No
28	Wilton	Colloidal	borosilicate	In-house	2.7	A	Ambient	Roller, Mica	Good consistency	
29	Wilton	Sharp	Si ₃ N ₄	Purchased	2.7	A	Ambient	PET FF, Mica	Testing variety of normal forces	Yes
30	Wilton	Sharp	Si ₃ N ₄	Purchased	35	A	Ambient	PET FF, Mica	Testing variety of normal forces	Yes
31a	Wilton	Colloidal	borosilicate	In-house	2.7	A	Ambient	PET FF, Mica	Comparing colloidal tips	Yes
31b	Wilton	Colloidal	borosilicate	Purchased	2.7	A	Ambient	PET FF, Mica		No
32a	Wilton	Sharp	Si ₃ N ₄	Purchased	0.2	A	Ambient	PET FF, Mica	Comparing sharp to colloidal tip	Yes
32b	Wilton	Colloidal	borosilicate	Purchased	0.3	A	Ambient	PET FF, Mica		No
33a	Wilton	Sharp	Si ₃ N ₄	Purchased	0.2	A	Ambient	PET FF, Mica	Comparing sharp to colloidal tip	Yes
33b	Wilton	Colloidal	borosilicate	Purchased	0.3	A	Ambient	PET FF, Mica		No
34a	Wilton	Sharp	Si ₃ N ₄	Purchased	0.2	A	Ambient	PET FF, Mica	Comparing sharp to colloidal tip	Yes

34b	Wilton	Colloidal	borosilicate	Purchased	0.3	A	Ambient	PET FF, Mica		No
35a	Wilton	Sharp	Si ₃ N ₄	Purchased	3	A	Ambient	PET FF, Mica	Comparing sharp to colloidal tip	Yes
35b	Wilton	Colloidal	borosilicate	Purchased	5	A	Ambient	PET FF, Mica		No
36	Birmingham	Colloidal	borosilicate	Purchased	1.65	B	Ambient	PET FF, Mica	Repeat exactly the same procedure to check consistency but with no cleaning. Good consistency	No
37	Birmingham	Colloidal	borosilicate	Purchased	1.65	B	Ambient	PET FF, Mica		No
38	Birmingham	Colloidal	borosilicate	Purchased	1.65	B	Ambient	PET FF, Mica		No
39	Birmingham	Colloidal	borosilicate	Purchased	1.65	B	Ambient	PET FF, Mica		No
40	Birmingham	Colloidal	borosilicate	Purchased	1.65	B	Ambient	PET FF, Mica	Introduced a tip clean before each sample	Yes
41	Birmingham	Colloidal	borosilicate	Purchased	1.21	B	Low humidity	PET FF, Mica	No cleaning	No
42	Birmingham	Colloidal	borosilicate	Purchased	1.21	B	Low humidity	PET FF, Mica	Cleaned tip before each sample	Yes
43	Wilton	Colloidal	borosilicate	Purchased	1.5	A	Ambient	PET FF, Mica	Introduced tip cleaning, reduced overall values but trend remained the same	No
44	Birmingham	Colloidal	borosilicate	Purchased	1.7	A	Ambient	PET FF, Mica	Data inconsistent	
45	Birmingham	Colloidal	borosilicate	Purchased	1.7	A	Ambient	PET FF, Mica	Data inconsistent/curved baselines	
46	Birmingham	Colloidal	borosilicate	Purchased	1.7	A	Ambient	PET FF, Mica	Data inconsistent/curved baselines	
47	Birmingham	Colloidal	borosilicate	Purchased	1.7	A	Ambient	PET FF, Mica	Data inconsistent/curved baselines	
48	Birmingham	Colloidal	borosilicate	Purchased	1.75	A	Ambient	PET: FF, FWD & Cast, Roller, Mica, Graphite	Curved baselines on mica, rest ok	Yes
49	Birmingham	Colloidal	borosilicate	Purchased	1.75	A	Ambient	PET: FF, FWD & Cast, Roller, Graphite	Graphite had high variability	
50	Birmingham	Colloidal	borosilicate	Purchased	1.75	A	Low humidity	PET: FF & Cast, Roller, Graphite	Good consistency	
51	Birmingham	Colloidal	borosilicate	In-house	1.62	A	Low humidity	PET: FF & Cast, Roller, Graphite	Bad consistency	

52	Birmingham	Colloidal	borosilicate	In-house	1.62	A	Ambient	Mica, Graphite, Glass	Bad consistency	
53	Birmingham	Colloidal	borosilicate	In-house	2.14	B	Ambient	PET FF, Mica, Graphite	Bad consistency	Yes
54	Birmingham	Colloidal	borosilicate	In-house	2.14	A	Ambient	PET FF, Mica	Good consistency	Yes
55	Birmingham	Colloidal	borosilicate	In-house	2.14	A	Liquid	PET FF, Mica	Good consistency	No
56	Wilton	Colloidal	PE	In-house	2	A	Ambient	PET FF, Mica	Bad consistency	Yes

9.5 MODELLING ADHESION

9.5.1 MODEL BASIS

Based on the work of (Xiao and Qian, 2000; Rabinovich *et al.*, 2002), which are still some of the most comprehensive empirical models that can include both surface roughness and humidity, a model was built. The inputs of contact angles, relative humidity, surface roughness, and contact radius were to calculate adhesion for the surfaces of interest. This is shown schematically in Figure 110.

As mentioned above this was originally used to help predict the trends rather than absolute values of adhesion. The surfaces of interest were measured using goniometer to find their contact angle with water values. Of particular interest were the trends of adhesion with humidity as the relative humidity on the production line within DTF are kept deliberately high (50-60%) to aid in other processing aspects.

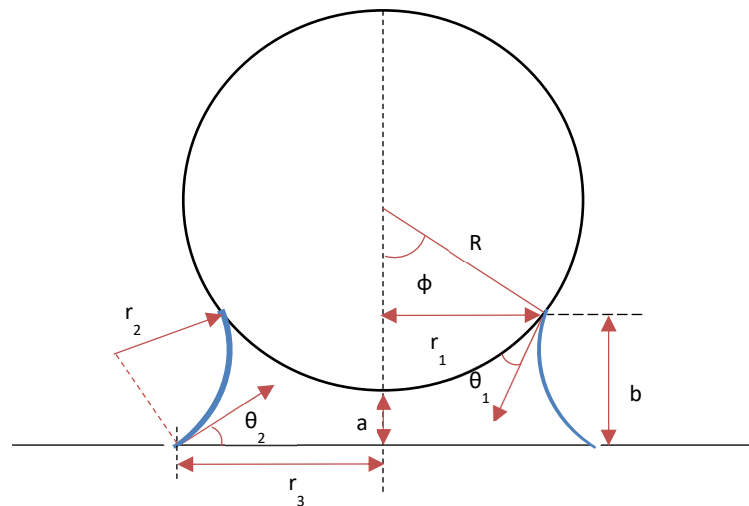


Figure 110: Schematic of sphere on plane contact for predicting adhesion from theory.

In line with the understanding that there will be a critical relative humidity where the calculation of adhesion will require the inclusion of capillary forces, the force of adhesion above this threshold ($F_{adh, wet}$) was taken to be:

$$F_{adh, wet} = F_{capillary} + F_{vdW}$$

Equation 30

With $F_{capillary}$ being solved by equation

$$F_{capillary} = 4\pi\gamma_L R \left(\frac{\cos\theta_1 + \cos\theta_2}{2} \right) \left[1 - \frac{a}{2r_2 \left(\frac{\cos\theta_1 + \cos\theta_2}{2} \right)} \right]$$

Equation 31

Where R is the radius of the contacting sphere, γ_L is the surface tension of water, θ_1 and θ_2 are the contact angles with water for the sphere and the surface, r_2 is the radius of curvature of the meniscus formed between the surface and the sphere and according to the empirical theory put forward by (Rabinovich *et al.*, 2002), a , the separation distance was taken to be:

$$a = 1.817 \cdot RMS$$

Equation 32

Where RMS is the root mean square value for the surface. r_2 is found from the Kelvin equation according to:

$$r_2 = \frac{-V\gamma_L}{N_a k T \ln\left(\frac{P}{P_s}\right)}$$

Equation 33

Where N_a is Avogadro's number, k is the Boltzmann constant, T is temperature and V is the molar volume of water, P/P_s is the relative humidity expressed as a fraction.

And the van der Waals contribution calculated via:

$$F_{vdw} = \frac{AR}{6(a_0 + 2r_2 \cos \theta_2)^2}$$

Equation 34

Where the A is the Hamaker constant in water as suggested by (Rabinovich *et al.*, 2002) and a_0 is the minimum separation distance where as recommended by (Israelachvili and Adams, 1977) for the case of van der Waals approximations a is taken to be $\sim 2 \times 10^{-10}$ m.

If the above calculation returned a value less than zero, indicating that the critical relative humidity has not been reached, instead the dry adhesion is calculated according to:

$$F_{adh,dry} = \frac{3\pi\gamma_s R \lambda^2}{(\lambda^2 + 58.14R \cdot RMS)^2} + \frac{AR}{6(a_0 + 1.817RMS)^2}$$

Equation 35

Where A is the Hamaker constant for air, γ_s is the surface energy of the surface, and λ is the average separation distance between asperities on the surface. This relation of roughness to dry adhesion was assessed by (Laitinen *et al.*, 2013) who found good correlation to dry adhesion measurements by colloidal probe AFM as long as the values for RMS roughness and λ were accurate in trends, but tended to under-predict true values. They theorised this was due to colloidal roughness effectively increasing contact area. They found however that this

model was on average an order of magnitude better at predicting adhesion than its predecessor - the Rumpf model (Rumpf, 1953).

A small decay factor was added to this proportional with relative humidity to reflect the fact that even prior to the critical humidity, the value of dry adhesion will be decreasing due to the decrease in Hamaker constant as the transition from air medium to water medium occurs.

9.5.2 MODEL INPUTS

The inputs for the model for the samples of interest are listed in Table 16. Since the exact composition of the roller surface is not known it was omitted from the model. It was also omitted since the high roughness value (orders of magnitude larger than the film) disqualifies it from being applicable to the model above which is for nanoscale roughness. Values of Hamaker for mica were taken from (Bergstrom and Ennart, 1997). Hamaker values for PET were taken from (Wang *et al.*, 2015). In all cases the contacting sphere was assumed to be made of SiO₂.

	Mica	PET
Hamaker ($A \times 10^{-20}$) in air	8	9
Hamaker ($A \times 10^{-20}$) in water	0.7	0.9
γ_s (determined experimentally using goniometry: harmonic)	72	50
a_0 / nm (REF)	0.2	
RMS /nm (Determined experimentally by CSI)	0.5	2
θ_1 / rad (determined experimentally)	0.35	
θ_2 / rad (determined experimentally)	0.27	1.31
γ_L / N/m	0.07286	
V / m^3	1.8×10^{-10}	
λ / nm	100	

Table 16: Values used in model of adhesion.

9.5.3 ASSUMPTIONS OF THE MODEL

The model makes the following assumptions:

1. $R \gg r_2$. The radius of the sphere (AFM tip) is much larger than the radius of the meniscus of the capillary layer. In the case of colloidal probe AFM this holds. In the case of sharp AFM tips, it may not.
2. The contacting sphere is smooth. The model does however include an optional factor of surface roughness of the surface in the value of a via Equation 32.

3. No deformation occurs during wet contact. This will likely hold for mica and the roller but may not for the PET sample.
4. There are no contributions from bonding or electrostatic interactions. This should largely be the case, especially if the contact duration is long enough that the system comes to equilibrium.
5. An experimentally derived RMS and λ value capture the entirety of the surface roughness.
6. $R \approx \lambda$. Since the addition of the surface roughness terms in Equation 35 are empirically derived, this model is only valid for a range of λ values.

Theoretically, if a surface has regularly spaced protrusions of a given height, then during contact, a sphere will touch the tops of these asperities and the adhesion will be effectively reduced compared to a perfectly smooth surface. As the λ spacing increases however, there will be a point where the spacing is large enough that the tip will come into contact with the surface between the asperities, increasing the contact area of contact and thereby increasing adhesion.

However, it will also be the case that at infinitely small λ the sphere will contact such a large number of the tops of these asperities that it will be effectively as though it is contacting a flat surface. Therefore, it can be predicted that there will be a quadratic like relationship between λ and adhesion for a particular value of R , where at infinitely small λ adhesion will be high, and at infinitely large λ , adhesion will also be high, with a minimum value between the two extremes that depends upon the value of R .

However, this theory is not reflected in the mathematics of the model as shown by Figure 111 below, and the top-down view of the modelled surfaces shown in Figure 112.

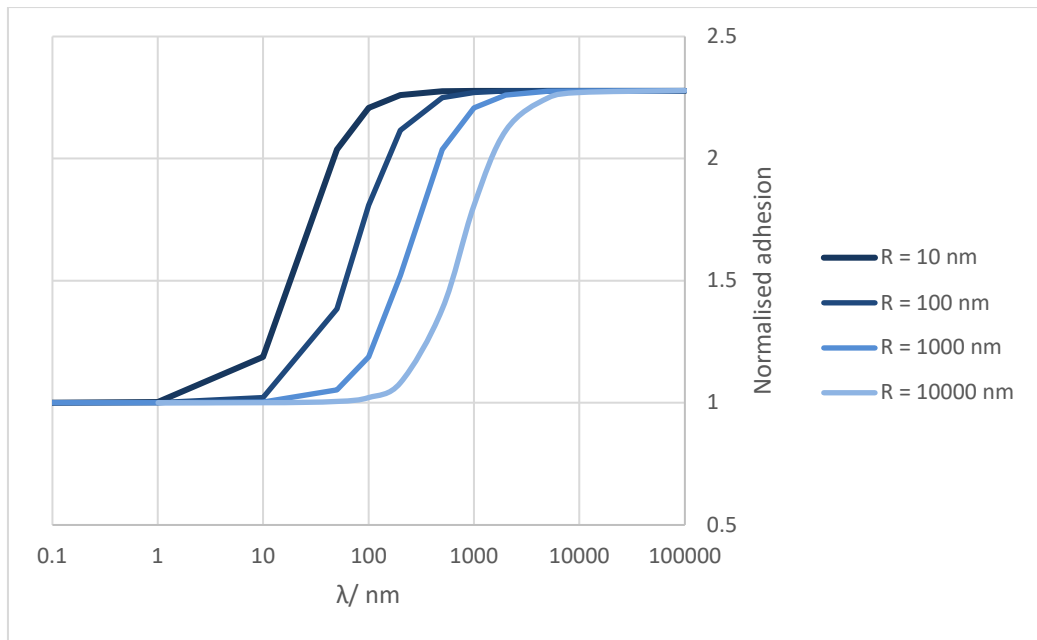


Figure 111: Graph of normalised dry adhesion against λ values for sphere's of different radii.

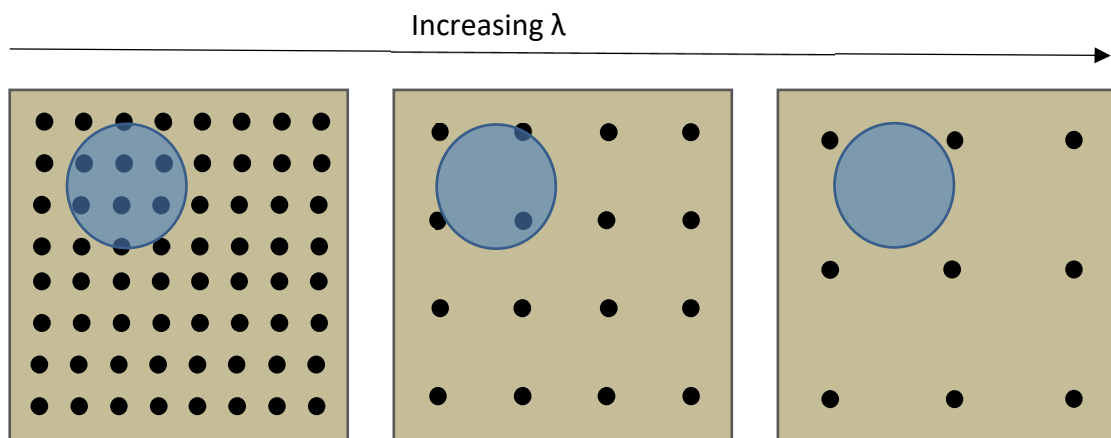


Figure 112: Schematic to show how varying models the surface compared to a sphere of a given radius (blue). Going from small λ on the left to large λ on the right.

Adhesion is normalised to allow easy comparison of the modelled data here. The model does not reflect the case of the infinitely small λ value, only the increase caused by increasing λ with the point of this increase increasing with increasing sphere radius. As such the model is only valid for values of λ which are no more than 2 orders of magnitude smaller than R . Therefore, a value of λ was selected and maintained throughout use of the model.

9.5.4 RESULTS OF THE MODEL

For the case of a 5 μm radius colloidal tip, contacting perfectly smooth surfaces of PET and mica the wet and dry adhesion predicted by the model is shown in Figure 113.

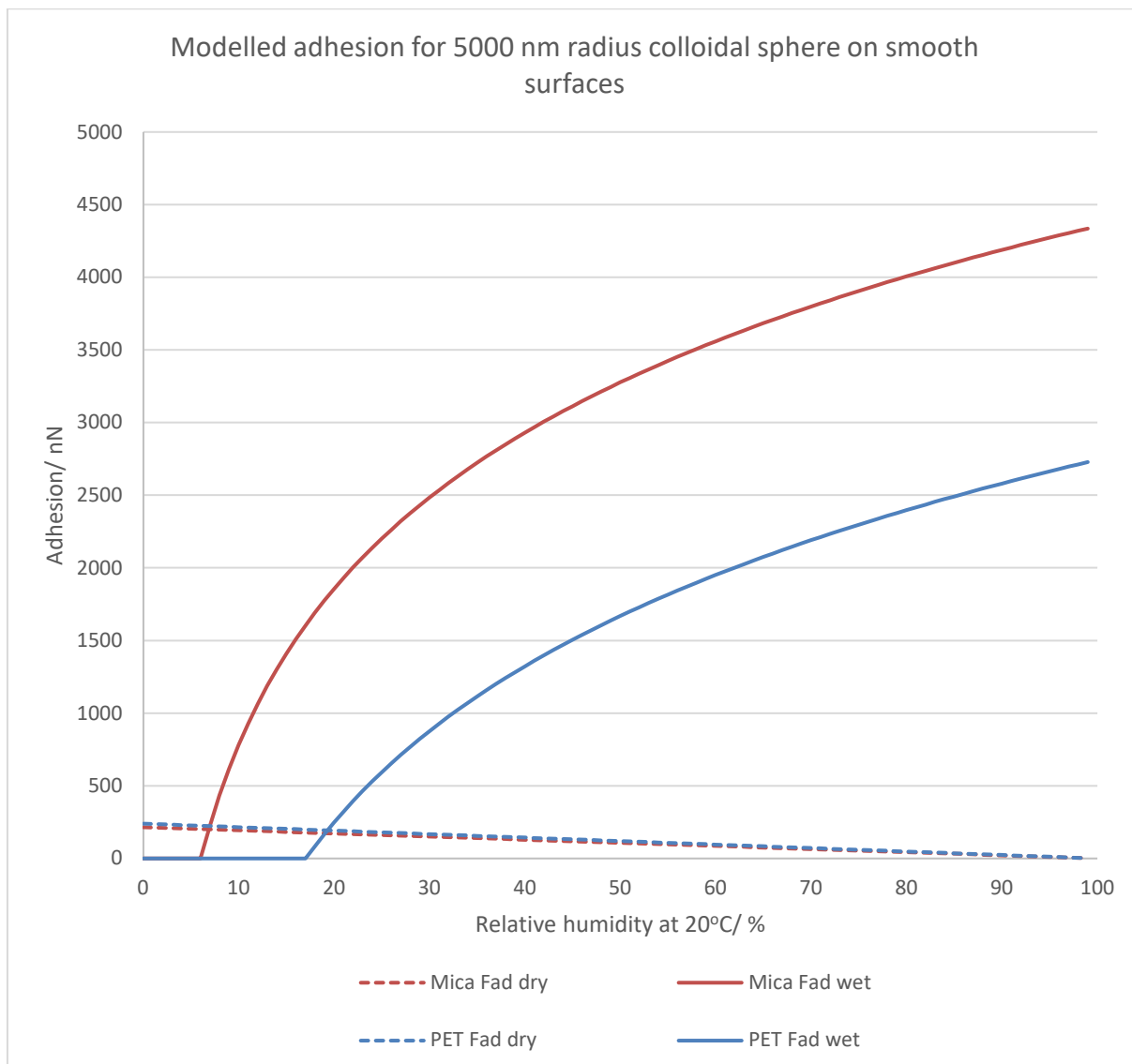


Figure 113: Graph of adhesion vs relative humidity at 21°C for a 5000 nm radius sphere contacting perfectly smooth surfaces of PET and mica.

The adhesion values in this case show a critical relative humidity of 7% for mica and 18% for PET, with a dependence on relative humidity thereafter. The capillary forces possible at higher humidity values far exceed the possible values of dry surface adhesion. The difference in

critical relative humidity between the surfaces is due to their difference in hydrophobicity. At very low humidity, where the value of adhesion should be taken as the dry adhesion value, PET has a slightly higher adhesion than mica due to its slightly higher Hamaker value.

For the case of a 0.005 μm radius sharp AFM tip contacting perfectly smooth surfaces of PET, and mica, the wet and dry adhesion predicted by the model is shown in Figure 109.

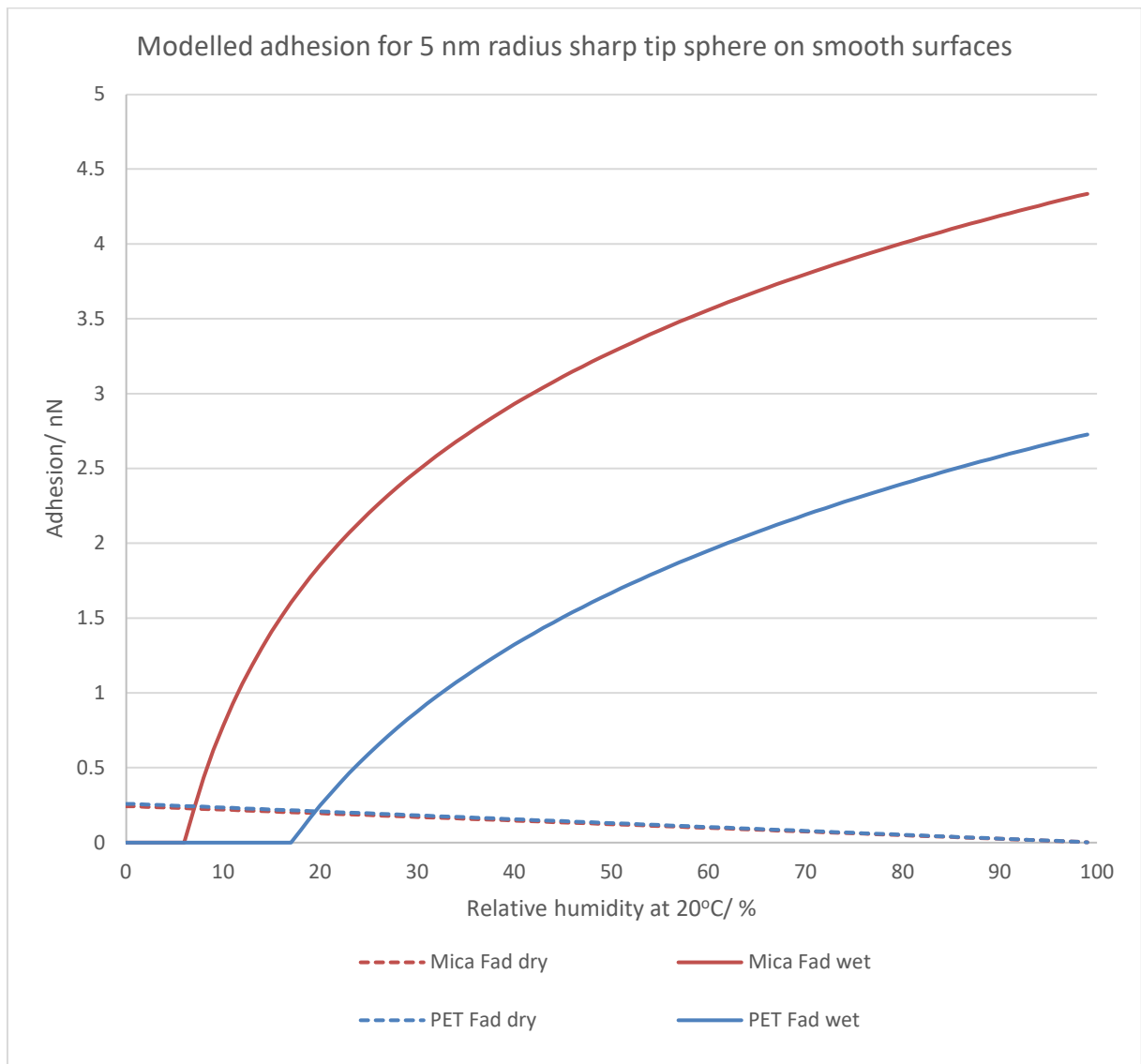


Figure 114: Graph of adhesion vs relative humidity at 21°C for a 5 nm radius sphere contacting perfectly smooth surfaces of PET and mica.

Comparing Figure 113 and Figure 114 they show identical trends, with critical humidity values again falling at 7 and 18% for mica and PET respectively, but with absolute values orders of magnitude apart. This is expected due to the reduced contact area and is one of the reasons colloidal probe AFM is used, as using a normal probe produces values which are too small to detect via direct measurement. As before the value of PET adhesion only exceeds that of mica between 0 and 7% relative humidity due to the larger dry adhesion.

For the case of a 5 nm and 5000 nm radius AFM tips, contacting surfaces of PET and mica with roughness values as in Table 16, the total adhesion predicted by the model is shown in Figures 115 and 116. The values are plotted logarithmically for clarity.

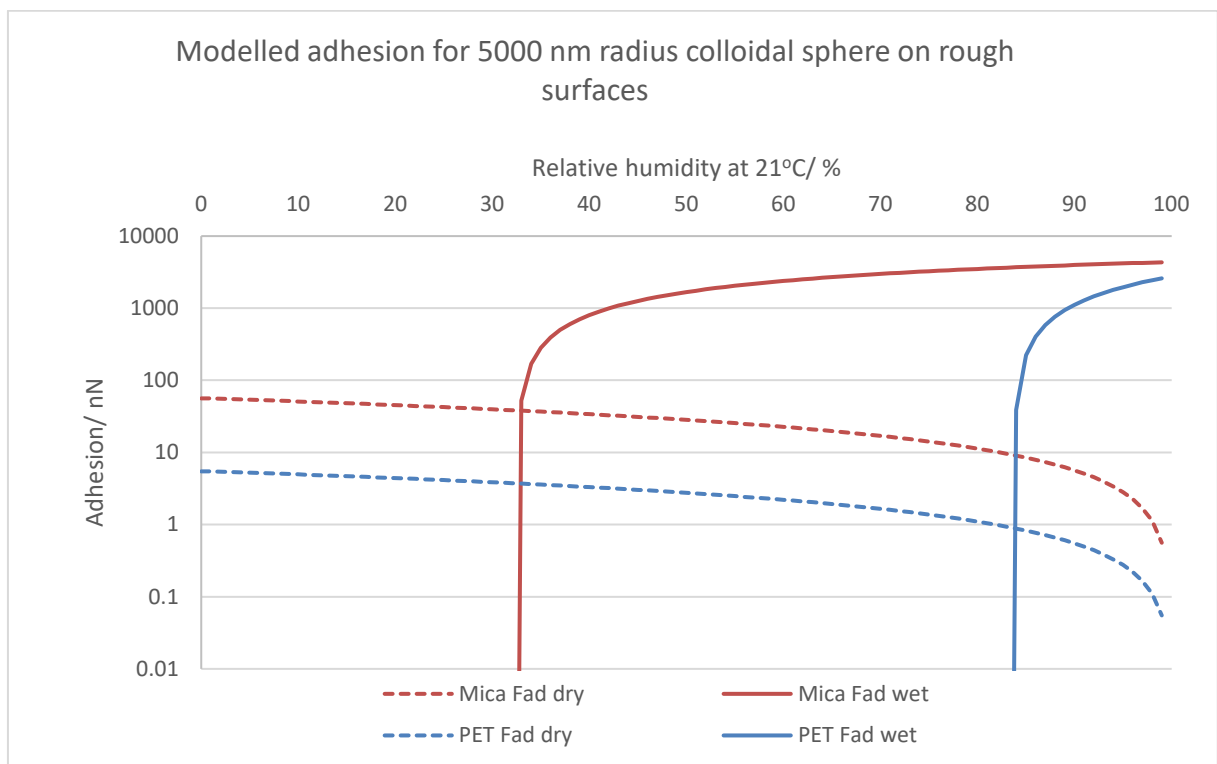


Figure 115: Graph of adhesion vs relative humidity at 21°C for a 5000 nm radius sphere contacting surfaces of PET and mica with RMS values of 2 and 0.5 nm respectively.

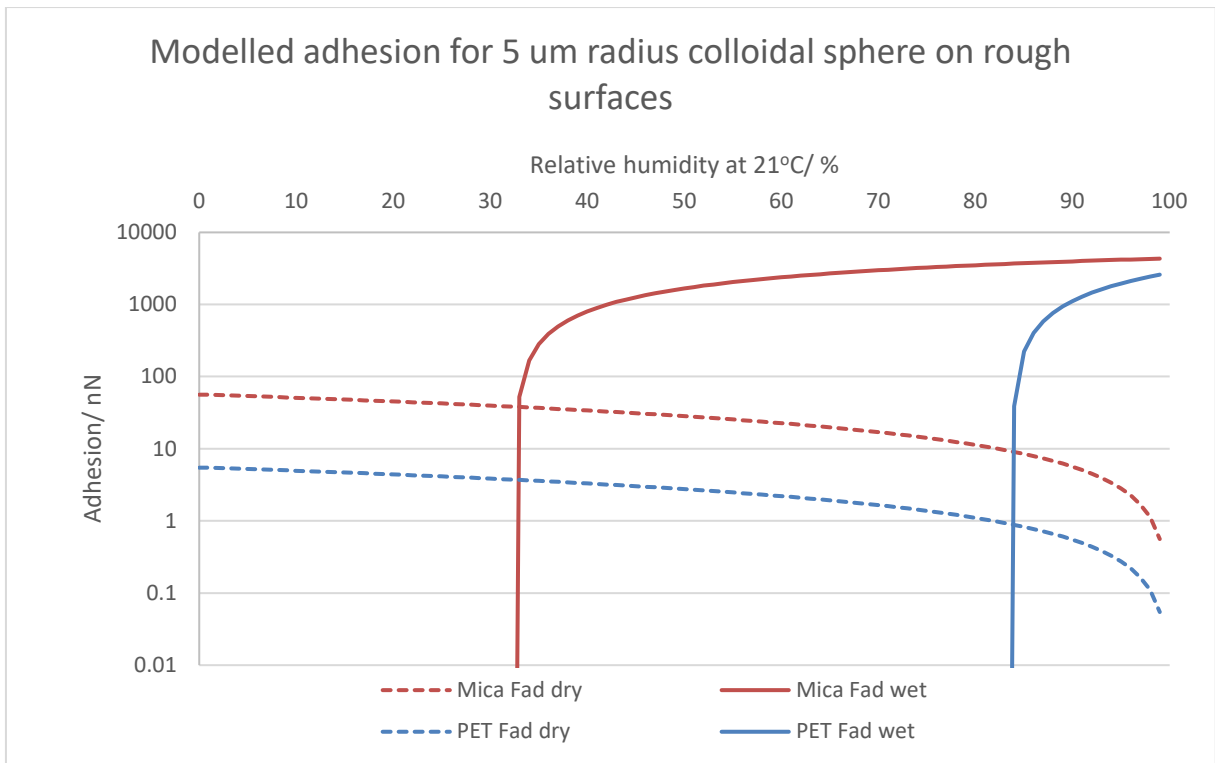


Figure 116: Graph of adhesion vs relative humidity at 21°C for a 5 nm radius sphere contacting surfaces of PET and mica with RMS values of 2 and 0.5 nm respectively

The introduction of surface roughness dramatically changes both the order of magnitude of the absolute values, but also the values of critical relative humidity which now fall at 34% for mica and 84% for PET. The difference in the order of magnitude that is introduced by surface roughness is due to the reduction in effective contact area of the adhesive contact. This captured the idea that the surface is less able to form a capillary bridge, which explains the increase in critical relative humidity. Critical relative humidity on mica is increased less than for PET both because it is a more hydrophilic surface, and also because mica has a smoother surface than PET. Even below critical relative humidity mica has a higher adhesion value than PET in contrast to the smooth case, which is also due to mica having a smoother surface than PET. The trends are the same for the two AFM tip cases, with, as before, the absolute values for the 0.005 μm case being several orders of magnitude lower.

According to this modelling work it can be seen that the balance of vdW forces and capillary forces is crucial to understand, but difficult to model. Above a critical humidity (which depends on surface roughness and surface hydrophobicity) capillary forces will dominate, and the most hydrophilic surface will be the most adhesive. Below this threshold, the adhesion is much lower in absolute value.